Unraveling Structure-Property Relationships in Polymer Blends for Intelligent Materials Design

A DISSERTATION
SUBMITTED TO THE FACULTY OF THE GRADUATE SCHOOL
OF THE UNIVERSITY OF MINNESOTA
BY

Matthew Tyler Irwin

IN PARTIAL FULFILLMENT OF THE REQUIREMENTS
FOR THE DEGREE OF
Doctor of Philosophy

Timothy P. Lodge

August 2016

Acknowledgements

My time in graduate school has been marked by numerous meaningful experiences, collaborations, and relationships, and it's certainly challenging to distill five years worth of memories into two pages. I first want to thank my advisor, Tim Lodge, for his help and guidance throughout my entire time in graduate school. The support and freedom that Tim has given me during these past five years has allowed me to investigate a variety of research topics that I personally found meaningful and interesting, and I believe that this experience has helped me understand what it means to be a successful research scientist.

I also want to thank Rob Hickey, who has been a close collaborator and good friend throughout much of my time at the University of Minnesota. Our work together has shown me that productive research can consist of forming pie-in-the-sky theories that can be readily tested by well-designed experiments. I also would like to thank my other collaborators with whom I have had the opportunity to work throughout graduate school: Lucas McIntosh, Morgan Schulze, Aaron Lindsay, and Marc Hillmyer on polymer electrolyte membranes; Tim Gillard and Frank Bates on ternary polymer blends; Shuyi Xie, Soonyong So, and Frank Bates on salt-doped ternary polymer blends; and Rob Hickey and Frank Bates on sphere-forming block polymers. Thanks also to Prof. Nitash Balsara for inviting me to his lab and Dr. Didier Devaux for spending an entire week with me to teach me about lithium battery fabrication, assembly, and characterization. This insightful experience opened my eyes to the possibility of performing many of the experiments detailed in this thesis.

I am also grateful for the consistently friendly and collaborative culture of the

Lodge, Bates, Hillmyer, and Mahanthappa groups. Brian Habersberger and Adam Moughton spent many hours helping me get started in the lab, and Cecilia Hall, Sujay Chopade, Sid Chanpuriya, Alex Mannion, Ron Lewis, Tessie (Panthani) Ewert, Chris Thurber, Seyoung Jung, Peter Schmidt, Aakriti Kharel, Jenny Laaser, John McAllister, Megan Hoarfrost Beers, Gray Jackson, Andrew Peters, Kyungtae Kim, and many others frequently took time out of their days to discuss research and a plethora of other topics with me. Thanks also to my classmates who helped me slog through pages of derivations for Fluid Mechanics and Transport problem sets. The camaraderie we built through those late nights persisted throughout graduate school, and I always knew I had help outside my lab any time that I needed it.

Finally, thanks to my fiancé, Trí, and my family both in Minnesota and Tennessee for their constant love and support throughout my Ph.D. studies. Research doesn't always go as planned, and I am grateful to have a such a caring and considerate support network. I couldn't have made it without you.

Dedication

For Trí and my family.

Abstract

Block polymers provide an accessible route to structured, composite materials by combining two or more components with disparate mechanical, chemical, and electrical properties into a single bulk material with nanoscale domains. However, the characteristic lengthscale of these systems is limited, and the choice of components is restricted to those that are able to undergo microstructural ordering at accessible temperatures. This thesis details routes to overcoming these limitations through the addition of a lithium salt, a blend of homopolymers, or both. Chapter 2 describes a study wherein complex sphere phases such as the Frank-Kasper σ phase can be observed in otherwise disordered asymmetric block polymers through the addition of a lithium salt. Chapter 3 discusses the development and characterization of a ternary polymer blend of an AB diblock copolymer and A and B homopolymers doped with a lithium salt. Detailed characterization showed that doping blends that are otherwise disordered with lithium salt induced microstructural ordering and largely recovers the phase behavior of traditional ternary polymer blends. A systematic study of the ionic conductivity of the blends at a fixed salt concentration demonstrates that, at a given composition, disordered, yet highly structured blends consistently exhibit better conductivity than polycrystalline morphologies with long range order. Chapter 4 extends the methodology of Chapter 3 and details a systematic study of the effects of cross-linker concentration on the performance of polymer electrolyte membranes produced *via* polymerization-induced microphase separation that exhibit a highly structured, globally disordered microstructure. Finally, Chapter 5 details efforts to develop a water filtration membrane using a polyethylene template derived from a polymeric bicontinuous microemulsion. Throughout all of this work, the goal is to better understand structure-property relationships at the molecular level in order to ultimately inform design criteria for materials where simultaneous control over morphology and mechanical, chemical, or electrical properties is important.

Contents

List of Tables

List of Figures

Chapter 1

Background

1.1 Introduction

Modern technology drives innovation in materials science, demanding the ability to create and control structure and properties at smaller and smaller lengthscales. There is a growing need for materials that can combine two or more components with disparate material or chemical properties, yet are macroscopically homogeneous. For example, rechargeable lithium batteries that employ a lithium metal anode are projected to have a twenty-fold increase in energy density compared to conventional lithium ion batteries,[1,2] but the formation of lithium metal dendrites upon cycling prematurely short out the battery.[3–8] Replacing the liquid electrolyte currently used in such batteries with a solid electrolyte composite of a mechanically robust component and an ionically conductive component is projected to mitigate the formation of dendrites while maintaining sufficient power delivery for end-user applications, thereby overcoming the major hurdle that limits commercial adoption of the technology.[9,10] In a similar vein, the performance of bulk heterojunction solar cells is limited by the fraction of exciton electron-hole pairs, formed *via* sample irradiation, that recombine with each other prior to being separated into electron donor and acceptor materials. One route to improving the properties of such solar cells is to make the donor and acceptor materials co-continuous with domain spacings on the order of 10 nm, the approximate electron-hole

diffusion length prior to recombination.[11–18] The performance of filtration membranes is also tied to the underlying structure of the material. In such systems, achieving high permeability requires that the matrix material is mechanically robust enough to withstand large applied pressures, while high selectivity is achieved by ensuring that the pore size is well-controlled.[19–24] In all of these cases, simply developing a bulk material with a single set of properties is insufficient for simultaneously meeting all necessary design criteria.

One relatively simple route to composite materials is through the use of block polymers, which consist of two or more chemically distinct polymers covalently bound together. These macromolecules exhibit a variety of nanoscale morphologies with characteristic lengthscales of 5 to 50 nm that can be "dialed in" by tailoring the chemistry, identity, and ratio of the constituent components.[25,26] Broadly speaking, this framework indicates that by simply linking together two or more chemically distinct polymers of suitable length, it is possible to generate nanocomposite materials with disparate and unique properties that assemble into a well-ordered morphology. For example, polystyrene-*block*-poly(ethylene oxide) (PS-PEO) combines a glassy PS component with an ionically conductive PEO component that, when doped with a lithium salt, leads to the properties desirable for an effective polymer electrolyte in rechargeable batteries utilizing a lithium metal anode.[27–29] Mean-field theories have been developed to predict the phase behavior of a prototypical AB diblock copolymer as a function of the volume fraction of the A block, f_A, and the segregation strength of the polymers, χN, which is the product of the effective Flory-Huggins parameter, χ_{eff}, and the volumetric degree of polymerization of the block polymer, N. Note that, throughout this thesis, this product is often written as χN, rather than $\chi_{eff} N$, for simplicity. The mean-field-derived phase portrait of a prototypical AB diblock copolymer, along with several commonly observed morphologies, is shown in Figure 1.1. This phase portrait suggests that developing a material simply involves making a block polymer such that f_A and χN fall within the boundaries for the desired morphology.

In reality, the phase behavior of real block polymers is often more complex and is not quantitatively described by Figure 1.1. This is largely because the framework of

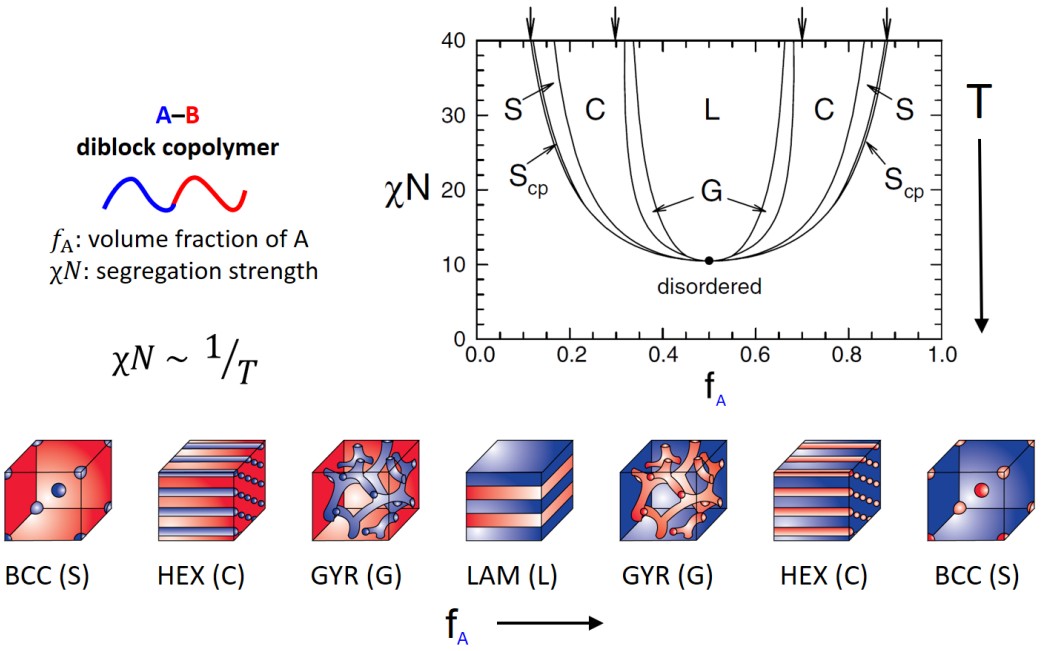

Figure 1.1: Mean field-calculated phase portrait for an AB diblock copolymer, with several representative morphologies. Note that S_{cp} refers to close-packed spheres. The vertical arrows above the phase portrait indicate the phase boundaries predicted by strong-segregation theory. Phase portrait adapted from Ref. 30.

mean-field theory makes several simplifying assumptions: the block polymers are of infinite molecular weight, there is no difference in how the repeat units of A and B fill space, and that all interactions between A and B units is determined by their interactions with the "mean", or average, field.[31,32] In contrast, extensive work has shown that the phase behavior of block polymers can be affected by a variety of factors such as dispersity in either molecular weight or volume fraction of each component,[33–40] conformational asymmetry,[31,41–45] and end group effects.[46] The mean-field nature of this framework also inherently ignores local composition fluctuations that occur due to the finite molecular weight of real polymers.[47] To illustrate this distinction, we reproduce the experimentally-determined phase portrait for polystyrene-*block*-polyisoprene (PS-PI) block polymers in Figure 1.2.[48] Beyond a shifting of the phase

boundaries for various morphologies, a phase not predicted by mean-field theory, hexagonally-perforated lamellae (HPL), was also found. The authors attributed the features of this phase portrait to a combination of conformational asymmetry and finite molecular weight effects.

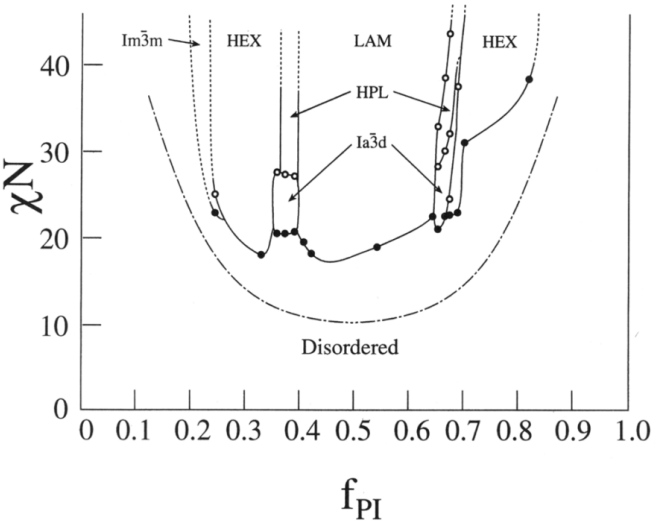

Figure 1.2: Experimentally determined phase portrait for PS-PI block copolymers. The dash-dot line represents the mean-field prediction for the line of order-disorder transitions (ODT). Im3m corresponds to BCC ordering, whereas Ia3d is gyroid. Reprinted with permission from Ref. 48. Copyright 1995 American Chemical Society.

Although the work shown in Figure 1.2 was conducted more than 20 years ago, there is still much to be understood about the complex phase behavior of block polymers. Recent work has found that at segregation strengths greater than that necessary to form a BCC phase, some block polymers can form complex sphere phases such as a dodecagonal quasicrystal (DQC) or the Frank-Kasper σ phase.[49–51] Recent progress in this field will be detailed further in the Introduction to Chapter 2.

While neat block polymers provide access to morphologies and potentially useful combinations of mechanical and chemical properties, their utility in end-user applications can be limited by a variety of factors. First, a large portion of the research on block polymers has focused on polymers synthesized through anionic polymerization, which leads to block polymers with well-controlled molecular

weights and low dispersities. Some dispersity can actually be beneficial for polymer properties,[35,39] and many commercially relevant polymers exhibit large dispersities that range from 2 to 10,[26] but there is relatively less understood about these polymer systems, making it difficult to predict their properties *a priori*. Furthermore, the use of ordered block polymers for transport applications can be limited by grain boundaries that serve to cut off the transport channels.[10,52–56] Finally, the fabrication of block polymers typically involves multiple monomer addition steps, adding, on a commercial scale, additional cost to the synthesis relative to a homopolymer. Finally, the identity and molecular weight of the constituent polymer blocks is limited to those that can form the ordered morphology of interest, ultimately constraining the design space.

These restrictions have motivated significant work on blends of block polymers with other components, such as epoxies, homopolymers, and salts. These systems take advantage of the properties of block polymers to ultimately produce materials that would otherwise be difficult to obtain. For example, amphiphilic block polymers can substantially improve mechanical properties such as fracture toughness and strain-at-break of epoxies and polymer blends by acting as deformable micelles and interfacial compatibilizers in epoxies[57–60] and polymer blends,[61–63] respectively. The work described in this thesis focuses primarily on the behavior of blends that combine AB diblock copolymers with a lithium salt (Chapter 2), A and B homopolymers (Chapter 5), or some combination of both (Chapters 3 and 4). Both salt-doped block polymers and ternary blends have a rich history, so we will provide a brief review of each prior to describing the remaining chapter of this thesis.

1.2 Salt-doped block polymers

An emerging field of interest over the past decade has been block polymers wherein one domain is selective doped with a salt. Such blends have applications in technologies such as rechargeable lithium batteries that utilize a lithium metal anode, which could exhibit up to a 20-fold increase in energy density relative to lithium ion batteries if the formation of lithium metal dendrites upon cycling could be suppressed,[1] in

addition to applications as in proton exchange fuel cells where the salt-doped block polymer could serve as an electrolyte that is both durable and provides fast proton transport.[56,64] For battery applications, frequently studied polymer electrolyte systems involve block polymers of a polystyrene (or related) species and a polyether such as PEO that has been doped with a lithium salt.[10,28,65–69] The primary utility of these blends is that, when microphase separated, they combine a mechanically robust domain (*i.e.* PS) with a domain that is highly ionically conductive (*i.e.* PEO). The driving force for such a combination of properties rests on theoretical calculations performed by Monroe and Newmann that suggested that the formation of lithium metal dendrites, which grow from the lithium metal anode and can span to the cathode upon cycling, shorting out the cell, could be suppressed if the modulus of the polymer electrolyte were sufficiently high.[9] Work by Singh *et al.* demonstrated that lamellae-forming PS-PEO block polymers doped with lithium bis(trifluoromethane)sulfonamide (LiTFSI) exhibited a reasonable elastic modulus (*ca.* 10^7 Pa) below T_g of the PS, but the ionic conductivity of the system was lower than that anticipated, even after considering the effects of the tortuosity of the lamellae. Furthermore, the authors found that the conductivity of the system decreased as the molecular weight of the block polymers decreased.[28] Later work by Panday *et al.* also found that the conductivity of polymer electrolytes decreases with decreasing block polymer molecular weight,[70] but a follow-up study by Yuan *et al.* found that, once the block polymer molecular weight is 10 kg/mol or below, the conductivity, measured at 90 °C, instead increases with decreasing molecular weight, which the authors suggest was due to the suppression of the T_g of PS to below that of the measurement temperature.[71]

This observation that the conductivity of ordered, salt-doped block polymer systems is lower than predicted based on simply the tortuosity of the conducting phase, with few exceptions,[64] appears to be general. Many authors have described the upper bound of the accessible conductivity of an ordered phase by invoking the idea of a morphology factor, f, which suggests that a microstructured system inherently exhibits a lower conductivity than the pure conducting phase because not all diffusive movements contribute to the measured conductivity.[28] Thus, for an ideal electrolyte, these authors

suggest that the measured conductivity, σ, should be related to the conductivity of the pure conducting phase, σ_{cond}, by

$$\sigma = f\phi_{\text{cond}}\sigma_{\text{cond}} \tag{1.1}$$

where ϕ_{cond} is the volume fraction of the conducting phase. This argument is inspired by the work of Sax and Ottino,[72] and commonly cited ideal morphologies factors, which require perfect grain connectivity,[73] are 2/3, 1/3, and 1 for lamellae,[28,68,70,73–76] cylinders,[73] and a co-continuous structure like a gyroid, respectively.[73,75] These ideal morphologies act like an inverse tortuosity, τ, which describes the multiplicative increase in the path length ions must travel relative to a straight line, with $\tau = 1/f$. Curiously, however, a morphology factor of 1 for a gyroid would also imply that the gyroid has a tortuosity of 1, whereas real co-continuous structures have tortuosities between 1.5 and 3.[10,20] Regardless, many experimental measurements of conductivity find conductivities lower than that predicted by Equation 1.1.

Several groups have suggested that interfacial mixing of PS and PEO over a lengthscale of *ca.* 5 nm leads to a reduction in the observed ionic conductivity, but that this effect is mitigated as the molecular weight of the block polymer increases and the size of the interfacial mixing zone becomes negligible relative to the domain spacing.[71,77] Other work has suggested that the conductivity of lamellae-forming systems increases as the nominal grain size decreases.[54,78] In this work, grain size, L, is quantified by determining the full width at half max, F, of the primary scattering peak from a small-angle X-ray scattering (SAXS) experiment and invoking the Scherrer equation, which suggests that $L \approx 1/F$.[54] Through this analysis, and transmission electron microscopy (TEM) imaging, the authors conclude that smaller grains lead to higher conductivity. However, this relationship makes the assumption that the only cause for the broadening of a scattering peak is a reduction in the size of a grain, and that there is no change in how strongly structured the lamellae are within a given grain. However, as will be detailed in an upcoming publication, distinguishing between swollen, yet still ordered, lamellae and a fluctuating, structured disordered state is challenging with SAXS and TEM alone,[79] thus indicating that the increase in

conductivity that is assumed to be due to smaller grain size may actually be the result of the difference between a disordered and ordered state.[74] We consider this factor and more in the work described in Chapter 3.

Beyond studies on the conductivity of lithium salt-doped polymers, there has been significant work dedicated to understanding the thermodynamics of such blends. In general, studies have found that χN increases as the salt loading is increased,[29,80–85] and that the salt selectively partitions to the polyether domain.[81,86,87] This result is not intuitively obvious. One might expect the addition of salt to compatibilize the blend and lower χ_{eff} between the insulating and conducting phase due to the entropic penalty of selectively partitioning the salt to a single domain in microphase separated structures. Hover, work by Wang and coworkers has demonstrated that the preferential solvation energy of the anion by the polar component causes the salt to act as a highly selective solvent that instead increases χ_{eff}.[66,80,81,88] Recent work by Ren *et al.* has demonstrated that χ_{eff} is further increased by the effects of lithium ion-induced cross-linking that serves to increase the effective degree of polymerization of the polyether phase.[84] Although there remains much to be understood about the fundamentals of these systems, the results can be of practical use. For example, Teran *et al.* performed a systematic study in which they showed that microstructural ordering can be induced *via* addition of LiTFSI in low molecular weight PS-PEO block polymers.[82] We take advantage of this phenomenon in the work described in Chapters 2 and 3 to induce order in asymmetric block polymers and ternary polymer blends, respectively.

1.3 Ternary polymer blends

Discovery of a polymeric bicontinuous microemulsion

As described in the introduction, methods to develop materials that simultaneously exhibit a controlled structure and domain interconnectivity are crucial for applications such as water filtration membranes,[52,89] bulk heterojunction solar cells,[11,90] and

polymer electrolytes.[10,91,92] Although block polymers are able to assemble into well-defined periodic structures, their applications can be limited due to the narrow range of accessible domain spacings (*ca.* 5 to 50 nm)[26] and the presence of grain boundaries that cut off either transport or conducting channels.[10,52–56] One relatively simple route to avoiding these problems is through the use of ternary polymer blends that allow access to additional morphologies and larger domain spacings. Perhaps the most commonly studied ternary polymer blend consists of an AB diblock copolymer diluted with A and B homopolymers. Although the potential phase space for such work is immense, many studies have focused on the phase behavior of such blends as a function of the total homopolymer loading (ϕ_H), where the relative loading of the two homopolymers is held equal (*i.e.* $\phi_A = \phi_B = \phi_H/2$). Mean-field theory predicts that the blend will exhibit a lamellar phase at low ϕ_H, a phase separated region at high ϕ_H, and a disordered melt at all compositions at sufficiently high temperature.[93] This framework further predicts that as more homopolymer is added to the blend, the lamellar domains become progressively more swollen with homopolymer, and the lamellar domain spacing ultimately diverges at an unbinding transition, resulting in a multiphase blend.[93] In practice, however, seminal work by Bates *et al.* in 1997 on a blend of polyethylene (PE), poly(ethylene-*alt*-propylene) (PEP), and a block copolymer PE-*b*-PEP, where $N_{PE} \approx N_{PEP} \approx 0.2N_{PE-PEP}$ and $f_{PE,diblock} \approx 0.5$, demonstrated that the unbinding transition is replaced by a narrow composition channel in which a bicontinuous microemulsion (BμE) is observed.[94] This equilibrium morphology consisted of interpenetrating domains of PE and PEP that were locally correlated but lacked long-range order. The authors hypothesized that the formation of this morphology was the result of thermal fluctuations in the system that were unaccounted for in mean-field theory. Regardless of the nature of its formation, the authors suggested that the behavior of the PE/PEP/PE-PEP system may be general for many sets of A and B homopolymers with a corresponding AB diblock copolymer. This concept is shown schematically in Figure 1.3.

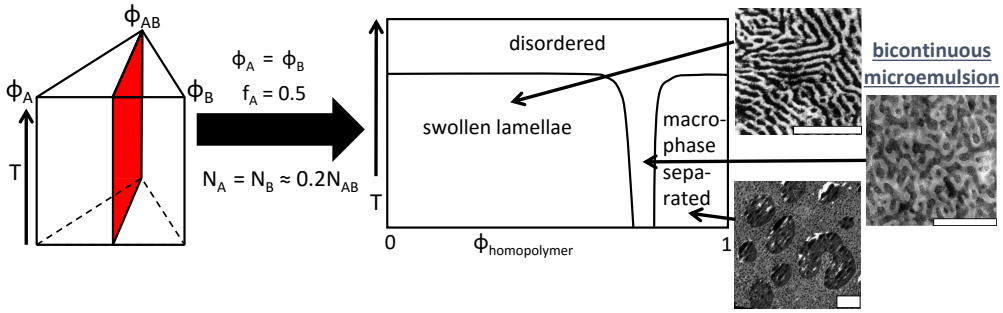

Figure 1.3: Overview of phase behavior for ternary blends of two homopolymers with a corresponding block copolymer. In a narrow composition window, a BμE phase can be observed in which the domains are co-continuous. Scale bars are 1μm for the top two blends and 5 μm for the phase separated blend. Reproduced in part from ref 94, which is copyright 1997 by the American Physical Society.

Definition of a BμE

The BμE is a thermodynamically stable morphology that consists of interpenetrating, co-continuous domains that are locally correlated, yet lack long-range order. By definition, a BμE has zero mean curvature, H, and negative Gaussian curvature, K, *i.e.*

$$H = \frac{\kappa_1 + \kappa_2}{2} = 0 \tag{1.2}$$

and

$$K = \kappa_1 \kappa_2 < 0 \tag{1.3}$$

where κ_1 and κ_2 are the principal curvatures.[95] A 2-dimensional cross section of this morphology is shown schematically in Figure 1.4.

Prior to their discovery in polymeric systems, BμEs were first observed in blends of oil, water, and non-ionic surfactant. In these systems, droplet microemulsions were frequently observed, and it was initially found that water-in-oil droplet microemulsions that formed in oil-rich phases would directly transition to oil-in-water droplet microemulsions upon dilution with water.[96] Despite this observation, Scriven predicted

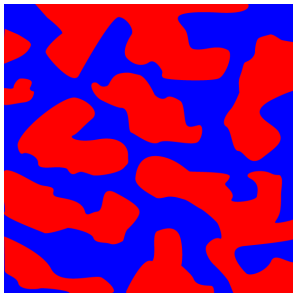

Figure 1.4: Two-dimensional depiction of a bicontinuous microemulsion.

that, at some composition, such a system should exhibit a structure in which the oil and water phases are co-continuous.[97] This prediction of a BμE was later confirmed experimentally *via* freeze-fracture electron microscopy of equivolume blends of n-octane and water over a small range of temperatures and concentrations of the surfactant n-dodecyl-pentaethylene glycolether ($C_{12}E_5$). These compositions and temperatures were found to correspond to conditions under which the energy of the curvature of the surfactant-compatibilized interface was comparable to k_BT.[98] An image of this freeze-fractured blend is shown in Figure 1.5.

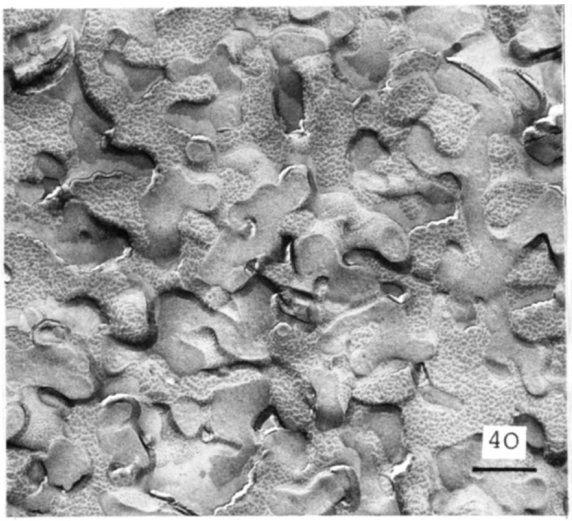

Figure 1.5: Electron micrograph of an n-octane/water/$C_{12}E_5$ BμE. The scale bar indicates 200 nm. Reproduced with permission from reference 99. Copyright 1988 American Chemical Society.

Despite the definition of a BμE requiring that the systems exhibit zero mean curvature, many experimental studies on such systems do not attempt to directly measure the mean curvature of the system, perhaps due to the experimental complexity of such a measurement. More commonly, what is considered a BμE is identified on the basis of a combination of scattering and/or direct imaging *via*, for example, scanning electron microscopy (SEM) or transmission electron microscopy (TEM). One should use caution, however, when not considering curvature, as systems that do not exhibit identically zero mean curvature may be misidentified as a BμE. Scattering of a BμE is characterized by a single, broad peak followed by, in some cases, higher-order correlation peaks at larger values of the scattering vector, q. At large q, the interface of the BμE results in a scattered intensity that scales according to Porod's law, *i.e.* $I(q) \sim q^{-4}$. In 1987, Teubner and Strey developed a scattering model to describe the broad primary scattering peak.[100] By performing an order parameter expansion of the free energy density, the authors developed what came to be termed the Teubner-Strey model:

$$I(q) = \frac{1}{a_2 + c_1 q^2 + c_2 q^4} \tag{1.4}$$

where $a_2 > 0$, $c_1 < 0$, and $c_2 > 0$ are coefficients of the free energy expansion.[100] The bounds of these parameters have several important implications: $c_1 < 0$ is a result of the spontaneous formation of interface by the surfactant in the system, while $c_2 > 0$ indicates the stability of the system.

These fitting coefficients not only describe the microemulsion, but they can also be used to quantitatively assess its structure. Specifically, using the coefficients, the domain spacing, d, correlation length, ξ, and amphiphilicity factor, f_a, can be calculated *via*

$$d = 2\pi \left[\frac{1}{2} \left(\frac{a_2}{c_2} \right)^{1/2} - \frac{1}{4} \frac{c_1}{c_2} \right]^{-1/2} \tag{1.5}$$

$$\xi = \left[\frac{1}{2}\left(\frac{a_2}{c_2}\right)^{1/2} + \frac{1}{4}\frac{c_1}{c_2}\right]^{-1/2} \tag{1.6}$$

$$f_{\mathrm{a}} = \frac{c_1}{(4a_2c_2)^{1/2}} \tag{1.7}$$

The amphiphilicity factor is a quantitative measure of structure in a microemulsion. A value of $f_{\mathrm{a}} = -1$ indicates that the system has a lamellar microstructure, while a value of $f_{\mathrm{a}} = 0$ corresponds to the crossover at which the spontaneous formation of interface is no longer energetically favorable.[100–102]

Additional studies on ternary polymer blends

Through the work by Bates *et al.*, several design guidelines for the study of ternary polymer blends were laid out.[103,104] In general, the systems were prepared such that volumetric degrees of polymerization, N, of the homopolymers were equal and approximately 1/5 that of the block copolymer (*i.e.* $N_{\mathrm{A}} = N_{\mathrm{B}} = 0.2N_{\mathrm{AB}}$), and the block copolymer was symmetric ($f_{\mathrm{A}} = f_{\mathrm{B}}$). These choices were made in part so that both the order-disorder transition temperature (T_{ODT}), the temperature at which a block copolymer microphase separates, and the critical temperature (T_{c}), the temperature at which a blend transitions from a single homogeneous phase to two or more phases, would be experimentally accessible, as $(\chi N)_{\mathrm{ODT}}$ = 10.5 for a symmetric diblock copolymer and $(\chi N)_{\mathrm{c}}$ = 2.[26]

Although mean-field theory failed to anticipate the formation of the BμE channel, one of its key aspects was still relevant for experimental studies on ternary polymer blends, as the region of phase space over which the BμE forms was found to be in the proximity of the predicted Lifshitz multicritical point.[94,103] In mean-field theory, this point represents the intersection of the line of order-disorder transitions, the line of critical points, and the line of the unbinding transition. Broseta and Fredrickson determined that the Lifshitz point occurs at a homopolymer volume fraction of

$$\phi_{\mathrm{L}} = \frac{1}{1+2\alpha^2} \tag{1.8}$$

and an incompatibility of

$$(\chi N)_{\mathrm{L}} = \frac{2+4\alpha^2}{\alpha} \tag{1.9}$$

where $\alpha = \sqrt{N_{\mathrm{A}} N_{\mathrm{B}}}/N_{\mathrm{AB}}$, χ is the segment-segment interaction parameter, and N is the volumetric degree of polymerization of the diblock copolymer.[105] Thus, so long as N of the three polymers and a functional form for $\chi(T)$ are known, it is possible to identify the temperature and composition at which the theoretical Lifshitz point occurs. Bates *et al.* suggested that the BμE channel should span compositions close to ϕ_{L} and incompatibilities higher (or, equivalently, temperatures lower) than $(\chi N)_{\mathrm{L}}$.[94] Therefore, even though mean-field theory fails to predict the existence of a BμE, its result can still be of practical use for identifying what conditions lead to a BμE morphology.

Using these design criteria, other groups extended this methodology to study BμE morphologies in other ternary blends. Examples of other systems include PE/head-to-head PP/PE-PP,[106] PEE/PDMS/PEE-PDMS,[102,104,107–110] PE/PEO/PE-PEO,[104] PS/PI/PS-PI,[39,111,112] PEP/PBO/PEP-PBO,[113] and PCHE/PE/PCHE-PE.[114,115] Beyond these systems, several studies were conducted on A/B/AC systems, including PIB/PE/PE-PP[116,117] and PB (89% 1,2-addition), polyisobutylene, and a block polymer of hydrogenated PB, wherein the first block had 89% 1,2-addition, and the second had 63% 1,2-addition.[118–120] These systems contained both attractive and repulsive interactions and were able to form a microemulsion only in a limited range of phase space. Beyond these findings, both experimental[39] and theoretical[34] work has indicated that significant molecular weight dispersity in the block polymer does not prevent the formation of the BμE and may even serve to promote its formation. Hierarchical systems have also been studied using mixtures of a PCHE-PE-PCHE triblock copolymer, PP homopolymer, and a PCHE-PE-PCHE-PE-PCHE-PP hexablock terpolymer, and it was found that these systems can assemble a BμE with ordered lamellae of PCHE and PE within one domain.[121,122]

In A/B/AB ternary polymer blends, the domain spacing of the BμE can be nearly an order of magnitude larger than the corresponding block polymer, permitting access to significantly larger lengthscales than possible with neat diblock copolymers.[94] Furthermore, the lack of long-range order in BμEs should reduce the number of dead ends like grain boundaries that could otherwise cut off the domains. Several groups have taken advantage of these desirable properties of BμEs to develop a variety of functional materials. In 2006, Zhou *et al.* developed a rigid, porous material with a pore size of *ca.* 40 nm by cross-linking the PI domain of a PI/PS/PI-PS BμE, then washing out the PS homopolymer.[112] Later work by Jones *et al.* improved upon this idea by making a sacrificial, porous PE template by kinetically trapping a PE/PEP/PE-PEP BμE at room temperature *via* crystallization of PE, then selectively dissolving the PEP homopolymer in solvent.[123] This PE template was then used to make a variety of interesting materials such as a ceramic,[124] an epoxy,[125] a polyurethane,[125] a conductive polymer (poly(3,4-ethylenedioxythiophene), or PEDOT),[126] and more.[127] Additional details about this work will be discussed in Chapter 5, where we also discuss the use of thin PE templates also derived from PE/PEP/PEP-PE BμEs to fabricate water filtration membranes.

Throughout all of this work, one of the primary underlying assumptions was that the formation of the BμE was the result of the bending energy of the swollen lamellae approaching $k_{\mathrm{B}}T$, where thermal fluctuations in the system would be sufficient to cause the interfaces to bend and form the co-continuous system. However, work by Zhou *et al.* found that, for a system of PEP/PBO/PEP-PBO, the BμE channel was consistently cut off by the formation of a hexagonal (HEX) phase, and the so-called BμE morphology only formed at temperatures above T_{ODT} of the HEX phase. They attributed the cutoff of the channel to the conformational asymmetry between the PEP and PBO.[113] Conformational asymmetry quantifies the difference between how two polymers A and B fill space and is defined as

$$\varepsilon_{\mathrm{AB}} = \frac{b_{\mathrm{A}}^2/6v_{\mathrm{A}}}{b_{\mathrm{B}}^2/6v_{\mathrm{B}}} \geq 1 \tag{1.10}$$

where b is a statistical segment length and v is the reference volume by which b is defined.[42,43] In the PEP and PBO system, the conformational asymmetry was 1.6.[112]

This work inspired the development of a PCHE/PE/PCHE-PE system with an even larger conformational asymmetry of 2.[79,114,115,128] Curiously, this work did not reveal the presence of a HEX phase for blends assembled along the volumetrically symmetric isopleth (*i.e.* for blends with $0 < \phi_H < 1$ and $\phi_A = \phi_B = \phi_H/2$). However, optical light scattering experiments revealed that, along this isopleth, homopolymer-rich lamellar blends went through a two phase window prior to disordering.[114] Additional work with the system found the presence of a congruent isopleth of first-order lamellar-to-disorder transitions along which the two-phase LAM+DIS window could be bypassed.[79] These congruent transitions only occurred when more of the PCHE homopolymer was added relative to the PE homopolymer, and the trajectory of the line of congruent transitions traced itself to the critical composition of the PCHE/PE homopolymer blends. Interestingly, the critical composition of the homopolymer blend is itself likely influenced by the conformational asymmetry in the system. By assembling blends along the congruent isopleth, Hickey *et al.* found that the width of the BμE channel narrows significantly, from about 5 vol% homopolymer to less than 1%. Perhaps one of the most interesting implications of this work is that there is no apparent distinction by either transmission electron microscopy (TEM) or small-angle X-ray or neutron scattering (SAXS or SANS) between the so-called "bicontinuous microemulsion" and a highly fluctuating disordered state at temperatures close to T_{ODT}. Furthermore, the formation of what has historically been classified as a "BμE" at a variety of ratios of PE to PCHE homopolymer indicates that at compositions that are not along the congruent isopleth, the morphology cannot consistently exhibit zero mean curvature (Equation 1.2), a necessary requirement for a true BμE. Taken altogether, these recent, still unpublished findings bring into question the driving force for the formation of the so-called BμE channel in ternary polymer blends and indicate that there is still much to be learned about the fundamentals of these systems nearly 20 years after they were first described.[94]

1.4 Thesis overview

The work detailed in this thesis combines the concepts studied in lithium salt-doped block polymers and ternary polymer blends. The overarching themes involve understanding structure-property relationships in systems where structure can be induced either thermally or by addition of salt. These experiments use a variety of experimental techniques such as SAXS, DMS, TEM, SEM, electrochemical impedance spectroscopy, and optical transmission determination. This thesis is largely organized in order of increasing system complexity. Chapter 2 details a study where order can be induced in asymmetric block polymers using a lithium salt.[129] Chapter 3 takes this concept further by showing that lithium salt can be used to induce structure in ternary polymer blends, thus permitting studies that quantitatively demonstrate that disordered, yet highly structured morphologies provide better transport properties than ordered morphologies.[85,130] Chapter 4 then follows this logic to describe a route to polymer electrolytes that contains co-continuous, yet disordered domains of an ionically conductive domain and a cross-linked mechanical domain through a polymerization-induced microphase separation scheme. Finally, Chapter 5 details the use of a salt-free ternary polymer blend to make a thin, porous template that is used to attempt to make water filtration membranes.

Chapter 2

Readily Tuning the Phase Behavior of Sphere-forming Block Polymers *via* Lithium Salt Addition[i]

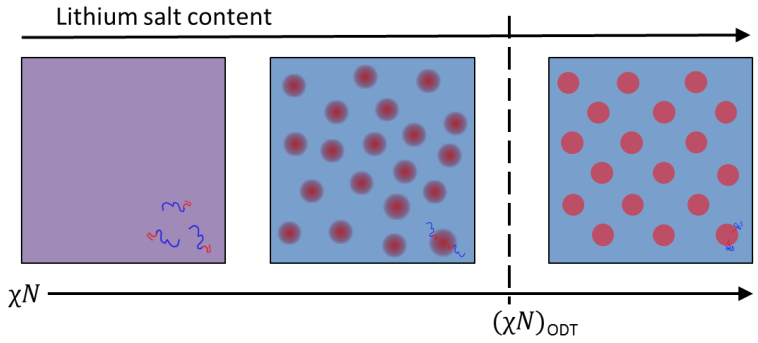

Figure 2.1: Table of contents graphic: Schematic representation of the how lithium salt content drives microstructure and ordering in block copolymer systems by driving up the segregation strength, χN.

[i] This work was done in collaboration with Robert J. Hickey and Frank S. Bates.

2.1 Abstract

Recent work has revealed that, with the correct thermal treatment, asymmetric block polymers can form interesting morphologies such as a dodecagonal quasicrystal or the Frank-Kasper σ phase. The work detailed in this chapter shows that additional morphologies can be obtained by doping asymmetric polystyrene-*b*-poly(ethylene oxide) (PS-PEO) and poly(ethylene-*alt*-propylene)-*b*-poly(ethylene oxide) (PEP-PEO) diblock copolymers with a lithium salt that acts as a selective solvent for one of the domains. Small-angle X-ray scattering analysis revealed that, upon addition of the salt, block polymers that are disordered when neat can form a variety of morphologies such as BCC, a dodecagonal quasicrystal, Frank-Kasper σ phase, hexagonal spheres, or hexagonally close packed spheres, depending on the salt loading and thermal treatment. χN of the salt-doped PS-PEO diblock copolymers is estimated using two models from the literature, and comparing the results to a theoretical phase diagram suggests that χ_{eff} increases approximately linearly with salt loading. Annealing studies with the salt-doped PEP-PEO block polymer confirmed that the equilibration rate is inversely proportional to the energetic penalty for chain exchange. Taken altogether, the results of this chapter outline a unique route to probing a wide range of χN in a single polymer system without the need to modulate temperature.

2.2 Introduction

Block polymers have long been studied as a route to combine the properties of multiple chemically distinct molecules with well-defined structure at the nanometer length scale. The simplest type of block polymer is termed a diblock copolymer, where the prefixes di- and co- indicate that the polymer consists of two "blocks" of polymers that are linked together and two types of polymers, respectively. Due to the seeming simplicity of this type of system, the phase behavior of diblock copolymers has been widely studied for decades. In 1980, Leibler developed a mean-field theory to describe the phase behavior of AB diblock copolymers as a function of the relative volume fraction

of A in the polymer, f_a, and the segregation strength of the system, χN, where, χ is the effective interaction parameter that describes the energetic cost of mixing a unit of A with a unit of B, while N is a volumetric degree of polymerization that quantifies the total number of A and B units in the block polymer.[33] This work demonstrated that when χN exceeded a value necessary to induce microphase separation ($\chi N > 10.5$ for $f_a = 0.5$), these block polymers establish ordered morphologies with nanoscale features such as lamellae (LAM), hexagonally close packed cylinders (HEX), or body-centered cubic (BCC) spheres.[33] Later work established the existence of additional morphologies, such as the Ia3d gyroid[41] and face-centered cubic (FCC) micelles,[131] while other morphologies, such as close-packed spheres with space groups other than that corresponding to FCC,[30,31] have been predicted but not yet experimentally realized for neat diblock copolymers. We note that referring to particle-forming phases as "sphere" phases is not rigorously correct, as the structures more closely resemble micelles or multi-faceted particles depending on the conditions. However, for the sake of simplicity, such systems will be described as either particle- or sphere-forming throughout the course of this chapter.

Recent work on asymmetric diblock copolymers has indicated that the phase behavior of sphere-forming block polymers is significantly more complex than was anticipated from mean-field theory. Experimental work with a poly(isoprene)-*block*-poly(lactide) (PI-PLA) diblock copolymer, termed IL-15 (M_n = 3.9 kg/mol, f_{PLA} = 0.22), revealed that, at segregation strengths larger than that necessary to form a BCC phase, the block polymer forms the Frank-Kasper σ phase, a low symmetry morphology consisting of 30 particles per unit cell, which we will refer to as the σ phase for simplicity.[49] Further studies with this system revealed that the formation and growth of this phase is slow and occurs through the formation of metastable, intermediate morphologies such as a dodecagonal quasicrystal (DQC), a morphology that consists of the same tiling elements as the σ phase and exhibits 12-fold rotational symmetry, yet lacks long-range periodic order.[50,51] Detailed annealing studies on a more asymmetric PI-PLA block polymer of slightly higher molecular weight, termed IL-5.1 (M_n = 4.6 kg/mol, f_{PLA} = 0.18), revealed that the time required to form the σ phase was highly

temperature dependent, as the phase forms on the time scale of months, days, and minutes at 25 °C, 35 °C, and 50 °C, respectively.[51] Furthermore, samples that exhibited liquid-like packing (LLP) of particles had to be annealed for days prior to the formation of a DQC phase. The mechanical properties and scattering patterns obtained from such samples, in addition to the fact that LLP served to nucleate the DQC phase, suggested that the LLP phase consisted of particles that formed a jammed, glassy solid and consisted of icosahedral clusters, although the exact structure of this phase is still a matter of debate.[51] Taken altogether, the slow and highly temperature dependent equilibration dynamics of the PI-PLA systems indicated that molecular chain exchange, wherein the core block pulls out into the corona matrix, was likely the dominant method of equilibration, and the time scale, τ, of such a process is set by $\tau \sim \exp[\alpha\chi N]$,[132–134] where α is an experimentally-derived fitting coefficient and we note that $\chi \sim 1/T$. We briefly note that, although the time scale for equilibration should increase as a diblock copolymer approaches the glass transition temperature, T_g, of one of its blocks, this effect does not dominate the orders-of-magnitude change in the slowing dynamics of the current system. Gillard *et al.* noted that, at the same quench depth (*i.e.* $T_{ODT}-T$, where T_{ODT} is the order-disorder transition temperature), IL-5.1 (annealed at 40 °C) ordered approximately five times faster than IL-15 (annealed at 25 °C) due to the relatively larger distance between the annealing temperature and the glass transition temperature of the PLA core-block ($T_{g,PLA} \approx 0$ °C).

Beyond diblock copolymers, the σ phase has also been shown to form in tetrablock terpolymers of polystyrene-*b*-poly(isoprene)-*b*-polystyrene'-*b*-poly(ethylene oxide) (PS-PI,PS-PEO or SIS'O), which, when ordered, form core-shell micelles wherein the core is PEO, the shell is PS, and the corona is PI and PS.[135–137] Depending on the conditions, the terminal PS can loop or bridge into the PS shell or intermix with the PI, as the system is designed such that $\chi_{SI} \leq \chi_{SO} \ll \chi_{IO}$. As detailed in a recent study that varied the ratio of the size of the internal and terminal PS blocks, the added complexity of these systems appears to lead to the formation of a variety of metastable morphologies beyond a DQC, including an A15 phase, hexagonally-packed

spheres (HEX_s), hexagonally close-packed (HCP) spheres, coexistence between face-centered cubic (FCC) and HCP spheres, and an as-yet not fully described rhombohedral morphology.[137] These findings demonstrate the potential complexity of the phase behavior of nominally single component systems.

Although a rigorous set of guidelines that detail what factors promote the formation of low symmetry phases like the σ phase has yet to be established, recent work by Xie *et al.* has suggested that conformational asymmetry may play a role.[45] For an AB diblock copolymer, the conformational asymmetry between the blocks quantifies the difference between how the two polymers fill space and is defined by

$$\varepsilon_{AB} = \frac{b_A^2/6v_A}{b_B^2/6v_B} \geq 1 \tag{2.1}$$

where b is a statistical segment length and v is the reference volume by which b is defined. Using a self-consistent field theory (SCFT) framework, Xie *et al.* found that, as the conformational asymmetry of AB diblock copolymers is increased, the region over which the σ phase is preferred widens and, in some cases, forms through a metastable A15 intermediate morphology.[45] However, recent SCFT work performed by Chanpuriya *et al.* found that the free energy difference between the A15 and σ phase is only approximately $1 \times 10^{-3} k_B T$ per chain,[137] indicating that predictions of equilibrium phase behavior are sensitive to the framework used to calculate phase boundaries.[138]

One challenge in the studies to date is that the range of χN that can be studied is limited by the accessible temperature range, where the lower temperature is set by the vitrification or crystallization of one or more of the blocks, while the upper working temperature is where the polymer degrades. Ultimately, this setback is due to the fact that many studies rely simply on temperature modulation to set the segregation strength, as, in many systems, $\chi \sim 1/T$. However, introducing a second component can provide a route to tuning χN without the need to change temperature. One route of particular interest is the introduction of a lithium salt, such as lithium bis(trifluoromethane)sulfonamide (LiTFSI), into a system containing an insulating component, like PS, and a system that contains ether moieties that can solubilize

the salt.[28,65–69] Of these systems, blends of a PS-PEO block copolymer with LiTFSI have been arguably the most thoroughly studied, as the combination of a mechanically robust (PS) and ionically conductive (PEO) components make them potentially useful as polymer electrolytes in next-generation lithium metal batteries.[9,28,66,67,69] In such systems, the LiTFSI is exclusively solubilized by the PEO component.[81,86,87] Although the specific quantitative effects of LiTFSI salt loading are a matter of debate, there is general agreement that χ_{eff} between the PS and the salt-doped PEO increases as the concentration of salt in the system increases.[29,80–85] Several groups have taken advantage of this phenomenon to tune the phase behavior of block polymer systems and induce microstructural ordering; this concept is shown schematically in Figure 2.2.

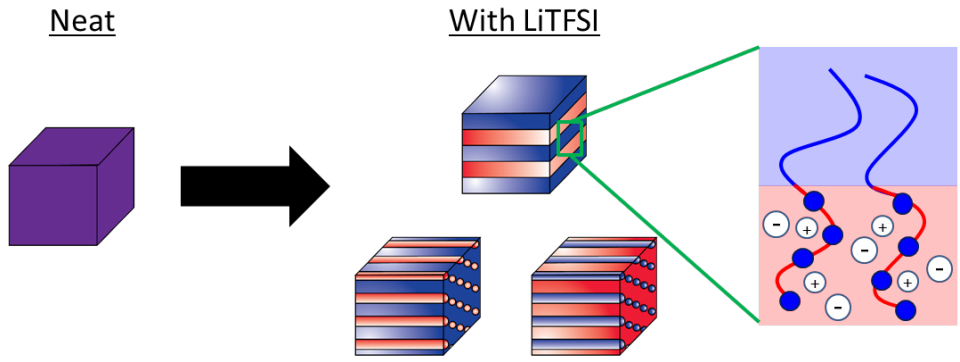

Figure 2.2: Schematic representation of several different microstructured morphologies that have been previously studied.[66,80,82,84] In each case, the onset on microstructural ordering was due to the increase in segregation strength with salt content.

Although there has been extensive work demonstrating that the addition of salt can induce structure in roughly symmetric block polymers, to the best of our knowledge there has been no systematic study investigating the behavior of salt-doped sphere-forming block polymers. In this work, we analyze the phase behavior and ordering kinetics of asymmetric PS-PEO and poly(ethylene-*alt*-propylene)-*b*-PEO (PEP-PEO) block copolymers, disordered when neat, that can exhibit a variety of microstructures when doped with LiTFSI. Unlike in previous studies on neat sphere-forming block polymers, the construct in the current work permits a wide range of χN to be

accessed without the need to modulate temperature. We demonstrate that by simply changing the relative salt loading, χN can be readily modulated, allowing for a variety of morphologies to be "dialed in". The key principle of this study is illustrated schematically in Figure 2.3, where the phase diagram is that predicted by Xie *et al.* for a diblock copolymer with $\varepsilon = 2$. Beyond understanding the phase behavior of the system, we also perform annealing experiments on salt-doped PEP-PEO block polymers where the morphology can be monitored over the time scale of months at a fixed temperature below T_{ODT}, where T_{ODT} is set by the salt loading. These studies confirm previous findings by Lee *et al.* and Gillard *et al.* that suggest that the rate of equilibration is largely set by χN.[50,51]

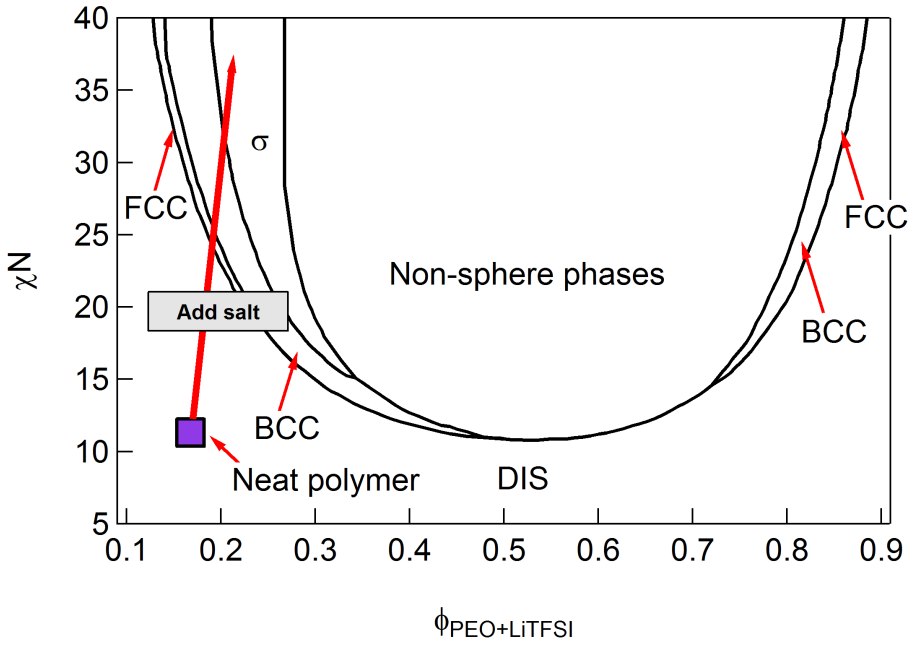

Figure 2.3: Phase diagram predicted by SCFT calculations by Xie *et al.* for a diblock copolymer with a conformational asymmetry of 2.[45] The diagram shows schematically one goal of the current work: to induce microstructural ordering of an asymmetric PS-PEO diblock copolymer through lithium salt addition. Phase diagram adapted with permission from Ref. 45. Copyright 2014 American Chemical Society.

Ultimately, this chapter outlines a unique route to isothermally tuning the phase

behavior of sphere-forming block copolymers. The techniques and understanding developed in this work permit future studies where the phase behavior of such systems could be studied at higher segregation strength (*e.g.* $\chi N \gg \chi N_{\mathrm{ODT}}$) that would otherwise be inaccessible due to the vitrification or crystallization of one of the components in the block polymer.

2.3 Experimental Section

Materials

Lithium bis(trifluoromethane)sulfonamide (LiTFSI) was purchased from 3M (St Paul, MN) and used as received. Because LiTFSI is highly hygroscopic, it was stored under vacuum when not being used or transferred. Polymers used for this study were synthesized by anionic polymerization. Polystyrene-*block*-poly(ethylene oxide) (PS-PEO) block copolymers were synthesized as described previously.[139] Briefly, styrene monomer was purified and polymerized from a *sec*-butyllithium initiator in cyclohexane at 40 °C for at least 4 hours. Purified ethylene oxide was then added to the reaction to end-cap the PS chain and yield a PS-OH macroinitiator, which was precipitated, dried, and characterized. The PS-OH was then reinitiated by first dissolving the polymer in purified THF in a reaction vessel, then introducing to the reaction vessel a solution of potassium napthalenide in THF. Additional THF was added to bring the solution volume to approximately 500 mL, and purified ethylene oxide was then added to the reaction vessel, which was maintained at 45 °C. The ethylene oxide was allowed to polymerize for 24 hours, after which purified methanol was added to the reaction to yield a hydroxyl end-capped PS-PEO block copolymer. The synthesis of the PEP-PEO block copolymer was nearly identical, except that the PEP-OH macroinitiator was synthesized by first polymerizing isoprene monomer from a *sec*-butyllithium initiator, then end-capping with purified ethylene oxide, to yield PI-OH, which was then hydrogenated in cyclohexane at 80 °C and 500 psi H_2 for 12 hours using a Pt/Re catalyst to yield the PEP-OH macroinitiator. The polymerization schemes

for PS-PEO and PEP-PEO are shown in Figures 2.4 and 2.5. A list of the densities and species molecular weights is shown in Table 2.1. A summary of the polymers used in this study are shown in Table 2.2. Due to the low molecular weight of the polymers, the crystallization temperature of the PEO in all cases is below room temperature. We note that, at 140 °C, the PS-PEO block polymer exhibits a conformational asymmetry of 2.1,[26,140] while PEP-PEO has a conformational asymmetry of 1.3.[140–142]

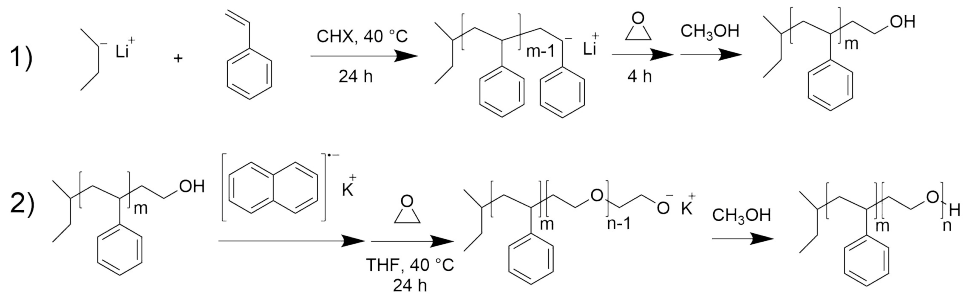

Figure 2.4: Reaction scheme for the anionic polymerization of PS-PEO.

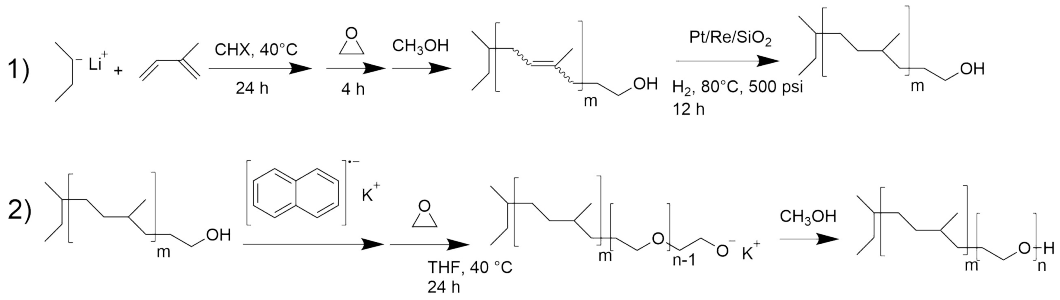

Figure 2.5: Reaction scheme for the preparation of PEP-PEO.

Table 2.1: Molecular weights and densities of the components used in this study.

Species	M_0 (g/mol)	ρ at 140 °C (g/mL)	Ref.
PS	104	0.969	Fetters (Ref. 140)
PEP	70	0.790	Fetters (Ref. 140)
PEO	44	1.064	Fetters (Ref. 140)
LiTFSI	287	2.023	Teran (Ref. 82)

Table 2.2: Characteristics of polymers used in this study.

Polymer	M_n (kg/mol)[a]	Chem. N_n^a (PS or PEP, PEO)	Vol. N^c	f_{PEO}^a	$Đ^b$	T_{ODT} (°C)
PS-PEO(8-2)	10.1	80, 40	170	0.16	1.04	$< 25^d$
PS-PEO(11-2)	13.4	107, 51	226	0.16	1.06	$< 25^d$
PEP-PEO(3-1)	3.0	36, 12	61	0.13	1.08	15^e
PEP-PEO(4-1)	4.3	53, 14	88	0.11	1.07	30^e

[a] *via* ^{1}H NMR; [b] *via* LS-SEC; [c] Using densities at 140 °C (ref 140) and $V_{ref} = 0.1$ nm^3
[d] *via* SAXS; [e] *via* DMS

Sample preparation

PS-PEO blends were prepared by dissolving LiTFSI and the block copolymer in THF. To prepare samples for small-angle X-ray scattering (SAXS) analysis, the homogeneous solution was transferred to nominally 1 mm diameter boron-rich capillaries (Charles Supper Company, Natick, MA). The THF was removed through a sequential process. First, capillaries were placed in warm ($\sim$ 70 °C) water in a fume hood for about 6 hours, then left at room temperature in the fume hood overnight. Next, the capillaries were dried using a vacuum oven by first drying for roughly 4 hours at room temperature, then 12 hours at moderate ($\sim$ 50 °C) temperatures. PEP-PEO blends were prepared by directly combining the LiTFSI with the block polymer in a capillary, heating to elevated temperature, then centrifuging to fill the bottom of the capillary. For all types of blends, in an attempt to erase the thermal history, samples were brought to elevated temperature ($\sim$ 200 °C) for 10 minutes. In the case of PS-PEO samples, blends were then ambiently cooled to an annealing temperature and held for an extended period of time, then rapidly quenched by immersing the capillary in room temperature water. In the case of PEP-PEO samples, the blends were either rapidly quenched in room temperature water or ambiently cooled to room temperature. After quenching, capillaries were transferred to a glass test tube with a sealable lid to mitigate the uptake of water by the samples. These sample treatments are summarized in Table 2.3.

The preparation of samples for dynamic mechanical spectroscopy (DMS)

Table 2.3: Annealing treatments used for these studies.

Polymer	T_{anneal} (°C)	Anneal time (days)
PS-PEO(8-2)	120	1.5
	150	7
PS-PEO(11-2)	150	4
PEP-PEO(3-1)	r.t.[a]	–[b]
PEP-PEO(4-1)	r.t.[a]	–[b]

[a]Room temperature, [b]Multiple, see Results section

measurements was comparatively simpler. The THF solution containing LiTFSI and block copolymer was dried under vacuum, first at room temperature, then elevated temperature ($\sim$ 50 °C) overnight. The samples were then stored under vacuum until they could be tested using DMS experiments.

Dynamic mechanical spectroscopy (DMS)

DMS experiments were performed to determine the order-disorder transition temperature (T_{ODT}) of salt-doped PEP-PEO block polymers. Blends were loaded onto a 25 mm parallel plate geometry at room temperature, then heated to elevated temperature to allow the sample to flow and evenly fill the gap. Stain sweeps were first performed to determine the linear viscoelastic region. The sample was then brought above any anticipated T_{ODT}, and the elastic (G') and storage (G'') moduli were measured as the sample was cooled at 1 °C/min and probed at a frequency of 1 rad/s. The samples were then heated at a rate of 1 °C/min until there was a sharp drop in G', which is a sign of passing through the ODT. T_{ODT} was taken to be the temperature at which G' had dropped to 10% of its plateau value.

Small-angle X-ray scattering (SAXS)

SAXS experiments were conducted at DND-CAT sector 5-ID-D of the Advanced Photon Source at Argonne National Laboratory. 2D scattering patterns were collected on a Rayonix CCD area detector. The resulting scattering patterns were azimuthally

integrated to give the scattered intensity as a function of the magnitude of the wavevector $|\boldsymbol{q}| = q = 4\pi\sin(\theta/2)/\lambda$, where θ is the scattering angle and λ is the wavelength.

2.4 Results

This work primarily consists of two parts: (1) the phase behavior of PS-PEO block copolymers doped with LiTFSI, and (2) the kinetics of equilibration of LiTFSI-doped PEP-PEO block copolymers. In both cases, the thermal treatment of the sample appears to affect both the number of accessible phases and the speed at which they form. We note that, throughout all parts, the salt concentration is based on the molar concentration of lithium ions in the PEO phase and is given by $r = [Li^+]/[EO] = 0 - 0.08$. In this section, we first consider the phase behavior of LiTFSI-doped PS-PEO block copolymers that were annealed at high temperature for various lengths of time. Next, we discuss the phase behavior of LiTFSI-doped PEP-PEO block copolymers, where the low T_g of both species allows long-time equilibration studies to be conducted.

Salt-induced ordering in LiTFSI-doped PS-PEO block copolymers

For this study, we employed two diblock copolymers of similar architecture and molecular weight. The reason for using two different block copolymers was a practical one: after the initial studies with PS-PEO(8-2), there was not enough of the sample remaining to conduct additional studies. This section will detail the chronological order in which experiments with the two diblocks were conducted. We note briefly that a previous presentation on this work, given at the American Physical Society's March Meeting in 2016, was based on the results from the PS-PEO(11-2) block copolymer, which we detail last.

Phase behavior of LiTFSI-doped PS-PEO(8-2) annealed for 36 hours

Initial studies of LiTFSI-doped, asymmetric PS-PEO block copolymers were performed after annealing for a relatively short time. As detailed in the experimental section, these samples were prepared by bringing the blends to 200 °C, then ambiently cooling to 120 °C and annealing for 36 hours, or 1.5 days. The phase behavior of these samples as a function of salt loading is shown in Figure 2.6.

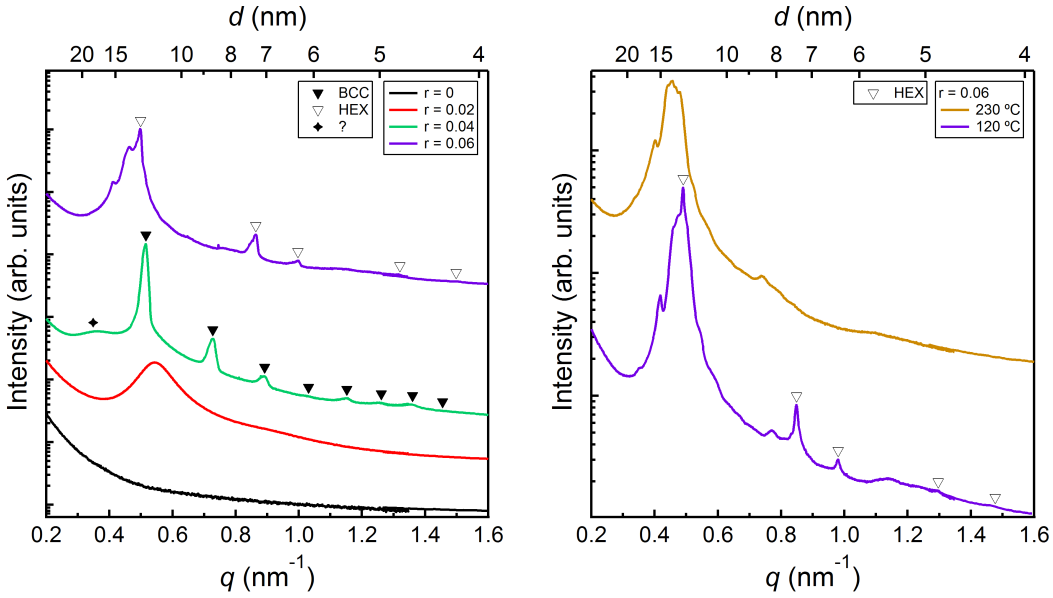

Figure 2.6: SAXS profiles for PS-PEO(8-2) with various salt loadings. Samples were annealed at 120 °C for 1.5 days prior to the measurement. (a) Isothermal scattering at 120 °C. (b) Comparison of scattering for blends containing r = 0.06 at 120 °C and 230 °C. BCC peaks correspond to q/q^* values of 1, $2^{1/2}$, $3^{1/2}$, $4^{1/2}$, $5^{1/2}$, $6^{1/2}$, $7^{1/2}$, and $8^{1/2}$. HEX peaks correspond to q/q^* values of 1, $3^{1/2}$, $5^{1/2}$, $7^{1/2}$, and $9^{1/2}$.

From this initial study, we found a variety of interesting microstructures that could be formed with relatively low salt loadings. The neat block polymer appears to be homogeneously mixed and only displays parasitic scattering, while the addition of salt to give r = 0.02 results in scattering consistent with liquid-like packing (LLP). A salt loading of r = 0.04 results in a BCC microstructure, while further increasing the salt loading to r = 0.06 results in scattering peaks corresponding to a hexagonally-packed

(HEX) microstructure in addition to another morphology, which will be described shortly. The results in Figure 2.6b indicate that, although the HEX morphology can be melted, the T_{ODT} of the remaining morphology is inaccessible, as suggested by the persistence of scattering peaks at 230 °C. We note briefly that it is not possible to discern whether the HEX scattering is from hexagonally-close packed cylinders or hexagonally-packed spheres without transmission electron microscopy (TEM) analysis. Unfortunately, the highly hygroscopic nature of these samples, in addition to their brittle nature, made TEM imaging challenging. Based on the volume fraction of salt-doped PEO in the sample ($f_{PEO+LiTFSI} = 0.19$ when $r = 0.06$), spheres seem more likely (see Figure 2.3).

There are two features worth noting in Figure 2.6a. The first is the presence of a wide feature centered around $q = 0.35$ nm^{-1} that corresponds to a size of approximately 18 nm. The origin of this feature is not obvious, but its size suggests a feature that is significantly larger than that for the domain spacing of the BCC structure. An additional feature in the scattering data is the presence of a significant number of peaks for samples with $r = 0.06$ that persist even when the sample is heated to 230 °C (Figure 2.6b). In order to understand what packing these peaks might correspond to, we have plotted the scattering of the blend at 230 °C alongside scattering traces corresponding to a dodecagonal quasicrystal (DQC) and the σ phase in Figure 2.7.

The relatively good agreement of the scattering peak locations in Figure 2.7a with the obtained scattering pattern suggests that the blends in the current study exhibited a dodecagonal quasicrystalline (DQC) morphology. As indicated by previous work with salt-free diblock copolymers,[50,51] this morphology appears to always be metastable relative to the σ phase. Based on this rationale, we decided to investigate LiTFSI-doped PS-PEO(8-2) block copolymers that had been annealed for a longer period of time.

Phase behavior of LiTFSI-doped PS-PEO(8-2) annealed for 7 days

In order to understand if the morphologies shown in Figure 2.6 would persist over long periods of time, we prepared samples with the same range of salt loadings but instead annealed them at 150 °C for 7 days. This slightly higher temperature was anticipated to

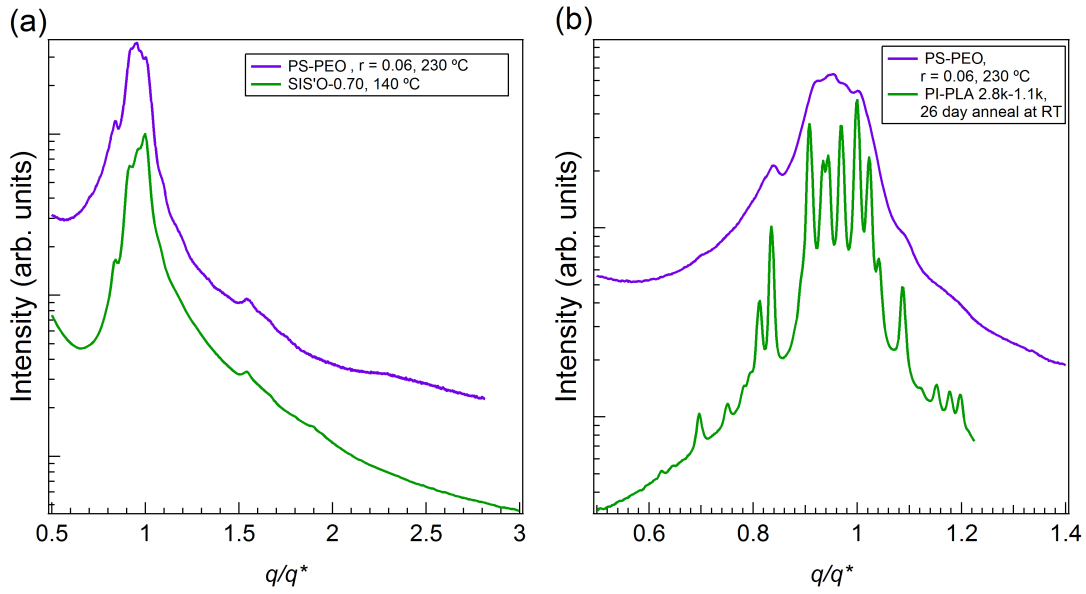

Figure 2.7: SAXS profiles for PS-PEO(8-2) compared with the scattering from (a) a PS-PI-PS-PEO (SIS'O) tetrablock terpolymer (from ref. 143) and (b) a PI-polylactide (PLA) (IL-15) block copolymer (from ref. 49). The phases of these two examples have been assigned in their respective references as (a) dodecagonal quasicrystal (DQC) and (b) Frank-Kasper σ phase.

speed up the equilibration dramatically, while the SAXS results in Figure 2.6b suggest that this temperature change was unlikely to affect what morphology formed to the fact that χN was primarily set by the salt loading. The scattering patterns for these blends are shown at 150 °C in Figure 2.8.

The scattering patterns in Figure 2.8 suggest that longer anneal times can lead to better-formed structures. Like the samples that had been annealed for 35 hours, blends with r = 0 and 0.02 are still fully disordered and exhibit LLP, respectively, but the morphology of other blends has changed. A sample containing r = 0.04, which exhibited BCC ordering when annealed at 120 °C for 36 hours, now exhibits many peaks, which may be consistent with a DQC phase. For blends with r = 0.05, the scattering exhibits sharper BCC peaks than the r = 0.04 sample in Figure 2.6a. Perhaps of most interest is the scattering from the r = 0.06 sample, shown in detail in Figure 2.8b. At shorter anneal times and slightly lower temperature, the sample exhibited a

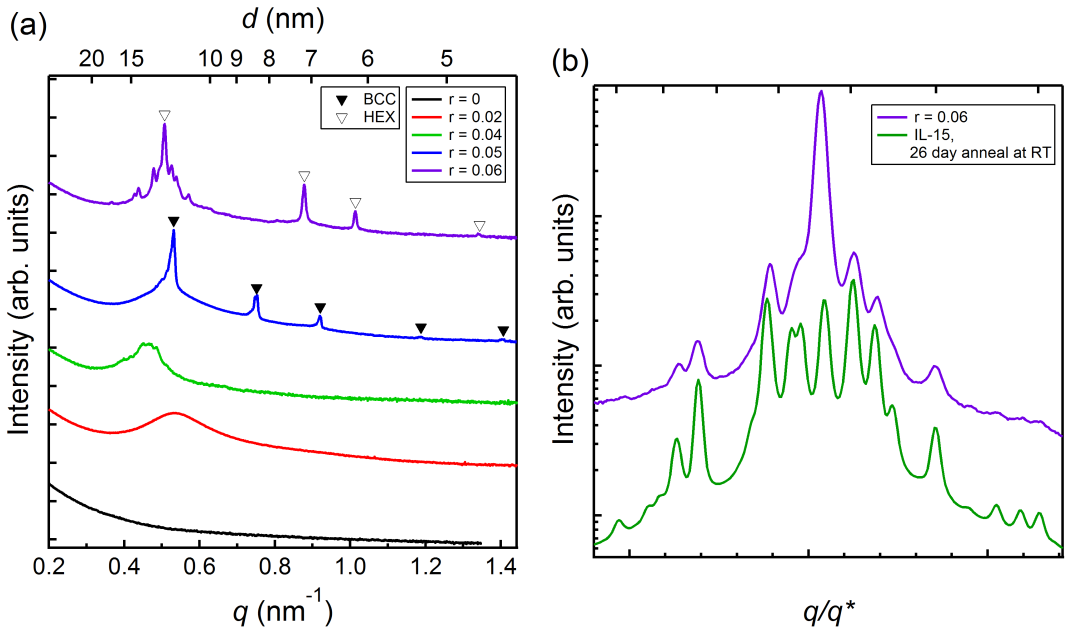

Figure 2.8: SAXS profiles for PS-PEO(8-2) with various salt loadings. Samples were annealed at 150 °C for 7 days prior to the measurement. (a) Isothermal scattering at 150 °C. (b) Comparison of scattering for the blend with r = 0.06 and Frank-Kasper σ phase scattering from the literature.[49] BCC peaks correspond to q/q^* values of 1, $2^{1/2}$, $3^{1/2}$, $4^{1/2}$, and $5^{1/2}$. HEX peaks correspond to q/q^* values of 1, $3^{1/2}$, $5^{1/2}$, and $7^{1/2}$.

combination of what was likely DQC and HEX ordering. However, after annealing the sample for 7 days, it formed coexisting σ and HEX phases, as indicated by the presence of many of the peaks found in a PI-PLA sample (IL-15) known to form the σ phase.[50]

Phase behavior of LiTFSI-doped PS-PEO(11-2) annealed for 4 days

After completing the two preliminary studies with the PS-PEO(8-2) system, we were curious to know if additional morphologies could be accessed by further increasing the salt loading. However, there was an insufficient amount of the block copolymer left to perform this study, so a similar, yet slightly larger, block copolymer, which we term PS-PEO(11-2), was instead used for this investigation. This polymer was graciously provided by Dr. Soonyong So. For this investigation, we prepared the block copolymer with salt loadings of r = 0 to 0.08 annealed at 150 °C for 4 days. The scattering patterns

from these samples are shown in Figure 2.9.

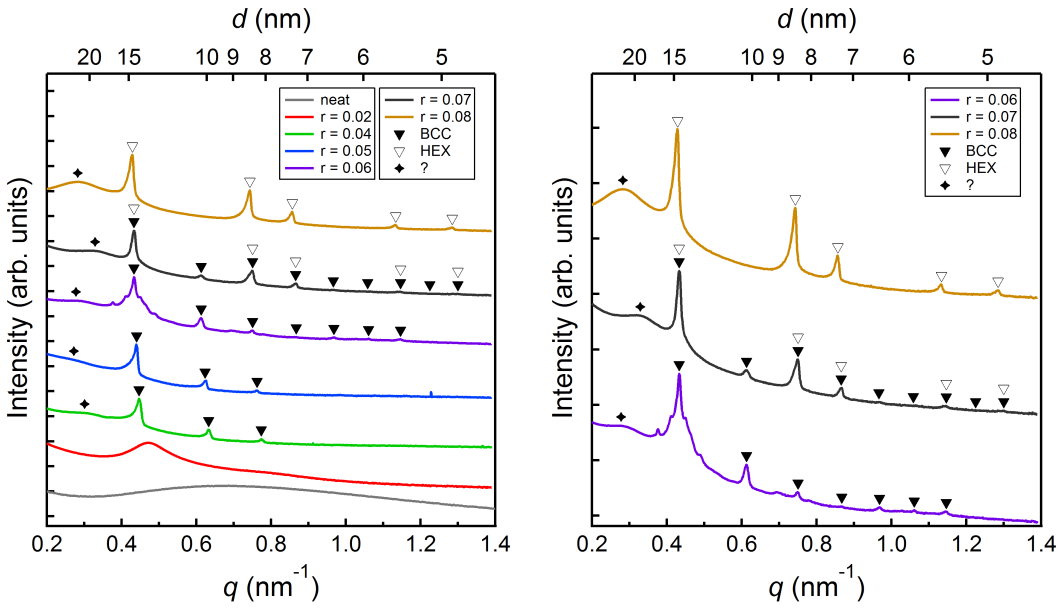

Figure 2.9: SAXS profiles for PS-PEO(11-2) with various salt loadings. Samples were annealed at 150 °C for 4 days prior to the measurement. (a) Isothermal scattering at 150 °C. (b) Zoomed view of select data from (a) that better shows the coexistence of multiple morphologies. BCC peaks correspond to q/q^* values of 1, $2^{1/2}$, $3^{1/2}$, $4^{1/2}$, $5^{1/2}$, $6^{1/2}$, $7^{1/2}$, $8^{1/2}$, and $9^{1/2}$. HEX peaks correspond to q/q^* values of 1, $3^{1/2}$, $5^{1/2}$, $7^{1/2}$, and $9^{1/2}$.

Overall, the phase behavior of the PS-PEO(11-2) block copolymer is similar to that of the PS-PEO(8-2). In nearly all samples, there is a feature at low q similar to that seen in the PS-PEO(8-2) system that corresponds to a lengthscale larger than the domain spacing of any of the morphologies. The neat block copolymer is disordered, but upon addition of a small amount of salt (r = 0.02), LLP is induced. Further increasing the LiTFSI concentration to r = 0.04 induces BCC ordering, as seen for the PS-PEO(8-2) diblock copolymer when annealed for 36 hours (Figure 2.6). The lack of higher order peaks beyond $q/q* = 3^{1/2}$ may suggest that the BCC ordering is poorly correlated. For r = 0.04, the PS-PEO(8-2) block copolymer adopted a DQC morphology after being annealed for 7 days at 150 °C. Although no evidence of a DQC phase can be seen in the PS-PEO(11-2) blend with r = 0.04 after annealing for 4 days, this does not preclude

the possibility that the BCC structure could be metastable toward either the DQC or σ phase, as previously described by Gillard *et al.*[51] Blends prepared with r = 0.05 look nearly identical to blends with r = 0.04, but with slightly larger domain spacing. At r = 0.06, there is the growth of peaks that appear reminiscent of the σ phase at low q and the growth of significantly more higher order BCC peaks. At higher salt concentrations of r = 0.07 and 0.08, the large number of peaks at low q disappear and give way to a HEX morphology. Blends containing r = 0.07 are particularly interesting, as, at first glance, the scattering data are consistent with a pure BCC phase. However, the intensity of the higher order reflections that correspond to HEX symmetry is much higher than that for peaks that correspond to only BCC, which extinguish much more quickly. This distinction is particularly noticeable in Figure 2.9b, where only select data have been replotted to allow for the trends in the data to be seen more clearly. The hypothesis that samples with r = 0.07 exhibit coexistence between BCC and HEX is further strengthened by the scattering data for r = 0.08, where the position of the HEX peaks is nearly identical to that assigned for r = 0.07. It is interesting to note that the assignment for BCC and HEX for r = 0.07 blends suggests that the two morphologies share a common q^* peak, indicating that there is a single preferred length scale for the spheres in the system, and transitions between morphologies maintains this preferred length scale.

Low q scattering for the blends with r = 0.06 is quite similar to the scattering for the PS-PEO(8-2) block copolymer with r = 0.06 after annealing at 150 °C for 7 days. We have plotted the scattered intensity alongside the σ phase scattering from the IL-15 sample in Figure 2.10. These results suggest that, after being annealed for 4 days, the salt-doped polymer is in the process of forming the σ phase. It is possible that if the sample had been annealed for longer, the peaks would have further developed and formed a more well-defined σ phase.

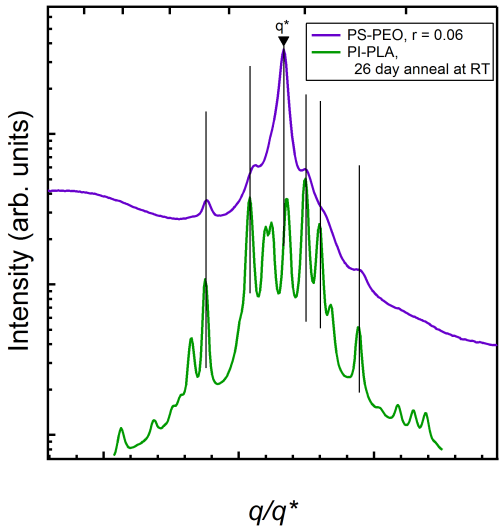

Figure 2.10: SAXS profiles for PS-PEO(8-2) compared with the scattering from a PI-PLA (IL-15) block copolymer (from ref. 49). The phases of this example has been assigned as Frank-Kasper σ phase. The vertical lines have been drawn to guide the eye.

Kinetics of equilibration in LiTFSI-doped PEP-PEO block copolymers

The studies on the PS-PEO system made it clear that the growth and evolution of microstructured morphologies in these particle-forming phases is slow, as evidenced by the slow formation of peaks corresponding to phases like the σ phase. Furthermore, at higher salt loading, it was not clear if the morphologies observed were the equilibrium morphologies or simply some metastable intermediate. Previous work by Gillard *et al.* on particle-forming PI-PLA block copolymers found that there is a temperature, T_{erg}, associated with the loss of ergodicity in the system and below which the dynamic mechanical response indicated a crossover from a liquid to a solid solution of jammed particles that exhibited liquid-like packing (LLP) (note that $T_{\mathrm{erg}} \gg T_{\mathrm{g}}$).[51] In their work, the authors found that, when samples were rapidly quenched from the disordered state to a temperature $T < T_{\mathrm{erg}}$ and then annealed at that temperature, this jammed solution of point particles (LLP) transitioned first to a DQC morphology, then, after

longer anneal times, eventually formed a Frank-Kasper σ phase. However, the time required for the phase transitions increases exponentially as the sample is cooled to temperatures approaching T_g, which the authors attributed to the increased energetic penalty associated with chain pullout of the core block through the corona at higher segregation strength, which goes as $\sim\exp(\alpha\chi N)$.[132–134] However, one difficulty with this interpretation is that chain exchange dynamics should also be expected to slow down as the system approaches the glass transition temperature of the core block. This relationship can be seen from the Vogel-Fulcher-Tammann-Hesse (VFTH) equation, which indicates that the viscosity of a solution can be expressed by

$$\eta = A\exp\left(\frac{B}{T-T_0}\right) \tag{2.2}$$

where A and B are empirical fitting parameters and T_0 is the Vogel temperature. For many polymers, T_0 is about 45 °C below T_g. Thus, Equation 2.2 indicates that the viscosity of a polymer melt should increase exponentially as a solution is cooled close to its T_g. This increase in viscosity would further slow down the equilibration of the system above and beyond the increased energetic penalty for chain pullout.

In short, one lingering question from this previous work is: what is the dominant factor that sets the rate of equilibration, the temperature approaching T_g, or the increasing segregation strength? Because $\chi N \sim 1/T$, systems that use temperature to tune χN are ill-equipped to answer this question. To answer this question, we decided to move beyond the LiTFSI-doped PS-PEO system to investigate a system with low T_gs: LiTFSI-doped PEP-PEO block copolymers. By replacing the PS block with PEP, T_g of the corona block can be reduced from *ca.* 80 °C to −67 °C. This produces two key advantages compared to other systems: (1) unlike the PS-PEO system described above, the system can be annealed at room temperature, thus allowing for long-time annealing experiments to be conducted, and (2) unlike the PI-PLA systems previously studied by Lee *et al.* and Gillard *et al.*,[49,51] the segregation strength of the system can be readily tuned by varying the concentration of LiTFSI in the PEO phase. In this work, we vary the salt loading from $r = [Li^+]/[EO] = 0 – 0.08$; previous work by Chintapalli *et al.* has suggested that, over this concentration range, the T_g of the PEO cores should

only range from *ca.* –51 °C to –41 °C,[78] while the T_{ODT} of the block polymer is anticipated to increase much more substantially based on results from LiTFSI-doped PS-PEO systems.[82,84,85]

This subsection of the results will first focus on the phase behavior and dynamics of the PEP-PEO(4-1) block copolymer when doped with salt. As shown in Table 2.2, this polymer has $f_{PEO} = 0.11$ and $M_n = 4.3$ kg/mol. After that, we will briefly consider the phase behavior of PEP-PEO(3-1), which has $f_{PEO} = 0.13$ and $M_n = 3.0$ kg/mol, before moving onto the Discussion section to discuss the general findings from all polymers involved in this study.

Structure and dynamics of LiTFSI-doped PEP-PEO(4-1) diblock copolymer

Prior to SAXS experiments, DMS experiments were carried out to determine T_{ODT} of blends as a function of salt loading. Results for PEP-PEO(4-1) are shown in Figure 2.11. There is a marked increase in T_{ODT} as the salt loading is increased. The neat system disorders at temperatures just slightly above room temperature, whereas, at a salt loading of $r = 0.08$, the system disorders at 140 °C.

After determining the relationship between T_{ODT} and salt loading for this system, we wanted to understand the phase behavior of these systems as they were ambiently cooled to room temperature from $T > T_{ODT}$. The SAXS traces from these blends, collected after annealing at room temperature for approximately 1 week, are shown in Figure 2.12. At many of the salt concentrations, there are peaks that can be assigned to well-established morphologies, but there are also additional peaks whose origin is not immediately obvious. We will return to indexing these additional peaks in the Discussion section. In general, the peak positions shift to lower q as the salt loading is increased, indicative of an increase in the periodic spacing. In Figure 2.12a, many of the remaining peaks have been indexed to FCC, whereas Figure 2.12b shows that, by picking a different peak to represent q^*, it is also possible to interpret many of the peaks as BCC. Of these two interpretations, FCC seems more likely. Our work with the PS-PEO(11-2) block copolymer suggests that coexisting σ+HEX and σ+BCC morphologies shared a common q^* peak position (Figures 2.8 and 2.9, respectively). In

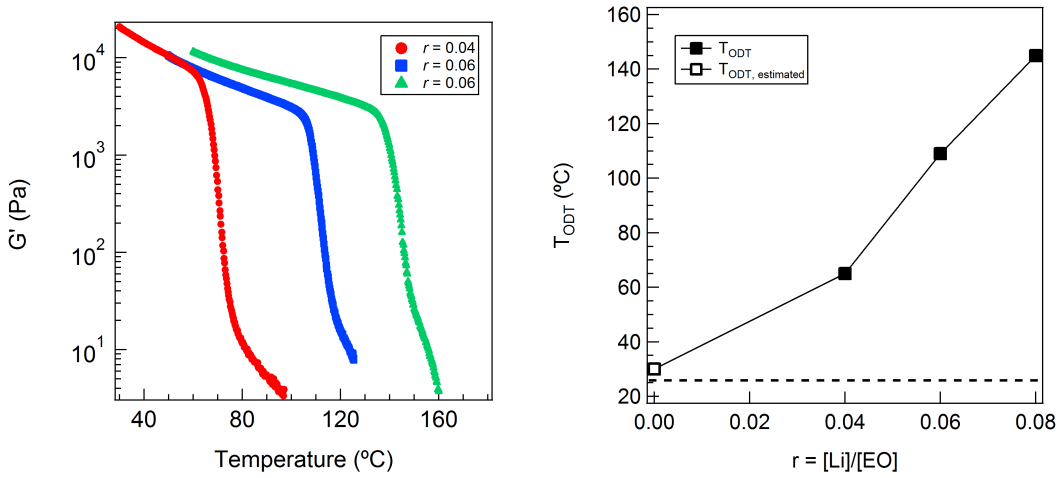

Figure 2.11: (a) Several heating ramps showing a drop in elastic modulus for several block polymers upon heating through T_{ODT}. (b) Dependence of T_{ODT} of PEP-PEO(4-1) on salt loading. The estimated temperature is based on the failure of the sample to order sufficiently quickly to observe a distinct ODT. The dashed line approximates room temperature. The estimated ODT for the neat block polymer is based on the observation of the crossover between liquid-like and solid-like behavior (*i.e.* $G' > G''$) consistent with microstructural ordering when held at 30 °C for long times. The solid line has been drawn to guide the eye.

addition, work by Lee *et al.* established that the σ phase grows from other ordered phases by chain exchange.[49] Lee *et al.* later elaborated on this interpretation by suggesting that the jammed micelle structure of the LLP morphology that ultimately results in the σ phase consists of micelles of a single size.[50] By this reasoning, it would be unusual for a system to, upon annealing, adopt the two distinct length scales necessary for the coexistence between BCC and the other microstructure that has not yet been indexed. Thus, in Figure 2.12, the indexing that suggests coexistence between FCC and the additional phase is likely the correct assignment.

Many recent reports on these sphere-forming systems have indicated that the phase behavior of these systems is highly path dependent, a result of the system becoming kinetically trapped in metastable morphologies for long periods of time.[50,51,137] Therefore, we performed a series of systematic quenching experiments and monitored the morphology *via* SAXS at Argonne National Labs. Capillaries containing the

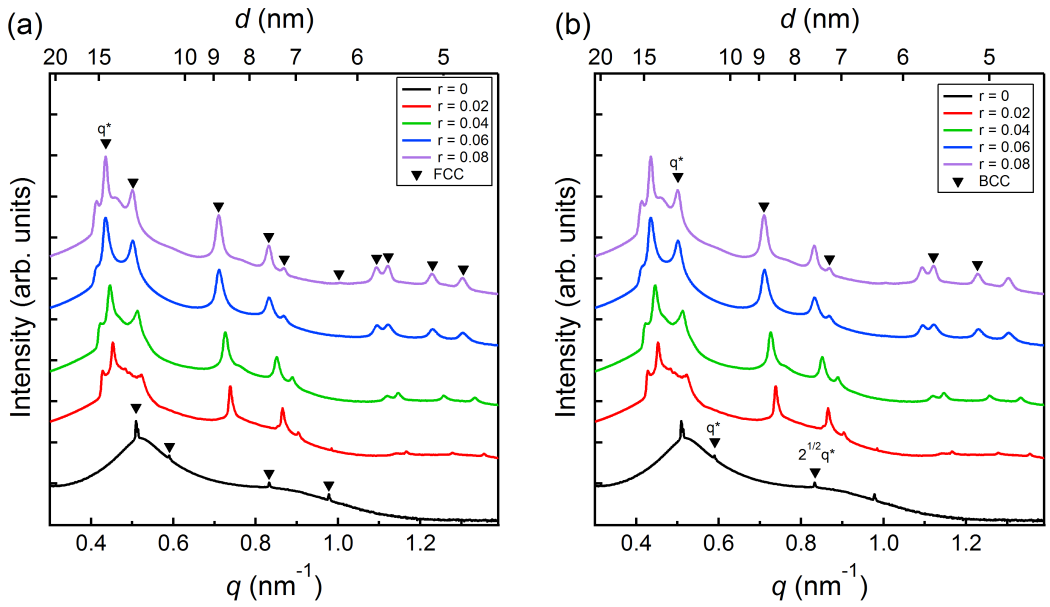

Figure 2.12: The phase behavior of the polymers after being brought above T_{ODT}, then ambiently cooled to room temperature. (a) shows the peaks being indexed to FCC reflections, while (b) shows the peaks being indexed as BCC. Samples annealed at room temperature for at least one week prior to data collection. The FCC markers correspond to peaks at q/q^* multiples of 1, $(4/3)^{1/2}$, $(8/3)^{1/2}$, $(11/3)^{1/2}$, $(12/3)^{1/2}$, $(16/3)^{1/2}$, $(19/3)^{1/2}$, $(20/3)^{1/2}$, $(24/3)^{1/2}$, and $(27/3)^{1/2}$. The BCC markers correspond to peaks at q/q^* multiples of 1, $2^{1/2}$, $3^{1/2}$, $4^{1/2}$, $5^{1/2}$, and $6^{1/2}$.

samples were heated to temperatures $T > T_{ODT}$ for 10 minutes, then quickly quenched using a room temperature water bath and placed in the beamline. The growth of ordered morphologies was then monitored as a function of time. The results of these experiments are shown in Figure 2.13.

The results in Figure 2.13 indicate that the rate of equilibration is highly dependent upon salt loading. Comparing (a) and (b), we see that samples with r = 0.02 largely achieve a persistent morphology after 10 minutes at room temperature, but samples with r = 0.04 have a largely fixed morphology after only 3 minutes. In both samples, there is the presence of FCC ordering along with an additional structure which leads to additional scattering peaks. In contrast, samples with higher salt loadings of r = 0.06 or 0.08 exhibit only LLP after annealing for 13 hours and 4 months, respectively.

The implications of this phase behavior and the origin of the additional peaks will be discussed further in the Discussion section.

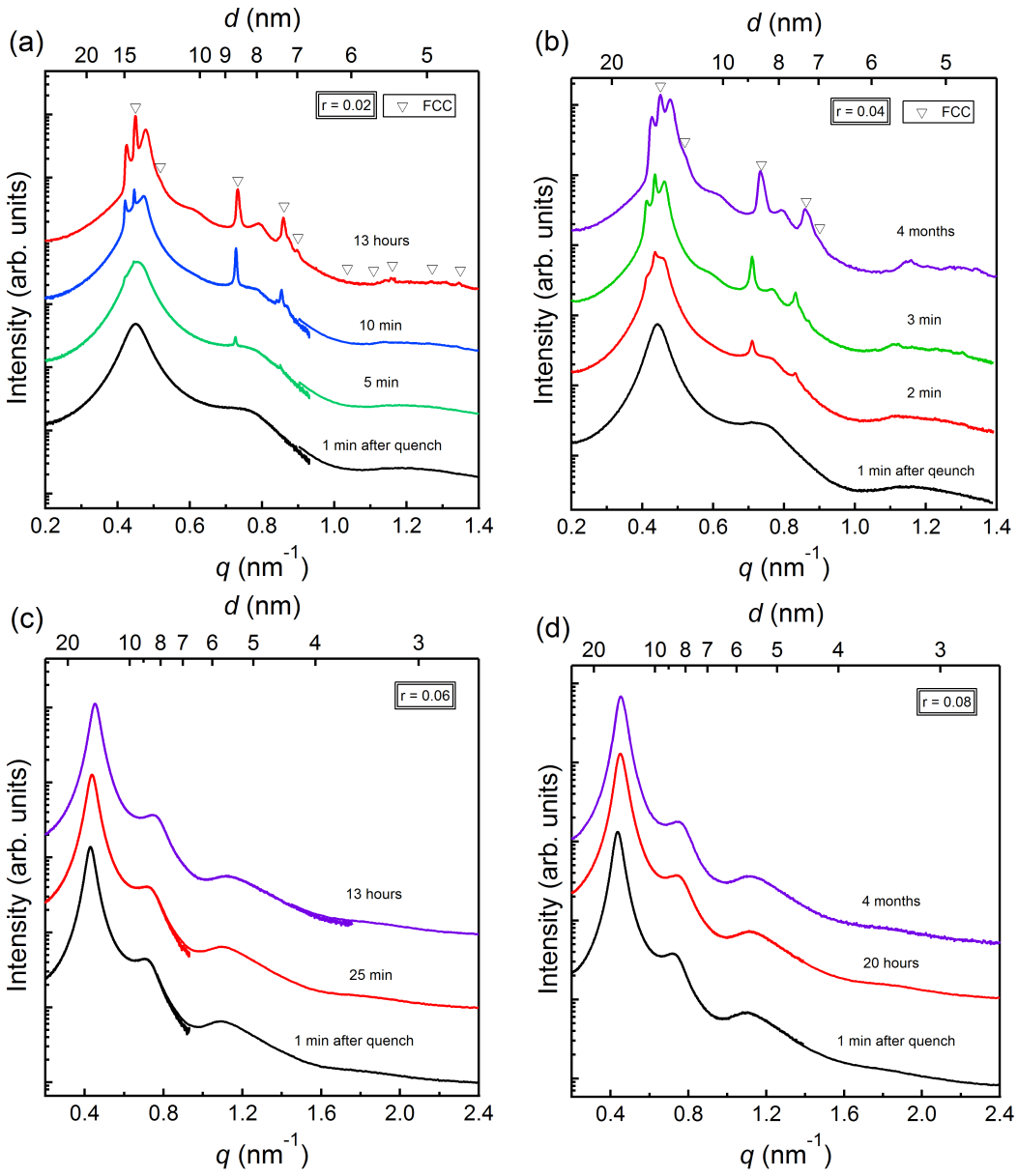

Figure 2.13: The growth of structure over time in the PEP-PEO(4-1) diblock copolymer melt with a salt-loading of r = (a) 0.02, (b) 0.04, (c) 0.06, and (d) 0.08 after being rapidly quenched to room temperature from above T_{ODT}. The FCC markers correspond to peaks at q/q^* multiples of 1, $(4/3)^{1/2}$, $(8/3)^{1/2}$, $(11/3)^{1/2}$, $(12/3)^{1/2}$, $(16/3)^{1/2}$, $(19/3)^{1/2}$, $(20/3)^{1/2}$, $(24/3)^{1/2}$, and $(27/3)^{1/2}$.

Structure and dynamics of LiTFSI-doped PEP-PEO(3-1) diblock copolymer

The phase behavior and dynamics of the PEP-PEO(3-1) block copolymer doped with LiTFSI were also investigated. As detailed in Table 2.2, this polymer has $f_{PEO} = 0.13$ and $M_n = 3.0$ kg/mol. The DMS-determined T_{ODT}s and the phase behavior of the blends when ambiently cooled from $T > T_{ODT}$ to room temperature is shown in Figure 2.14.

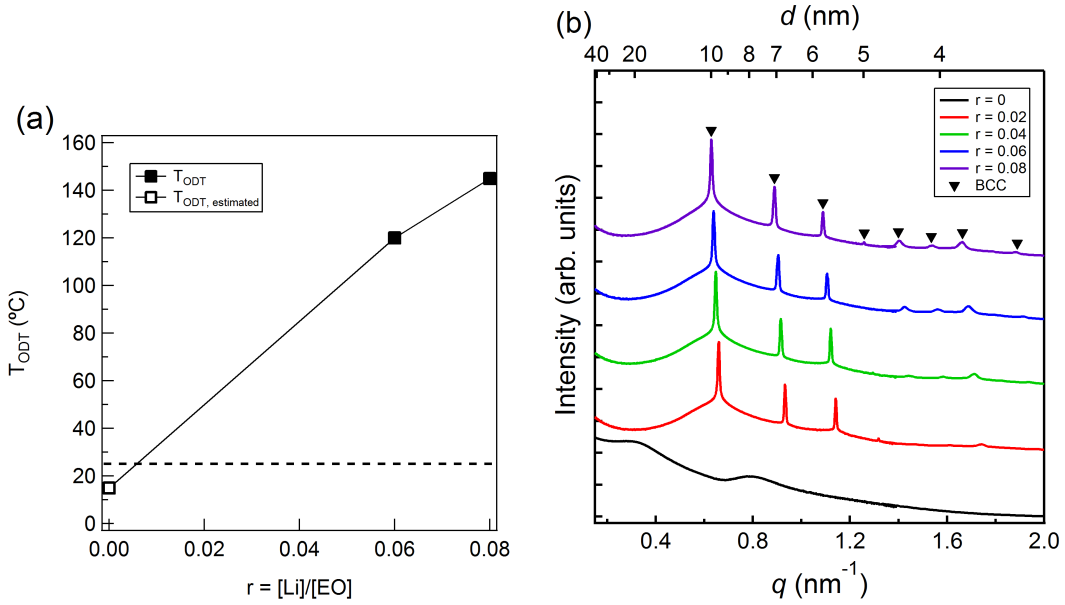

Figure 2.14: (a) Dependence of the T_{ODT} of PEP-PEO(3-1) diblock copolymer on salt loading. The estimated temperature is based on the difficulty of the rheometer to cool sufficiently well and the sample to order sufficiently fast to observe a distinct ODT. The dashed line approximates room temperature. The solid line has been drawn to guide the eye. (b) The phase behavior of the polymers after being brought above T_{ODT}, then ambiently cooled to room temperature. The BCC markers correspond to peaks at q/q^* multiples of 1, $2^{1/2}$, $3^{1/2}$, $4^{1/2}$, $5^{1/2}$, $6^{1/2}$, $7^{1/2}$, $8^{1/2}$, and $9^{1/2}$.

Interestingly, despite the similarities between PEP-PEO(4-1) and PEP-PEO(3-1), there is no indication of any phase other than BCC for these samples, despite having similarly large T_{ODT}s at various salt loadings. This is particularly surprising considering that PEP-PEO(3-1) contains $f_{PEO} = 0.13$, compared to 0.11 for PEP-PEO(4-1); the phase diagram presented by Xie *et al.* would predict that the sample with relatively

larger f_{PEO} would be more likely to exhibit σ or a metastable DQC phase (see Figure 2.3). Beyond this observation, there is also an interesting scattering feature at low q for the neat, salt-free PEP-PEO(3-1) block polymer that corresponds to a length scale of about 20 nm. This size is roughly consistent with the peak previously described for PS-PEO block copolymers.

Just like for PEP-PEO(4-1), rapid quenching experiments were also carried out with PEP-PEO(3-1). The results of these experiments are shown in Figure 2.15. In both cases, the morphology exhibits evidence of BCC ordering within only 1 minute of quenching that persists for at least 1.5 months. Interestingly, the BCC peaks at $r = 0.04$ sharpened relatively faster, with the peak width and intensity staying largely invariant after 2 minutes of annealing. Compared to the $r = 0.04$ sample, the BCC peaks at $r = 0.08$ sharpen much more slowly, with a significant change occurring between 8.5 hours and 45 days after the quench. At both salt concentrations and at all anneal times, there is evidence of a large disordered shoulder below the BCC peak that suggests the samples contain coexistence between LLP and BCC. Over even longer times, this LLP may grow into BCC or a different ordered phase, but the timescale of such transitions is not readily accessible. We briefly note that, after 172 days, the $3^{1/2}q^*$ peak in both samples appears to broaden, but this is likely an artifact of the detectors. At 172 days, the instrument was configured such that the MAXS detector collected the peak at that time point; at all other time points, the $3^{1/2}q^*$ peak was within the range of the SAXS detector. The $2^{1/2}q^*$ peak at 172 days also appears relatively broader because it occurs right at the overlap between the SAXS and MAXS detectors.

One possible explanation for the formation of only the BCC phase in this sample is that the annealing temperature was too high to access other ordered phases. Therefore, additional annealing experiments were conducted by quenching the samples from the disordered state to 0 °C by immersing them in ice water, then annealing in a temperature-controlled Linkham capillary stage held at 0 °C. The results from this study are shown in Figure 2.16 for a sample with $r = 0.04$. Although quenching to 0 °C appears to slow down the rate at which the BCC morphology grows compared to room temperature (Figure 2.15a), the difference in quench temperature does not affect

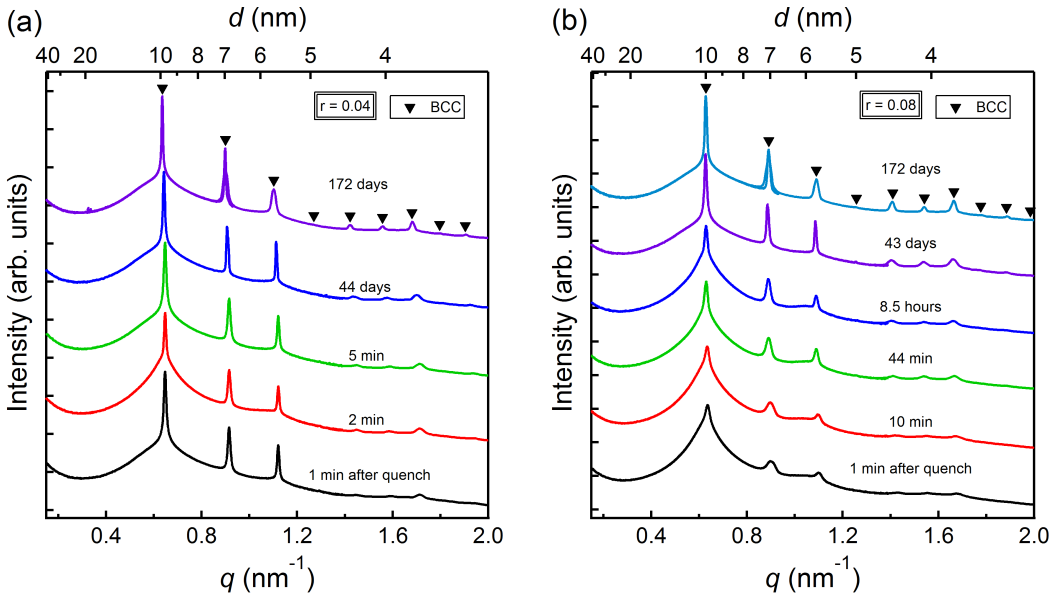

Figure 2.15: The growth of structure over time in the PEP-PEO(3-1) diblock copolymer melt with a salt-loading of r = (a) 0.04 and (b) 0.08 after being rapidly quenched to room temperature from above T_{ODT}. The BCC markers correspond to peaks at q/q^* multiples of 1, $2^{1/2}$, $3^{1/2}$, $4^{1/2}$, $5^{1/2}$, $6^{1/2}$, $7^{1/2}$, $8^{1/2}$, $9^{1/2}$, and $10^{1/2}$.

the resulting morphology over the timescale of the experiment.

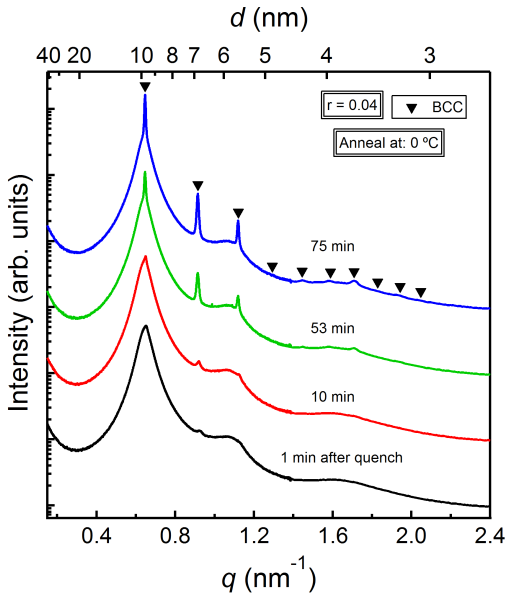

Figure 2.16: The growth of structure over time in the PEP-PEO(3-1) diblock copolymer melt with a salt-loading of r = (a) 0.04 and (b) 0.08 after being rapidly quenched to 0 °C from above T_{ODT}. The BCC markers correspond to peaks at q/q^* multiples of 1, $2^{1/2}$, $3^{1/2}$, $4^{1/2}$, $5^{1/2}$, $6^{1/2}$, $7^{1/2}$, $8^{1/2}$, $9^{1/2}$, and $10^{1/2}$.

2.5 Discussion

A primary goal of the current work was to investigate the phase behavior of asymmetric block polymers at high segregation strengths through the use of LiTFSI. Taken altogether, the phase behavior of the PS-PEO and PEP-PEO systems is highly path dependent, both in terms of the quench rate and anneal time. In this section, we first attempt to index many of the scattering traces shown in the Results section that did not correspond to immediately recognizable morphologies. We then perform an analysis of the thermodynamics and kinetics of the phase behavior of the block polymer systems described in the Results section.

Identifying and distinguishing morphologies in salt-doped PS-PEO and PEP-PEO

In many of the samples detailed in the Results section, there were additional peaks beyond traditional ordered morphologies such as HEX, BCC, and FCC. In this section, we revisit those scattering patterns and attempt to ascertain whether the scattering originates from an A15, Frank-Kasper σ, or HCP phase. A15, HCP, and σ were detailed extensively in a recent paper by Chanpuriya *et al.*[137] We briefly note that there is a distinction between HEX and HCP packings of spheres. HEX refers to spheres with 6-fold 2-dimensional symmetry with no discernible dependence on the dimension along which the planes are stacked, whereas HCP consists of more spheres per unit cell to form a close-packed system that lead to additional scattering peaks.[137] Interestingly, the location of higher-order reflections for the HEX spheres is the same as that found in HCP cylinders. For additional information about the distinction between HEX and HCP, and for more details about the A15 phase, we refer to reader to Ref. 137.

The allowed Miller indices (typically given as <*hkl*>) for HCP spheres, A15, and σ phase are well known and have been included in a number of recent publications.[49–51,137] A particularly useful list of the indices is included in the supporting information of recent work by Chanpuriya *et al.*[137] Converting the allowed Miller indices into predicted peak positions on a 1-dimensional SAXS trace requires knowledge of the type of crystal structure. A15 and σ phase have cubic and tetragonal structures, respectively, whereas HCP has a hexagonal structure. As a result, the number of lattice parameters required to describe the position of every particle within the unit cell depends on the type of structure. A15 requires only one lattice vector, a, whereas σ and HCP require two lattice parameters, a and c. For σ and HCP, these parameters are conventionally defined such that a is related to the spacing between atoms in a plane, whereas c is connected to the interlayer spacing.[51] By knowing the Miller indices and the lattice parameters, it is then possible to calculate all peak positions. For a cubic structure (*e.g.* BCC, FCC, A15 phases), this relationship is given by

$$q = 2\pi\sqrt{\frac{h^2+k^2+l^2}{a^2}} \tag{2.3}$$

If the structure is tetragonal (*e.g.* σ phase), the peaks can instead by calculated *via*

$$q = 2\pi\sqrt{\frac{h^2+k^2}{a^2}+\frac{l^2}{c^2}} \tag{2.4}$$

Finally, for a hexagonal structure (*eg.* HCP), the peak positions are given by

$$q = 2\pi\sqrt{\frac{4}{3}\left(\frac{h^2+hk+k^2}{a^2}\right)+\frac{l^2}{c^2}} \tag{2.5}$$

As discussed in the Results section, the scattering patterns from the blends also may correspond to a dodecagonal quasicrystal (DQC). The lack of real-space periodicity in these structures makes the indexing of the peaks conceptually trickier, but an instructive tutorial by Iwami *et al.* demonstrated how it is possible to convert the lattice parameters a and c and the five Miller indices necessary to describe the scattering produced by a DQC into 1-dimensional q peak positions.[144] For the sake of brevity, a description of the analysis presented in that work is not included here. By using the equations described above and in Ref. 144, and the Miller indices given by Chanpuriya *et al.*[137] for HCP, A15, and σ phases, we were able to calculate expected peak positions for a variety of morphologies. a and c for each phase were not known *a priori*, so they were adjusted until a visual best fit was obtained. The predicted peak positions for various morphologies that were not assigned in the Results section are shown in Figures 2.18 through 2.21.

Although the large number of both observed and predicted peaks makes definitive conclusions about the phase behavior challenging without the aid of a complementary technique such as TEM, some general remarks can still be made based on the presence and absence of several key peaks. In the Results section, we compared the scattering from the PS-PEO(8-2) with r = 0.06 at 230 °C to that from SIS'O block polymer that exhibited a DQC morphology (see Figure 2.7a). The results in Figure 2.18 largely confirm this conclusion; both HCP and A15 assignments fail to predict several key

peaks at low q, while the ratio of peak intensities is not strong enough to suggest the σ phase.[51] In Figure 2.8a, we found that the PS-PEO(8-2) block polymer with r = 0.04 formed an unusual structure when annealed at 150 °C for 7 days. However, as can be seen in Figure 2.19, the low signal-to-noise of the scattering makes discerning if the morphology is DQC, HCP, A15, σ, or some other phase challenging.

The PEP-PEO(4-1) block polymer also exhibits interesting phase behavior. As was shown in Figure 2.12, when PEP-PEO(4-1) blends are cooled from $T > T_{ODT}$ to room temperature (r.t.), they form a combination of FCC and an additional morphology. Based on the indexing shown in Figure 2.20 and comparing the relative peak intensities to those previously shown by Chanpuriya *et al.*,[137] an HCP assignment seems most likely. Although the DQC peaks appear to line up reasonably well with the data, there is a noticeable lack of a peak to the left of the first set of peaks that would come from interlayer stacking. Beyond samples cooled ambiently, it also appears that PEP-PEO(4-1) samples rapidly quenched to r.t. from the disordered state, then annealed, also likely exhibit an HCP morphology that may coexist with FCC (Figure 2.21)

Although these results are preliminary, they suggest that the use of LiTFSI can drive the formation of unique phases that are not typically observed in diblock copolymers. To the best of our knowledge, these results are the first example of the HCP phase in a diblock copolymer system. We briefly note that prior work has suggested that that the anticipated Miller indices for both the HCP and a Frank-Kasper C14 phase should be the same.[145] However, the low-q triplet peaks for the C14 phase occur at lower q than the first "bump" associated with the form factor. Therefore, an assignment of HCP for the PEP-PEO(4-1) system is much more likely than Frank-Kasper C14. We have included rough cartoons of the candidate phases in Figure 2.17.

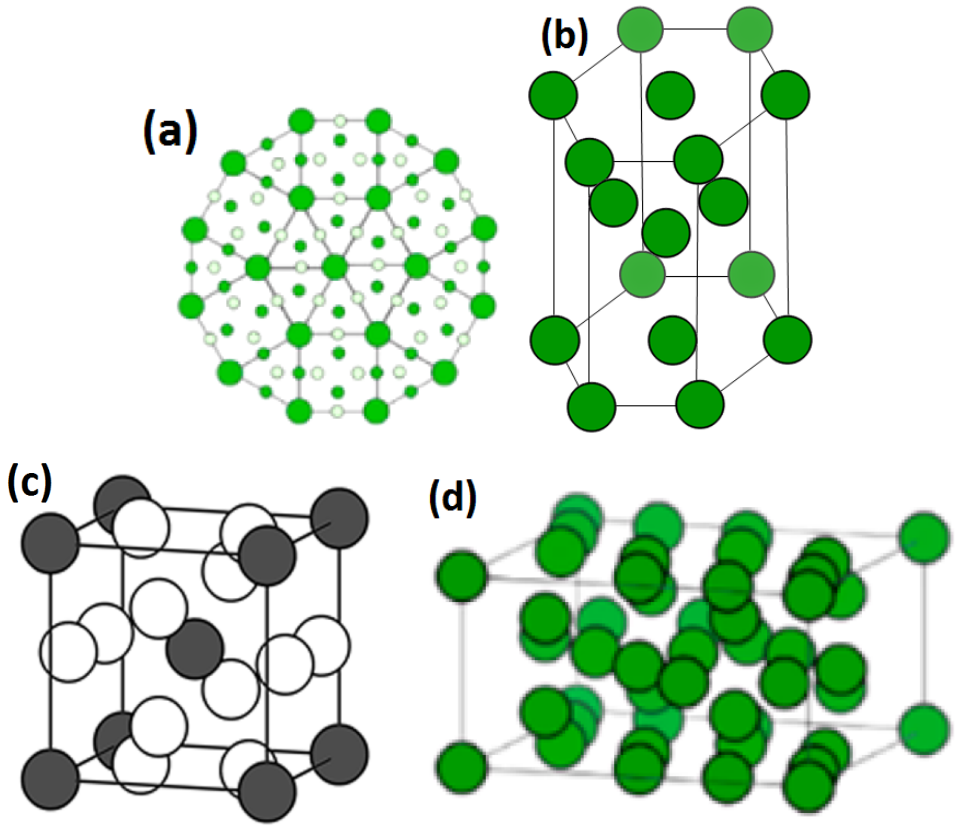

Figure 2.17: Rough cartoons and unit cells for (a) DQC, (b) HCP, (c) A15, and (d) σ phases. Adapted from Ref. 137 with permission. Copyright 2016 American Chemical Society.

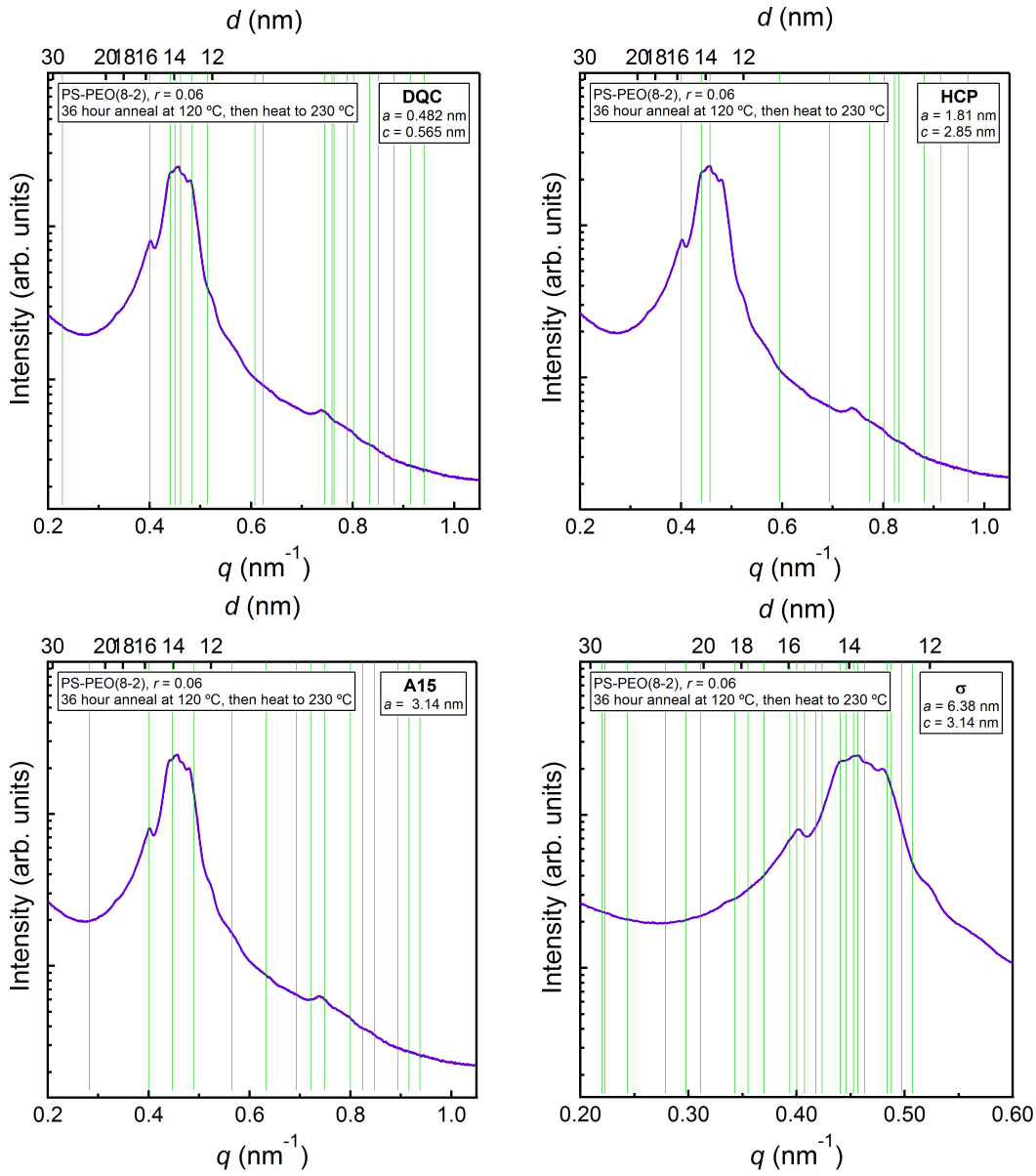

Figure 2.18: Expected peak positions for PS-PEO(8-2) with r = 0.06 annealed for 36 hours at 120 °C, then heated to 230 °C, if it were exhibiting a (a) DQC, (b) HCP, (c) A15, or (d) σ phase morphology. SAXS data from blend originally shown in Figure 2.6b.

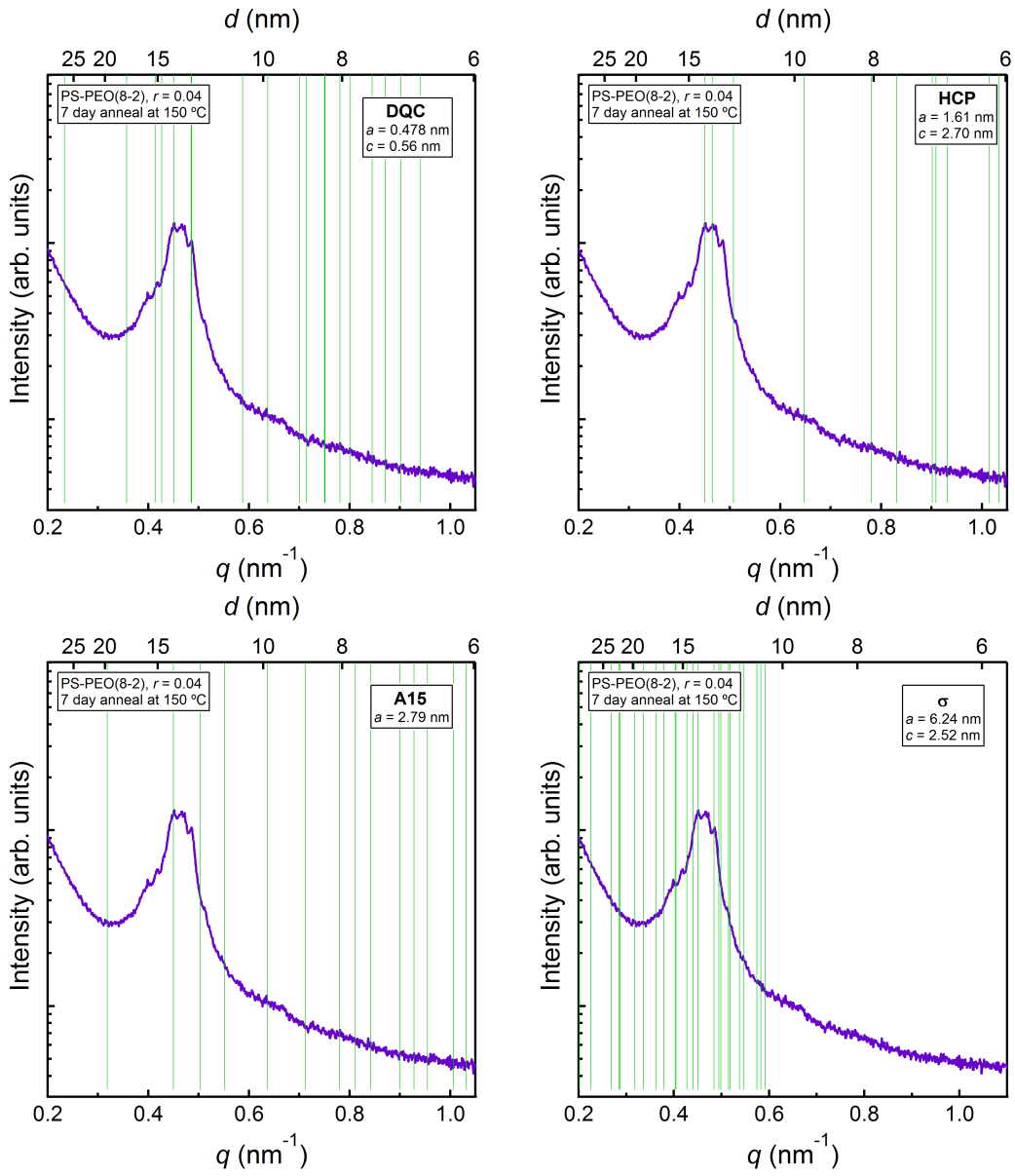

Figure 2.19: Expected peak positions for PS-PEO(8-2) with $r = 0.04$ annealed for 7 days at 150 °C if it were exhibiting a (a) DQC, (b) HCP, (c) A15, or (d) σ phase morphology. SAXS data from blend originally shown in Figure 2.8.

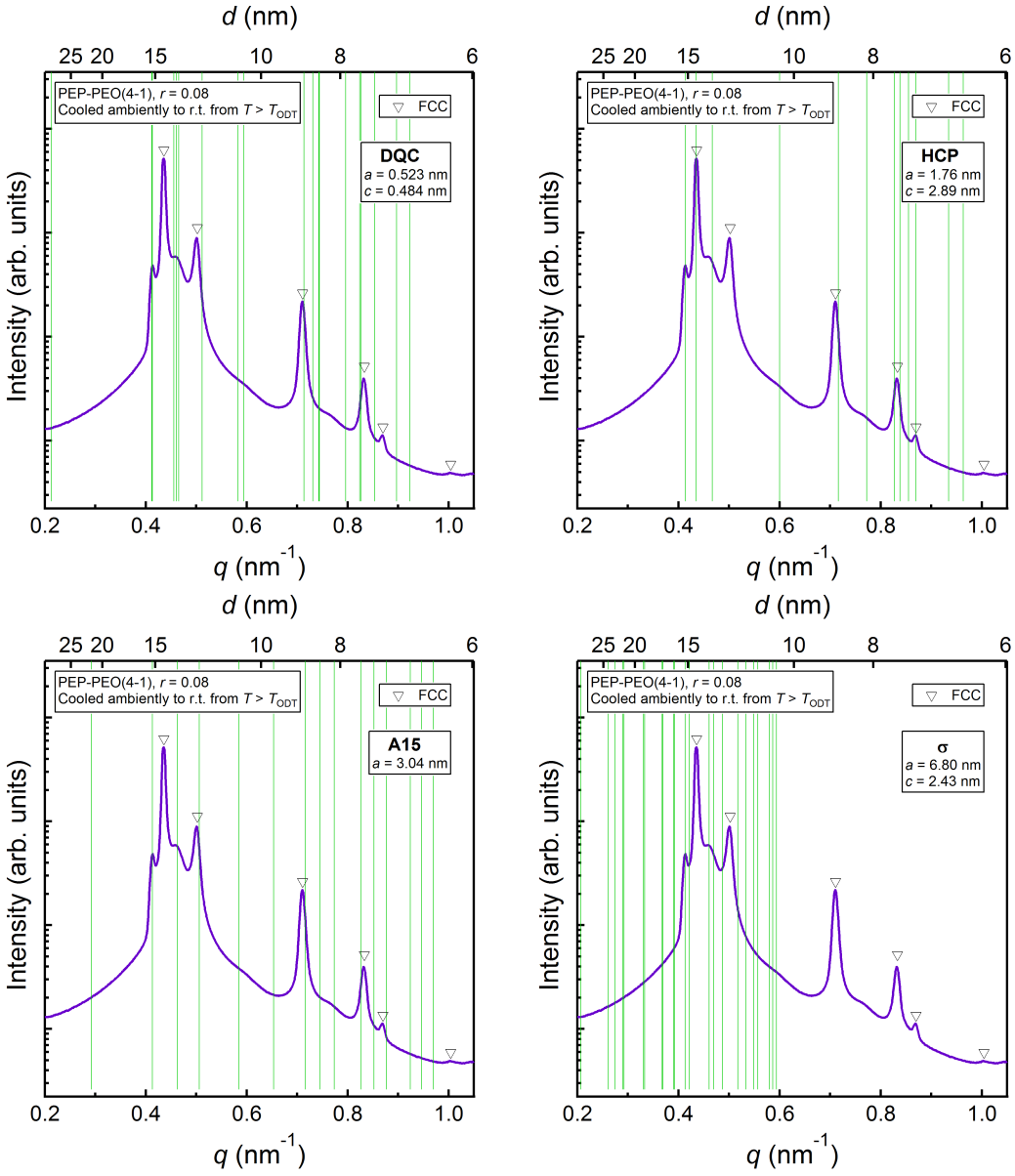

Figure 2.20: Expected peak positions for PEP-PEO(4-1) with r = 0.08 heated to $T > T_{ODT}$, then cooled to r.t., if it were exhibiting a (a) DQC, (b) HCP, (c) A15, or (d) σ phase morphology. SAXS data from blend originally shown in Figure 2.12. The FCC markers correspond to peaks at q/q^* multiples of 1, $(4/3)^{1/2}$, $(8/3)^{1/2}$, $(11/3)^{1/2}$, and $(12/3)^{1/2}$.

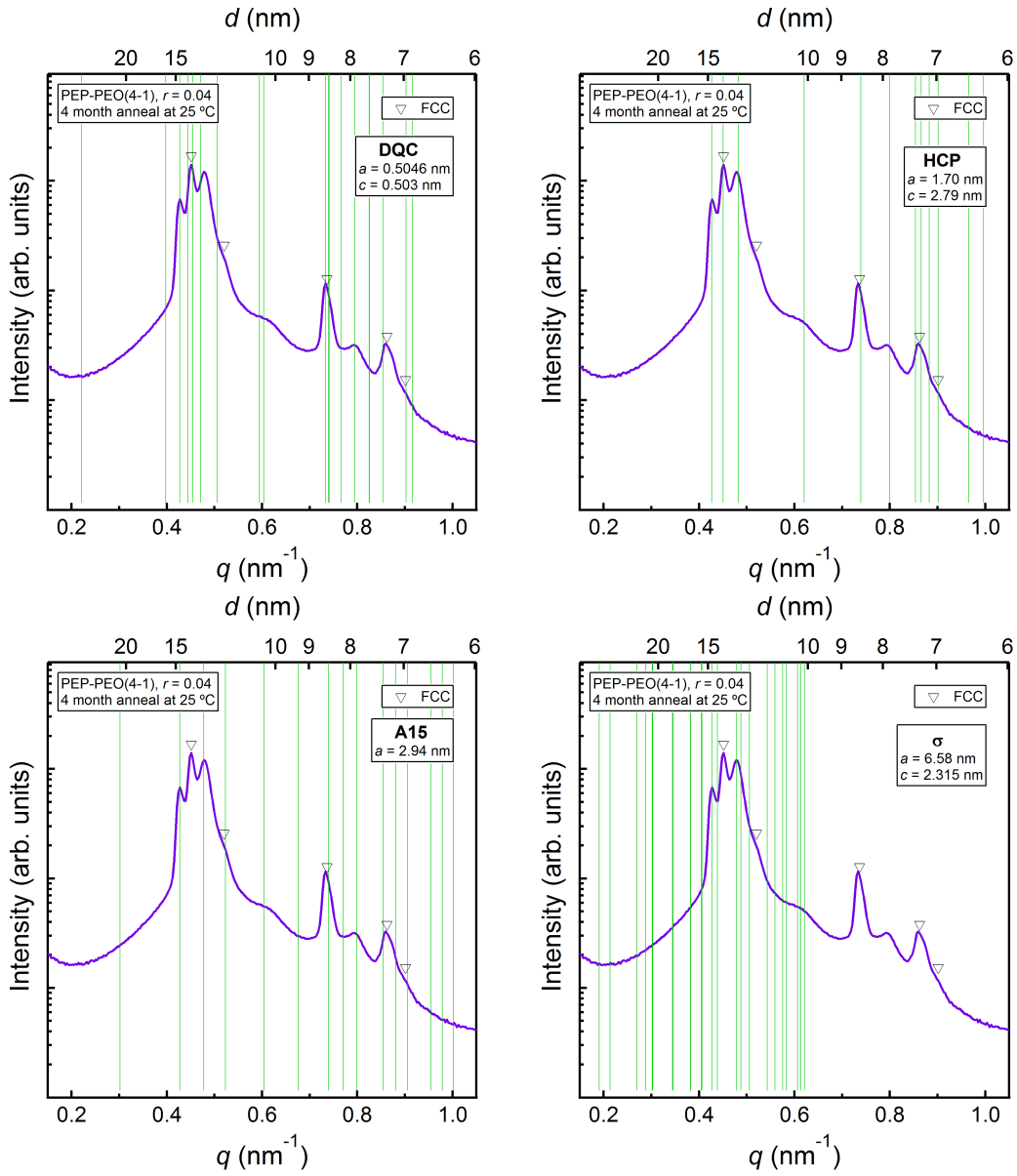

Figure 2.21: Expected peak positions for PEP-PEO(4-1) with r = 0.04 annealed for 4 months if it were exhibiting a (a) DQC, (b) HCP, (c) A15, or (d) σ phase morphology. SAXS data from blend originally shown in Figure 2.13b. The FCC markers correspond to peaks at q/q^* multiples of 1, $(4/3)^{1/2}$, $(8/3)^{1/2}$, $(11/3)^{1/2}$, and $(12/3)^{1/2}$.

For the remainder of this chapter, we consider the thermodynamics and kinetics of the observed phase behavior for the PS-PEO and PEP-PEO systems. We first look at the phase behavior of the PS-PEO(11-2) system by calculating $\chi_{\text{eff}}N$ as a function of salt loading, then consider what the phase behavior of the system suggests about the ability of the systems to reach equilibrium morphologies. We then assemble diagrams that track the evolution of the phase behavior of salt-doped PS-PEO or PEP-PEO at different segregation strengths or quench depths as a function of annealing time by assembling diagrams that are analogous to time-temperature-transformation (tTT) diagrams. tTT diagrams have previously been used to study the equilibration of the phase behavior of salt-free sphere-forming block polymers.[50,51]

Segregation strength of salt-doped PS-PEO blends

One of the most interesting features in Figure 2.10 is that, to a first approximation, the results suggest that at salt concentrations higher than that which forms the σ phase, other morphologies are formed. As discussed in the Introduction to this chapter, there is a significant body of work that has found that the addition of LiTFSI to PS-PEO diblock copolymer significantly increases the effective segregation strength, $\chi_{\text{eff}}N$ of the system. Thus, the results in Figure 2.10 may indicate that at higher segregation strengths, sphere phases other than the σ phase may be stable. To quantify the effect of salt loading in the current blends, we will consider two different functional forms for the relationship between χ_{eff} and salt loading. The first relationship, which was developed by Wanakule *et al.*, predicts a simple linear dependence of χ_{eff} with salt, *via*

$$\chi_{\text{eff}} = 0.049 + 1.52r \tag{2.6}$$

where V_{ref} = 0.1 nm^3 and the temperature is fixed at 100 °C.[80] This relationship was derived by extracting a χ_{eff} at the T_{ODT} by assuming that χN_{ODT} of the block polymer is accurately described by mean-field theory as shown in Figure 1.1. Later work performed on nearly symmetric PS-PEO diblock copolymer lead to the conclusion that this model was too simplistic to accurately capture the behavior of most systems.

As a result, Teran *et al.* worked to develop a more robust model for χ_{eff} by fitting disordered state SAXS scattering data of numerous, roughly symmetric PS-PEO diblock copolymers with the random phase approximation.[82] Their resulting model was given by

$$\chi_{eff} = \frac{10.2}{T} + \frac{1850}{TN} + \frac{0.0101T}{N}\left[1 - \exp\left(\frac{-22Tr}{N}\right)\right] \tag{2.7}$$

where V_{ref} = 0.1 nm^3, N is a volumetric degree of polymerization, and T [=] K. For the PS-PEO(11-2) block polymer, N = 226 (Table 2.2). Therefore, we can calculate $\chi_{eff}N$ for PS-PEO(11-2) for both models as a function of salt loading. This analysis is shown in Figure 2.22. Because Equation 2.6 is only given at 100 °C, $\chi_{eff}N$ is given for both models at 100 °C in Figure 2.22a. In Figure 2.22b, we compare the two models when a temperature of 150 °C, the annealing temperature for the samples, is used in Equation 2.7.

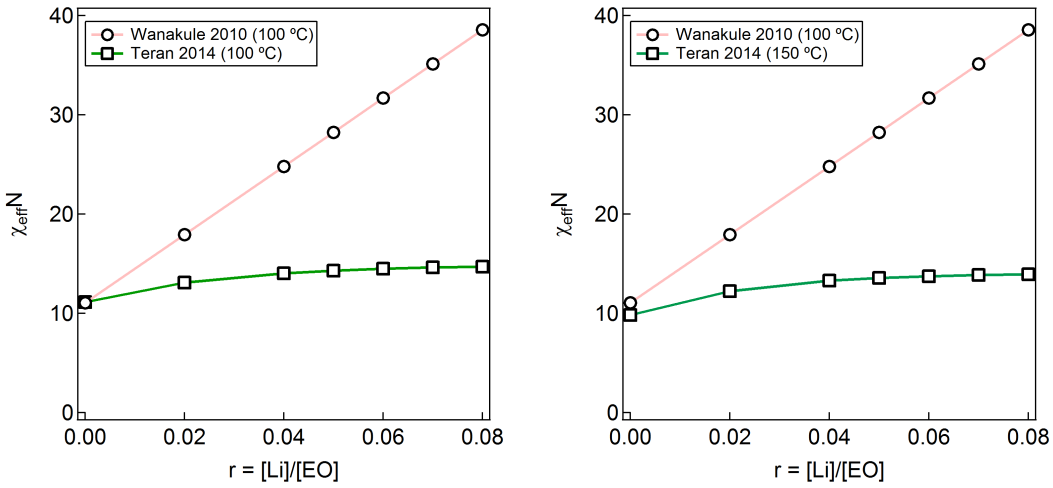

Figure 2.22: $\chi_{eff}N$ as a function of salt loading for LiTFSI-doped PS-PEO block copolymers. The Teran model is calculated at (a) 100 °C and (b) 150 °C.

As can be seen by comparing the Teran model at 100 and 150 °C in parts (a) and (b) of the figure, salt-loading has a stronger effect on $\chi_{eff}N$ than temperature, particularly compared to the effect of salt predicted by the Wanakule model. With the segregation

strengths thus calculated, it is possible now to revisit the SCFT phase diagram proposed by Xie *et al.* for systems with a conformational asymmetry of 2 originally shown in Figure 2.2.[45] The phase diagram, along with the calculated values for $\chi_{eff}N$ from Figure 2.22, are shown in Figure 2.23.

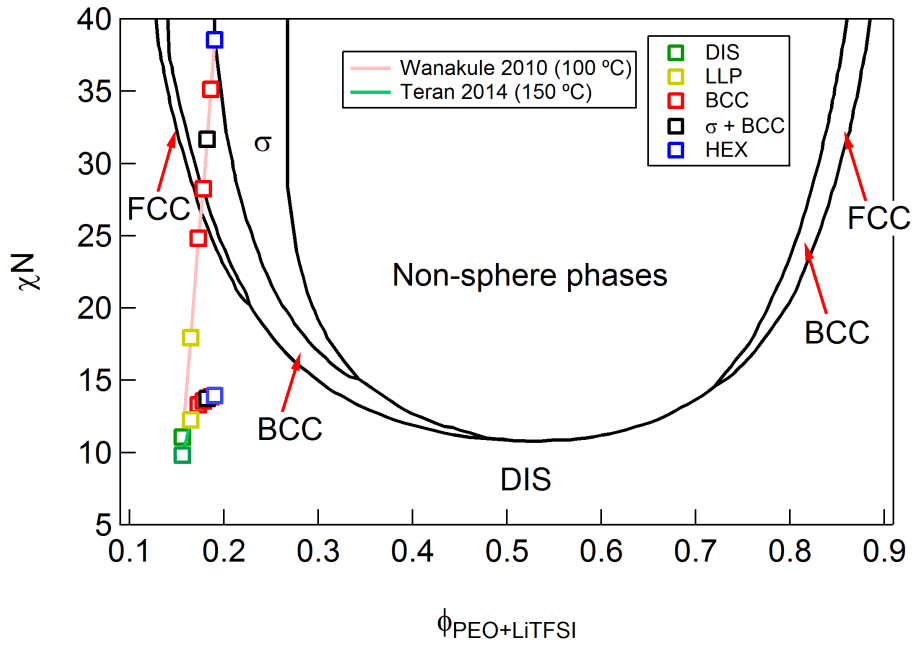

Figure 2.23: Comparison of expected $\chi_{eff}N$ for the LiTFSI-doped PS-PEO diblock copolymer *vs.* the volume fraction of the PEO phase, plotted on top of the phase diagram from Xie *et al.*[45] Surprisingly, the simpler model from Wanakule *et al.* qualitatively captures the phase behavior of this PS-PEO block copolymer. Phase diagram adapted with permission from Ref. 45. Copyright 2014 American Chemical Society.

Perhaps surprisingly, the simpler model developed by Wanakule *et al.* appears to do a better job of qualitatively predicted the trend in the phase behavior. In contrast, the model from Teran *et al.* predicts that the asymmetric PS-PEO block polymers should be disordered at all salt loadings. It is surprising that this model, which was rigorously extracted for symmetric diblock copolymers, should so completely fail to predict the phase behavior of sphere-forming block copolymers. This result suggests that a single

χ parameter is likely not sufficient to describe the energetics at all compositions in these salt-doped systems.[146]

Although the model from Wanakule *et al.* does a better job of anticipating the data, it still fails to completely predict all of the observed phase behavior. Comparing the phase behavior of the PS-PEO(11-2) blends with the predicted phase diagram, we see that the data are consistent with the phase diagram for salt loadings up to $r = 0.06$: the sample transitions from a disordered state to one with significant structure (LLP) for $r = 0.02$, then orders to give a BCC structure for $r = 0.04$ and 0.05. At higher segregation strengths, and slightly higher volume fraction of PEO+LiTFSI, a σ phase forms. However, when the salt loading is increased beyond this point, the phase behavior is no longer anticipated by the phase diagram: at $r = 0.07$, BCC reemerges, and at $r = 0.08$, a HEX morphology forms. At this point, a reasonable question might be: are these phases at high salt loading equilibrium morphologies, or are they kinetically trapped, metastable morphologies? As seen in the Results section, the differences in the phase behavior of PS-PEO(8-2) polymers annealed for 36 hours and 7 days demonstrates that annealing time is important in these samples. However, it is experimentally taxing to perform these annealing experiments with the current chemistry, as annealing must always be done at elevated temperature. This difficulty was one of the motivating factors that led us to investigate annealing in salt-doped PEP-PEO block copolymers.

In addition to calculating χN for PS-PEO(11-2), we also considered the behavior of PS-PEO(8-2) diblock copolymers annealed for 7 days. We show χN *vs.* salt loading in Figure 2.24. We have also prepared a phase diagram in Figure 2.25 that compares the behavior of the two PS-PEO block copolymers. Note that, at 150 °C, the Teran model predicts values of χN that are below the limits of the y-axis of Figure 2.25. As was the case for the PS-PEO(11-2) block copolymer, the Wanakule model does a better job of qualitatively predicting the phase behavior, yet the phase behavior of both block polymers is inconsistent with the phase diagram at high salt loading where the morphology may be kinetically trapped.

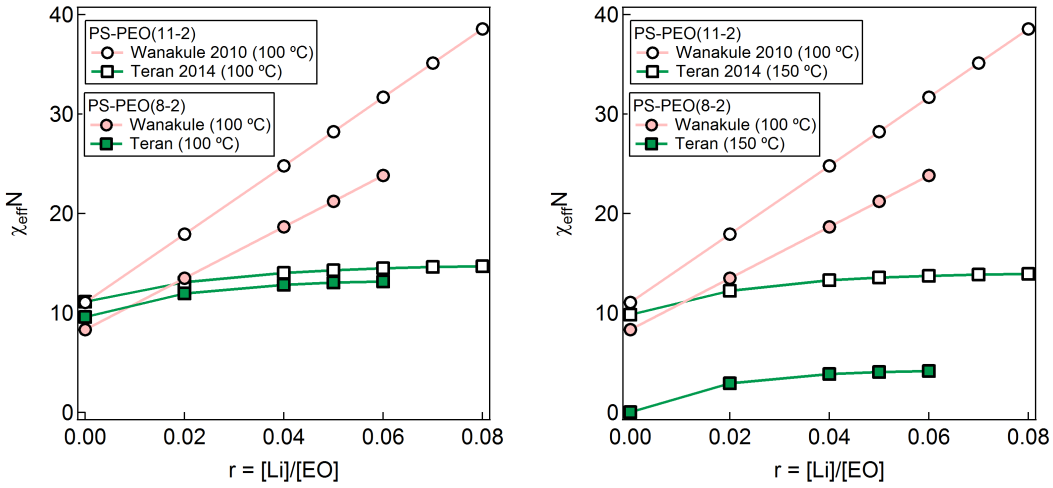

Figure 2.24: $\chi_{\text{eff}}N$ as a function of salt loading for LiTFSI-doped PS-PEO block polymers. The Teran model is calculated at (a) 100 °C and (b) 150 °C.

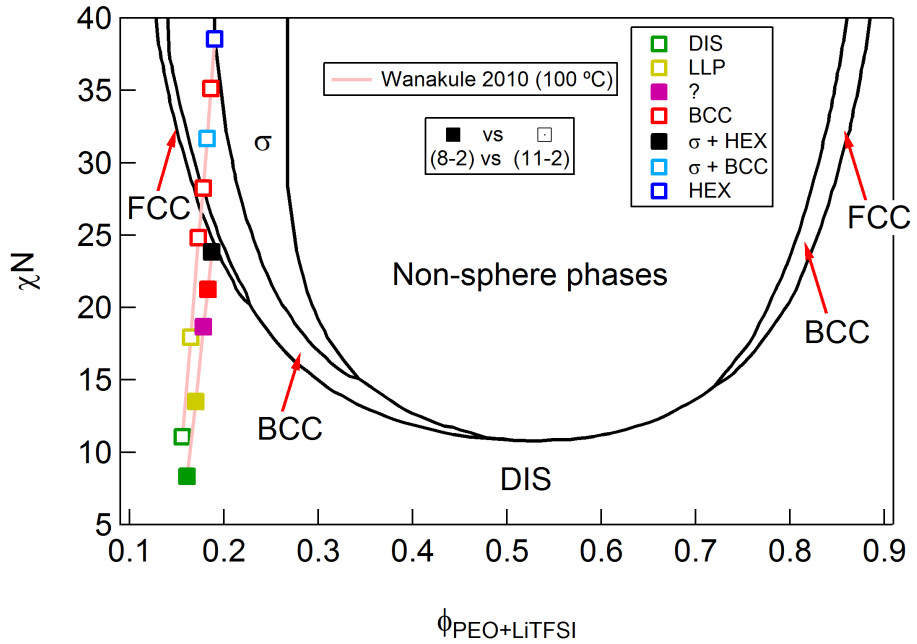

Figure 2.25: Comparison of expected $\chi_{\text{eff}}N$ for LiTFSI-doped PS-PEO block polymers *vs.* the volume fraction of the PEO phase, plotted on top of the phase diagram from Xie *et al.*[45]

Evolution of morphology in salt-doped PS-PEO and PEP-PEO

One common route to mapping this path dependence is through the use of time-temperature-transformation (tTT) diagrams, where the phase behavior is plotted as a function of time at a given temperature. In this work, the primary driving force for ordering was not the temperature, but rather the salt loading. Thus, we can assemble plots that are analogous to tTT plots, wherein we consider the phase behavior of the system at a particular segregation strength as a function of annealing time. We have assembled such a plot for the PS-PEO(8-2) system in Figure 2.26. We note that the effective χN displayed on the y-axis is only accurate for blends at 100 °C, whereas the samples were annealed at 120 °C and 150 °C for the 36 hour and 7 day annealing times, respectively. Regardless, the effect of temperature should not be as dramatic as the effect of salt loading. The results in Figure 2.26 indicate that, with only two annealing times studied, it is challenging to make meaningful conclusions about which morphologies are equilibrium. Regardless, we do find some trends, most notably with the DQC+HEX phase forming a σ+HEX phase at longer anneal times.

Although the PS-PEO system is ill-suited to long-time anneal studies due to the high T_g of the PS corona block, such experiments are relatively easier with the PEP-PEO system. In the PEP-PEO system, T_{ODT} of the blend is a function of salt loading. Therefore, for any annealing experiment, it is possible to quantify the quench depth, $T_{ODT} - T$, at which the annealing occurs. This quench depth can serve as a proxy for the segregation strength of the system, as the exact relationship between salt loading and χ_{eff} for salt-doped PEP-PEO blends is not known. In the quenching experiments, we monitored the phase behavior of the system as a function of time after quenching to room temperature. Taken altogether, we have assembled a plot of the observed morphology as a function of quench depth and annealing time in Figure 2.27 that uses data from the SAXS and DMS experiments. Here, we plot the morphology as a function of the quench depth (*i.e.* $T_{ODT} - T$) and time after quenching to room temperature. Overall, we find that the system appears to be kinetically trapped at high segregation strength, but can transition from an LLP state to an ordered morphology over experimentally accessible lengthscales for modest salt loadings (r = 0.02 and

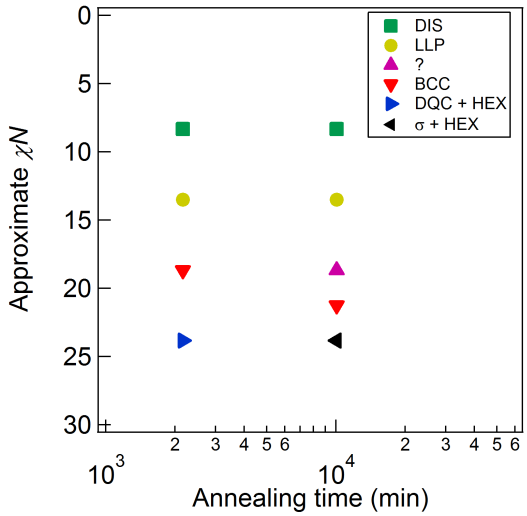

Figure 2.26: Phase map for salt-doped PS-PEO block copolymers that shows the morphology as a function of approximate χN and annealing time. χN was calculated using the Wanakule model (Equation 2.6), which is strictly only accurate at an annealing temperature of 100 °C.

0.04). Whether or not the resulting HCP and FCC morphologies are the equilibrium morphologies is an open question. We have also drawn a rough boundary to denote the transition region between LLP and HCP+FCC. The limited experimental results suggest a "nose" in the diagram, similar to what was described previously by Lee *et al.* and Chanpuriya *et al.*[50,51] Note that the transition from LLP to HCP+FCC is not as immediate or drastic as implied by the figure; in reality, there is likely a large region wherein the LLP slowly transitions into an HCP+FCC structure, as was recently seen for a PI-PLA system by Gillard *et al.*[51]

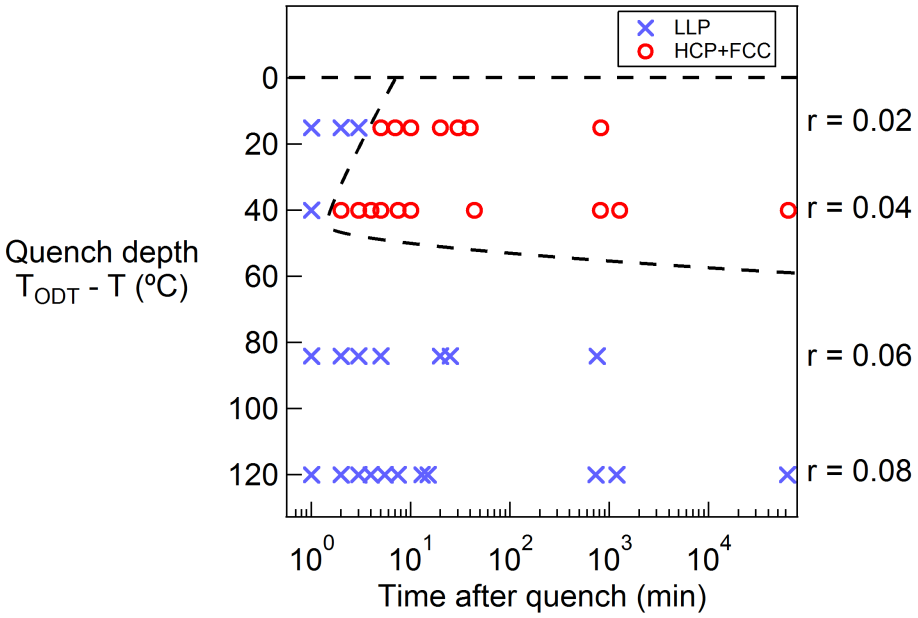

Figure 2.27: Time-temperature-transformation (tTT) diagram for salt-doped PEP-PEO(4-1) that shows the evolution of microstructural morphology as a function of quench depth (*i.e.* distance between T_{ODT} and annealing temperature) and logarithmic time. Despite the long annealing times, it is unlikely that any equilibrium morphology has been achieved. Note that the lines serve more to guide the eye than delineate strict phase boundaries. Based on the scattering, there is likely significant overlap where LLP transitions into the HCP+FCC phase.

2.6 Conclusions

This chapter detailed the phase behavior and equilibration dynamics of a series of asymmetric PS-PEO and PEP-PEO diblock copolymers doped with LiTFSI. The addition of LiTFSI to PS-PEO caused the otherwise disordered block polymer to exhibit a wide variety of microstructured morphologies such as LLP, BCC, DQC, Frank-Kasper σ, and HEX spheres. χN of these systems was calculated using two different models from the literature, one of which qualitatively agreed with an SCFT-predicted phase diagram from Xie *et al*. The appearance of potentially metastable morphologies at high salt loading in the PS-PEO system inspired additional studies on a PEP-PEO block polymer, where the low T_{g} of both blocks allowed for annealing experiments to be

conducted at room temperature. The neat PEP-PEO block polymers disordered near room temperature, but T_{ODT} of the system could be increased substantially through LiTFSI addition, leading to the formation of sphere phases such as LLP, BCC, HCP, and FCC. Annealing studies confirmed that χN, not proximity to T_g, sets the rate at which the microstructure of the blend equilibrates. Ultimately, the work in this chapter details a unique route to probing a wide range of χN in a single chemical system without the need for modulating temperature, opening the door for future studies to further investigate the unique phase behavior of sphere-forming block polymers.

2.7 Acknowledgments

I would like to thank Dr. Tim Gillard, Sid Chanpuriya, Ron Lewis, and Dr. Kyungtae Kim for many helpful discussions and late-night email exchanges about the work described in this chapter. This research was supported by the National Science Foundation under awards DMR-01206459 (TPL) and DMR-1104368 (FSB). Portions of this work were performed at the DuPont-Northwestern-Dow Collaborative Access Team (DND-CAT) located at Sector 5 of the Advanced Photon Source (APS). DND-CAT is supported by Northwestern University, E.I. DuPont de Nemours & Co., and The Dow Chemical Company. This research used resources of the Advanced Photon Source, a U.S. Department of Energy (DOE) Office of Science User Facility operated for the DOE Office of Science by Argonne National Laboratory under Contract No. DE-AC02-06CH11357. X-ray scattering data was collected using an instrument funded by the National Science Foundation under Award Number 0960140.

Chapter 3

Morphology-Conductivity Relationships in Salt-containing Diblock Copolymer/Homopolymer Blends[i] [ii]

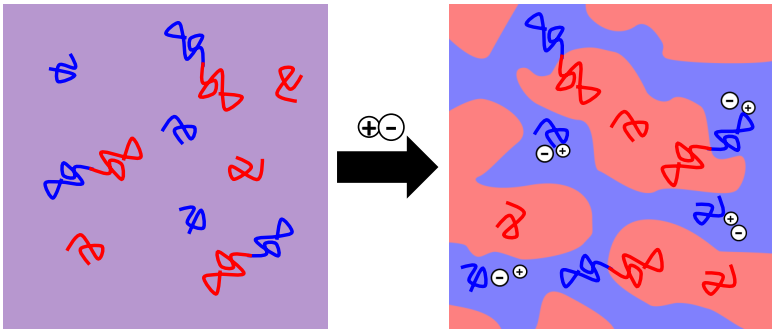

[i] Adapted with permission from Irwin, M. T.; Hickey, R. J.; Xie, S.; Bates, F. S.; Lodge, T. P. Lithium Salt-induced Microstructure and Ordering in Diblock Copolymer/Homopolymer Blends. *Macromolecules* **2016**. Copyright 2016 American Chemical Society.

[ii] This work was done in collaboration with Robert J. Hickey, Shuyi Xie, Soonyong So, and Frank S. Bates.

3.1 Abstract

This chapter details the phase behavior and ionic conductivity of a pseudo-ternary polymer blend system containing poly(ethylene oxide) (PEO) and polystyrene (PS) homopolymers, a PS-PEO block copolymer, and lithium bis(trifluoromethane)sulfonamide (LiTFSI). The phase behavior of the system is described along the volumetrically symmetric isopleth at a fixed LiTFSI concentration relative to the PEO component. The addition of LiTFSI dramatically increases the segregation strength of the blend, causing the otherwise globally disordered blends to exhibit a variety of microstructured morphologies typically found in salt-free ternary polymer blends, such as lamellae, a hexagonal phase, and a bicontinuous microemulsion, all of which have on average, the same number of ethylene oxide, styrene, Li^+, and $TFSI^-$ units.

After the phase behavior of the system is described, this chapter then details a study in which the range of accessible morphologies in this system is utilized to study the relationship between the structure and ionic conductivity. When heated through the order-disorder transition, all blends exhibit an increase in conductivity. Analysis of scattering data indicates significant structure in the disordered state for several blend compositions. By comparing the nature and structure of the disordered states with their corresponding ordered states, we find that this increase in conductivity through the order-disorder transition is most likely due to the elimination of grain boundaries. In either disordered or ordered states, the conductivity decreases as the total amount of homopolymer is increased, an unanticipated observation. This trend with increasing homopolymer loading likely results from an increased density of "dead ends" in the conducting channel, due to poor continuity across grain boundaries in the ordered state and the formation of net concave interfaces in the disordered state. The results demonstrate that disordered, microphase separated morphologies provide better transport properties than compositionally equivalent polycrystalline systems with long-range order, an important criterion when optimizing the design of polymer electrolytes. Further, the breadth of morphologies and segregation strengths that can be accessed

in this system by simply tuning blend composition establishes a new framework for the design of future ternary blend systems and, more broadly, polymeric materials where microstructured, well-segregated domains with tunable ion transport properties are desirable.

3.2 Introduction

Background

Polymeric materials with well-defined microstructures are desirable for a variety of applications, such as filtration,[52,89] bulk heterojunction solar cells,[11,18] and polymer electrolytes.[10,28] One common route to nanostructured materials is through the use of block polymers, which can assemble into a variety of potentially useful morphologies such as hexagonally-packed cylinders (HEX), lamellae (LAM), or a co-continuous gyroid.[23,75,147] Typically, an AB diblock copolymer is designed so that the product of the effective Flory-Huggins interaction parameter between its A and B repeat units, χ_{eff}, and the degree of polymerization of the diblock, N, gives a sufficiently high segregation strength, χN, to achieve microphase separation (*e.g.* $\chi N \geq 10.5$ for a symmetric diblock copolymer within mean-field theory).[33] Because χ_{eff} is a function of T, a frequent route to tuning segregation strength is to simply increase or decrease the temperature. However, the range of segregation strengths that can be probed using temperature modulation alone is limited by degradation at high temperature and either vitrification or crystallization of one or both blocks at low temperature.

An alternate route to tuning the segregation strength of block polymers is through the addition of a selective diluent. One example that has garnered significant interest is polystyrene-*block*-poly(ethylene oxide) (PS-PEO) block polymers doped with lithium salts, which have been proposed for use as polymer electrolytes in rechargeable lithium batteries.[27–29] In such systems, lithium salts have been shown to partition exclusively to the PEO domain.[86,87] Wang and coworkers have suggested that this selective partitioning is primarily due to the large solvation energy gained when the lithium

salts complex and associate with the polar PEO domains, leading to a large increase in the effective segregation strength with lithium salt loading.[84,88] Experimental studies have taken advantage of this intriguing behavior to readily and dramatically tune the segregation strength of PS-PEO block copolymers through the addition of a lithium salt, and these studies have shown a wide range of morphologies can be accessed without the need to modulate temperature.[29,78,82] Theoretical studies have suggested that lithium salts affect the segregation strength of PS/PEO homopolymer blends less strongly than PS-PEO block copolymers, but an experimental study of this proposed distinction has not yet been reported.[81]

One of the largest motivations for the study of lithium-salt doped block copolymers has been their potential use as polymer electrolytes in rechargeable batteries that use a lithium metal anode. Rechargeable batteries incorporating a lithium metal anode are predicted to attain a twenty-fold increase in energy density relative to current lithium-ion batteries.[1] A major challenge in the development of next generation batteries is that, upon cycling, dendrites grow from the lithium metal anode to the cathode and short out the battery, drastically reducing battery lifetimes.[1–3] One method for suppressing dendrite growth is to use a mechanically robust (*i.e.* modulus > 1 GPa) polymer electrolyte, an idea supported by calculations by Monroe and Neumann.[9] This theoretical work has motivated development of a variety of microstructured polymer electrolytes that aim to simultaneously suppress dendrite growth while also providing sufficiently high conductivity for applications. Prominent examples include microstructured block copolymers that combine a mechanically robust domain [*e.g.*, polystyrene,[27–29] poly(styrene-*co*-divinylbenzene),[10,148] or cross-linked polyethylene[149]] with an ion-conducting domain [*e.g.*, poly(ethylene oxide) or poly(oligo(oxyethylene)methacrylate)[87]] that contains a lithium salt [*e.g.*, lithium bis(trifluoromethane)sulfonamide (LITFSI)[28]]. These systems often exhibit either a polycrystalline microstructure with long-range order such as lamellae[28] or hexagonally close-packed (HEX) cylinders,[150] or a globally disordered, but locally correlated, co-continuous microstructure.[10,148] Of these, systems consisting of lamellae-forming polystyrene-*block*-poly(ethylene oxide) (PS-PEO) block copolymers doped with

lithium bis(trifluoromethane)sulfonamide (LiTFSI) have been the most thoroughly studied,[27,28,70] in part due to the anticipated connectivity of salt-doped, ionically-conductive PEO lamellae and the relative ease of their preparation, in addition to the known interactions among PS, PEO, and LiTFSI.[80,82,84,85]

Despite extensive work, there is still an evolving understanding of which morphology and polymer should be chosen to optimize ionic conductivity. In an ideal microstructured electrolyte, one domain provides high ionic conductivity, while the other provides the mechanical robustness necessary for dendrite suppression. In such a case, the measured conductivity, $\sigma(T)$, would be related to the conductivity of the pure conducting phase, $\sigma_{\text{cond}}(T)$, by

$$\sigma(T) = \frac{\phi_{\text{cond}}\sigma_{\text{cond}}(T)}{\tau} \tag{3.1}$$

where ϕ_{cond} and τ are the volume fraction and tortuosity of the conducting phase, respectively. The tortuosity describes the increased average path length an ion must travel relative to a straight path.[74] For randomly oriented lamellae and HEX cylinders, τ has been calculated to be 1.5 and 3, respectively.[72] Ironically, for bicontinuous cubic structures such as the double gyroid, τ is also estimated to be between 1.5 and 3.[20]

Unfortunately, the conductivity of polymer electrolytes consistently falls short of this prediction. These deviations have been attributed to a variety of factors beyond that considered in Equation 1, such as grain boundaries in ordered phases that lead to "'dead ends" in the conducting channels,[54,73,150] the restriction of conducting block segmental mobility due to being tethered to an immobile insulating block,[71] and mixing of the conducting and insulating blocks at the interface, resulting in a region of slower ion diffusion.[151] These factors are depicted visually in Figure 3.1.

To explore these effects, several groups have analyzed how the conductivity of a polymer electrolyte changes as it is heated through an order-disorder transition temperature (T_{ODT}) or an order-order transition temperature (T_{OOT}). Because both the ordered and disordered states have generally well-established morphological properties, any differences in the conductivity through T_{ODT} should be due to a change in one or more of the four factors shown in Figure 3.1. In one example, Cho *et al.* prepared

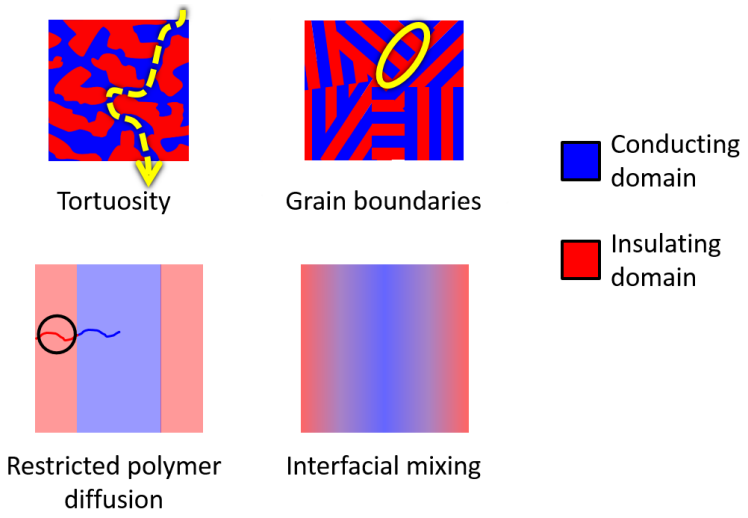

Figure 3.1: Examples of factors that may reduce the conductivity of microstructured polymers.

amphiphilic dendrons containing linear poly(ethylene oxide) (PEO) doped with lithium triflate salt, and they found an order-of-magnitude increase in conductivity through a transition from HEX cylinders to Ia3d gyroid, which they attributed to better continuity of the conducting phase across grain boundaries, due in part to an increase in the dimensionality of the conducting phase from 1- to 3-dimensional.[152] Similarly, Teran *et al.* found that the conductivity of a PS-PEO diblock copolymer (M_n = 3 kg/mol) doped with LiTFSI exhibited a nearly two-fold increase in the conductivity as it was heated through a lamellar-to-disorder (LAM-to-DIS) transition, which they suggested was due to a reduction in tortuosity and an increase in chain mobility in the disordered state.[74] However, Wanakule *et al.* had previously not seen a similar jump in a LiTFSI-doped PS-PEO diblock copolymer of slightly larger molecular weight (M_n = 7 kg/mol) when heated through a LAM-to-DIS, hexagonally close packed cylinders-to-disorder (HCP-to-DIS), or lamellar-to-gyroid (LAM-to-GYR) transition.[80]

Despite the work done to date, definitively understanding the relationship between microstructure and conductivity has been hindered by experimental complications. Many properties vary across studies that may subtly affect the measured conductivity of the microstructured systems, including salt loading, salt identity, volume fraction of

each block, and polymer molecular weight.[54,70,78,81] Furthermore, even comparing the conductivity of the disordered and ordered states is not necessarily straightforward, as there are significant composition fluctuations in the disordered state for low molecular weight block polymers.[47,153,154] In contrast, some experimental studies of polymer electrolytes make a simplifying assumption that the disordered state is homogeneous and, thus, has a tortuosity of 1.[82]

This work: salt-containing ternary polymer blends

In this work, we extend the work on lithium salt-doped PS-PEO block copolymers and PS/PEO homopolymer blends to ternary polymer blends consisting of PS and PEO homopolymers, a PS-PEO block copolymer, and LiTFSI. In contrast to neat block copolymers, the current system allows for morphology to be tuned by modulating the relative fraction of the two homopolymers and the salt concentration independently, thereby accessing a large number of morphologies with a single set of polymers. One key advantage of this system is that every blend contains the same number of ethylene oxide, styrene, Li^+ and $TFSI^-$ units per unit volume. The framework for this study rests on extensive studies of ternary polymer blend systems consisting of a volumetrically symmetric AB diblock copolymer and corresponding immiscible A and B homopolymers.[94] Typically, the A and B homopolymers in such systems are roughly 1/5 the molecular weight of the diblock and are added to the blend such that $\phi_A = \phi_B = \phi_H/2$. In such blends, the domains of the lamellae-forming diblock swell with the addition of the homopolymers, increasing the characteristic length scale.[101] At a homopolymer loading near that of the predicted Lifshitz composition, it is hypothesized that the bending energy of the interface becomes comparable to the energy of thermal fluctuations in the system, and the lamellae give way to a bicontinuous microemulsion (BμE) morphology, which consists of co-continuous domains that are locally correlated, but globally disordered.[94] This phase behavior appears to be universal, and has been seen a large number of polymer blends.[18,39,94,102,111,112,114,121]

By incorporating the ability to isothermally tune segregation strength *via* lithium

salt addition into the framework of ternary polymer blends, we have developed a new family of polymer blends that mirrors what has been studied in oil/water/surfactant systems,[155] which we term pseudo-ternary polymer blends. Despite the complexity of the system, its behavior largely mirrors what has been seen in traditional ternary polymer blends, with the formation of a bicontinuous microemulsion morphology at compositions between a region of ordered morphologies at low homopolymer loading and a multiphase region at high homopolymer loading. However, despite the superficial similarity of this phase behavior, we find that there is a large increase in the T_{ODT} of the ternary blends with increasing homopolymer content, even though the average molecular weight of the polymers is decreasing significantly. This surprising result appears to be due to a χ_{eff} for the PS/PEO blends that is five times larger than for a PS-PEO diblock copolymer.

Significant work in the polymer electrolyte community has indicated that control over material structure and ionic domain connectivity is critical for obtaining the high ionic conductivity necessary for good performance in battery applications.[10,54,156] Ultimately, this work establishes a route to polymer electrolytes wherein multiple morphologies can be accessed with nominally the same chemistry by simply tuning the homopolymer and salt loading.

After mapping out the phase behavior of these pseudo-ternary polymer blends, experiments were carried out to determine the relationship between microstructure and conductivity in polymer electrolytes. To this end, we present a quantitative analysis and comparison of the ionic conductivity of these pseudo-ternary polymer blends wherein the molecular composition for each blend is nominally the same at the repeat unit level, yet the microstructure and morphology can be readily tuned by modulating the ratio of the blend components. By tuning the blend composition and monitoring the conductivity as a function of temperature, it is possible to access multiple morphologies and order-disorder transitions with nominally the same molecular architecture.[86,87] In this work, we use this framework to compare the structure and ionic conductivity of ordered and disordered morphologies. We find that the conductivity of ordered (2-dimensional) LAM morphologies exceeds that of a (1-dimensional) HEX morphology,

despite having nominally the same molecular composition. Further, we find that disordered blends are highly structured even at temperatures well above T_{ODT}, yet their conductivity decreases as the relative loading of low molecular weight homopolymer increases, likely due to a simultaneous increase in the density of net concave interfaces that lead to "dead ends" in the fluctuating disordered state. Finally, through a systematic analysis of the ionic conductivity as a function of blend composition and temperature, we demonstrate that globally disordered, locally correlated, fluctuating morphologies are able to provide significantly better transport properties than ordered, polycrystalline systems like LAM or HEX.

3.3 Experimental Section

Materials

Hydroxyl-terminated poly(ethylene oxide) (PEO) homopolymer ($M_n \approx 400$ g/mol) was purchased from Fischer Scientific (Catalog #AC192230010). The polymer was dried under dynamic vacuum for 24 hours, then stored under static vacuum. Polystyrene (PS) homopolymer ($M_n \approx 600$ g/mol) was purchased from Scientific Polymer Products and was used as received (Catalog #541). Lithium bis(trifluoromethane)sulfonamide (LiTFSI) was purchased from 3M and dried under dynamic vacuum for 24 hours, then stored under static vacuum. The polystyrene-*block*-poly(ethylene oxide) (PS-PEO) diblock copolymer was synthesized via sequential anionic polymerization, as described previously.[139] Briefly, PS-OH was synthesized from a *sec*-butyllithium initiator in cyclohexane at 40 °C for 4 hours, end-functionalized with purified ethylene oxide, and terminated with purified methanol. The PS-PEO diblock copolymer was synthesized by reinitiating the PS-OH macroinitiator by reacting the polymer with a potassium naphthalenide solution to create the PS-O^- anion, and the poly(ethylene oxide) block was subsequently grown at 45 °C in tetrahydrofuran (THF) for 24 hours, after which the reaction was terminated with purified methanol. The resulting polymer was purified by precipitating in cold methanol three times and drying under dynamic vacuum for 24

hours. A summary of the polymer properties is shown in Table 3.1. Note that the repeat unit is defined as a volumetric degree of polymerization, N, based on a volume of 0.1 nm^3.

Table 3.1: Characterization and properties of salt, homopolymers, and diblock copolymer.

Component	M_n (g/mol)	N^c	f_{PEO}	$Đ = M_w/M_n^d$	ρ (g/mL)
PEO	400[a]	5	–	1.13	1.037[e]
PS	600[d]	9	–	1.24	1.002[e]
PS-PEO	4700[b]	67	0.40[b]	1.05	1.016[f]
LiTFSI	287	–	–	–	2.023[g]

a) From supplier. b) Via ^{1}H NMR. c) Calculated using a reference volume of 0.1 nm^3. d) Via SEC. e) Calculated at 140 °C from Ref. 157. f) Volume-weighted density of each component. g) From Ref. 82.

Sample preparation

Blends were prepared by dissolving the desired amounts of polymer with or without LiTFSI in a small volume of THF and stirring until homogeneous. Blends were then dried under dynamic vacuum overnight. Due to the hygroscopic nature of LiTFSI, salt-containing blends were either transferred to and stored in an argon-filled glovebox or stored under static vacuum after drying. For all blends containing PS and PEO homopolymers and the PS-PEO diblock copolymer, the molar ratio of lithium ions to ethylene oxide repeat units, r, was maintained at 0.06 (*i.e.* $r = [Li^+]/[EO] = 0.06$). PS and PEO homopolymer blends were prepared by dissolving all components in THF, drying under air flow for one day, then further drying under dynamic vacuum overnight. The salt concentration in the homopolymer blends was varied between $r = 0$ to 0.10 to assess the effect of salt concentration on phase behavior and conductivity. Note that the blends were prepared by approximating the mixing of LiTFSI and PEO as ideal, *i.e.* $\rho_{PEO+LiTFSI} = \phi_{PEO}\rho_{PEO} + \phi_{LiTFSI}\rho_{LiTFSI}$, where ϕ is the relative volume fraction of each component in the mixed phase. Although the mixing of LiTFSI and PEO is known to be non-ideal, previous work has shown that an ideal mixing approximation is

accurate to within 5%.[82]

Thermal gravimetric analysis (TGA)

TGA was performed on neat, salt-free polymers to determine the upper working temperature limit for further analysis. Approximately 2 mg of polymer was loaded into a platinum pan and placed in a TA Instruments Discovery TGA, and the sample was heated at a rate of 10 °C/min to 400 °C under a nitrogen environment. The weight loss was recorded as a function of temperature.

Differential scanning calorimetry (DSC)

DSC was performed using a TA Instruments Discovery differential scanning calorimeter. Samples were loaded into T-zero pans, then hermetically sealed. Samples were then heated to high temperature to erase thermal history, cooled to below room temperature, then heated again. Data presented are from the second heating. All experiments were conducted at a temperature ramp rate of 10 °C/min.

Dynamic mechanical spectroscopy (DMS)

The linear-viscoelastic response of polymer blends was determined using a Rheometrics Scientific ARES strain-controlled rheometer. Blends were loaded onto a 25 mm diameter parallel plate geometry at room temperature, then brought to elevated temperature to allow the sample to flow and evenly fill the gap. Strain sweeps were first performed both above and below T_{ODT} to determine the linear viscoelastic regime. Samples were then brought above the anticipated order-disorder transition temperature (T_{ODT}), and the storage (G') and loss (G'') moduli were measured as the sample as cooled and heated through the T_{ODT} at a rate of 1 °C/min and a frequency of 1 rad/s. Upon heating, a sudden drop in storage modulus was measured, and the T_{ODT} was taken to be the temperature at which the magnitude of G' fell to 10% of its plateau value.

Small-angle X-ray scattering (SAXS)

SAXS experiments were conducted at DND-CAT sector 5-ID-D of the Advanced Photon Source at Argonne National Labs. Samples were loaded into nominally 1 mm diameter boron-rich capillaries (Charles Supper Company, Natick, MA) and annealed at 120 °C for 3 days prior to the start of the experiment. 2D scattering patterns were collected on a Rayonix CCD area detector. The resulting isotropic scattering patterns were azimuthally integrated to give the scattered intensity as a function of the magnitude of the wavevector $|\boldsymbol{q}| = q = 4\pi\sin(\theta/2)/\lambda$, where θ is the scattering angle and λ is the wavelength.

Cloud point measurements

The cloud point of binary PS/PEO homopolymer blends was determined using optical transmission measurements. The apparatus consisted of a 10 mW helium-neon laser (λ = 633 nm) that was directed through a neutral density filter, followed by a cylindrical glass ampule heating stage which held the sample under dynamic vacuum at a controlled temperature (± 1 °C). The laser light transmitted through the sample then passed through a lens that focused the beam onto a photodiode detector.

A typical experiment involved heating the sample above the anticipated cloud point temperature (T_{cloud}) until a homogeneous solution was obtained. The sample was subsequently cooled at a rate of 1 °C/min until a sudden drop in the transmitted intensity was recorded. The temperature at which the transmitted intensity dropped to 10% of its plateau value was taken to be T_{cloud}. To assess the effects of hysteresis, the sample was then heated back through the T_{cloud} until a homogeneous solution was recovered. Throughout the entire measurement, the sample was stirred to maintain good mixing within the sample-containing cylindrical ampule.

Electrochemical impedance spectroscopy (EIS)

Impedance spectroscopy was performed using a Solartron 1255B frequency response analyzer connected to a Solartron SI 1287 electrochemical interface. All samples were prepared in a glovebox. Polymer blends were loaded into a standard 2032 coin cell geometry (MTI Corporation, Richmond, CA), where the blends were placed in the center of a PTFE washer and sandwiched between stainless steel electrodes, then crimped. This fabrication method was necessary to maintain an inert sample environment and prevent the uptake of water by the sample. The fabricated coin cells were then placed in a custom-built heating block and brought to $T > T_{\mathrm{ODT}}$ to erase thermal history, then slowly cooled to room temperature. The sample was then heated in steps of either 10 or 20 °C and annealed at each temperature for 1 hour prior to the measurement. The impedance (Z' and Z'') was measured as an oscillatory voltage with an amplitude of 100 mV was applied at frequencies from 1 Hz to 1 MHz. The bulk resistance, R, was measured by extracting the high-frequency plateau value of the in-phase component of the impedance, Z'. The conductivity was then calculated as $\sigma(T) = l/[R(T) \times a]$, where the electrolyte superficial area, a, and thickness, l, were determined by opening the coin cells after completion of the experiment. Calculations (see Results section) suggest that the length scales of ion motion probed by these experiments were approximately an order of magnitude greater than the domain spacing (Figure 3.17b). Thus, the impedance used to calculate the bulk resistance of the blends represents the resistance across multiple domains and grain boundaries.

Pulsed-field gradient nuclear magnetic resonance (PFG-NMR)

PFG-NMR experiments were performed using a Bruker Advance III 500 MHz NMR spectrometer. Samples were prepared using a double-capillary geometry in which the bulk sample was placed in the outer capillary, and DMSO-d_6 was placed in the inner capillary. This geometry was necessary for locking and shimming, as the bulk samples did not contain any solvent. All experiments were carried out at 75 °C by Soonyong So.

3.4 Results

Characterization of polymers and blends

To determine the thermal properties of the polymers, TGA and DSC analysis was conducted. The polymers used in this study are of low molecular weight, which resulted in a depression in T_g and T_m that was evident even when handling the samples at room temperature. To determine the upper working temperature of our system, we performed TGA on the PS-PEO block copolymer. The heating trace is shown in Figure 3.2. There is slight weight loss from 200 °C to 300 °C, followed by pyrolysis at temperatures exceeding 300 °C. The slight weight loss from 200 °C to 300 °C was anticipated to be largely from residual solvent evaporation; TGA analysis of a PS-PEO block copolymer of slightly larger molecular weight also prepared by us *via* anionic polymerization indicated less than 0.5 wt% loss at 300 °C. Based on these analyses, all subsequent experiments were carried out at temperatures of 250 °C or below.

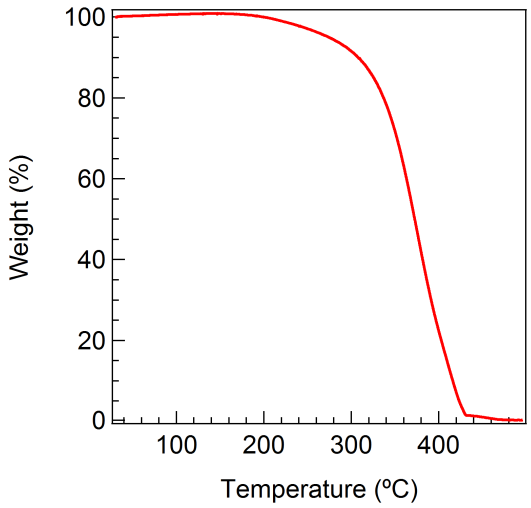

Figure 3.2: TGA of the PS-PEO diblock copolymer used in this study.

DSC analysis was performed on the PS, PEO, and PS-PEO, all without salt, in addition to blends with various volume fractions of homopolymer, ϕ_H, relative to the block copolymer. These results are shown in Figure 3.3. The data indicate that the glass

transition temperature of the PS domain was depressed with increasing homopolymer loading, concurrent with a decrease in the average molecular weight in the PS domain. There is also significant fluctuation in the data from the PS homopolymer, which is likely from residual solvent left by the supplier. When the PS homopolymer is used in blends, this residual solvent is removed through the standard sample preparation steps detailed in the Experimental section. The neat PEO and PS-PEO indicated some crystallinity in the PEO domain, whereas there was no observable crystallinity in the blends at room temperature. The crystalline fraction of the neat polymers can be calculated using

$$X_{\mathrm{c,PEO}} = \frac{\Delta H_{\mathrm{m,PEO}}}{w_{\mathrm{PEO}} \Delta H^{0}_{\mathrm{m,PEO}}} \tag{3.2}$$

where $\Delta H_{\mathrm{m,PEO}}$ is the integrated area under the peaks centered at 5 °C and 27 °C in the PEO and PS-PEO, respectively. $\Delta H^{0}_{\mathrm{m,PEO}}$ is the enthalpy of melting of pure PEO, which is approximately 186 J/g.[76] Table 3.1 indicates that the PS-PEO diblock is 40 vol% PEO, which corresponds to 41 wt%. Integration of the peaks in Figure 3.3 gives $\Delta H_{\mathrm{m,PEO}}$ of 99 and 4.7 J/g for the PEO and PS-PEO, respectively, which, *via* Equation 3.2, indicates that $X_{\mathrm{c,PEO}}$ in the PEO homopolymer and the PEO block of the PS-PEO block copolymer is 0.53 and 0.06, respectively.

Phase behavior

Previous work on systems containing PS and PEO have shown that the LiTFSI is solubilized by the PEO phase.[86–88] This selective association is hypothesized to be a result of a large solvation energy gain that occurs when the PEO phase dissolves the lithium anion, resulting in a significant increase in the effective segregation strength, $(\chi N)_{\mathrm{eff}}$, of the system.[74,80–82] Thus, through the addition of LiTFSI, it is possible to induce microstructural ordering isothermally in a system that would otherwise be disordered.

All blends containing both the PS and PEO homopolymers and the PS-PEO diblock copolymer were prepared with a fixed concentration of LiTFSI relative to the PEO

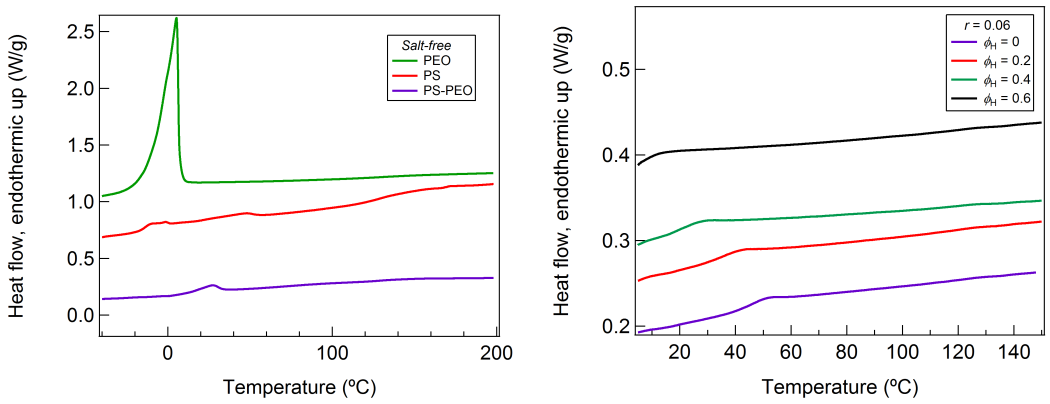

Figure 3.3: DSC thermograms for (a) the three polymers used in this study and (b) four salt-containing blends. Traces have been offset vertically for visual clarity by multiples of (a) 0.4 W/g and (b) 0.05 W/g. Data shown are from a second heating at 10 °C/min.

component. This concentration was defined as the ratio of the moles of lithium ions to the moles of ethylene oxide units, r = [Li^+]/[EO] = 0.06. By fixing the salt concentration, the number of effective components in the system was reduced from four to three, and thus the blends can be described by three volume fractions: PS homopolymer, ϕ_{PS}, LiTFSI-doped PEO homopolymer, $\phi_{PEO+LiTFSI}$, and the LiTFSI-doped block polymer, $\phi_{PS-PEO+LiTFSI}$. Due to the number of effective components in this system, we refer to these systems as pseudo-ternary polymer blends, following the naming convention of previous work on pseudo-ternary blends of salt-doped oil/water/surfactant systems.[158–160]

The fact that there are three effective components allows the phase behavior of the system to be compared directly to previous studies on salt-free ternary polymer blends. Most commonly, these studies investigated the phase behavior of ternary polymer blends consisting of homopolymers A and B and a volumetrically symmetric AB diblock copolymer. Of most interest in these studies was the phase behavior of the blends along the volumetrically symmetric isopleth, defined by setting the homopolymer volume fractions equal to each other, *i.e.* $\phi_A = \phi_B = \phi_H/2$ and $\phi_A + \phi_B = \phi_H$.[94,104] Thus, the phase behavior along the volumetrically symmetric isopleth was mapped out as a function of temperature, T, and homopolymer volume fraction, ϕ_H. In

this study on pseudo-ternary polymer blends, we employ a similar strategy, where A is PS and B is LiTFSI-doped PEO (PEO+LiTFSI). Here, the "homopolymer" loading is held at $\phi_{PS} = \phi_{PEO+LiTFSI} = \phi_H/2$. This is depicted in the ternary phase prism of Figure 3.4, where possible morphologies such as lamellar (LAM), hexagonally packed cylinders (HEX), and a BμE are shown as a function of the overall homopolymer volume fraction, $\phi_H = \phi_{PS} + \phi_{PEO+LiTFSI}$.

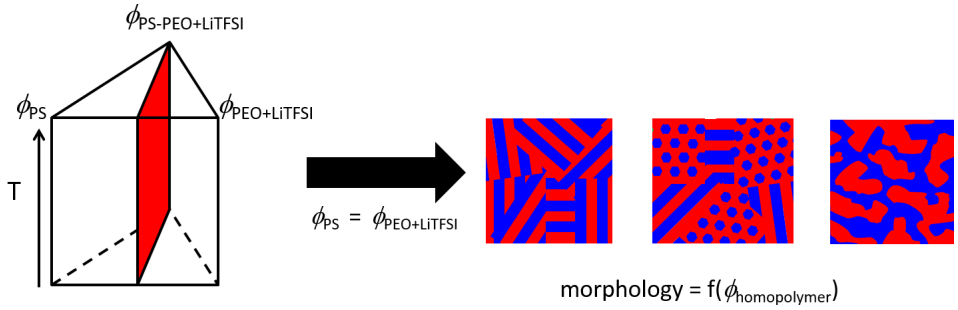

Figure 3.4: Depiction of the volumetrically symmetric isopleth of a pseudo-ternary polymer blend prism.

Prior to other experiments, T_{ODT}s were determined *via* DMS temperature sweeps, where G' and G'' were measured at a frequency of 1 rad/s as the sample was heated at 1 °C/min. The results of this study are shown shown in Figure 3.5. The ordered-state plateau value of G' generally decreases with increasing ϕ_H, but increases for blends with $\phi_H = 0.65$ and 0.7, which, as will be shown shortly, have a significant fraction of HEX (Figure 3.10). Frequency sweeps were performed above the measured T_{ODT} for several blends, and the results of these experiments are shown in Figure 3.6. For a fully disordered blend, the expected terminal scaling of G' and G'' with frequency is 2 and 1, respectively.[26] Although G'' nearly scales as 1 for most blends, G' never scales at a value of close to 2 for any blend. It is unclear if this is the result of poor signal-to-noise due to the low measured torque of these blends, or if it is caused by "excess" linear viscoelasticity[114,115] that may result from ion-induced cross-linking of the PEO phase.[84] Regardless of the nature of the scaling of G', the relatively better signal for G'' allows for the zero-shear viscosity, η_0, of the blends to be determined *via*

$$\eta_0 = \lim_{\omega \to 0} \eta' = \lim_{\omega \to 0} \left(\frac{G''}{\omega} \right) \tag{3.3}$$

Applying this equation to the data in Figure 3.6 yields the values for η' and η_0 shown in Figure 3.7. We note that the data shown were collected at different temperatures; this makes quantitatively comparing the data challenging, as η is a function of temperature. Despite this, there still appears to be a decrease in η_0 as homopolymer is added, as would be expected based on the low molecular weight of the homopolymers.

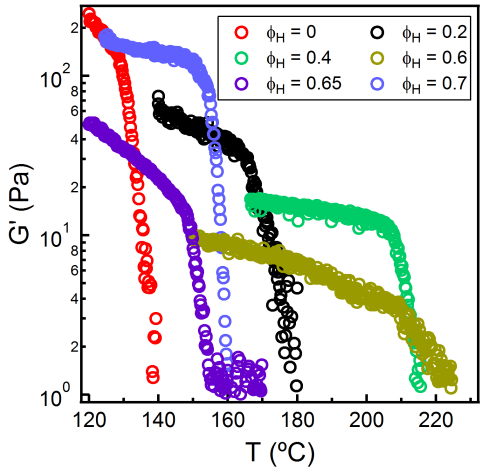

Figure 3.5: Elastic modulus for various blend compositions at a frequency of 1 rad/s upon heating at 1 °C/min. The sudden drop in the elastic modulus at a particular temperature is a signature of the order-disorder transition.

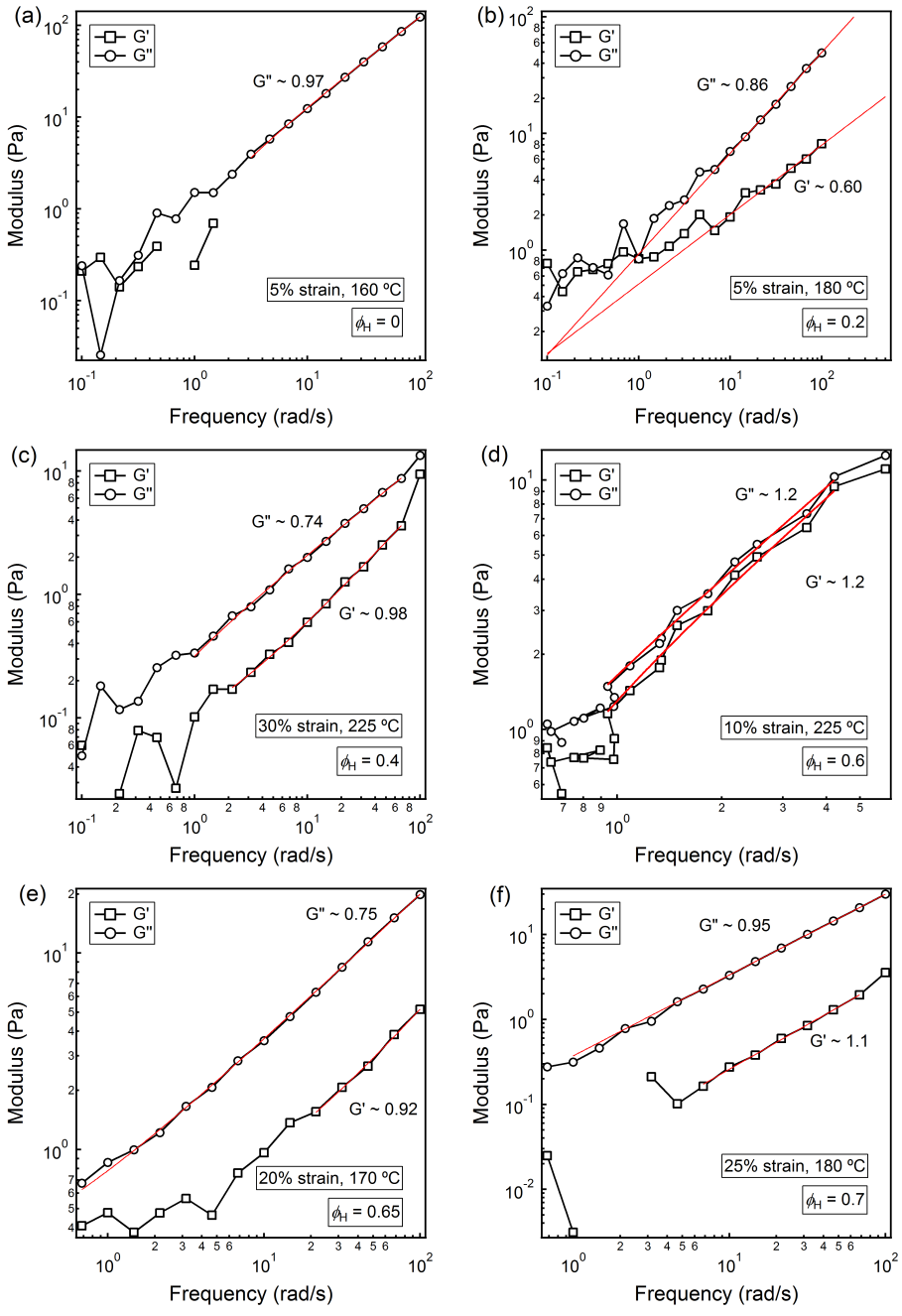

Figure 3.6: G' and G'' for disordered blends as a function of frequency.

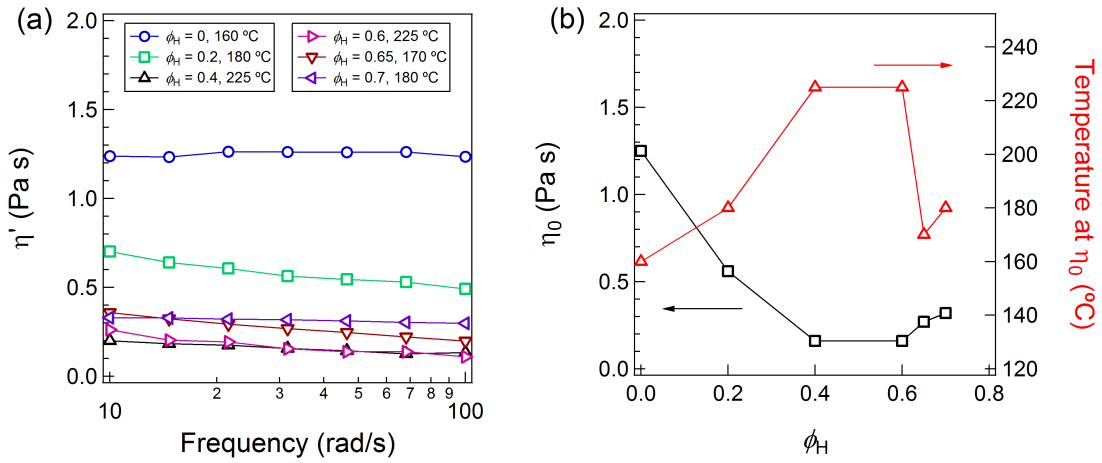

Figure 3.7: η' and η_0 for disordered blends.

The experimental phase diagram along the volumetrically symmetric isopleth for these pseudo-ternary blends with $r = 0.06$ is shown in Figure 3.8. Note that, without the addition of LiTFSI, all blends examined were either disordered (copolymer-rich) or macrophase-separated (homopolymer-rich) at all accessible temperatures. Thus, the addition of salt appears to be responsible for the onset of microstructural ordering. T_{ODT}s were determined *via* DMS, shown in Figure 3.5 and the morphologies were assigned based on SAXS analyses. One striking result is that the phase diagram presented in Figure 3.8 is superficially similar to that seen in previous reports on AB/A/B ternary polymer blends. There is a region of phase space in which the polymeric bicontinuous microemulsion (BμE) channel splits the isopleth into two separate categories: a diblock-rich region consisting of ordered, microphase-separated morphologies, and a homopolymer-rich region of macroscopic phase-separation.[94] At low to moderate homopolymer loading ($\phi_H < 0.4$) and moderate temperatures, the blends exhibit exclusively a LAM morphology, as assessed by SAXS. At intermediate homopolymer loading ($0.4 \leq \phi_H \leq 0.7$), there is a region where LAM and HEX morphologies coexist. A BμE morphology was found for samples with $\phi_H = 0.65$ and 0.7 when $T > 160$ °C. For $\phi_H = 0.65$ blends, there is a temperature window (~ 40 °C) over which LAM and BμE coexist. At increased homopolymer loadings ($\phi_H > 0.7$), there is a multiphase region that lacks well-defined structure, as determined visually by the onset of macrophase separation in samples containing as little as $\phi_H = 0.73$.

It is not at all obvious that the addition of a lithium salt to a ternary polymer blend should largely recover the phase behavior of a traditional ternary polymer blend system. This result implies that, to a first approximation, the lithium salt simply drives up the segregation between the PEO and PS domains without fundamentally changing the nature of the interactions. This observation suggests that a strategy to tune a system *via* relative homopolymer loading, then "dial-in" a desirable morphology through adding a prescribed concentration of lithium salt. This generally differs from block copolymers, where tuning the segregation strength of the system inevitably leads to order-order transitions.[41,82,161]

Nevertheless, despite the similarities of the phase diagram in Figure 3.8 with

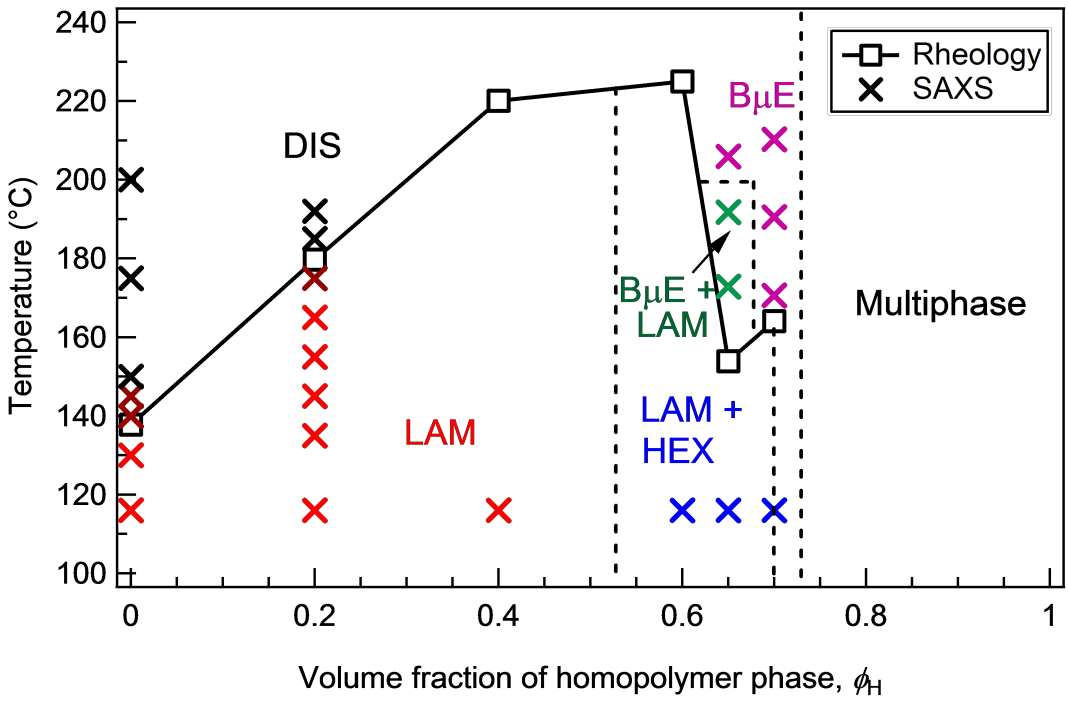

Figure 3.8: Experimentally determined phase diagram for blends with $[Li^+]/[EO] = r = 0.06$ and $\phi_{PS} = \phi_{PEO+LiTFSI} = \phi_H/2$. Open squares represent order-disorder transition temperatures as assessed via DMS. The crosses represent temperatures and compositions at which SAXS data were used to assign morphologies. All lines are connecting data points to guide the eye.

previous diagrams of ternary polymer blend systems, one marked difference is the increase along the line of T_{ODT}s with increasing homopolymer loading, even though the average molecular weight of the polymer components decreases by about an order of magnitude between $\phi_H = 0$ and 1. Note that in all AB/A/B ternary systems reported, when the ratio of copolymer and homopolymer degrees of polymerization is comparable to that used here, the addition of equal amounts of A and B homopolymer to the diblock always reduces T_{ODT}. This increase in the case of $r = 0.06$ is so dramatic that at high homopolymer loading ($\phi_H > 0.7$), blends were macrophase separated at all accessible temperatures. The implications of this behavior will be further explored in the Discussion section.

SAXS traces obtained at 120 °C for ordered phase compositions are shown in Figure 3.9a. The primary peak positions for each ordered phase (q^*_{lam} and q^*_{hex}) were used to calculate their respective domain spacings ($d = 2\pi/q^*$), which have been plotted as a function of homopolymer loading in Figure 3.9b. This trend in domain spacing as a function of composition is also observed in traditional ternary polymer blends,[39,94,104] indicating a diverging length scale as the BμE channel of the phase diagram is approached.[105] Additionally, comparing $I(q^*_{\text{lam}})$ and $I(q^*_{\text{hex}})$ at 120 °C suggests that blends that contain coexisting LAM + HEX phases become more HEX rich as ϕ_{H} increases from 0.6 to 0.7 (Figure 3.10). It should be noted that a definitive assignment of a cylindrical phase, as opposed to related packings such as hexagonally-perforated layers, cannot be made without microscopy, but the low molecular weights in this system preclude direct imaging by transmission electron microscopy (TEM).

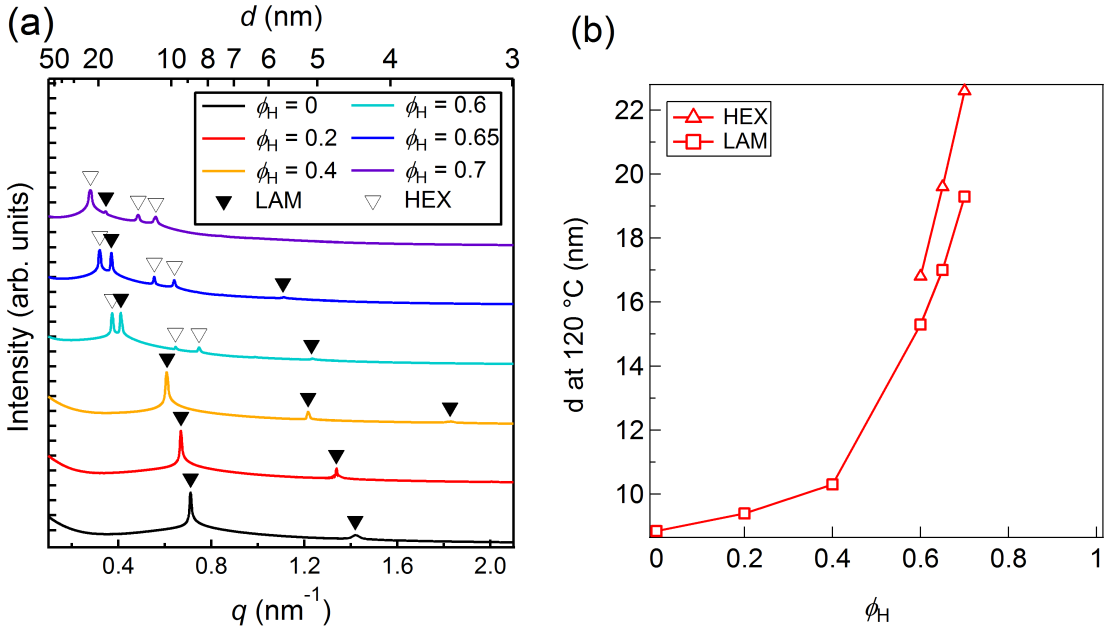

Figure 3.9: (a) Small angle X-ray scattering traces for various blends at 120 °C. Markers for LAM indicate q/q^* multiples of 1, 2, and 3, where q^* is the primary peak position, while markers for HEX indicate q/q^* multiples of 1, $3^{1/2}$, and $4^{1/2}$. (b) Domain spacing for ordered morphologies at 120 °C as determined from q^*.

SAXS traces were also collected upon heating for several blend compositions. In

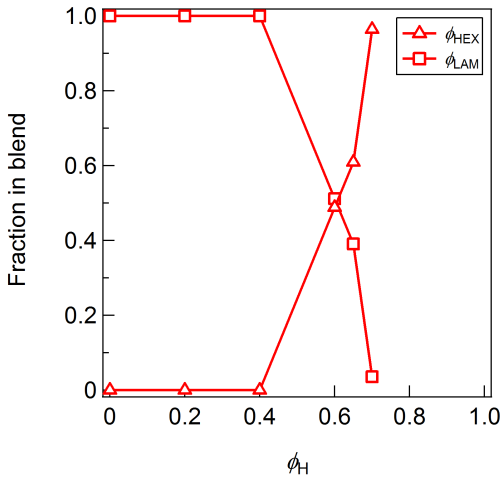

Figure 3.10: Comparison of the relative fraction of LAM and HEX of blends at 120 °C as a function of ϕ_H. The relatively fraction of each ordered phase was estimated by comparing the relative intensities of the primary scattering peaks for the LAM and HEX morphologies as assessed from SAXS experiments. The lines are drawn to guide the eye.

Figure 3.11a, a $\phi_H = 0.2$ blend appears to undergo an order-disorder transition over an approximately 10 °C temperature window around 175 °C, in contrast to salt-free block copolymers where the ODT is typically much sharper. Evidence of this coexistence can be seen more clearly in Figure 3.11d. This region of coexistence is consistent with the predictions of Nakamura *et al.* and was experimentally reported by Thelen *et al.* for a LiTFSI-doped PS-PEO block copolymer.[66,162] Similarly, the diblock copolymer plus salt also appears to go through a window in which LAM + DIS phases coexist (Figure 3.11c). Conversely, in Figure 3.11b, $\phi_H = 0.65$ blends undergo a much subtler ODT. Up to 145 °C, there is coexistence between LAM and HEX, and the expected peak for the LAM phase at $2q^*$ is extinguished, likely due to approximate volume symmetry of the lamellar domains that leads to structure factor extinction.[163] At approximately 150 °C, peaks corresponding to the HEX phase disappear and give rise to a single broad peak, while the scattered intensity from the LAM phase remains largely unchanged up to 190 °C. Finally, from 190 °C to 205 °C, the intensity of the q^* peak for the LAM phase begins to dissipate until a scattering pattern consistent with a pure BμE morphology

is obtained at 205 °C. Conversely, ϕ_H = 0.7 blends appear to transition directly from coexisting LAM+HEX phases to a pure BμE morphology through an approximately 10 °C window, without first transitioning through a LAM + BμE region (Figure 3.12).

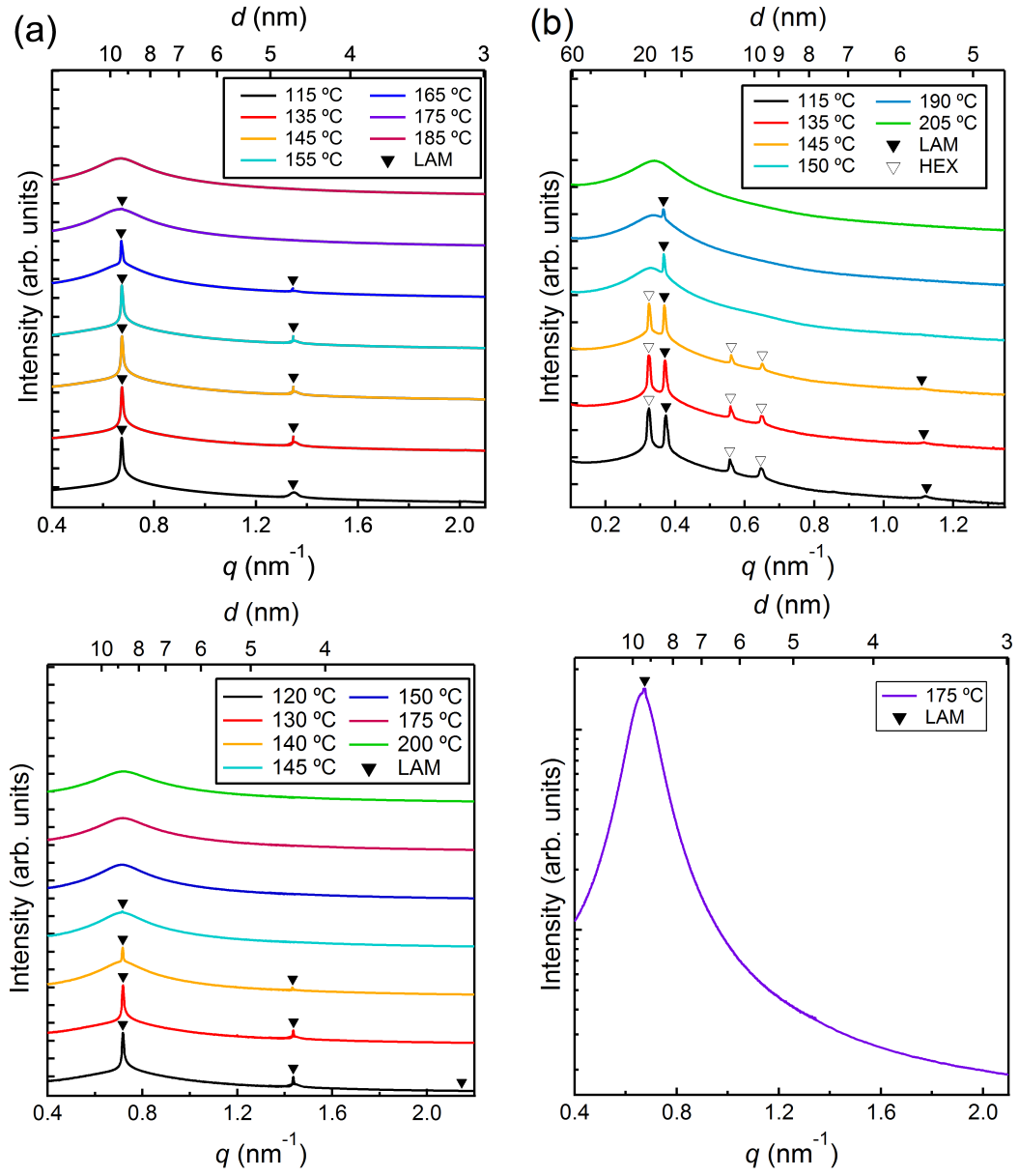

Figure 3.11: Small angle X-ray scattering traces for blends containing (a) $\phi_H = 0.2$, (b) $\phi_H = 0.65$, and (c) the diblock copolymer ($\phi_H = 0$) doped with LiTFSI at a molar ratio $r = [Li^+]/[EO] = 0.06$. Markers for LAM indicate q/q^* multiples of 1, 2, and 3, where q^* is the primary peak position, while markers for HEX indicate q/q^* multiples of 1, $3^{1/2}$, and $4^{1/2}$. (d) Marker indicates the presence of a slight, but observable, q^* peak that suggests the coexistence of LAM and DIS phases in $\phi_H = 0.2$ blend.

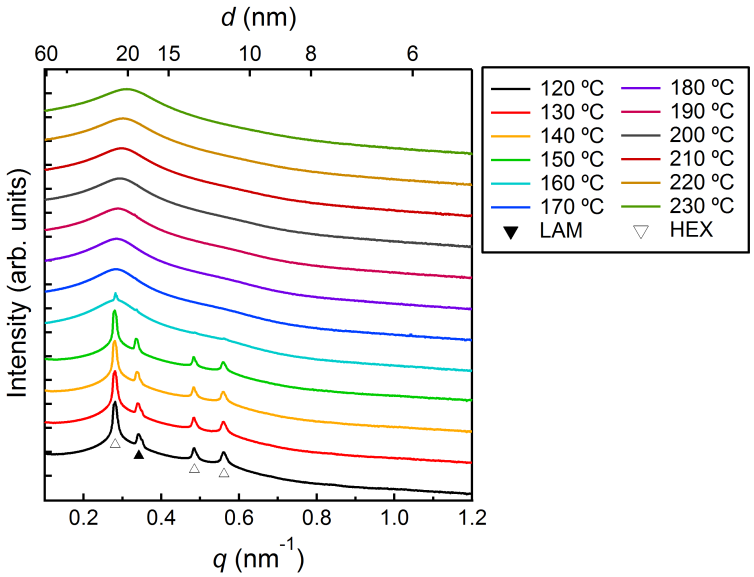

Figure 3.12: Small angle X-ray scattering traces for a blend containing $\phi_H = 0.7$ doped with LiTFSI at a molar ratio $r = [Li^+]/[EO] = 0.06$. The LAM marker indicates only the primary peak, q^*, while markers for HEX indicate q/q^* multiples of 1, $3^{1/2}$, and $4^{1/2}$.

SAXS traces for a $\phi_H = 0.7$ blend at temperatures that produce a BμE morphology are shown in Figure 3.13a. Unlike in previous studies on polymeric BμEs, this system maintains a strong primary peak over a very large temperature range.[115,164] To quantitatively assess the structure of the microemulsion, the data were fit with the Teubner-Strey model, given by

$$I(q) = \frac{1}{a_2 + c_1 q^2 + c_2 q^4} \tag{3.4}$$

where $I(q)$ is the background-subtracted scattered intensity and a_2, c_1, and c_2 are fitting parameters.[100] An example of the fitting is shown in Figure 3.13b. From this model, three structural characteristics can be calculated. The domain spacing, d, correlation length, ξ, and amphiphilicity factor, f_a, are given respectively by

$$d = 2\pi \left[\frac{1}{2} \left(\frac{a_2}{c_2} \right)^{1/2} - \frac{1}{4} \frac{c_1}{c_2} \right]^{-1/2} \tag{3.5}$$

$$\xi = \left[\frac{1}{2}\left(\frac{a_2}{c_2}\right)^{1/2} + \frac{1}{4}\frac{c_1}{c_2}\right]^{-1/2} \tag{3.6}$$

$$f_a = \frac{c_1}{(4a_2c_2)^{1/2}} \tag{3.7}$$

The amphiphilicity factor is a quantitative measure of structure in a microemulsion. A value of $f_a = -1$ indicates that the system is lamellar, while a value of $f_a = 0$ corresponds to the crossover at which the spontaneous formation of interface is no longer energetically favorable.[100–102] Thus, a value of the amphiphilicity factor close to 1 indicates that the system is highly structured, but still globally disordered.

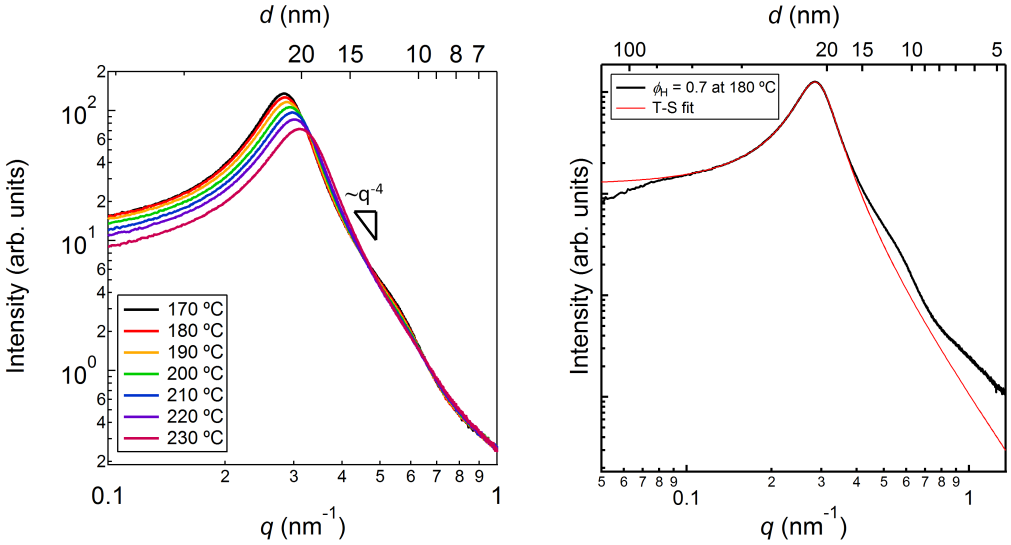

Figure 3.13: (a) Background subtracted SAXS data for blends with ϕ_H = 0.7. (b) Example of a fit of the Teubner-Strey model to background-subtracted SAXS data for blends containing ϕ_H = 0.7 at 180 °C.

The calculated structural values determined using the fitting parameters of the Teubner-Strey model are shown in Figure 3.14. The error bars represent one standard deviation and were calculated by propagating the error in the fitting parameters. Through the 60 °C temperature range studied, the domain spacing and correlation length decrease very modestly, and the amphiphilicity factor only increases from about

-0.95 to -0.93 over the same temperature range. For comparison, recent work on a salt-free ternary polymer blend of polyethylene (PE) and poly(cyclohexylethylene) (PCHE) homopolymers and a PCHE-PE diblock copolymer found that the structure of a salt-free BμE morphology changes quite dramatically with temperature, with the amphiphilicity factor changing from -0.93 to -0.49 when heated through a 75 °C temperature range (125 °C to 200 °C).[115] In the current study, the insensitivity of the microemulsion structure to temperature suggests that the relative salt loading, r, not the temperature of the system, primarily dictates the segregation strength and thus the phase behavior for this system, as has previously been described for a variety of salt-containing diblock copolymers.[82]

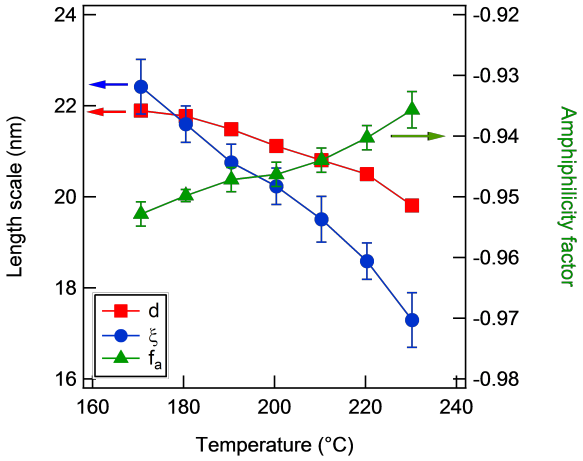

Figure 3.14: Domain spacing (d), correlation length (ξ), and amphiphilicity factor (f_a) as a function of temperature. Values were calculated from the fitting parameters of the Teubner-Strey model as applied to the small angle X-ray scattering data shown in Figure 3.13a. Error bars represent $\pm$ one standard deviation, calculated by propagating the error in the fitting parameters.

At high homopolymer concentrations ($\phi_H > 0.7$), blends with salt loadings of r = 0.06 could not be rendered homogeneous upon heating, despite the low average molecular weight of the system. To better understand this result, the phase behavior of PEO and PS homopolymer blends (ϕ_H = 1) with various salt concentrations, $r = 0 - 0.02$, was studied using cloud point measurements, and the results are shown in

Figure 3.15.

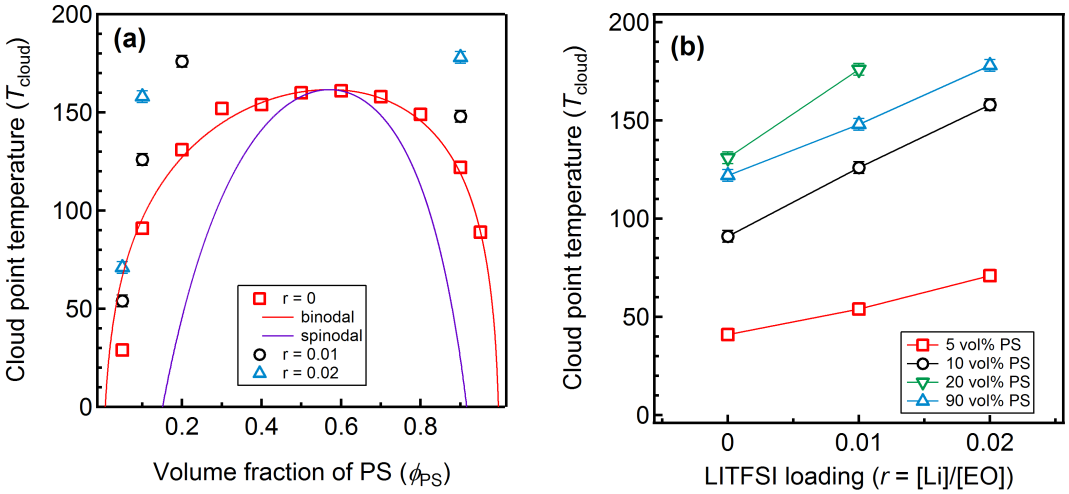

Figure 3.15: Phase diagram showing the binodal for blends of PS and PEO homopolymers at various concentrations of LiTFSI, r. Individual points represent transitions located via cloud point measurements. Lines in (a) represent the fitted binodal and calculated spinodal curves, while lines in (b) are drawn to guide the eye.

The phase diagram for the salt-free blends has been plotted in Figure 3.15a alongside binodal and spinodal curves calculated using a composition-dependent segment-segment interaction parameter, given by

$$\chi_{\text{eff}} = \left(\frac{366}{T} - 0.55\right)\left[1 - 0.3\left(1 - \phi_{\text{PS}}\right)\right] \tag{3.8}$$

where V_{ref} = 0.1 nm^3, T [=] K.[165] The need for a composition dependent segment-segment interaction parameter is not immediately obvious, but it may be related to the conformational asymmetry between the salt-doped PEO and PS homopolymers.[114] This equation results in a critical temperature and composition of 162 °C and $\phi_{\text{c,PS}} \approx$ 0.57, respectively. This expression for χ_{eff} was adjusted to reasonably approximate the experimentally-obtained cloud point temperatures, T_{cloud}, and suggests that, at room temperature (25 °C), χ_{eff} = 0.59 for the neat, salt-free PS/PEO homopolymer blends at the critical composition. In contrast, Teran *et al.* found that, for neat, symmetric PS-PEO diblock copolymers,

$$\chi_{\text{eff}} = \frac{10.2}{T} + \frac{1850}{TN} \tag{3.9}$$

where V_{ref} = 0.1 nm^3, T [=] K, and N is based on V_{ref}. This indicates that the PS-PEO diblock in the current study would have χ_{eff} = 0.11 at room temperature.[80,82] Beyond the large value for χ_{eff} for the salt-free blend, Figure 3.15 also indicates that even a small amount of LiTFSI can dramatically affect the segregation strength of a blend, qualitatively consistent with previous predictions by Wang and coworkers.[82,84] At most compositions, salt concentrations beyond r = 0.02 lead to an immeasurably high T_{cloud}.

Relationship between morphology and conductivity

After establishing the phase behavior of the blends, one primary goal was to determine the relationship between microstructured morphology and ionic conductivity in the blends. In order to determine the ionic conductivity, electrochemical impedance spectroscopy was performed on blends both above and below their T_{ODT}. An important parameter to determine when performing these alternating current (AC) impedance experiments is the lengthscale that is probed by the experiments. Therefore, prior to discussing the results of the study, we first will consider the relevant time and lengthscales probed by the AC conductivity experiments.

Determination of ion diffusion coefficients with PFG-NMR

To better understand how the conductivity of both the lithium and TFSI ions change with blend composition, PFG-NMR experiments were conducted to determine the diffusion coefficients of PEO, Li^+, and $TFSI^-$ in the salt-doped PEO homopolymer. The values for the diffusion coefficient of the three components in our LiTFSI-doped PEO homopolymers are compared against literature values for both other salt-doped PEO homopolymer systems and a PS-PEO block copolymer in Table 3.2 and Figure 3.16.

The results in the table and figure indicate that the hydroxyl-terminated PEO homopolymer, Li^+, and $TFSI^-$ in the current study diffuse approximately an order

of magnitude slower than the same salt dissolved in the dimethoxy-terminated PEO homopolymer studied by Orädd *et al.*[166] This result is likely due to significant hydrogen bonding in the hydroxyl-terminated PEO homopolymer that results in a more viscous solution and lower diffusion coefficients. Compared to the high molecular weight PEO homopolymer and salt-doped block copolymers, however, the diffusion coefficients for Li^+ and $TFSI^-$ in the hydroxyl-terminated PEO homopolymer are approximately 2 – 5 times larger, indicating that the low molecular weight, hydroxyl-terminated PEO homopolymer still provides enhanced ion transport. These results suggest that blends that are relatively more block copolymer-rich should exhibit lower diffusion coefficients of Li^+ and $TFSI^-$ relative to the case of low molecular weight PEO homopolymer.

Table 3.2: Diffusion coefficients of various species in various solvents.

		Diffusion Coefficients (m^2/s)				
System	M_n (kg/mol)	D_{Li^+}	D_{TFSI^-}	D_{PEO}	Method	Ref.
HO-PEO-OH, r = 0.06, 75 °C	0.4	3.0×10^{-11}	4.3×10^{-11}	3.0×10^{-11}	PFG-NMR	Our study
H_3CO-PEO-OCH_3, r = 0.05, 85 °C	0.4	1.1×10^{-10}	1.6×10^{-10}	1.3×10^{-10}	PFG-NMR	166
PS-PEO, r = 0.085, 90 °C	> 20	3.6×10^{-12}	1.4×10^{-11}	–	EIS, assumes $t^+ = 0.2$	167

Analysis of electrochemical impedance spectroscopy (EIS) measurements

When reporting conductivity data derived from EIS experiments, the length scale probed by the experiment is important. Because the interpretation of the data is dependent upon this length scale, we have worked to provide a reasonable estimate of the length scales explored. A simple route to this estimate is through a calculation of the root mean squared (r.m.s.) displacement, given by

$$l = \sqrt{6Dt} \tag{3.10}$$

where D is a diffusion coefficient and t is the experimental time. As an example, consider the r.m.s. displacement of ions in blends containing $\phi_H = 0.7$ as a function

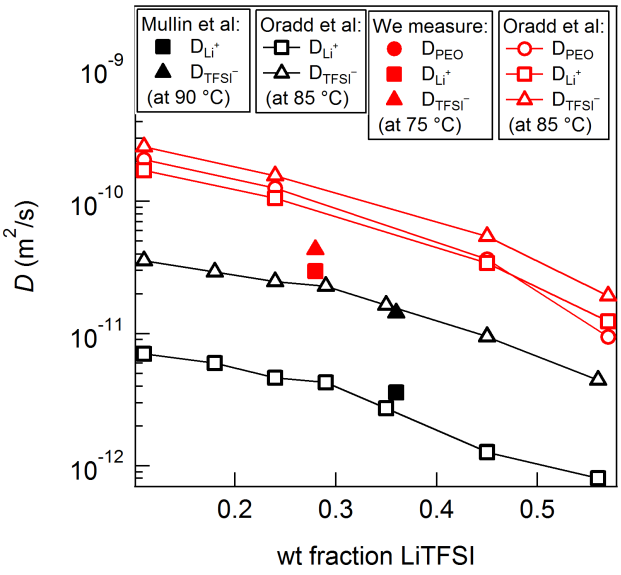

Figure 3.16: Diffusion coefficients of PEO, Li^+, and $TFSI^-$ in various environments and temperatures. The symbols in black refer to diffusion coefficients assessed in high molecular weight PEO (M_n > 20 kg/mol). The red symbols refer to measured diffusion coefficients for low molecular weight (M_n = 400 g/mol) PEO homopolymers. In our study, we employ a hydroxyl-terminated PEO homopolymer, whereas Orädd *et al.* used a dimethoxy-terminated PEO homopolymer. Data in figure are reproduced from Refs. 166 and 167.

of temperature during EIS experiments. To perform this calculation at various temperatures, then, we must know both $D(T)$ and $t(T)$. As stated in the Experimental Section, the conductivity of the sample was determined by extracting the value of the in-phase impedance, Z', at the high frequency plateau. Specifically, the value of Z' was chosen where Z'' was at a minimum. Thus, it is possible to calculate a time scale associated with the measurement by taking the inverse of the dielectric frequency, *i.e.* $t \sim 1/f$. This time scale is shown at different temperatures in Figure 3.17a. Lines protruding from the symbols indicate the range of time scales represented by the width of the plateau (see Figure 3.18 for an example). From the PFG-NMR experiments (Figure 3.16), we expect that both the Li^+ and $TFSI^-$ species in this study exhibit a diffusion coefficient of approximately 10^{-11} m^2/s or greater at 75 °C. The

Vogel-Fulcher-Tammann-Hesse (VFTH) equation provides a method for calculating the viscosity of a blend at a given temperature and is given by

$$\ln\eta = A + \frac{B}{T - T_0} \tag{3.11}$$

where A is an empirical constant, T_0 is the Vogel temperature which is typically about 45 °C below the T_g, and B describes the energetic barrier to, in this case, ion motion. Because $D \sim 1/\eta$, we can take the difference of the VFTH equation at two temperatures to yield

$$\ln\eta - \ln\eta_r = \ln\frac{\eta}{\eta_r} = \ln\frac{D_r}{D} = B\left(\frac{1}{T - T_0} - \frac{1}{T_r - T_0}\right) \tag{3.12}$$

where the subscript r refers to the parameter at a reference temperature. As will be shown shortly, for blends with $\phi_H = 0.7$, fits of the VFT equation to the conductivity of the ordered state give a B of 2600 K and T_0 of 115 K. From the PFG-NMR results, we can use a value of 10^{-11} m^2/s and 75 °C for D_r and T_r, respectively. This approximate route to determining diffusion coefficients was used to calculate the curve seen in Figure 3.17a. With the values for the diffusion coefficient thus calculated and the time scales extracted from the conductivity data, it was then possible to approximate the root mean squared displacement using Equation 3.10. These results are shown in Figure 3.17b, along with the domain spacings and conductivity data determined using SAXS and EIS experiments, respectively.

Figure 3.17b indicates that, throughout the entire temperature range probed, the r.m.s. displacements are about 3 to 10 times larger than the domain spacings of the blends. This indicates that the bulk resistance used to calculate conductivity considers the resistance ions experience when traversing over distances of multiple domain spacings. Furthermore, there is no correlation between the trend in the conductivity data with the r.m.s. displacement.

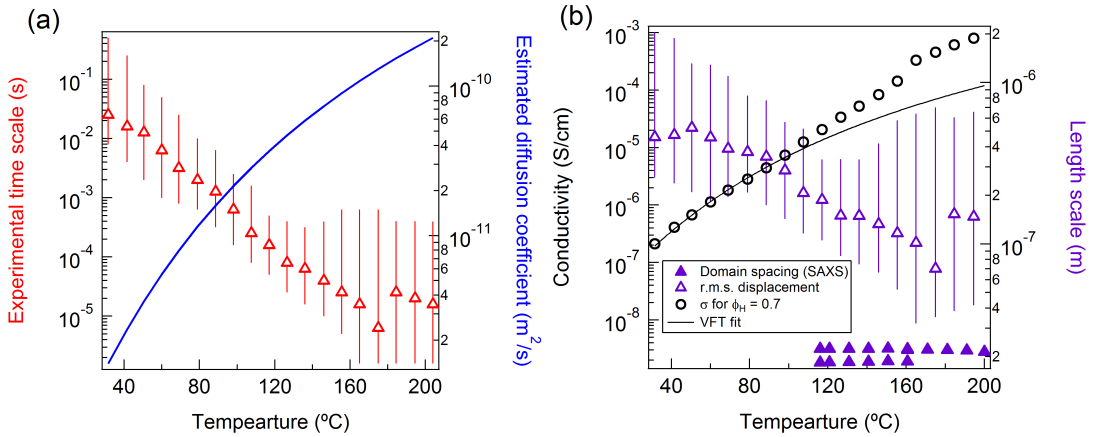

Figure 3.17: (a) Experimental time scales from EIS experiments and estimated diffusion coefficients for ions as a function of temperature. (b) Comparison of the estimated r.m.s. displacement of ions with the domain spacing from SAXS and conductivity data from EIS. The open triangles refer to the points at which Z'' was at a minimum, while the lines protruding from the triangles indicate the range of either time scales or lengths within the plateau region of the EIS spectra.

Results from study

With a good understanding of what lengthscales and morphologies the EIS experiments probes, it is now possible to make insightful analysis into the relationship between structure and conductivity in these polymer blends. In Figure 3.19, representative conductivity for blends containing $\phi_H = 0.2$ and $\phi_H = 0.7$ are plotted alongside the elastic modulus. Data from additional blends are included in Figure 3.20. The conductivity for the blends in the ordered state has been fit with the Vogel-Fulcher-Tammann (VFT) equation, given by

$$\sigma = \sigma_0 \exp\left(\frac{-B}{T - T_0}\right) \tag{3.13}$$

where σ_0 is the conductivity at infinite temperature, B is related to the energy required for ion motion, and T_0 is the Vogel temperature, typically about 45 °C lower than the glass-transition temperature.[26] These fitting parameters are summarized in Table 3.3.

A precipitous drop in the elastic modulus upon heating is a signature of passing

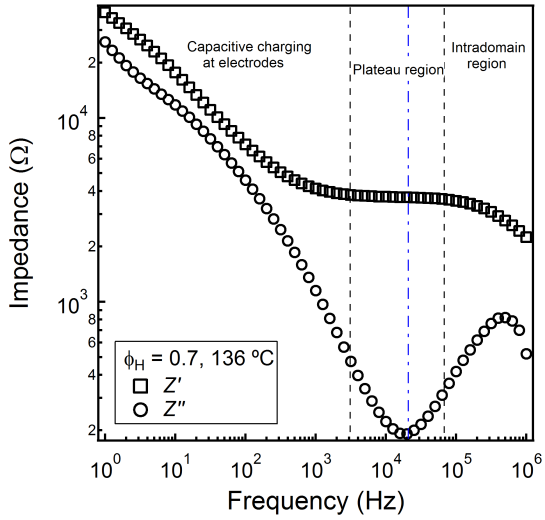

Figure 3.18: Representative EIS plot of Z' and Z'' vs dielectric frequency. The dashed lines represent the cutoffs of the high-frequency plateau region, while the dash-dot line indicates the frequency within the plateau region at which Z' was a minimum and, therefore where the bulk resistance of the sample was extracted. In the intradomain region at higher frequencies, the ions do not have enough time to traverse enough of the sample and thus experience a lower Z'. At lower frequencies, ions have enough time to build up concentration gradients near the electrodes that lead to capacitive overpotentials, thus increasing Z'.

through T_{ODT}.[168] As can be seen in Figure 3.19, this drop in elastic modulus is concomitant with an increase in conductivity that departs from the VFT form. This abrupt change in conductivity was previously observed by Teran *et al.* in LiTFSI-doped PS-PEO diblock copolymers as they were heated through T_{ODT}.[74] In that work, and in the present system when $\phi_H = 0.2$, this change occurs over about a 10 °C temperature range. For the $\phi_H = 0.7$ blend, the increase in conductivity occurs in two steps: a broad transition from 110 °C to 160 °C, then a jump at 170 °C. To better understand these transitions, we refer the reader back to the plotted SAXS data from the $\phi_H = 0.7$ blend at temperatures below and above T_{ODT} in Figure 3.12. Analysis of the relative intensity of the primary scattering peaks for the LAM and HEX morphologies from this SAXS data is shown in Figure 3.21 and indicates that both the ratio of LAM to HEX, and the ratio of the measured conductivity to the conductivity predicted by extrapolating the VFT

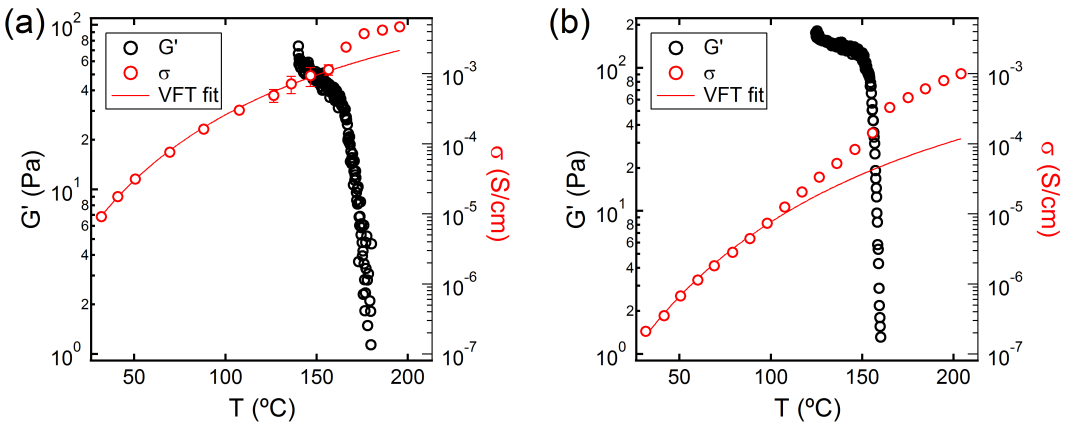

Figure 3.19: Representative conductivity and rheological behavior for blends containing (a) ϕ_H = 0.2 and (b) ϕ_H = 0.7. The solid lines represent a VFT fit to the ordered state data.

Table 3.3: VFT fitting parameters used for fitting the ordered state data in Figures 3.19 and 3.20.

ϕ_H	σ_0 (S/cm)	B (K)	T_0 (K)
0	0.265	1400	175
0.2	0.202	1360	169
0.4	0.019	906	198
0.6	0.010	906	191
0.65	0.019	1252	169
0.7	0.167	2600	115

fit, $\sigma_{meas}/\sigma_{VFT}$, increases with increasing temperature through the broad transition. This trend is consistent with previous work that suggests LAM should provide a significantly higher conductivity than HEX.[152] After this broad transition, the SAXS data in Figure 3.12 indicates that the sample transitions from LAM + HEX to BμE over an approximately 10 °C window centered around 160 °C, resulting in the jump in the conductivity at 170 °C.

The conductivity of these blends is compared in Figure 3.22. Plotted along with the data from the pseudo-ternary blends is the ionic conductivity for the same PEO homopolymer used in the blends doped with the same molar salt loading of r = 0.06. In order to compare the data for the microstructured pseudo-ternary blends to a

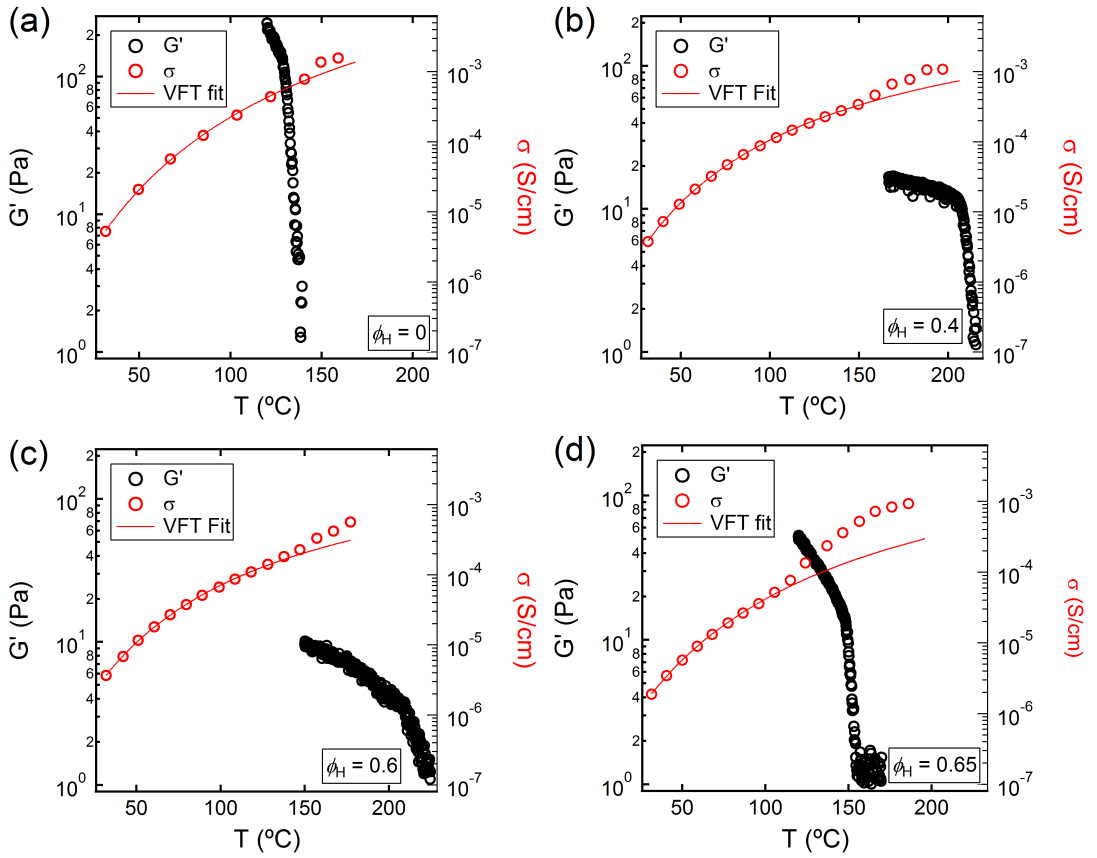

Figure 3.20: Representative conductivity and rheological behavior for blends containing (a) $\phi_H = 0$, (b) $\phi_H = 0.4$, (c) $\phi_H = 0.6$, and (d) $\phi_H = 0.65$. The solid lines represent a VFT fit to the ordered state data.

homogeneous conducting phase, Equation 3.1 was used to calculate a range of predicted ionic conductivities for the blends using the volume fraction of the conducting phase ($\phi_{cond} = 0.5$) and the tortuosity of the microstructure ($\tau = 1.5$ to 3). The results of this calculation are shown as the yellow shaded region. Clearly, this window overestimates the conductivity for almost all compositions and temperatures, indicating that the trends in conductivity in the current system cannot be explained solely on the basis of variations in tortuosity among different morphologies.

Figure 3.22 also shows that all blends exhibit an abrupt change in conductivity when heated through T_{ODT}, demonstrating that, for every blend composition, the disordered

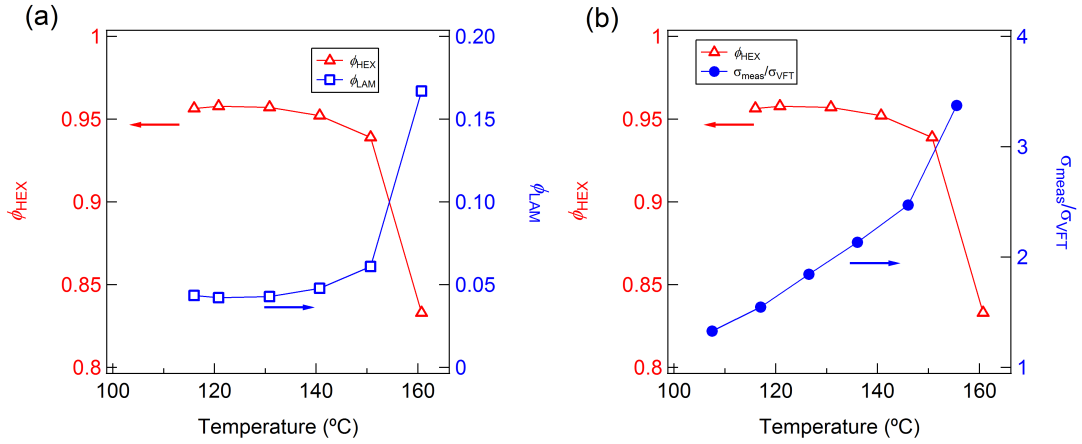

Figure 3.21: Analysis of ordered-state SAXS data from Figure 3.12 for a blend containing $\phi_H = 0.7$ doped with LiTFSI at a molar ratio $r = [Li^+]/[EO] = 0.06$. Figure (a) shows the relative fraction of each ordered phase as a function of temperature, while (b) shows that the ratio between the measured and extrapolated conductivity values increases as the fraction of HEX decreases. The relative fraction of each phase was determined by comparing the relative intensity of the primary scattering peak of each phase. Lines have been drawn to guide the eye.

state enhances ion transport. For blends in the ordered state, there is generally a decrease in the conductivity as the homopolymer content is increased. This decrease is especially pronounced for blends with ϕ_H = 0.6 to 0.7 with coexisting LAM and HEX morphologies. Interestingly, the disordered state conductivity also decreases as homopolymer is added, even though these systems exhibit no long-range order. This result is unanticipated, because the average molecular weight of the polymer components decreases by roughly an order of magnitude as the homopolymer content is increased from ϕ_H = 0 to 0.7. Furthermore, the failure of the disordered state data at higher ϕ_H to fall within the yellow shaded region determined using Equation 3.1 suggests that the disordered state is not homogeneously mixed, as was assumed in previous studies of LiTFSI-doped PS-PEO block copolymers.[82] The width of the jump in conductivity that occurs between the ordered and disordered states also appears to widen with increasing homopolymer loading, perhaps due to larger regions of phase coexistence or the coalescing of grains upon heating, as suggested above. The behavior

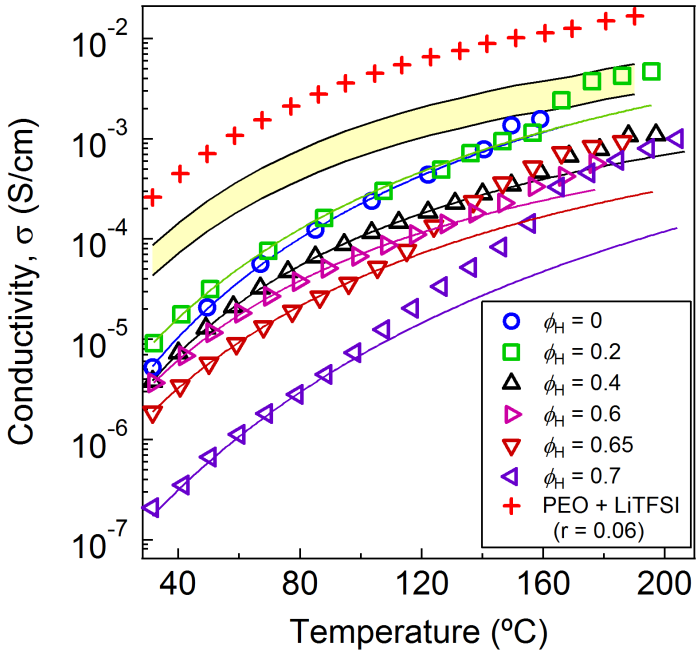

Figure 3.22: Comparison of conductivity for various blend compositions. The lines through data represent VFT fits to the ordered-state data and help to visualize the large change in conductivity through the order-disorder transition. The red crosses represent the conductivity measured for a PEO homopolymer and LiTFSI blend with r = 0.06, and the shaded region below the crosses represent the conductivity adjusted for a range of blend morphologies according to Equation 3.1.

of both the ordered and disordered states, in addition to the nature of the width and magnitude of the jump in the conductivity, will be examined in more detail in the Discussion section.

From Figure 3.22 alone, it is impossible to distinguish how each individual blend component influences the conductivity with increasing homopolymer content. Thus, several additional experiments were carried out. First, the ionic conductivity of the PEO homopolymer was measured as a function of salt loading (r = 0.01 to 0.10) and temperature. The results from these experiments are shown in Figure 3.23a. The conductivity generally increases as the salt loading is increased, as previously reported for LiTFSI-doped PEO homopolymer of modest molecular weight ($M_n \approx$

5 kg/mol).[78] However, at low temperature, there is a drop in the conductivity when the salt loading is increased from r = 0.02 to 0.06, and the sharp curvature of the data at high salt loadings indicates that the Vogel temperature and, thus, the glass transition temperature is increasing with salt-loading.[78] In the current study, we employ a low molecular weight PEO ($M_n \approx 400$ g/mol). Previous reports have suggested that low molecular weight polymers can provide vehicular transport of lithium ions *via* Rouse chain diffusion, which can account for a significant fraction of the measured conductivity.[71,169,170] However, Ren *et al.* have recently shown that the addition of lithium salt to PEO homopolymers leads to significant ion-induced cross-linking,[84] which may serve to increase the viscosity and effective molecular weight of the PEO phase. Thus, at higher salt loadings, the increase in the number of charge carriers that would serve to increase the measured conductivity is likely partially offset by a simultaneous increase in ion-induced cross-linking and, thus, the viscosity of the salt-doped PEO homopolymers, leading to a suppression of vehicular transport and a muted change in the ionic conductivity of the blends.

After establishing the role that salt concentration plays on conductivity, blends of PS and PEO homopolymer (ϕ_{PS} = 0.05 or 0.9) at low salt concentrations (r = 0.01 – 0.06) were prepared to assess the effects of the intermixing of the two species on conductivity. This analysis intends to act as a proxy for the effects of interfacial mixing, as shown in Figure 3.1, where there could be a region of the conducting channel that is intermixed with the insulating domain. The results are shown in Figure 3.23. Interestingly, there is no change in the conductivity at the cloud point, likely because there is no stirring in the sample to promote phase separation. Surprisingly, the temperature dependence of the conductivity of blends in Figure 3.23b and 3.23c does not deviate at the cloud point, potentially due to the lack of stirring within the coin cells to promote phase separation. The cloud point of the blend was determined separately using an optical transmission experiment, as described in the Experimental section. Blends with ϕ_{PS} = 0.9 exhibited an impedance that was too large to be resolved by the instrument, indicating that the blends exhibited very low conductivity as expected based on the large volume fraction of the insulating component.

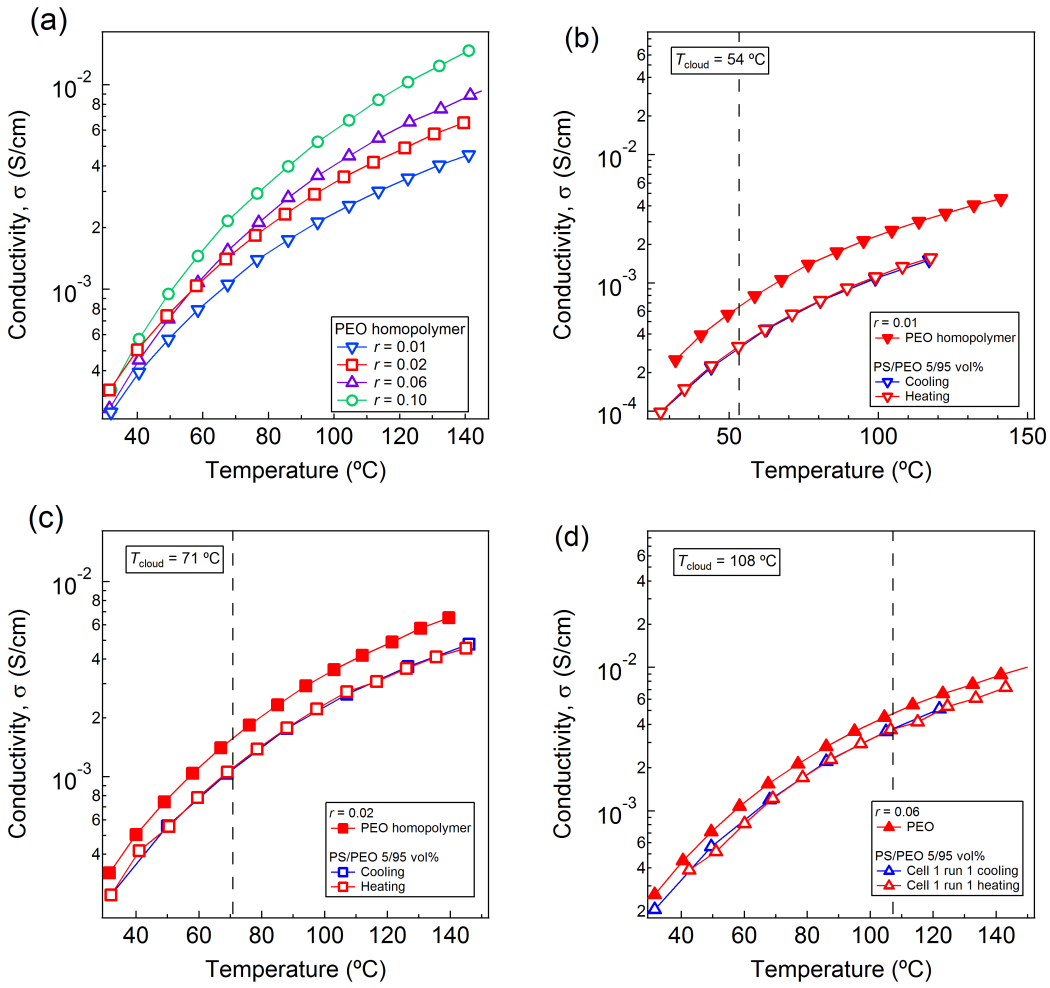

Figure 3.23: Ionic conductivity for blends that blends that contain (a) PEO homopolymer at various salt loadings, and PS/PEO homopolymer blend (5/95 vol%) with (b) $r = 0.01$, (c) $r = 0.02$, and (d) $r = 0.06$. Lines have been drawn to guide the eye.

3.5 Discussion

Phase behavior

Overall, the phase behavior of pseudo-ternary blends closely resembles that of traditional ternary polymer blend systems. Mean-field theory predicts that, as homopolymer is added to lamellar-forming blends, the characteristic length scale of the morphology diverges (*i.e.* $d \to \infty$) at an unbinding transition. This unbinding transition was anticipated to meet the line of order-disorder transitions at low to moderate homopolymer loading and the Scott line of critical points at high homopolymer loading, at a Lifshitz multicritical point.[105] However, experimental studies on ternary polymer blends consisting of polyethylene (PE), poly(ethylene-*alt*-propylene) (PEP), and PE-PEP demonstrated that the unbinding transition was instead preempted by the presence of the BμE channel.[94] The formation of this channel was attributed to thermal fluctuations driving the swollen lamellar microstructure to disorder. Further studies demonstrated that this behavior was universal for A- and B-type homopolymers and a corresponding AB diblock copolymer.[18,39,94,102,111,112,114,121] Much like these "traditional" ternary polymer blends, the phase diagram in Figure 3.8 for the pseudo-ternary blends shows that a BμE channel separates the region of microphase separated, ordered morphologies at low homopolymer concentration from the phase separated region at high homopolymer loading.

One particularly surprising feature of the phase diagram in Figure 3.8 is that the line of T_{ODT}s increases strongly with increasing ϕ_{H}, even though the average molecular weight of the polymers decreases with increasing ϕ_{H}. This trend appears to continue into the phase-separated region of the phase diagram, where the Scott line of T_{c}s occurs at inaccessibly high temperatures. In the current system, the ratio of the average degree of polymerization of the homopolymers to the degree of polymerization of the diblock copolymer is $\alpha = (N_{\mathrm{PEO}}N_{\mathrm{PS}})^{1/2}/N_{\mathrm{PS-PEO}} = 0.10$. If a single function for χ_{eff} could be used to describe the excess free energies of both the diblock copolymer and the homopolymer blends in the presence of LiTFSI,[146] the relatively small volume of the homopolymers would suggest that the T_{c} of the homopolymer blend should be

lower than the T_{ODT} of the diblock copolymer, not higher, as $(\chi N)_{ODT} = 10.5$ for a volumetrically symmetric diblock copolymer and $(\chi N)_c = 2$ for a binary homopolymer blend ($\phi_A/\phi_B = 1$).

To understand the difference in the behavior of the block polymer *vs.* the homopolymer blends, phase diagrams for PS/PEO homopolymer blends were assembled at various salt loadings $r = 0 - 0.02$. The resulting binary phase diagrams in Figure 3.15a show that even the salt-free blends exhibit a high degree of incompatibility. As stated in the Results section, there is a remarkable difference in the χ_{eff} for the diblock copolymer and the homopolymer blend: at 25 °C, the diblock in this study exhibits χ_{eff} = 0.11,[82] compared to χ_{eff} = 0.59 for the binary homopolymer blend at the critical composition. Taken at face value, this suggests a substantial difference in the interactions between homopolymers compared to the corresponding diblock copolymer.

Although differences in χ_{eff} for AB diblock copolymers and A/B homopolymer blends have been described before, the magnitude of the current difference is striking. For example, Maurer *et al.* have previously shown that, for polymer species that should exhibit purely dispersive interactions, the characteristically small values of χ_{eff} of A/B homopolymer blends and an AB diblock copolymer differ by at most *ca.* 50%.[146] Further, although previous work has shown that there is not perfect quantitative agreement between χ_{eff} measured from different techniques (here, RPA analysis of SAXS data for the block copolymer *vs.* cloud point measurements for the homopolymer blend), the substantial difference in the χ_{eff} is beyond the margin of error expected by comparing these two types of systems.[146] One potentially important factor in the current study is the effect of the end groups of the PEO homopolymer. The PEO homopolymer (M_n = 400 g/mol) is hydroxyl-terminated, leading to two hydroxyl groups per every nine ethylene oxide units, as compared to only one hydroxyl end group for every 43 ethylene oxide units for the PS-PEO diblock copolymer. As a result, the PEO homopolymer is especially hydrophilic compared to the hydrophobic PS homopolymer. For comparison, previous studies found that polystyrene/poly(4-hydroxystyrene) systems, where the only difference between the

two species is a hydroxyl group on the monomer, exhibits a χ_{eff} that is about 4 times larger than for polystyrene/polyacrylate systems, where there are significant differences in the monomer identities.[171,172] Similarly, Gillard *et al.* found an approximately 15% difference in $(\chi N)_{ODT}$ between theory and experiment for a short poly(1,4-isoprene)-b-poly(DL-lactide) (PI-PLA) diblock copolymer (M_n = 2750 g/mol), which they attributed to hydrogen bonding between PLA-terminal hydroxyl end groups and PLA-backbone carbonyl groups.[47] Jo *et al.* also demonstrated that the microstructure and ionic conductivity of PS-PEO block copolymers can be radically affected by the identity of the PEO end group (-OH, -SO3H, or -SO3Li).[46] Thus, it is likely that the high density of hydroxyl end-groups on the short PEO homopolymer makes it more hydrophilic relative to the hydrophobic PS homopolymer, leading to a significantly higher χ_{eff} for the homopolymer blends. Studies are currently underway to compare the behavior hydroxyl-, monomethoxy-, and dimethoxy-terminated PEO, which should shed further light on the substantial difference in χ_{eff} between the block polymer and the homopolymer blends.

Figure 3.15 also indicates that the addition of even a small amount of salt dramatically increases the cloud point temperature, T_{cloud}, of the blend. Previous theoretical work on LiTFSI and PS/PEO homopolymer blends has shown that significant amounts of Li^+ ion-induced "cross-linking" occurs in the PEO, even at low salt loadings $r \leq 0.02$, leading to a significant increase in segregation strength.[84] However, Nakamura *et al.* have previously suggested that the addition of lithium salts results in a relatively larger increase in χ_{eff} for PS-PEO block copolymers than for PS/PEO homopolymer blends.[81] Quantitatively determining χ_{eff} as a function of salt loading for both the PS-PEO block copolymer and the PS/PEO blends is beyond the scope of this work. Ultimately, these findings indicate that, for the same salt content, it is possible to have a thermally accessible T_{ODT} for a PS-PEO diblock copolymer and a thermally inaccessible T_c for a PS/PEO homopolymer blend, even when the ratio of homopolymer molecular weight to that of the block polymer is sufficiently small (*e.g.*, 0.2) that mean-field theory would anticipate $T_c \leq T_{ODT}$, as discussed in Chapter 1 for ternary blends.

Coexistence of LAM and HEX morphologies

The coexistence of LAM and HEX morphologies at moderate homopolymer loadings, although initially striking, is analogous to two-phase windows found in salt-containing diblock copolymers. Specifically, the coexistence of LAM and HEX phases is analogous to the coexistence of LAM and DIS phases near T_{ODT} for blends containing $\phi_H = 0$ and 0.2. Both Nakamura *et al.* and Thelen *et al.* have shown that LAM and DIS phases are able to coexist in LiTFSI-doped block copolymers, and that, within the two phase-region, the relative amount of salt differs according to the lever rule.[66,162] By extension, it is possible that the coexisting LAM and HEX phases in the current study may also be the result of unequal salt loadings. Specifically, a difference in salt loading could lead to selective partitioning of the PS and salt-doped PEO phases in each of the ordered morphologies, thereby leading to two different microstructures with different volume fractions of each domain.

The formation of coexisting LAM and HEX phases has also been observed in salt-free AB/A/B ternary polymer blend systems with equal volume fractions of A and B.[104,113] Several factors that result in this phase coexistence have been previously suggested, and they are reviewed in this Discussion section: (1) differences in the volume fraction of each phase, (2) a mismatch in the relative size of each homopolymer, and (3) conformational asymmetry between the two domains.

The simplest explanation for the formation of a HEX phase would be that there is sufficiently less salt-doped PEO phase than the PS phase, or *vice versa*, to lead to a preferred curvature, but this is not the case. In this experiment, equal volume fractions of the two homopolymer components were added, so that $\phi_{PS} = \phi_{PEO+LiTFSI} = \phi_H/2$. However, as shown in Table 3.1, the diblock copolymer is asymmetric and relatively PS-rich. Even after salt doping at $r = [Li^+]/[EO] = 0.06$, the volume fraction of the conducting phase (*i.e.* $\phi_{cond} = \phi_{PEO+LiTFSI}$) in the diblock is only 0.44. By design, $\phi_{cond} = 0.5$ at $\phi_H = 1$, so from linear interpolation it follows that, at $\phi_H = 0.6 - 0.7$ where the HEX phase is observed, $\phi_{cond} \approx 0.48$. However, mean-field theory for a pure diblock copolymer would predict that, for the entire range of possible $\phi_{cond} = 0.44 - 0.5$, only a LAM morphology would form,[33] which suggests that in the blended system, the

formation of the HEX phase is not due to $\phi_{cond} < \phi_{PS}$.

An alternative explanation for the formation of the HEX phase involves the relative size of the PS and PEO homopolymers. Self-consistent field theory studies by Janert and Schick predicted that blends with $\alpha_A = N_A/N_{AB} = 0.3$ and $\alpha_B = N_B/N_{AB} = 0.2$ will pass from a LAM phase through a LAM+HEX window with increasing homopolymer content, prior to disordering at high homopolymer loading.[173] In this work, $\alpha_{PEO} \approx 0.08$ and $\alpha_{PS} \approx 0.13$, indicating a similar imbalance in the relative size of the homopolymers. However, it is also possible that the addition of LiTFSI salt to the blends could result in an increase in the effective volume of the salt-doped PEO homopolymer relative to the PS homopolymer.This would, in turn, lead to an effective increase in chain length, thus causing $\alpha_{PEO+LiTFSI}$ to approach α_{PS}). If this were the case, the effect of mismatched homopolymer chain length would be less pronounced.

Another possible explanation for the formation of the HEX phase is the conformational asymmetry, ε, between the two polymer species of the blends.[104,113,174] Conformational asymmetry describes the difference between how two polymers A and B fill space per a given molar volume, and can be quantified by $\varepsilon_{AB} = [R^2_{g,A}/V_{mol,A}]/[R^2_{g,B}/V_{mol,B}] \geq 1$.[42] In the current study, $\varepsilon \approx 2$ for PEO and PS, where PEO is the more flexible component (*i.e.* PEO is A, PS is B). This value is similar to that found in other systems with coexisting LAM and HEX morphologies.[113] However, Li^+ is known to form ion-induced cross-links in PEO that could stiffen the PEO chains,[84] making it less flexible and, thus, possibly reducing the extent of conformational asymmetry.

Ultimately, the presence of a HEX morphology is likely due to some combination of slight volume fraction mismatch between the conducting and PS phases, the difference in the relative size of the homopolymers, and conformational asymmetry. Based on this preceding analysis, it is also anticipated that the PEO, which is the more flexible, minority component, forms the cylinders of the HEX phase, while the matrix consists of PS. However, without TEM analysis, it is challenging to definitely establish whether the PS or salt-doped PEO forms the matrix of the HEX phase. Previous work has shown that ionic phases can form the matrix even when it occupies less than 50 vol% of

the blend.[175,176] One route to definitively establishing which phase forms the matrix would be through ionic conductivity experiments, where a low ionic conductivity would be expected if the ionic phase formed the minority phase.[152] Such measurements are currently underway.

To better understand under what conditions the coexistence between LAM and HEX phases occurs, several additional ϕ_H = 0.7 blends were prepared wherein the ratio of LiTFSI-doped PEO homopolymer to PS homopolymer was increased. This allowed us to tune the volume fraction of the conducting phase and obtain blends with ϕ_{cond} = 0.5, 0.55, and 0.6. SAXS traces for these blends at 120 °C are shown in Figure 3.24.

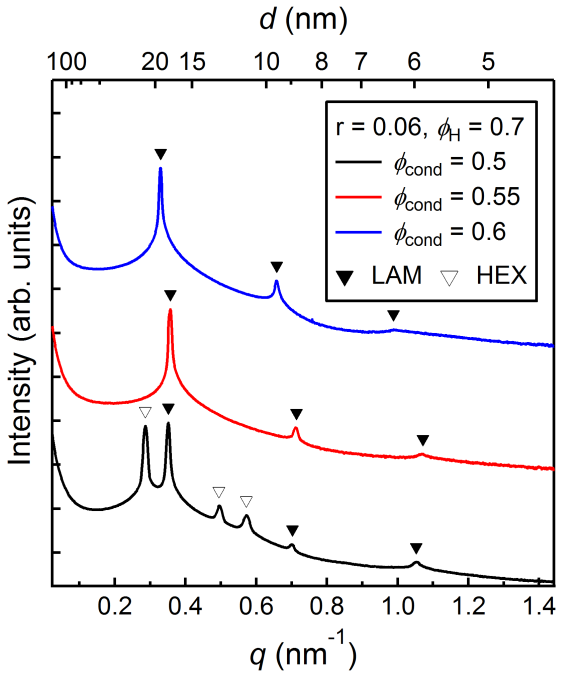

Figure 3.24: Small angle X-ray scattering traces for a blend containing ϕ_H = 0.7 and different loadings of salt-doped PEO homopolymer to give different ϕ_{cond} relative to ϕ_{PS}. The LiTFSI loading is kept constant at a molar ratio of r = [Li^+]/[EO] = 0.06.

Figure 3.24 indicates that a pure lamellar phase only forms when blends are constructed off the volumetrically symmetric isopleth and are rich in LiTFSI-doped PEO. Temperature-dependent SAXS studies revealed that ϕ_{cond} = 0.55 blends disorder at temperatures greater than 220 °C (Figure 3.25), well above the T_{ODT} of 160 °C for

the $\phi_H = 0.7$ and $\phi_{cond} = 0.48$ blend shown in Figure 3.8. This result mirrors findings from theory and experiments on block polymers. Both strong segregation limit theory and experimental studies on conformationally asymmetric block polymers have shown that order-order transitions occur at higher f_A when $\varepsilon_{AB} > 1$.[43,177] Thus, it is likely that the conformational asymmetry between PEO and PS promotes curvature towards the conducting domains and, thus, the formation of a hexagonal phase when blends contain approximately equal amounts of PS and conducting phases. To overcome this preferential curvature and obtain a pure lamellar phase, relatively more of the conducting phase must be added. It is still striking, however, just how significant the shift in the order-order boundaries is for a relatively modest value of conformational asymmetry and difference in relative homopolymer size. This observation, along with the fact that the HEX phase only appears at relatively large ϕ_H, suggests that, as the homopolymers swell the block polymer domains, they also screen the interactions between block polymer interfaces. This screening, along with the conformational asymmetry between PS and PEO, may reduce the energetic barrier to form the curved interface required for the formation of a HEX phase.[42,43,113,128]

Taken altogether, the phase behavior of the system described in this work could have significant implications for the future development of polymer electrolytes. Prior work has suggested that well-ordered, 3D morphologies should provide better connectivity and, thus, conductivity than 1D structures such as cylinders.[152] In addition, both interfacial mixing[71,151] and salt loading[78] have been shown to have an influence on the conductivity of polymer electrolytes. With the system described in the current work, the extent to which these phenomena affect ionic conductivity could be directly compared, as it is possible to obtain 1D (HEX), 2D (LAM), and 3D (BμE) morphologies with tunable T_{ODT}s, segregation strengths, and nominally the same chemical identities by simply tuning the blend ratios. Thus, these blends permit future quantitative comparisons of the performance of each morphology, one of which is described in the next subsection.

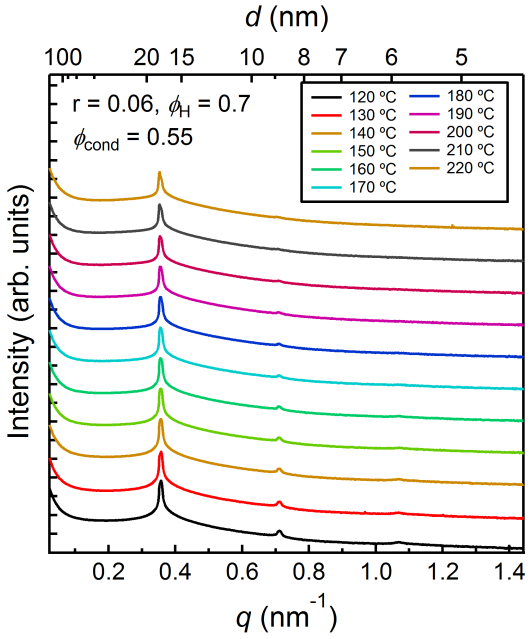

Figure 3.25: Small angle X-ray scattering traces for a blend containing ϕ_H = 0.7 and ϕ_{cond} = 0.55 doped with LiTFSI at a molar ratio r = [Li$^+$]/[EO] = 0.06.

Conductivity through the Order-Disorder Transition

The conductivity of microstructured polymer blends of various homopolymer loadings was measured as a function of temperature when heated through T_{ODT}. Overall, the trend in the data obtained in Figure 3.22 indicate that the conductivity of the blends decreases as the overall volume fraction of homopolymer increases. This result is particularly surprising, because the average molecular weight of the polymers in the system decrease by about an order of magnitude as the volume fraction of homopolymer is increased from ϕ_H = 0 to 0.7. Furthermore, the conductivity of the pure PEO homopolymer is significantly higher than that of any of the ordered systems. This conductivity for the PEO homopolymer is also plotted in Figure 3.22, and the yellow shaded region represents the conductivity predicted by Equation 3.1 for the current blend systems, where ϕ_{cond} = 0.5 and the tortuosity range used should encompass all ordered blends, as they contain lamellae (τ = 1.5) and/or hexagonally close-packed cylinders (τ = 3).[72]

Clearly, almost all of the measured conductivities fall well below this prediction, indicating that effects such as interfacial mixing of conducting and insulating domains,[151] the width of the ion-conducting channel,[71] inferior grain connectivity at lower overall block polymer molecular weights,[70] and restricted polymer diffusion[54] could all be leading to further decreases in ionic conductivity. Thus, in the following discussion, we consider and analyze: (1) the relationship between structure and conductivity in the ordered state, and (2) the structure and dynamics of the disordered state. After establishing an understanding of the overall trends in the conductivity, we use that insight (3) to elucidate the origin of the jump in conductivity.

Conductivity of ordered blends

The data in Figure 3.22 show a general decrease in the ordered state conductivity as the amount of homopolymer is increased. In Figure 3.26, the conductivity of the blends at 120 °C is compared against both the relative fraction of LAM and HEX morphologies (Figure 3.26a) and the domain spacings of those two morphologies (Figure 3.26b). Figure 3.26a indicates that the decrease in conductivity for blends with ϕ_H= 0.6 to 0.7 is concomitant with an increase in the fraction of a HEX relative to LAM. Previously, Cho *et al.* observed a dramatic decrease in conductivity as a sample transitioned from LAM to hexagonally close-packed cylinders.[152] They attributed the drop in conductivity to a reduction in the dimensionality of the conducting phase from 2 (LAM) to 1 (HEX), leading to reduced continuity of conducting domains across grain boundaries.[53,152] Furthermore, the tortuosity of hexagonally close-packed cylinders is twice that of lamellae, which would further reduce the conductivity of blends with high HEX content.[72] Interestingly, Figure 3.26b shows that this drop in conductivity occurs despite the significant increase in the domain spacing with increasing ϕ_H, suggesting that any enhanced ion transport properties that come as a result of having larger conducting domains is negligible in this system.[71] Ultimately, then, it appears that the ordered state conductivity decreases in magnitude with increasing ϕ_H in large part due to the growing presence of the HEX phase relative to the LAM phase, leading to increases in both tortuosity and number of grain boundaries. However, this does not

explain the drop in the conductivity by a factor of about 2 that occurs from ϕ_H = 0.2 to 0.4, where both samples exclusively exhibit a LAM morphology. This indicates that there is some additional mechanism by which the conductivity of ordered blends is decreasing with increasing homopolymer loading. A definitive answer remains elusive, but it may involve increases mixing of styrene and ethylene oxide segments as more homopolymer is added, and preferential curvature towards the conducting domains at grain boundaries, leading to dead ends.

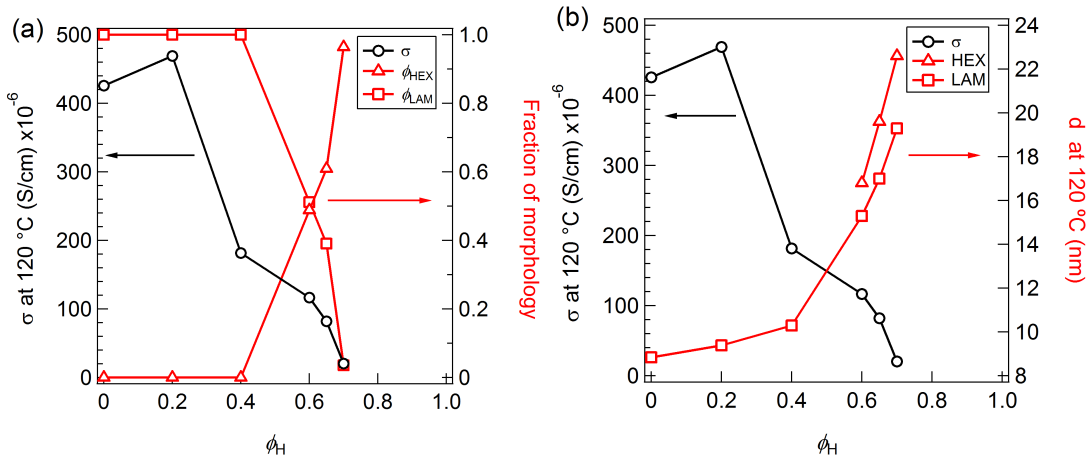

Figure 3.26: Comparison of ionic conductivity at 120 °C for coexisting LAM/HEX *vs.* (a) fraction of each morphology, and (b) domain spacing. The volume fractions in (a) were determined by comparing the relative intensity of the primary peak positions of the two morphologies, while the domain spacings in (b) were determined based on the primary peak positions, both as assessed via SAXS analysis. Lines have been drawn to guide the eye.

Conductivity of disordered blends

The conductivity of the disordered state also appears to depend on homopolymer loading. Specifically, Figure 3.22 indicates that the disordered state for blends containing ϕ_H = 0.7 have approximately an order of magnitude lower conductivity than blends with ϕ_H = 0.2. To understand the reason for this difference, we first consider how the structure of the BμE in ϕ_H = 0.7 blends evolves with temperature. As was

shown in Figure 3.13, the SAXS traces from these blends exhibit a single, broad peak with nearly constant intensity over a wide temperature window of 170 °C to 230 °C. The data were fit with the Teubner-Strey model given in 3.4. These parameters were then used to calculate the domain spacing, d, correlation length, ξ, and amphiphilicity factor, f_a, using equations 3.5, 3.6, and 3.7, respectively. The amphiphilicity factor is a measure of structure in a microemulsion, where $f_a = -1$ indicates the system is lamellar, while a value of $f_a = 0$ corresponds to the point at which the spontaneous formation of interface is no longer energetically favorable.[101,102,178] From the scattering analysis shown in Figure 3.21 and discussed above, we found that f_a is largely temperature invariant and remains between –0.9 and –1 throughout the 60 °C window, indicative of a highly structured, yet still disordered, blend. This high level of structure, even at high temperature, suggests that the presence of lithium salt serves to promote the formation of well-defined domains in the disordered state. As a result, heating these blends to form a perfectly homogeneous melt (*i.e.* molecularly mixed PS, PEO, and LiTFSI) is untenable, as the salt-laden disordered blends will exhibit at least some structure at all accessible temperatures.

After analyzing the structure of the BμE, it is interesting to ask whether the extensive structure in the disordered state for blends containing $\phi_H = 0.7$ was also present for other compositions. Thus, the Teubner-Strey model was fit to disordered state scattering data obtained at 190 °C for blends containing $\phi_H = 0.2$, 0.65, and 0.7. The results of this fitting, and the structural parameters derived from the fitting parameters, are given in Figure 3.27. Within reasonable error, the Teubner-Strey model appears to describe the scattering data from blends containing as little as $\phi_H = 0.2$. The structural characteristics derived from this fitting indicate extensive structure in all three blends, consistent with the findings in our previous study on blends containing $\phi_H = 0.7$.

The results in Figure 3.27 suggest that, much like the BμE, blends containing $\phi_H = 0.2$ are not homogeneously mixed in the temperature range studied. This suggestion is consistent with previous studies on neat, salt-free diblock copolymers that have unambiguously demonstrated that at temperatures well above T_{ODT} ($T - T_{ODT} \leq$

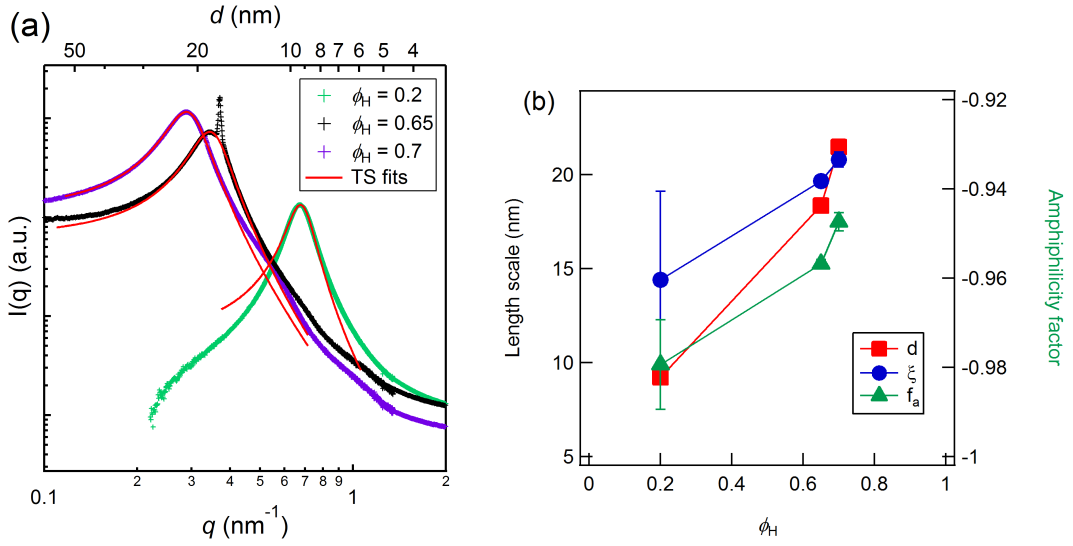

Figure 3.27: Both (a) the SAXS and (b) the fitting parameters derived from fitting the Teubner-Strey model to the disordered state scattering data at 190 °C. The error bars represent the propagation of error of one standard deviation in the values of the fitting parameters.

50 °C), composition fluctuations lead to an equilibrium morphology that resembles a spinodally decomposing binary mixture.[153,154] Thus, the disordered blend with ϕ_H = 0.2 exhibit significant structure.

With a better understanding of the structure of the disordered state for ϕ_H = 0.2 and ϕ_H = 0.7 blends, we can now address the more than order of magnitude difference in the conductivity between these two disordered states. We first note that the conductivity of the disordered ϕ_H = 0.2 blend falls within the shaded region in Figure 3.22, suggesting that the composition fluctuations in the blend lead to a co-continuous, tortuous network through which ions can travel.[154] Next, based on both the current analysis and information in the literature, we have proposed structures for the blends in Figure 3.28. Based on the large magnitude of the amphiphilicity factor and the strong scattering for both the ϕ_H = 0.2 and 0.7 blends, Figure 3.28 suggests that both blends likely consists of well-segregated domains with sharp interfaces. Recent work by Hickey *et al.* has demonstrated that, in bicontinuous microemulsions with

amphiphilicity factors of approximately –0.9 or lower, the diblock copolymer at the interface excludes homopolymer from the interface to form a "dry brush", resulting in a molecular environment similar to that of the neat, undiluted lamellar morphology.[115] Thus, in the present system, it is likely the PEO block of the interface also excludes the PEO homopolymer to yield a "dry", stretched chain.

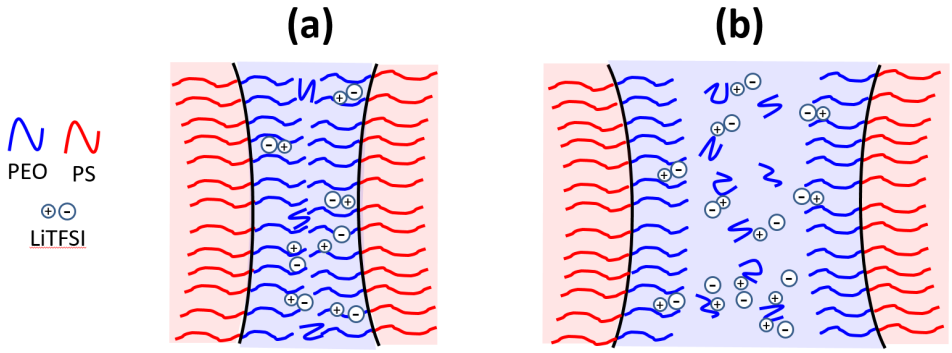

Figure 3.28: Schematic representation of the proposed structure of disordered blends containing (a) $\phi_H = 0.2$ and (b) $\phi_H = 0.7$.

Despite the suggestion that both of the blends depicted in Figure 3.28 have a similar local molecular environment, there is still an order of magnitude difference in conductivity between the $\phi_H = 0.2$ and 0.7 blends. One reason for the low conductivity for the $\phi_H = 0.7$ blends could be a significant number of dead ends and defects in the BμE structure. From Figure 3.26, the ordered state of blends with $\phi_H = 0.7$ consists of more than 90 vol% HEX phase at 120 °C, where the salt-doped PEO is anticipated to be the minority phase. Furthermore, we have suggested in our discussion of the phase behavior that the conformational asymmetry between PEO and PS leads to preferential curvature toward the PEO domains. Thus, when the HEX morphology melts into a BμE morphology, this preferential curvature might lead to the formation of closed-off salt-doped PEO domains. If so, in order to avoid this reduction in the conductivity, blends should be designed so that they compensate for this preferential curvature. One route to doing this would be to add relatively more of the salt-doped PEO homopolymer as compared to the PS homopolymer. As shown in Figure 3.24, blends containing $r = 0.06$, $\phi_H = 0.7$, and approximately 55 vol% salt-doped PEO homopolymer in

the homopolymer phase exhibited an exclusively LAM morphology. The increased symmetry of these blends resulted in a significantly larger and thermally inaccessible T_{ODT}, indicating that relatively less LiTFSI is needed to induce microstructural ordering in these systems. Ultimately, due to the inherent asymmetries in the current system, future studies should look at blends along an isopleth wherein these asymmetries can be balanced, rather than the volumetrically symmetric isopleth.

Beyond dead ends, the relative difference in the relaxation times of composition fluctuations in blends containing $\phi_H = 0.2$ *vs.* 0.7 may also play a role in the observed trend in conductivity. Although, at a snapshot in time, both blend structures appear co-continuous, the finite lifetime of composition fluctuations causes the structure to change constantly. The lifetime, τ, of these fluctuation is a function of the characteristic lengthscale, d, which scales as $\tau \sim d^2$ if the relaxation is diffusive. The domain spacing of the BμE morphology of the $\phi_H = 0.7$ blend is approximately two times larger than the characteristic lengthscale in the $\phi_H = 0.2$ blend, indicating that the BμE relaxes about four times more slowly. Previously, Morkved *et al.* found that in a structured ($f_a \approx -0.8$) and moderately viscous ($\eta \approx 5$ Pa·s) BμE consisting of polydimethylsiloxane (PDMS), polyethylethylene (PEE), and PDMS-*b*-PEE, monomer composition fluctuations exhibited a relaxation time of approximately 100 ms.[102] In contrast, composition fluctuations in disordered diblock copolymers appear to exhibit shorter relaxation times: Stepanek *et al.* found that at $T - T_{ODT} \approx 30$ °C, composition fluctuations in a poly(ethylene-alt-propylene)-b-PDMS block copolymer ($\eta \approx 0.4$ Pa·s) relaxed over a time scale of only 10 μs. In the current system, we expect that η of the conducting phase in $\phi_H = 0.7$ blends should be lower than that in $\phi_H = 0.2$, because higher ϕ_H leads to a lower average M and, thus η. Figure 3.7 indicated that η_0 of the blend in $\phi_H = 0.7$ blends is about half that of $\phi_H = 0.2$ blends. Thus, based on the literature values for relaxation times, and assuming that $\tau \approx \eta^{-1}$, the lifetime of composition fluctuations in the disordered, lightly diluted diblock is approximately 500 times shorter than for the BμE. As discussed above, the time scale of the AC conductivity experiments when blends are disordered is on the order of 10^5 to 10^3 s (Figure 3.17). Thus, during the conductivity experiments, it is possible that the

composition fluctuations in the disordered $\phi_H = 0.2$ blends are sufficiently short-lived that the ions effectively "see" only a sea of PEO. In contrast, the lifetime of composition fluctuations in the BμE may be so long that the structure of the morphology suppresses ion transport.

Other possible reasons for the difference in the conductivities of the disordered states can be considered. First, if the "dry brush" interface of the $\phi_H = 0.7$ blends also excluded salt, there would be a higher salt concentration in the PEO homopolymer phase (*i.e.* $r > 0.06$ in PEO homopolymer). However, Figure 3.23a indicates that this result would increase the conductivity, not lower it, so this does not explain the differences in disordered state conductivities. Alternatively, previous reports have suggested that interfacial mixing of the PS domain into the salt-doped PEO domain could also lead to a decrease in the conductivity.[71] However, in the current study, the strong scattering and "dry brush" interfaces suggest that interfacial mixing is minimized. Further, Figure 3.23b indicates that, even though a small amount of PS can lead to a noticeable reduction (*ca.* 25%) in conductivity, this alone cannot explain the experimentally measured order of magnitude difference. Finally, the PFG-NMR experiments detailed in Table 3.2 demonstrated that both the Li^+ and $TFSI^-$ ions diffuse more rapidly in the PEO homopolymer than in higher molecular weight PS-PEO block copolymers, thus indicating that the reduction in the conductivity with increasing homopolymer loading cannot be explained by a simultaneous decrease in the ion diffusion coefficients. This result is not surprising, as low molecular weight PEO is known to undergo Rouse diffusion when complexed with Li^+ ions, thereby enhancing the Li^+ diffusion coefficient.[71]

Ultimately, analysis of the current blends suggests that there is not a significant change in the local molecular environment in the blends as they are heated through their ODT, consistent with the suggestion by Lee *et al.* for diblock copolymers.[154] Instead, the ODT simply reflects the loss of long range order and melting of grains as the sample transitions from a LAM or HEX morphology to a structure that is locally correlated but globally disordered. To explore this in more quantitative detail, we will now consider the nature of the jump in the conductivity through the ODT.

Jump in the conductivity through the T_{ODT}

To consider the origin of the jump in the conductivity when blends are heated through T_{ODT}, we compare the ordered and disordered state conductivities.[74] Figure 3.22 shows that, at every blend composition, the disordered state provides higher conductivity than the ordered state. This difference can be quantified at any temperature of interest as the ratio of the disordered state conductivity, σ_{dis}, to the conductivity obtained by extrapolating the ordered-state VFT fit, σ_{VFT}. In Figure 3.29, we have plotted this ratio, $\sigma_{dis}/\sigma_{VFT}$, as a function of ϕ_H. Previously, it has been hypothesized that an increase in the conductivity at an ODT is primarily due to the sample transitioning from a tortuous, microstructured morphology, where τ = 1.5 and 3 for lamellar and hexagonally close-packed cylinders, respectively, to a homogeneously mixed disordered state, where τ = 1.[74] To a first approximation, then, the jump in conductivity at a given blend composition could be estimated by a linear combination of the volume fraction of the lamellar and hexagonal morphologies multiplied their respective tortuosities, given by

$$\sigma_{dis}/\sigma_{VFT} = 1.5\phi_{LAM} + 3\phi_{HEX} \tag{3.14}$$

We briefly note that this equation implicitly assumes that grain boundary resistance acts in series, whereas, in the limit of a direct current experiment, the resistance should act in parallel. In the current work, ϕ_{LAM} and ϕ_{HEX} were calculated from the SAXS scattering profiles and shown as a function of homopolymer loading in Figure 3.26a. The prediction for the jump in conductivity given by Equation 3.14 is shown along with the experimentally determined jump in Figure 3.29. Interestingly, the simple model presented in Equation 3.14 provides a reasonable qualitative prediction of the observed trend in the jump in conductivity through the ODT, which suggests that the jump in the conductivity is largely due to a loss of tortuosity as the samples disorder. However, the preceding analysis of the disordered state indicates that there is significant structure in the disordered state and that the samples are not homogeneously mixed.[154] Instead, the disordered state more likely resembles a co-continuous, tortuous

structure of PEO+LiTFSI and PS domains, as indicted by the fitting of the Teubner-Strey model to the SAXS data in Figure 3.27. Previous work has suggested that such co-continuous media exhibit a range of tortuosity from 1.5 to 3, which, coincidentally, is equivalent to the range of tortuosities predicted for a combination of LAM and HEX morphologies.[20,72,179] Thus, it is unlikely that there is a significant reduction in tortuosity as samples transition from an ordered to a disordered state in a temperature range near the ODT.

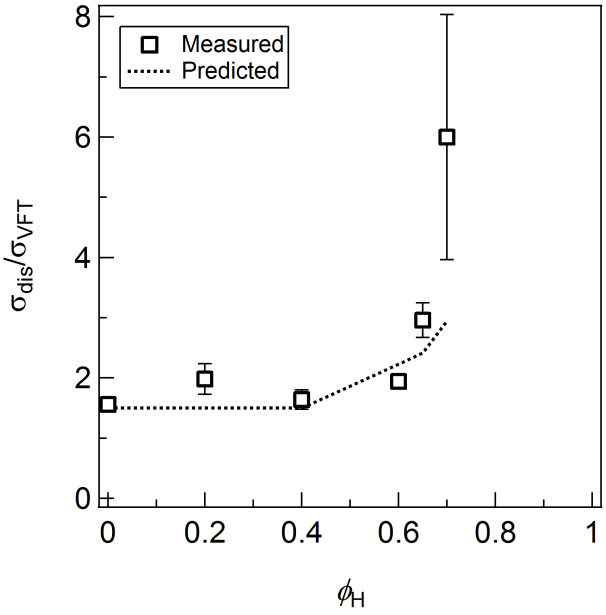

Figure 3.29: Comparison of the jump in conductivity relative to an extrapolation of the VFT fit for various blend compositions. The dashed line represents the predicted shift in conductivity given by Equation 3.14. The error bars represent a range of the values of the jump determined.

Although there is no significant change in tortuosity through the ODT, there is the removal of long-range ordering of the domains. We therefore suggest that the observed jump in conductivity is primarily the result of the removal of grain boundaries and, thus, increased phase continuity at temperatures above the ODT, as the sample transitions from a polycrystalline, ordered morphology to a disordered, yet highly fluctuating and co-continuous morpohlogy.[54] To roughly quantify the expected change in conductivity

upon removal of grain boundaries, we show a simplified model of three types of grain boundaries in Figure 3.30. Note that real grain boundaries would be a superposition of the three situations shown in the figure.

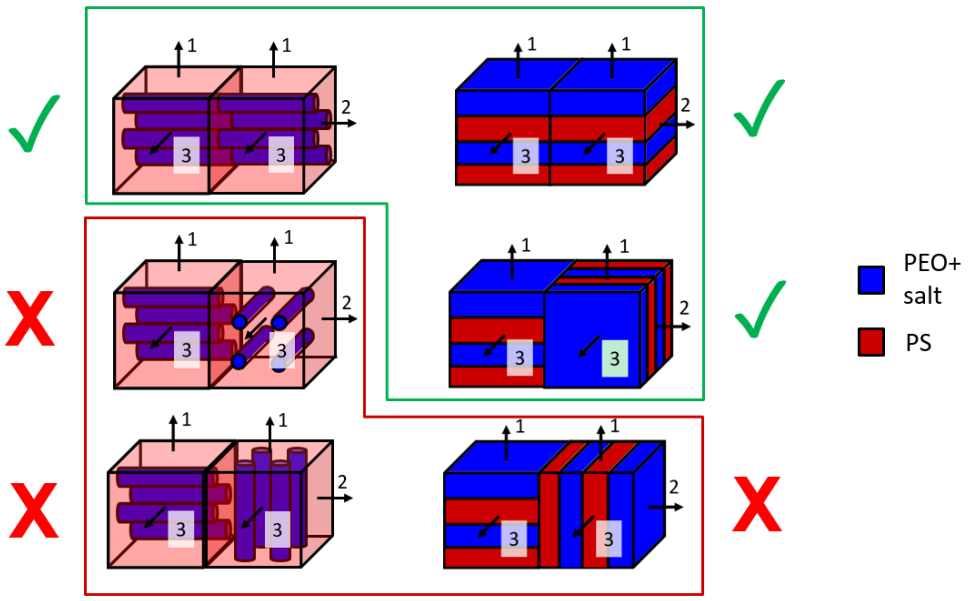

Figure 3.30: Schematic representation of how different grain orientations can lead to dead ends in conducting channels for morphologies consisting of cylinders and lamellae. Green check marks indicate continuous conducting channels, while red X's indicate dead ends. On average, only one out of three orientations is effective for cylinders, compared to two out of three for lamellae.

These simple illustrations suggest that, on average, only one out of three orientations lead to continuity of the conducting domain across grain boundaries in cylinders. On the other hand, grain boundaries only cut off one out of every three channels in lamellae-forming blends. When these blends are heated though the ODT, the grain boundaries are removed. Upon removal of grain boundaries, then, Figure 3.30 illustrates that the number of accessible, continuous conducting channels in cylindrical and lamellar morphologies would increase by a factor of 3 and 1.5, respectively, roughly consistent with the measured jump in conductivity through the ODT (Figure 3.29). We note that blends containing $\phi_H = 0.7$ exhibit approximately an order of magnitude jump

in conductivity when transitioning from LAM+HEX, which is majority (1-dimensional) HEX, to (3-dimensional) BμE, significantly larger than the factor of 3 predicted by Figure 3.30. However, the measured jump is consistent with previous work by Cho *et al.* that also found an approximately order of magnitude jump in conductivity when samples transitioned from HEX to gyroid, which suggests that the model of Figure 3.30 overstates the probability that 1-dimensional, minority phase structures will connect across grain boundaries. With this caveat, it is interesting to note that, although Equation 3.14 was derived to describe a jump in conductivity as a result of the removal of tortuosity, it could also be used to roughly describe a jump in conductivity due to removal of grain boundaries. Although the models in Figures 3.29 and 3.30 are simplistic, they appear to capture the experimental phenomena and are consistent with the scattering analyses that indicate the presence of significant structure in both the ordered and disordered states. Ultimately, the jump in conductivity through the ODT is almost certainly a result of macroscopic changes in the conducting channels *via* grain boundary removal, while the local molecular environment remains largely unchanged.

3.6 Conclusions

We have presented the phase behavior of pseudo-ternary polymer blends consisting of polystyrene (PS), poly(ethylene oxide) (PEO), a PS-PEO diblock copolymer, and lithium bis(trifluoromethane)sulfonamide (LiTFSI). A combination of SAXS and DMS were used to map out the morphologies and T_{ODT}s for blends along the volumetrically symmetric isopleth at a fixed salt concentration. The first surprising result is that the phase behavior of salt-containing PS/PEO/PS-PEO ternary polymer blends is broadly similar to that of traditional ternary polymer blend systems. The BμE channel splits the volumetrically symmetric isopleth into two separate zones: a diblock-rich region consisting of ordered, microphase separated morphologies, and a homopolymer-rich region in which homopolymers are macroscopically phase-separated. It is remarkable that the presence of LiTFSI acts to significantly increase the segregation strength of the blends without destroying the general features of a ternary polymer blend

system. In the diblock-rich region, blends exhibited a LAM to LAM+HEX transition with increasing homopolymer loading, likely due to the increasing influence of conformational asymmetry. At certain compositions, a pure lamellar morphology could only be formed for blends with unequal PS and PEO homopolymer loadings, which suggests that future studies on AB/A/B ternary polymer blends should consider blend morphologies away from the volumetrically symmetric isopleth where $\phi_A = \phi_B = \phi_H/2$. One such investigation is underway.[79] An increase in T_{ODT} with homopolymer loading and an immeasurably high T_c for the salt-doped PS/PEO homopolymer blend appeared to be due to a striking five-fold difference in the χ_{eff} for the PS/PEO homopolymers and for the PS-PEO block copolymer, possibly due to significant end group effects that increased the hydrophilicity of the PEO homopolymer. These results demonstrate that the nature of inter- and intramolecular interactions in these low molecular weight systems is not yet fully understood. This, paired with a still-developing understanding of how lithium salts affect the χ_{eff} of homopolymer blends and block polymers differently, indicates that there is still much more to be understood about these complex systems.

This work also presents an analysis of the evolution of ionic conductivity in the pseudo-ternary blend system. A key attribute of these blends is that they contain the same number of ethylene oxide, styrene, Li^+, and $TFSI^-$ units. The ordered state conductivity of the blends was found to decrease substantially with increasing homopolymer content, which was attributed to an increase in the fraction of dead ends in conducting channels as the fraction of HEX morphology in the blends increased and, potentially, greater intermixing of PS into the conducting domain. An analysis of the disordered states indicated that all blends exhibit a strongly segregated, “dry brush” interface that excludes homopolymer, while the decrease in the conductivity of the disordered blends with increasing homopolymer content may be due to dead ends in the BμE structure and the relatively long lifetimes of composition fluctuations in the BμE compared to those in the disordered state of diblock-rich blends. By comparing the structure of the ordered and disordered states, we suggest that the jump in conductivity through the ODT is primarily due to the removal of grain boundaries,

not a reduction in tortuosity as had been previously hypothesized. Taken together, these results confirm that disordered, microphase separated morphologies exhibit relatively better conductivity than polycrystalline morphologies with long-range order.

3.7 Acknowledgments

This research was supported by the National Science Foundation under awards DMR-01206459 (TPL) and DMR-1104368 (FSB). Portions of this work were performed at the DuPont-Northwestern-Dow Collaborative Access Team (DND-CAT) located at Sector 5 of the Advanced Photon Source (APS). DND-CAT is supported by Northwestern University, E.I. DuPont de Nemours & Co., and The Dow Chemical Company. This research used resources of the Advanced Photon Source, a U.S. Department of Energy (DOE) Office of Science User Facility operated for the DOE Office of Science by Argonne National Laboratory under Contract No. DE-AC02-06CH11357. X-ray scattering data was collected using an instrument funded by the National Science Foundation under Award Number 0960140. The authors thank Prof. Phillippe Bühlmann for allowing access to Solartron electrochemical impedance spectroscopy equipment.

Chapter 4

Polymer Electrolyte Membranes *via* Polymerization Induced Microphase Separation for Lithium Anode Batteries[i]

4.1 Introduction

The lithium-ion battery was brought to market in 1991, but despite the growing power and energy density demands of electronic devices, the next generation of this now aging technology has yet to be commercially realized.[1] Recent research has suggested there could be a 20-fold increase in the theoretical energy density of such batteries if the lithium metal oxide cathode that is currently used could be replaced with either sulfur or air.[2] Despite the huge gains that could be realized with these technologies, their design assumes the use of lithium metal as the anode. The challenge is that, when used as an anode material, lithium metal forms dendrites upon repeated cycling, which are needle-like structures that can span the electrolyte, shorting out the battery and

[i] This work was done in collaboration with Aaron P. Lindsay.

drastically reducing battery lifetime.[3]

In attempts to stabilize lithium metal anodes so that they can be used in rechargeable batteries, many research groups have been working to develop high-modulus polymer electrolytes that are able, at least in theory,[9] to suppress dendrite growth, while still providing sufficiently high conductivity for end user applications. As discussed in Chapter 3, significant research efforts have attempted to solve this materials design challenge through the use of microstructured polymer electrolytes, wherein one domain provides mechanical stability and toughness, while the other domain provides a channel through which ions can easily conduct. Previously, groups have targeted microstructured morphologies for electrolytes, such as lamellae[28,82] or hexagonally-packed cylinders.[46,180] However, one of the primary conclusions reached from the work detailed in Chapter 3 is that locally correlated, globally disordered, isotropic, and microphase separated morphologies provide better conductivity than polycrystalline block polymers with long-range order, wherein grain boundaries serve as dead ends in conducting channels.[130]

Globally disordered, but locally correlated systems have been the focus of significant recent work at the University of Minnesota. In 2012, Seo *et al.* developed a method in which microphase separated, disordered, and co-continuous polymeric materials could be kinetically trapped by cross-linking the morphology during polymerization-induced microphase separation (PIMS).[147] In 2014, Schulze *et al.* used this strategy to develop polymer electrolytes consisting of globally disordered, co-continuous networks of poly(ethylene oxide) and highly cross-linked polystyrene that demonstrated a record combination of high ionic conductivity and high modulus.[10] In this work, the polymer electrolyte was prepared through the reversible addition-fragmentation chain-transfer (RAFT) polymerization of styrene (S) and divinylbenzene (DVB) onto poly(ethylene oxide) (PEO), which was end-functionalized with a RAFT chain transfer agent (CTA) in the presence of, in some samples, an ionic liquid 1-butyl-3-methylimidazolium bis(trifluoromethylsulfonyl)imide (BMITFSI) and lithium bis(trifluoromethane)sulfonamide (LiTFSI). During the course of the reaction, the poly(S-*co*-DVB) block would grow both through propagation and cross-linking *via* the

pendant vinyl group of the DVB, ultimately resulting in a co-continuous, yet disordered microstructure due to an increase in the segregation strength of the system that led to large-amplitude composition fluctuations,[148] as previously described by Lee *et al.* for short diblock copolymers.[154] Since its inception, variations of this synthetic strategy have also been used to make hierarchically porous polymer monoliths[24] proton-conducting polymer electrolyte membranes,[56] and additional variations are currently under development.

As detailed in Chapter 3, disordered, co-continuous, yet microphase separated morphologies exhibit better transport properties than systems with long-range order and grain boundaries. One route to corroborating this assertion is to compare the ionic conductivity of the microstructured electrolyte to that of the pure conducting phase. If the only factors that reduce the conductivity of the microstructured electrolyte relative to the pure conducting phase and the volume fraction of the conducting phase in nanostrctured material, ϕ_{cond}, and the tortuosity, τ, of the ion-conducting domain, then the conductivity of the polymer electrolyte, $\sigma(T)$, would be related to the conductivity of the pure conducting phase, $\sigma_{\text{cond}}(T)$, by

$$\sigma(T) = \frac{\phi_{\text{cond}}\sigma_{\text{cond}}(T)}{\tau} \tag{4.1}$$

Using this analysis to compare the conductivity of BMITFSI-doped PEO homopolymer to the conductivity of the PIMS electrolyte, Schulze *et al.* demonstrated that the ionic conductivity of the PIMS system achieved the maximum theoretical value for a conducting phase with a tortuosity between 1.5 and 3,[10] which is typical for co-continuous, disordered media.[181] This result suggested that the conducting domains in the polymer electrolytes were continuous over length scales (*ca.* 0.1 – 1 μm, see Figure 3.17) probed by the alternating current (AC) impedance experiments with little to no dead ends that impede ion motion. Thus, the globally disordered structure served to maximize the ionic conductivity with high efficiency. Less clear, however, was the extent to which the elastic modulus (E') of the system was optimized. In the initial study, Schulze *et al.* found that, at 50 °C, electrolytes containing 21 vol% BMITFSI had an E' of 0.2 GPa, short of the 1 GPa that has been hypothesized to be necessary

to prevent the growth and propagation of lithium dendrites in battery applications.[9] In addition, although this study demonstrated that these polymer electrolytes had good mechanical and transport properties, no work was performed to test these polymer electrolytes in lithium battery applications.

To build upon the previous work on PIMS polymer electrolytes, this project aimed to both better understand the conditions under which optimal conductivity and mechanical properties could be achieved, while also assessing the ability of the polymer electrolytes to perform in battery applications by performing cyclic voltammetry, galvanostatic cycling, and battery cycling experiments. To this end, experiments were carried out at various molar ratios of styrene to DVB to qualitatively assess how cross-linking density affected ionic conductivity and mechanical properties. In order to prepare polymer electrolytes with the geometry necessary for use in batteries, a method was developed where the polymer electrolytes could be produced *in situ* inside coin cells. The electrochemical stability window, *i.e.* the voltage range over which the electrolyte is stable relative to lithium metal, of the polymer electrolytes was determined, and this stability window was used to develop a battery cycling procedure. Ultimately, both galvanostatic cycling and battery cycling experiments demonstrated that PIMS polymer electrolytes exhibit power delivery and lifetimes that are comparable to microstructured polystyrene-*block*-poly(ethylene oxide) block copolymers doped with LiTFSI.[182] The work detailed in this chapter has resulted in procedures and preliminary results that could be used to more rigorously study polymer electrolyte systems in the future.

4.2 Experimental Section

Materials

Styrene (99%) and divinylbenzene (80% para, 20% meta, technical grade) were purchased from Sigma-Aldrich (St. Louis, MO) and were passed through an activated alumina column prior to use to remove inhibitor. Lithium

bis(trifluoromethylsulfonyl)imide (LiTFSI) was purchased from 3M and used as received. 1-butyl-3-methylimidazolium bis(trifluoromethylsulfonyl)imide (BMITFSI) was synthesized according to a previously established procedure.[10] Because both BMITFSI and LiTFSI are highly hygroscopic, they were stored under vacuum when not being used. The radical initiator azobisisobutyronitrile (AIBN) was purchased from Sigma-Aldrich and recrystallized two times from methanol, then dried *in vacuo* overnight. Materials for coin cell preparation were purchased from MTI Corporation (Richmond, CA).

The poly(ethylene oxide) macro-chain transfer agent (PEO-CTA) was prepared by end-functionalizing a commercial PEO homopolymer according to an established procedure.[10] Briefly, poly(ethylene glycol) monomethyl ether was purchased from Sigma-Aldrich. The chain transfer agent, (*S*)-1-dodecyl-(*S*′)-(α,α'-dimethyl-α''-acetic acid) trithiocarbonate, was prepared according to an established procedure,[183] and it was attached to the hydroxyl-terminus of the PEO by means of an acid chloride intermediate to yield the PEO-CTA. During the course of end-functionalization reaction, the reaction mixture becomes highly viscous and filled with a significant quantity of solid products. Thus, in order to maintain good mixing throughout the course of the reaction, a mechanical stirrer was used. The successful attachment of the CTA to the PEO was confirmed by performing a test polymerization, wherein styrene, the PEO-CTA, and 0.05 molar equivalents of AIBN relative to the CTA were added to a reaction flask, then reacted at 120 °C for 24 hours. Size exclusion chromatography of the resulting product indicated a monomodal peak that was shifted to lower elution volumes relative to the unreacted PEO-CTA, indicating the formation of PEO-*block*-PS and, thus, the successful end-functionalization of the PEO-CTA. A summary of properties of the components used in this study is shown in Table 4.1.

Reaction mixture preparation

The reaction mixture was prepared with slight modifications to a previously established procedure.[10] PEO-CTA, styrene, divinylbenzene, LiTFSI, BMITFSI, and AIBN were

Table 4.1: Properties of components used in study.

Species	M_0 (g/mol)	M_n (kg/mol)	$Đ$	ρ at 140 °C (g/mL)	refs
PEO	44	5	1.11	1.064	140
P(S-*co*-DVB)	104	–	–	1.05	10
BMITFSI	419	–	–	1.329	184
LiTFSI	287	–	–	1.334	10

added to a custom-made 5 mL Schlenk flask. The solution was stirred at room temperature until homogeneous. The solution was then cycled through three successive freeze-pump-thaw cycles to degas the solution. The flask was then backfilled with argon gas prior to removing it from the Schlenk line. The composition of the reaction mixture for all samples is as follows: 25 vol% PEO-CTA, 54 vol% S + DVB monomers, and 21 vol% LiTFSI + BMITFSI. The relative amounts of S and DVB, and of LiTFSI and BMITFSI, were varied, as is detailed in the text. The radical initiator AIBN was added at 0.1 molar equivalents *vs* PEO-CTA to some, but not all, samples, as detailed in the text.

Preparation and synthesis of polymer electrolytes

Polymer electrolytes were prepared in three different geometries: in 5 mL reaction vials, as tensile bars in a hot press, and *in situ* in hermetically-sealed coin cells. The preparation of samples in reaction vials and as tensile bars has been the primary focus of prior investigation.[10,148] In this work, coin cells were prepared to (1) determine the robustness of the synthetic strategy and (2) allow for immediate determination of ionic conductivity after successful synthesis. The details of the preparation of each geometry are described below.

Preparation of samples in vials

Samples were prepared by transferring the reaction mixture to 5 mL vials equipped with a stir bar and reacting the mixture in an oil bath at 120 °C for 24 hours. After the reaction, the samples was removed from the vial by breaking the glass and recovering

the sample. Unfortunately, no photos were taken of these samples, but similar samples can be found in reference 185.

Preparation of tensile bars

To prepare tensile bars, a custom-built PTFE hot pressing mold was used. The PTFE hot pressing hold was fabricated in the machine shop of the College of Science and Engineering at the University of Minnesota. This mold consisted of three slots that could yield tensile bars that are 10 mm wide by 60 mm tall by 2 mm thick. A schematic of the mold is shown in Figure 4.1. rather than this mold, we considered making a dogbone-style tensile bar mold, but we were concerned that the brittle nature of the samples would lead to them fracturing more readily when being removed from the mold. The reaction mixture was carefully pipetted into each of the holes, then a flat PFTE sheet was placed on top. This mold was then placed between two metal plates, and the entire assembly was then placed into a hot press that had been preheated to 120 °C. The mold was then pressed at 4000 pounds of pressure and 120 °C for 24 hours. After the reaction was complete, the tensile bars were removed from the mold. However, the formation of bubbles or cracks in the samples caused the resulting tensile bars to be significantly smaller than their maximum possible dimensions.

Styrene and divinylbenzene are known carcinogens, and prolonged exposure to their vapors is a known health hazard. Thus, during all steps of the hot pressing, all researchers wore a respirator from 3M (St Paul, MN) that was equipped with 3M-brand organic vapor filter cartridges (type 6001). Further, no other researchers were allowed near the hot press during the course of the reaction.

Preparation of polymer electrolytes within coin cells

Polymer electrolytes were also prepared *in situ* within coin cells. All cells were prepared within an argon-filled glove box. The argon-filled 5 mL Schlenk flask that contained the reaction mixture was transferred into the globe box. The coin cell was then assembled by stacking together multiple components to fill the vertical space

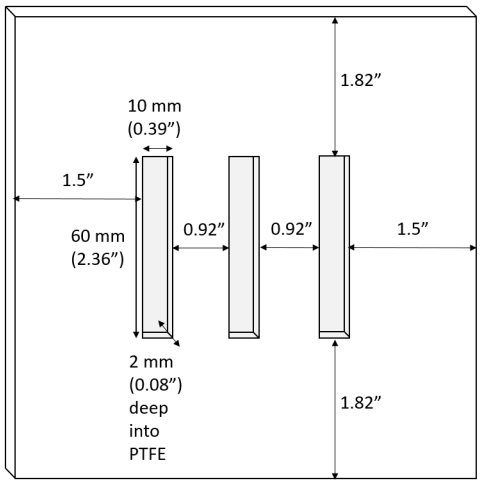

Figure 4.1: Schematic of hot pressing mold used to make tensile bars of the polymer electrolytes.

within the cell. All components were purchased from MTI Corporation, except as noted.

A typical cell assembly consisted of several steps. First, paper towels were laid down within the glove box to provide a clean surface. An anode case was then placed onto the clean surface. A metal wave spring (height, $h = 1.2$ mm; thickness, $t = 0.3$ mm) and four stainless steel spacers ($t = 0.2$ mm) were then placed in the case. The spacers were placed with the assistance of a vacuum pen. Next, a flat PTFE washer (7.1 mm inner diameter, 13 mm outer diameter, $t = 0.78$ mm), purchased from McMaster-Carr (Elmhurt, IL), was placed on top of the spacer. The reaction mixture was then added drop-wise to the middle of the washer until the volume inside the washer was filled and air bubbles had been removed. An additional four spacers were carefully placed on top of the washer, and the assembly was moved to the bottom half of the crimping die. Finally, the cathode case was placed on top of the cell assembly, the top half of the crimping die was placed on top of the cell assembly, and the cell was crimped using a coin cell crimper (Economical coin cell crimper, from BT Innovations, Nova Scotia, Canada). The cell assembly is shown schematically in Figure 4.2.

The cells assembled in this study are 2032 coin cells, which indicates that the final, crimped cell has a diameter of 20 mm and a thickness of 3.2 mm. Prior to crimping, the

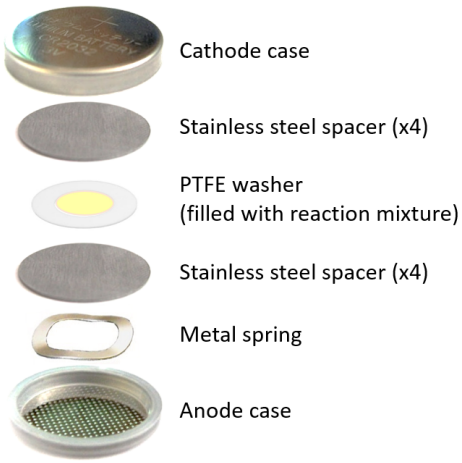

Figure 4.2: Schematic detailing the assembly of a symmetric coin cell with stainless steel electrodes. The polymer electrolyte is polymerized within the PTFE washer after assembly.

total thickness of all components was 3.6 mm, indicating that the components within the cell compressed by 0.4 mm during crimping. The most flexible component of the cell assembly is the metal wave spring; thus, the spring is compressed to 2/3 of its original height during the crimping. This spring compression provides the pressure necessary to prevent the reaction mixture from leaking out of the washer during the course of the reaction and helps to maintain good contact with the stainless steel spacers, which, during impedance experiments, act as the electrodes. A cross-section of the assembly of the coin cells is shown schematically in Figure 4.3.

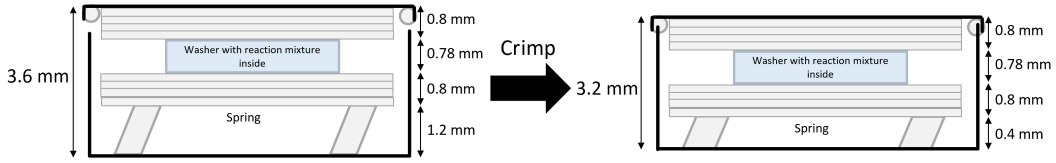

Figure 4.3: Cross-sectional schematic of the cell before and after crimping. The thickness of the cell decreases during crimping by compressing the metal spring. This compression serves to "seal" the reaction mixture and maintain contact between the stainless steel electrodes.

After crimping, cells were removed from the glove box and transferred to an oven,

where they liquid reaction mixture was polymerized at 120 °C for 24 hours. The cells were then removed from the oven and ready for testing in electrochemical impedance spectroscopy experiments.

Dynamic mechanical spectroscopy (DMS)

In order to study linear viscoelastic properties, DMS analysis was performed on the tensile bars *via* a 3-point bending test using a TA RSA-G2 (TA Instruments). Strain sweeps were first performed to determine the linear viscoelastic range. Frequency sweeps were then performed using linear strains to determine the elastic (G') and loss (G'') moduli as a function of frequency from 0.1 rad/s to 100 rad/s. These frequency sweeps were performed at fixed temperatures between 30 °C and 150 °C, spaced 10 °C apart.

Tensile testing

In order to probe the relationship between cross-linker content and mechanical toughness, strain-to-break experiments were performed at a strain rate of 1 mm/s on a Shimadzu tensile tester equipped with rubber grips. Due to the brittle nature of the samples, a unique sample loading procedure was developed. The Shimadzu tensile tester is equipped with pneumatic grips that hold the sample in place. Initial experiments found that, using the default pressure settings, the grips would cause the samples to fracture immediately upon loading. In order to avoid this problem, the pressure applied by the grips was decreased by about 75% during the sample loading process, then increased gradually to ensure the sample would not slip during the experiment.

Unfortunately, despite the steps taken to carefully load the sample, most samples tested would either slip or crack in the grips during the tensile test. A picture of a sample that has cracked in the grips is shown in Figure 4.4. In the picture, there is evidence of at least three cracks: two vertical cracks that have propagated from the grips, and one horizontal crack that extends to the right side. These macroscopic defects result

in strain-at-breaks that are significantly lower than would be expected for defect-free samples.

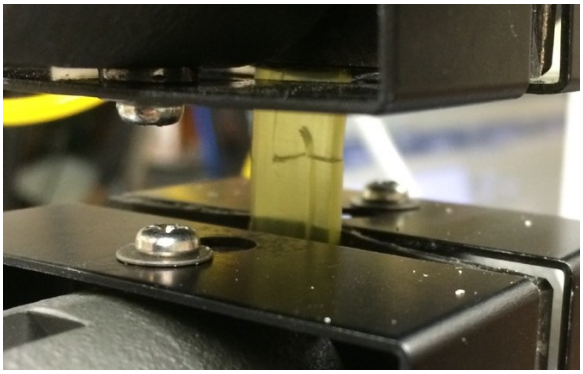

Figure 4.4: Sample containing 4:6 [DVB]:[S] that shows clear evidence of cracking, leading to premature sample failure.

Small angle X-ray scattering (SAXS)

SAXS experiments were conducted at DND-CAT's sector 5-ID-D of the Advanced Photon Source at Argonne National Labs. Monoliths were prepared and placed onto Kapton tape and analyzed at room temperature. 2D scattering patterns were collected on a Pilatus 2M area detector. The resulting isotropic scattering patterns were azimuthally integrated to give the scattered intensity as a function of the magnitude of the wavevector $|\mathbf{q}| = 4\pi\sin(\theta/2)/\lambda$, where θ is the scattering angle and λ is the nominal beam wavelength.

Thermal gravimetric analysis (TGA)

TGA was performed on neat, salt-free polymers to determine the upper working temperature limit for further analysis. Approximately 2 mg of polymer was loaded into a platinum pan and placed in a TA Instruments Discovery TGA, and the sample was heated at a rate of 10 °C/min to 400 °C under a nitrogen environment. The weight loss was recorded as a function of temperature.

Differential scanning calorimetry (DSC)

DSC analysis was performed using a TA Instruments Discovery differential scanning calorimeter. Samples were loaded into hermetically-sealed T-zero pans, and the sample was heated to 155 °C, then cooled to –90 °C, all at a temperature ramp rate of 10 °C/min. The heat response was then measured during the second heating from –90 °C to 155 °C.

Electrochemical impedance spectroscopy (EIS)

Electrochemical impedance spectroscopy was performed using a Solartron 1255B frequency response analyzer connected to a Solartron SI 1287 electrochemical interface. Samples were either prepared by either sanding to a uniform thickness of approximately 300 μm, then sandwiching between two stainless steel electrodes, or by directly testing coin cells wherein the polymer electrolyte was polymerized *in situ*, as described above. In either case, the samples were loaded into a custom-built heating block. The sample was heated to 150 °C, then cooled to 30 °C, then finally brought back to 150 °C, all in steps of either 10 or 20 °C, and annealed at each temperature for 1 hour prior to the measurement. The impedance (Z' and Z'') was measured as an oscillatory voltage of amplitude 100 mV was applied at frequencies from 1 Hz to 1 MHz. The bulk resistance, R, was determined by extracting the high-frequency plateau value of the in-phase component of the impedance, Z', and R could then be used to calculate the conductivity *via* $\sigma(T) = l/[R(T) \times a]$, where the superficial area, a, and thickness, l, were determined based on the sample geometry, which was either assessed prior to the start of the experiment (sanded samples) or determined by opening the coin cells after the end of the experiment (coin cells).

Lithium iron phosphate cathode preparation

A $LiFePO_4$ cathode was prepared in a fume hood on nickel foil as previously described.[182] Briefly, carbon black (Super P carbon, 80 wt%), lithium iron phosphate

($LiFePO_4$, 10 wt%) and poly(vinylidene fluoride) (10 wt%), which acts as a binder, were combined in a mortar and pestle and ground by hand for 5 minutes. The solids were the combined with the solvent *N*-methyl-2-pyrrolidone (NMP) and ground together to obtain a viscous slurry. The resulting slurry was then cast onto a sheet of electrochemical-grade nickel foil using a doctor blade. The solution was dried overnight in the fume hood, then further dried by heating the film in vacuum at 90 °C for an additional night. The cathode was then punched out of the nickel foil, and the thickness of the cathode was determined for every sample prior to cell assembly.

Preparation of coin cells with active cathodes and/or anodes

After assessing the structure, mechanical properties, and ionic conductivity of the polymer electrolytes, experiments were carried out to assess how well the electrolytes fabricated in this study would perform in battery applications. For these studies, the polymer electrolytes were prepared *in situ* in coin cells, as described earlier in the Experimental section. The polymer electrolyte, contained within the PTFE washer, was then removed from the coin cell, and the free-standing samples was transferred to the argon-filled glove box. Coin cells were then assembled in nearly the same fashion as described in the above section, but an anode or cathode material other than stainless steel was used, depending on the desired experiment. For example, symmetric lithium coin cells were prepared for galvanostatic cycling. This was done by placing a metal spring and four 0.2 mm thick stainless steel spacers into an anode case, then placing lithium foil (MTI Corporation) on top of the stack of spacers. The malleability of lithium metal provided good adhesion between the lithium and the stainless steel. The already-prepared polymer electrolyte was then placed on top of the lithium metal, and an additional layer of lithium metal was placed on top of the washer. In order to prevent the cell from short-circuiting, both sheets of lithium metal were trimmed so that they did not extend past the edge of the washer. Because initial experiments demonstrated that the lithium metal reacts with the PTFE washer, later experiments were conducted so that only the polymer electrolyte is in contact with the lithium metal foil. In these

experiments, the PTFE washer was cut into three pieces and placed around, but away from, the polymer electrolyte. The use of the PTFE as a spacer material was found to be necessary to prevent the polymer electrolyte from cracking when the coin cells were crimped. Finally, once all components were placed, four additional spacers and the cathode case were added to the top of the sample, and the cell was crimped. After completion of any desired experiment, post-mortem analysis was always performed by only opening the coin cell inside the glove box, as lithium metal can react violently with oxygen.

Coin cells for battery cycling were prepared in a similar manner, but a $LiFePO_4$ cathode was placed on top of the polymer electrolyte instead of a second lithium metal chip. Schematics that detail the assembly of both symmetric lithium cells and asymmetric battery cells are shown in Figure 4.5.

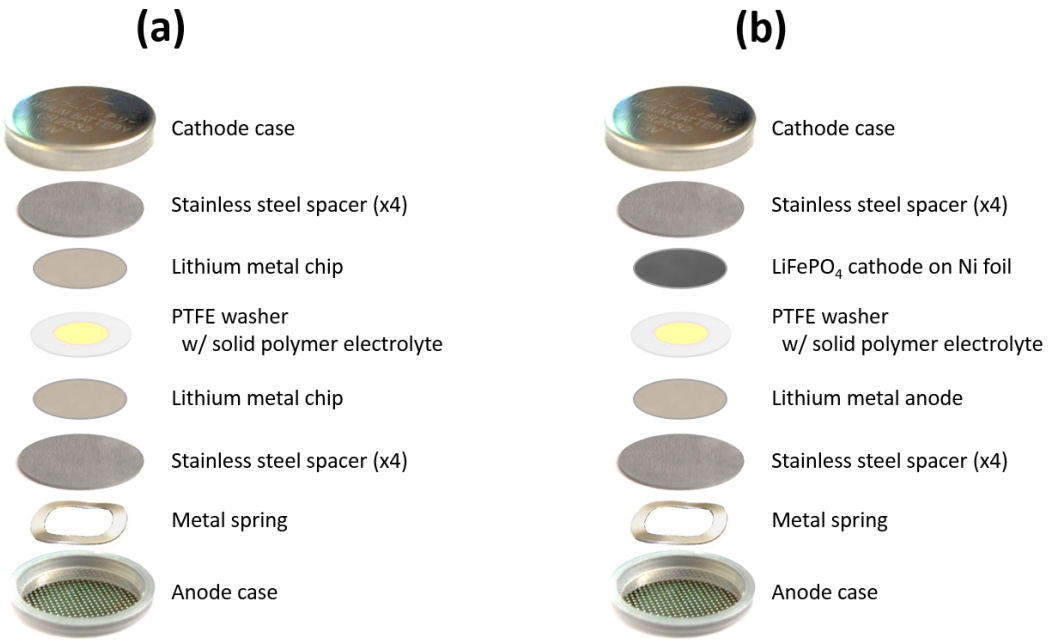

Figure 4.5: Schematic detailing the assembly of (a) the symmetric lithium metal coin cells and (b) the battery cells fabricated for this study.

Cyclic voltammetry

In order to determine the electrochemical stability window of the polymer electrolytes, cyclic voltammetry experiments were conducted on asymmetric lithium/stainless steel coin cells at room temperature. These cells were assembled as shown in Figure 4.5a, but with a lithium metal chip on only one side of the PTFE washer. The majority of the cyclic voltammetry experimental procedure was developed through personal communication with Dr. Didier Deveaux, who recently published the details of this method.[6] Additional details were developed by referencing work by Hallinan *et al.*[182]

The electrochemical stability window was determined by cycling the voltage three times each from 0.5 to 3.8 V, then 0.5 to 4.0 V, then –0.5 to 4.2 V, then finally –0.5 to 4.2 V, all *vs.* Li/Li^+, at a rate of 10 mV/s, with 45-minute rest periods between each cycle.

Galvanostatic cycling

Galvanostatic cycling experiments were performed on symmetric lithium coin cells assembled as shown in Figure 4.5a. The purpose of this test is to determine how much current can be passed through the polymer electrolyte and onto the lithium electrodes prior to failure, likely due to lithium dendrite formation. The cells was first subjected to 9 break-in cycles, wherein a current density of 11 $\mu A/cm^2$ was passed through the cell. The direction of current flow was reversed every 4.75 hours. After the break-in cycles, a current density of 36 $\mu A/cm^2$ were passed through the cell, with the current flow again being reversed every 4.75 hours. This process was continued until there was a sudden change in the cell voltage, a sign of cell failure.[182]

Battery testing

Batteries were assembled as shown in Figure 4.5b. The battery cycling procedure used in this study was developed by referring to the procedure used by Hallinan *et al.* in the Balsara lab at the University of California at Berkeley.[182] Each battery cycle consisted

of the following six steps:

1. Apply a constant current density until the cell reaches a desired cut off voltage. This cut off voltage is based on the upper limit of stability based on the assessment of the electrochemical stability window. A typical upper value is 3.7 V *vs.* Li/Li^+.
2. Maintain the cell potential at the upper cut off voltage until the current density diminishes. At this point, the battery is now charged.
3. Track the open circuit voltage (OCV) of the cell, *i.e.* the voltage of the cell in the absence of any applied potential, for 1 hour. During this time, capacitive overpotentials and concentration gradients will dissipate, restoring voltage toward $E_{eq} \approx 3.4$ V.
4. Discharge at constant current density until voltage reaches the lower cut off voltage (2.5 V).
5. Hold cell at 2.5 V to fully complete discharging.
6. Track OCV as system re-equilibrates to the initial cell potential.

Each of the charging steps was performed at a current of 50 μA. The battery for this study contained 0.56 mg of the active material $LiFePO_4$ in the cathode, which has a capacity of 170 mAh/g.[182] Therefore, the current used corresponds to a charging rate of C/1.9, *i.e.* using a current of 50 μA, the battery will charge in 1.9 hours. This procedure, along with the voltage and current, have been plotted and labeled as a function of time for a typical cycle in Figure 4.6.

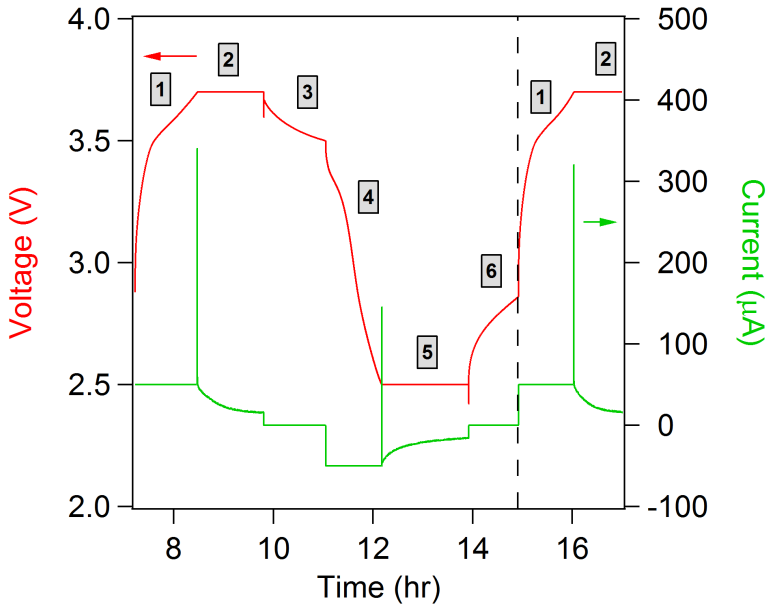

Figure 4.6: Typical charge-discharge battery cycle, with each of the six steps labeled. The dashed line represents the start of the next cycle.

4.3 Results

This work aimed to accomplish three goals: (1) determine the concentration of DVB cross-linker that optimizes and maximizes both ionic conductivity and mechanical properties, (2) develop a route to generating solid polymer electrolytes *in situ* inside of coin cells, and (3) determine the performance of these polymer electrolytes for use in battery applications by developing and using new testing methods. This results section will first focus on the how the properties of the polymer electrolytes vary when prepared in different geometries, then will discus the experiments performed to quantify electrolyte performance in batteries.

The first aim of this work was to determine what ratio of the DVB cross-linker to the styrene in the initial reaction mixture optimizes the ionic conductivity and structure of the polymer electrolytes. This study is closely related to work by Schulze *et al.* and McIntosh *et al.*, who previously reported on the evolution of structure and conductivity

of polymer electrolytes made from a reaction mixture of 25 vol% 5 or 28 kg/mol PEO-CTA, 21 vol% BMITFSI (which, for some samples, was doped with LiTFSI), and 54 vol% of DVB cross-linker and styrene (S) monomer at a molar ratio of 1:4 (*i.e.* [DVB]:[S] = 2:8).[10,148] Although the ionic conductivity of the polymer electrolytes prepared in that work achieved the theoretical maximum value,[10] the elastic modulus of the electrolytes was less than the 1 GPa that has been posited to be as necessary to prevent the growth of lithium dendrites in batteries with a lithium metal anode.[9] Thus, in the current work, we have attempted to improve the mechanical properties of the polymer electrolytes by varying the molar ratio of DVB to S from [DVB]:[S] = 1:9, 2:8, 3:7, and 4:6; these molar ratios correspond to overall DVB incorporations of 6, 13, 19, and 25 vol%, respectively. For this work, we use a 5 kg/mol PEO-CTA, as previously detailed by McIntosh *et al.*[148] As described in the Experimental Section, the volume of the insulating phase was held constant at 54 vol% (*i.e.* $\phi_{\mathrm{DVB}} + \phi_{\mathrm{S}} = 0.54$), and the conducting phase consists of 25 vol% PEO-CTA and 21 vol% LiTFSI and BMITFSI. The concentration of LiTFSI in the BMITFSI was varied between 1 and 2 M. In previous chapters, the concentration of LiTFSI was defined as $r = [\mathrm{Li}]/[\mathrm{EO}]$; 1 and 2 M of LiTFSI in BMITFSI correspond to $r = 0.04$ and 0.07, respectively. A summary of samples prepared for this study is given in Table 4.2.

Throughout most experiments, the radical initiator AIBN was not used, as there was some concern that it would lead to bubble formation inside the electrolytes. As will be shown soon, this worry was largely unfounded, and AIBN was found to be necessary to produce well-structured systems.

Table 4.2: Summary of samples prepared for study of DVB and LiTFSI variations

Sample geometry		[DVB]:[S]	LiTFSI in BMITFSI (M)
From vial	Without AIBN	1:9	neat
		2:8	neat
		3:7	neat
		4:6	neat
Tensile bars	Without AIBN	1:9	neat
		2:8	neat
		3:7	neat
		4:6	neat
	With AIBN	2:8	neat, 1 M, 2 M
Coin cells	Without AIBN	1:9	neat, 1 M
		2:8	neat, 1 M
		3:7	neat, 1 M
		4:6	neat, 1 M
	With AIBN	2:8	neat, 1 M, 2 M
		4:6	neat, 1 M

Morphology

The structure of the polymer electrolytes was assessed by a combination of direct observation and small-angle X-ray scattering (SAXS) to assess macroscopic defects and the microscale morphology, respectively. Representative images of coin cells prepared without AIBN, a radical initiator, at various DVB loadings, and with 1 M LiTFSI dissolved in the BMITFSI, are shown in Figure 4.7.

Perhaps the most striking feature of the samples prepared in coin cells is the presence of large, macroscopic heterogeneities. Some regions contain or are covered by a white powder, while other regions are entirely empty. Although it would be natural to believe that the white powder is simply LiTFSI solid that has crashed out of solution, this white powder also appeared in samples prepared without LiTFSI. Thus, the white powder is likely polystyrene homopolymer that polymerized *via* thermal radical initiation and subsequent prorogation. The presence of this white powder, which appears to be the result of macroscopic phase separation of the PS homopolymer from the PEO-rich phase, is most pronounced in samples containing 1:9 and 2:8 [DVB]:[S],

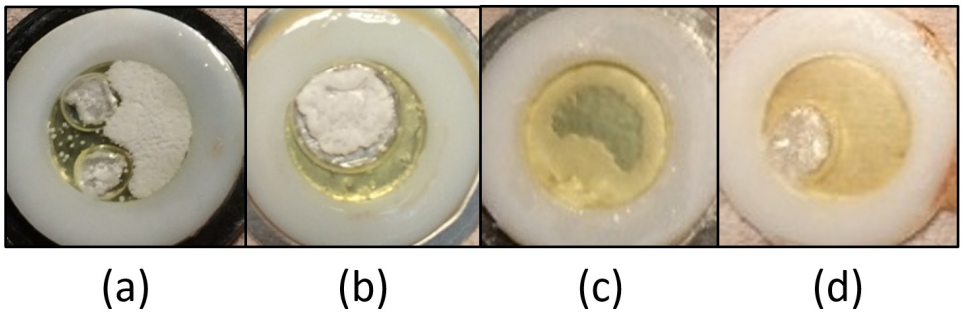

Figure 4.7: Photographs of representative samples prepared in coin cells with 1 M LiTFSI in the BMITFSI and without AIBN. Each sample is surrounded by a PTFE washer. Samples contain different amounts of DVB relative to the styrene loading, [DVB]:[S] of (a) 1:9, (b) 2:8, (c) 3:7, and (d) 4:6.

while samples with 4:6 [DVB]:[S], with significantly more cross-linker, are visually more homogeneous. Note that this phase separation phenomenon seen in Figure 4.7 was not systematically observed when the reaction was instead carried out in vials, which could be mixed during the reaction. This issue of phase separation in samples prepared without AIBN, which had a dramatic effect on all other properties of the polymer electrolytes, will be discussed further in the Discussion section.

For a point of comparison, representative images of samples prepared with 1M LiTFSI and 0.1 *eq*. of AIBN relative to PEO-CTA are shown in Figure 4.8. Even at relatively low DVB concentrations, AIBN appears to lead to significantly better controlled samples. Again, AIBN was initially not included in the reaction mixture due to concerns that it would lead to bubbles within the polymer electrolytes, but direct visual observation of the samples suggests that the inclusion of AIBN was necessary to produce a macroscopically homogeneous sample.

Beyond using visual observation to assess the macroscopic features of the sample, SAXS analysis was used to probe the microstructure of these polymer electrolytes. In samples that exhibited macroscopic phase separation, the transparent and yellow regions were analyzed. Representative SAXS data for several sample formulations and configurations are shown in Figure 4.9.

The SAXS data for all sample compositions, regardless of DVB content, exhibit a

Figure 4.8: Photographs of representative samples prepared in coin cells with 1 M LiTFSI and 0.1 *eq*. of AIBN relative to PEO-CTA. The sample in (a) is surrounded by a PTFE washer. Samples contain a loading of [DVB]:[S] of (a) 2:8 and (b) 4:6. On the left of (b), there is a bubble that may be due to the reaction mixture leaking from the cell during the reaction.

single, broad peak at q^*, with some samples exhibiting a higher order peak at $2q^*$. These scattering features are indicative of a highly correlated, but disordered, morphology. Interestingly, the scattering features found in these solid polymer electrolytes is strongly reminiscent of a polymeric bicontinuous microemulsion (BμE), which was discussed in great detail in Chapters 1 and 3, even though these samples were not derived from a blend of a block copolymer and two corresponding homopolymers. Based on this similarity to BμE systems, it was possible to quantitatively assess the level of structure in these systems by fitting the data were fit with the Teubner-Strey model for microemulsions:

$$I(q) = \frac{1}{a_2 + c_1 q^2 + c_2 q^4} \tag{4.2}$$

where $I(q)$ is the background-subtracted scattered intensity and a_2, c_1, and c_2 are fitting parameters.[100] From this model, the domain spacing, d, correlation length, ξ, and amphiphilicity factor, f_a, can be calculated as described in Chapter 1 using Equations 1.5, 1.6, and 1.7. In Figure 4.11, the average structural characteristics calculated for samples prepared from both vials and tensile bars are shown. Note that these calculated parameters represent the average value obtained from fitting at least two scattering traces, while the error bars represent the range of the values obtained.

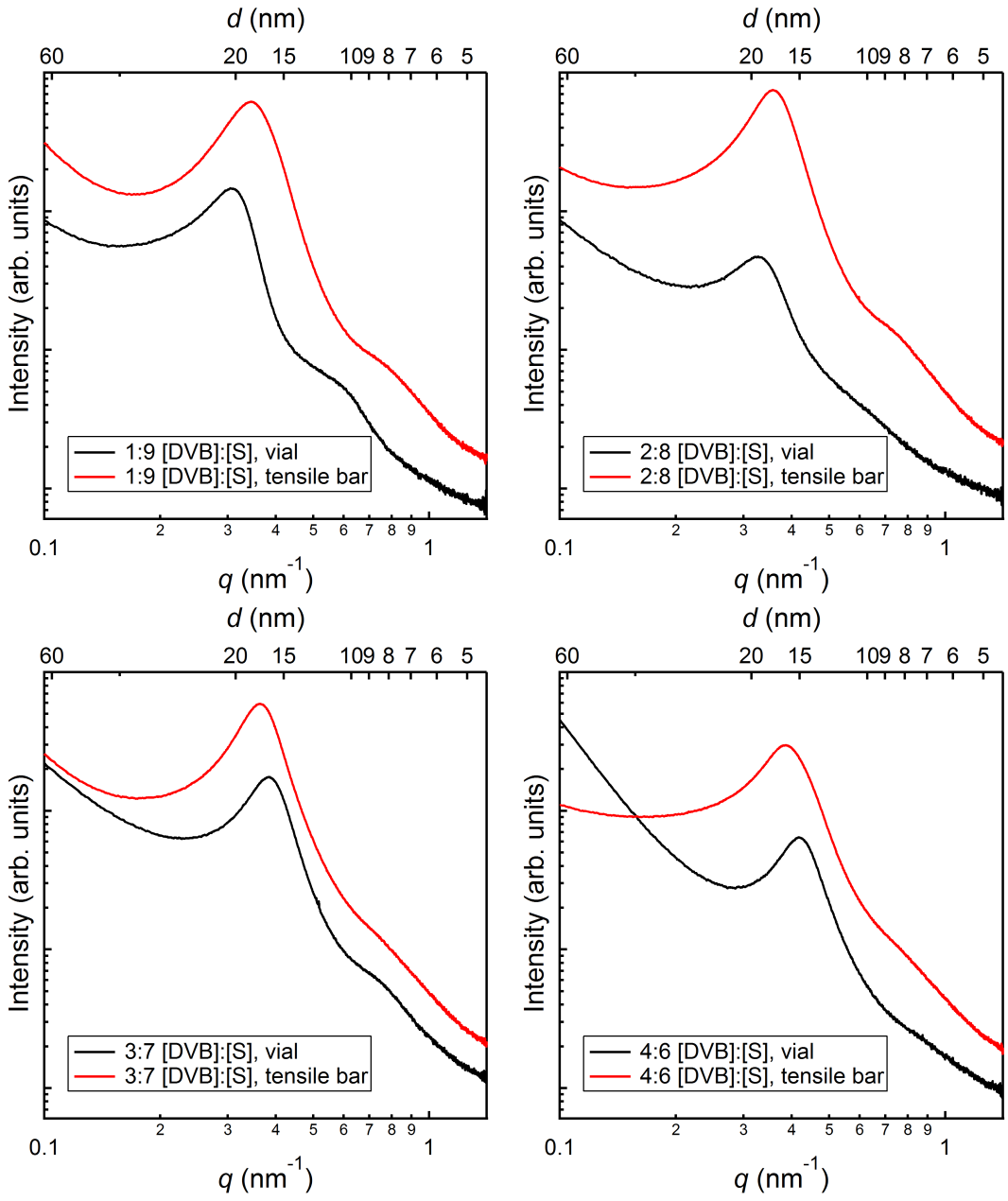

Figure 4.9: 1-D SAXS patterns for samples prepared with a variety of DVB concentrations relative to styrene. Comparison is between samples prepared in a vial and as a tensile bar.

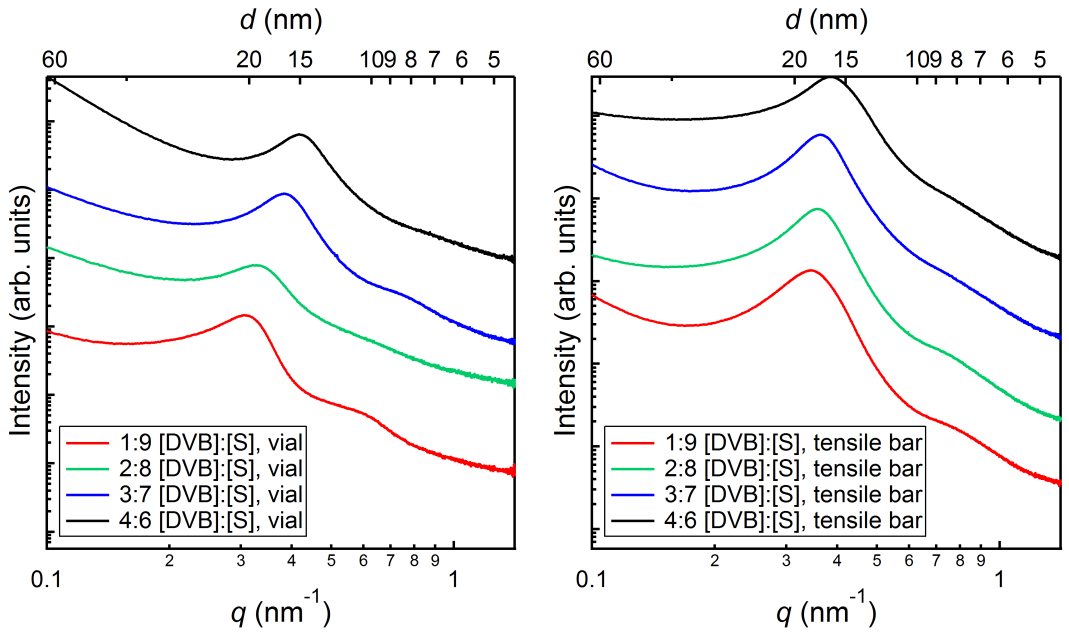

Figure 4.10: 1-D SAXS patterns for samples prepared with a variety of DVB concentrations relative to styrene. Comparison is between (a) samples prepared in a vial and (b) as a tensile bar.

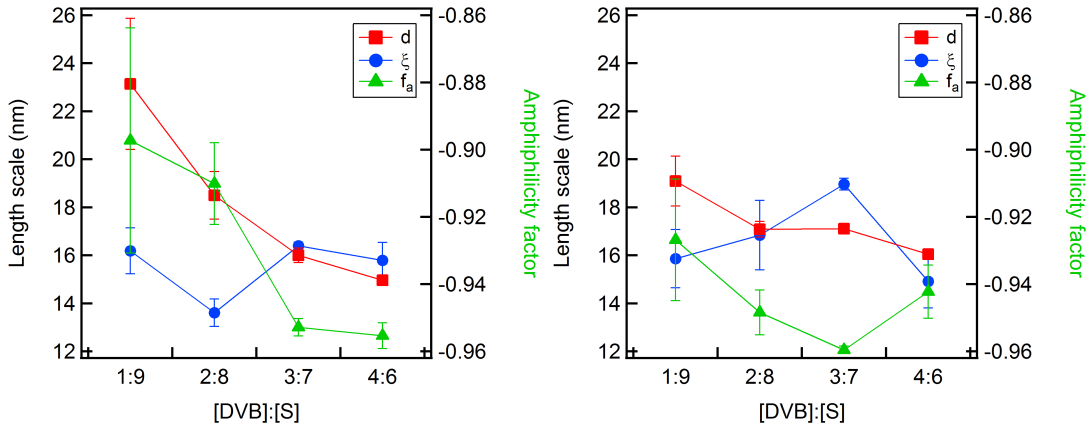

Figure 4.11: Structural characteristics derived from fitting SAXS data from samples prepared (a) in vials and (b) as tensile bars. Error bars represent the range of values calculated from the scattering traces of at least two samples.

Thermal stability

TGA was performed on tensile bars prepared with various DVB loadings to assess the thermal stability of the polymer electrolytes. The results of these experiments are shown in Figure 4.12.

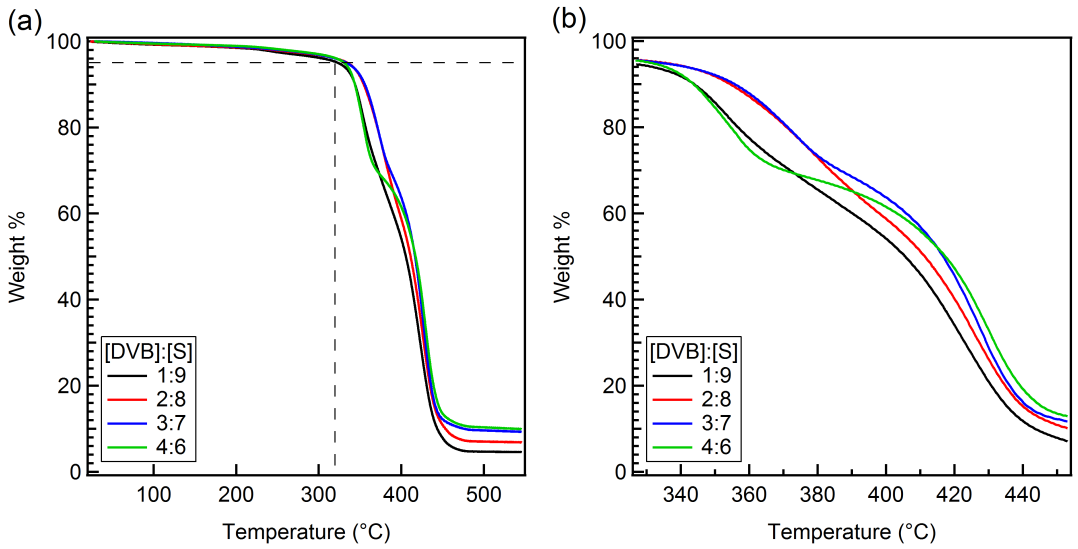

Figure 4.12: TGA of polymer electrolytes prepared as tensile bars. The graph in (a) has dashed lines to indicates the temperature at the weight loss totaled 5%. (b) is a zoomed view of (a) that shows the remaining degradation of the samples.

TGA indicates that the samples are thermally stable at temperatures of interest for battery applications (*ca.* 30 °C to 150 °C). The samples lose 5% of their mass when heated to approximately 300 °C. This weight loss may correspond, in part, to unreacted styrene and DVB monomer evaporating from the sample. The zoomed view of the data in Figure 4.12 indicates that the samples exhibit two degradation events: one centered at about 360 °C that results in 25 wt% loss, and another one centered around 420 °C that leads to approximately 65 wt% loss. Based on the sample composition, the first degradation event likely corresponds to removal of PEO, while the second indicates degradation of the BMITFSI and P(S-*co*-DVB).

Mechanical properties

The results of dynamic mechanical spectroscopy (DMS) analysis of tensile bars without AIBN or LiTFSI, performed using 3-point bending tests, are shown in Figures 4.13, 4.14, and 4.15. Note that all data have been superposed using the principle of time-temperature superposition (tTS). Although this method only rigorously applies for a homogeneous, single component system,[26] the cross-linked polystyrene phase is anticipated to dominate the mechanical response. Note that data for blends containing [DVB]:[S] of 1:9 could not be collected, as the blends had insufficient cross-linking to prevent the sample from sagging at room temperature in the 3-point bending fixture. The shift factors for these data were obtained by shifting the E' data visually to allow the data to overlap. Determining the shift factors by shifting on $\tan(\delta)$ was also attempted, but the data were too noisy for any significant analysis. Ultimately, as shown in Figure 4.15, the shifted data for E'' and $\tan(\delta)$ obtained from shifting on E' appear to describe the data reasonably well. Data for E'' $\tan(\delta)$ are only shown for the tensile bars containing [DVB]:[S] = 4:6, which had the least amount of macroscopic phase separation, as indicated in Figure 4.7. The shift factors were fit with the Williams–Landel–Ferry equation, given by

$$\log(a_{\mathrm{T}}) = \frac{-C_1(T - T_{\mathrm{r}})}{C_2 + (T - T_{\mathrm{r}})} \tag{4.3}$$

where T is the temperature, T_{r} is the reference temperature about which the data have been shifted (here, 30 °C for all samples), and C_1 and C_2 are empirical fitting constants. Note that the 3-point bending tests were performed on tensile bars that were not prepared with AIBN, and there was evidence of some macrophase separation that occurred during the polymerization of the tensile bars. Thus, the data in this section should be regarded as preliminary.

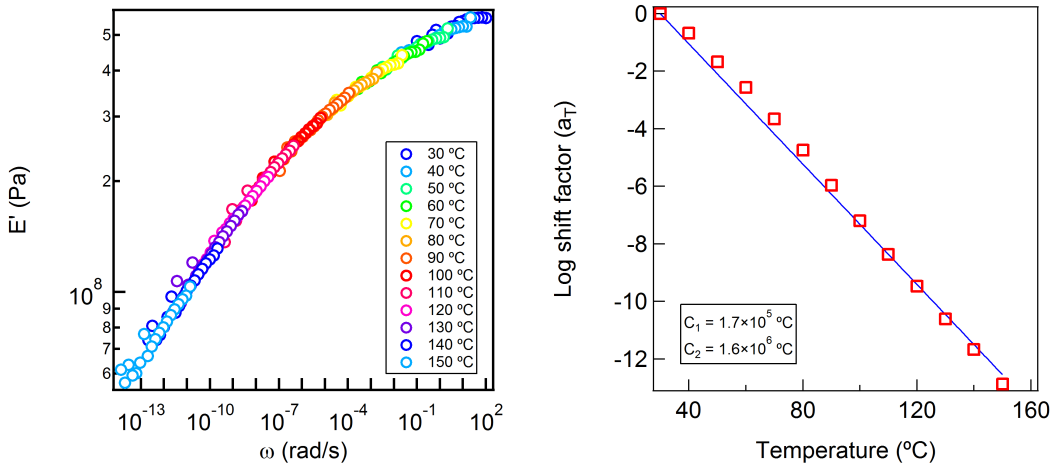

Figure 4.13: (a) Time-temperature superposition of E' *vs* shifted frequency for a tensile bar with [DVB]:[S] of 2:8. (b) Shift factors used to shift the data in (a) (T_r = 30 °C).

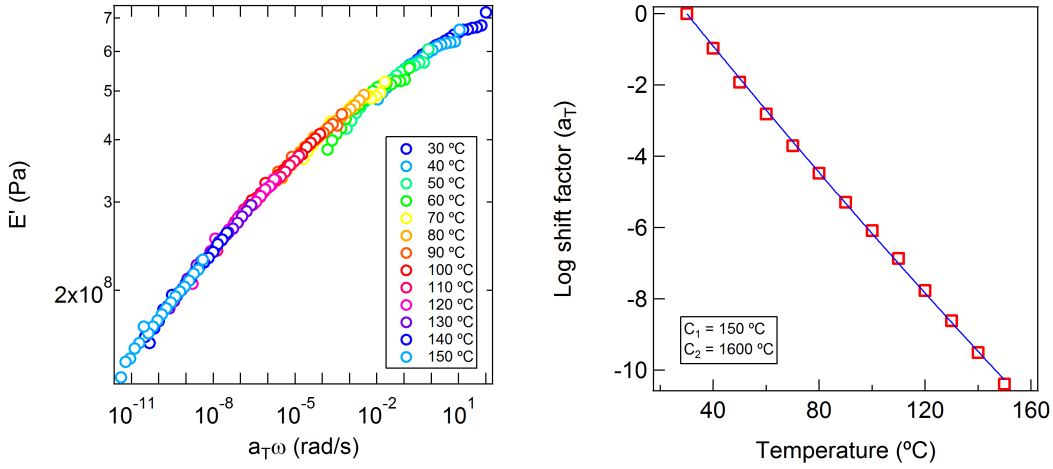

Figure 4.14: (a) Time-temperature superposition of E' *vs* shifted frequency for a tensile bar with [DVB]:[S] of 3:7. (b) Shift factors used to shift the data in (a) (T_r = 30 °C).

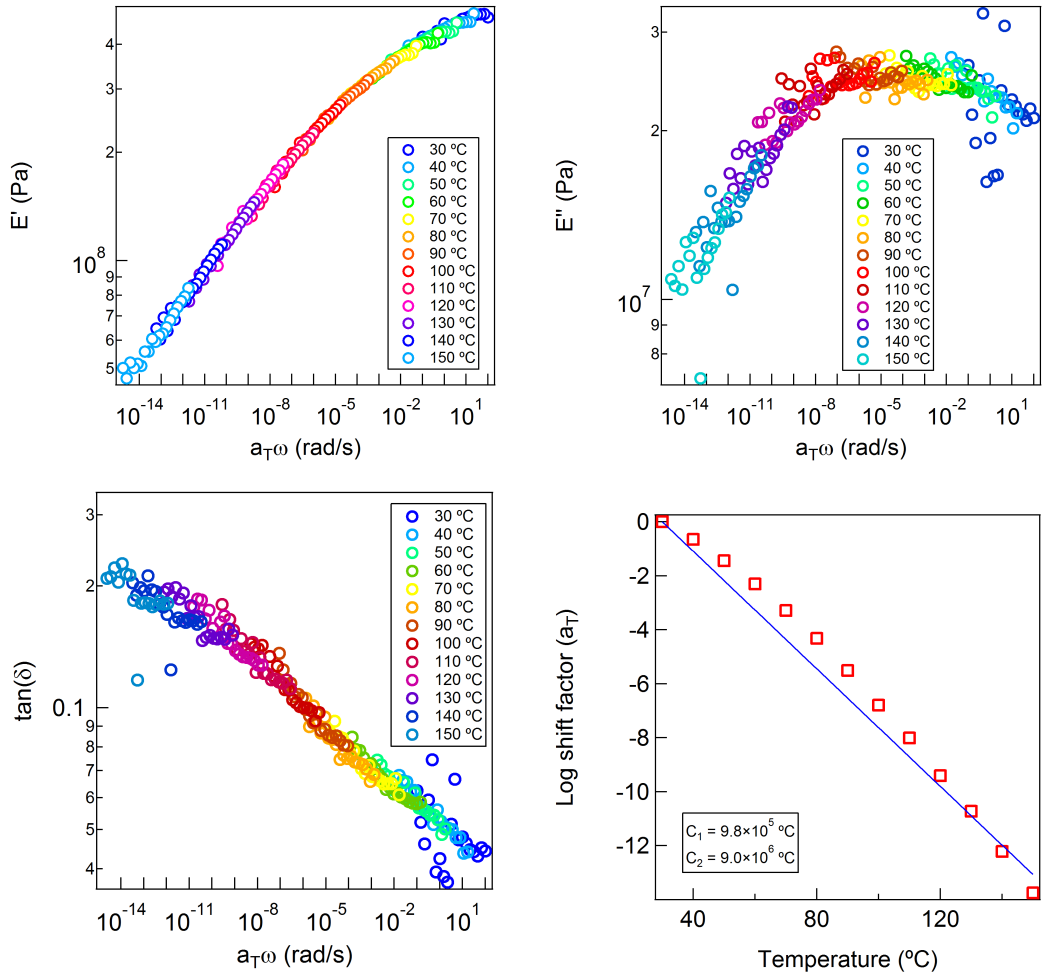

Figure 4.15: Time-temperature superposition of (a) E', (b) E'', and (c) tan(δ) *vs* shifted frequency for a tensile bar with [DVB]:[S] of 4:6. (d) Shift factors used to shift the data in (a–c) (T_r = 30 °C).

One surprising aspect of the DMS analysis was that the shift factors are not described by the WLF equation. Because the WLF equation is not anticipated to be valid below the T_g of polystyrene, the WLF fit was performed only using data points at which $T > 100$ °C. Despite this, blends containing [DVB]:[S] of 2:8 and 4:6 show significant deviations from this fit even at high temperatures. The reasons for this behavior are unclear. A summary of the fitting parameters for the WLF fits is shown in Figure 4.16.

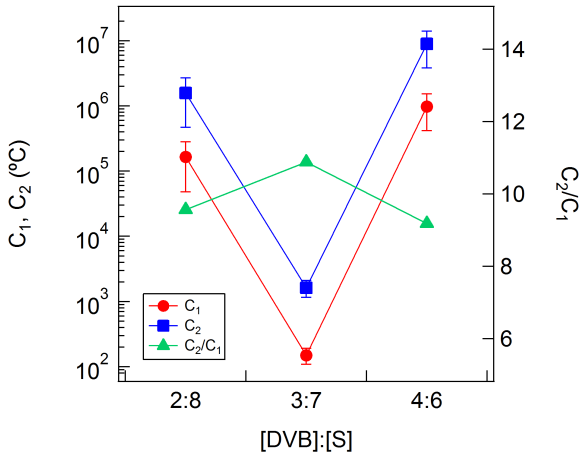

Figure 4.16: WLF parameters determined from fitting shift factors in Figures 4.13, 4.14, and 4.15. T_r is 30 °C.

Beyond probing the linear viscoelastic response, tensile testing was also performed with the aim of determining Young's modulus (E), strain-at-break (σ_{crit}) and mechanical toughness. Determining the toughness of these materials was of particular interest, as polymer electrolytes that are tough would, in theory, be able to withstand the large stresses imposed by the growth of lithium dendrites.[9] Unfortunately, the data obtained were highly unreliable, as the tensile bars cracked and/or slipped readily during testing, as described in the Experimental section. Despite careful modifications to the experimental procedure, we were unable to have the tensile tester to grip the tensile bars at a pressure high enough to prevent slip, yet low enough to prevent the sample from fracturing. Preliminary data were still collected, but the accuracy of the

data is plagued by the issues with the experimental setup.

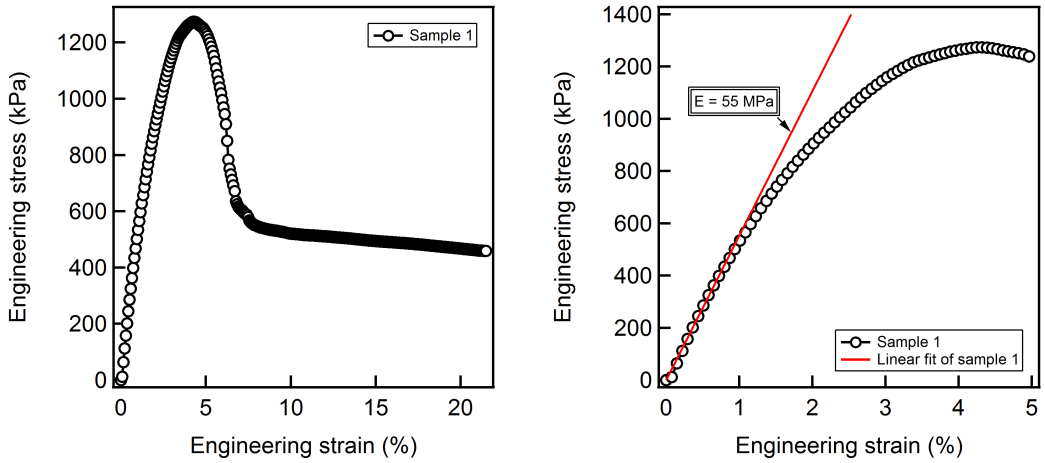

Figure 4.17: (a) Stress-strain curves for samples containing [DVB]:[S] of 1:9. (b) Zoomed view of linear region of stress-strain curves, along with a calculation of the apparent Young's modulus.

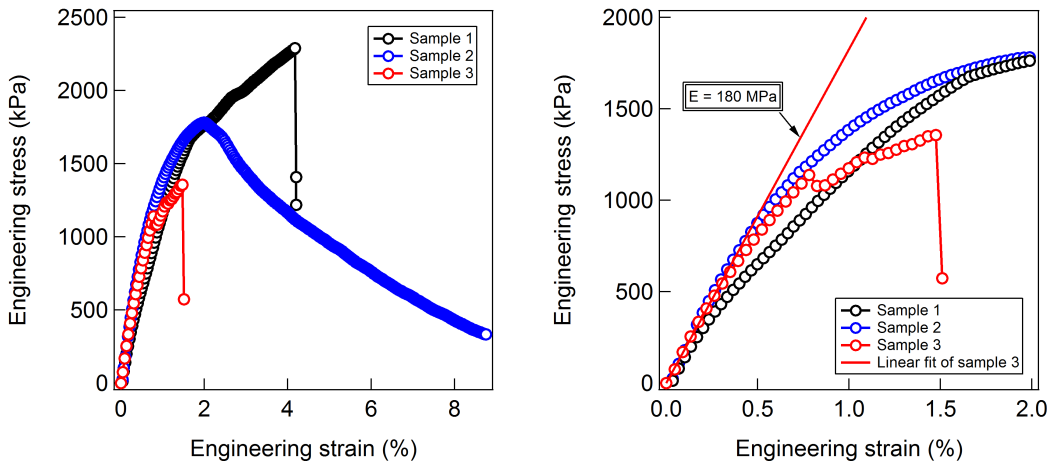

Figure 4.18: (a) Stress-strain curves for samples containing [DVB]:[S] of 2:8. (b) Zoomed view of linear region of stress-strain curves, along with a calculation of the apparent Young's modulus.

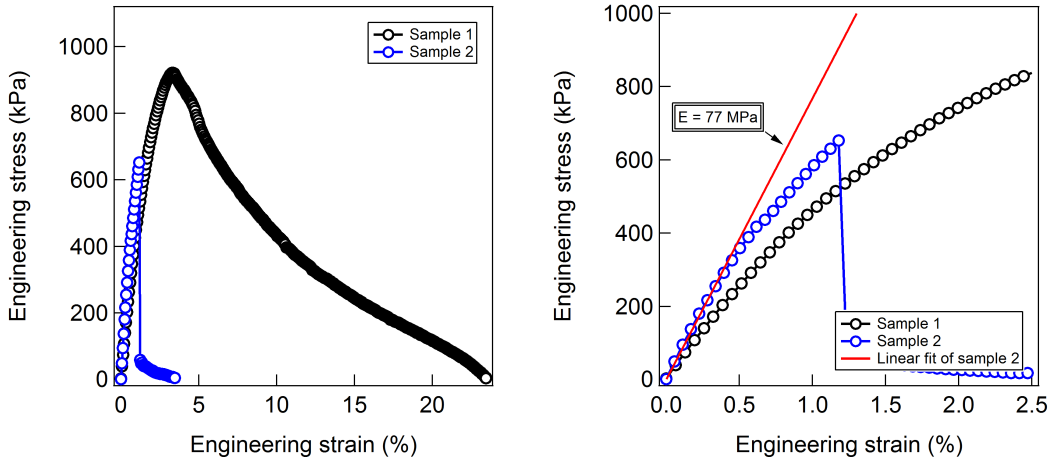

Figure 4.19: (a) Stress-strain curves for samples containing [DVB]:[S] of 3:7. (b) Zoomed view of linear region of stress-strain curves, along with a calculation of the apparent Young's modulus.

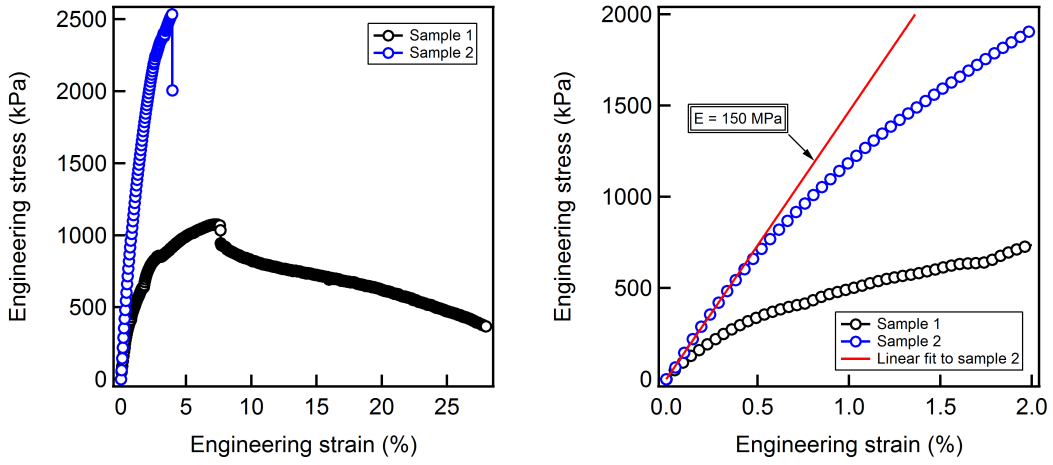

Figure 4.20: (a) Stress-strain curves for samples containing [DVB]:[S] of 4:6. (b) Zoomed view of linear region of stress-strain curves, along with a calculation of the apparent Young's modulus.

Table 4.3 summarizes the relationship between the relative amount of DVB and (a) the elastic modulus (E') determined from DMS analysis at 30 °C, and (b) the Young's modulus assessed *via* tensile tests.

Table 4.3: Summary of mechanical properties at *ca.* room temperature

[DVB]:[S]	Elastic modulus (E') (MPa)	Young's modulus (E) (MPa)
1:9	-[a]	55
2:8	550	180
3:7	670	77
4:6	480	150

[a]Sample too soft to load

As could be expected based on the difficulties with the experimental setup, there is significant discrepancy in the moduli obtained from the two tests. Further, there is no clear trend in the moduli, and the strain-at-break at each DVB loading varies significantly, inhibiting any meaningful assessment of mechanical toughness. Separate from these experiments, we qualitatively found that, based on handling the samples, as the cross-linker content was increased, the sample hardness and brittleness increased. Neither the DMS analysis nor tensile testing confirmed this qualitative finding. Ultimately, the lack of consistent testing results was likely a combination of heterogeneities in the samples due to the lack of AIBN used in their preparation, and the relatively large thickness of the samples, which made loading the samples in the tensile tester more challenging. In the future, tensile bars should be prepared both with AIBN and with reduced thickness.

Ionic conductivity

The ionic conductivity of the polymer electrolytes was assessed both for samples prepared in coin cells and for samples originally prepared as tensile bars, then sanded to approximately 300 μm in thickness. Additionally, the conductivity was assessed as a function of the amount of LiTFSI dissolved in the BMITFSI: 0 M, 1 M, and 2 M. In some cases, the radical initiator AIBN was included. Representative data are shown in

Figure 4.21.

Despite the breadth of data collected, there is no clear trend in how geometry, cross-linker concentration, or LiTFSI loading affect the conductivity. Further, there is extensive sample-to-sample variability in the conductivity for AIBN-free electrolytes prepared as coin cells, even when prepared from the same reaction mixture, as can be seen in Figure 4.22. For comparison, previously collected data from samples prepared in vials with AIBN, then sanded to 300 μm in thickness, are also included in the figure. Interestingly, there is better repeatability when the cross-linker content is increased from [DVB]:[S] of 2:8 to 4:6. This trend is consistent with the visual observation that samples with greater cross-linker content appear to have relatively less macroscopic phase separation, as seen in Figure 4.7.

As was shown in Figure 4.8, when samples were prepared with AIBN, they appeared relatively more homogeneous. The preliminary results in Figure 4.23 suggest that this homogeneity also makes the conductivity of samples prepared within coin cells more closely match that measured for samples prepared in vials, though the magnitude of the conductivity appears to be lower for samples prepared in coin cells.

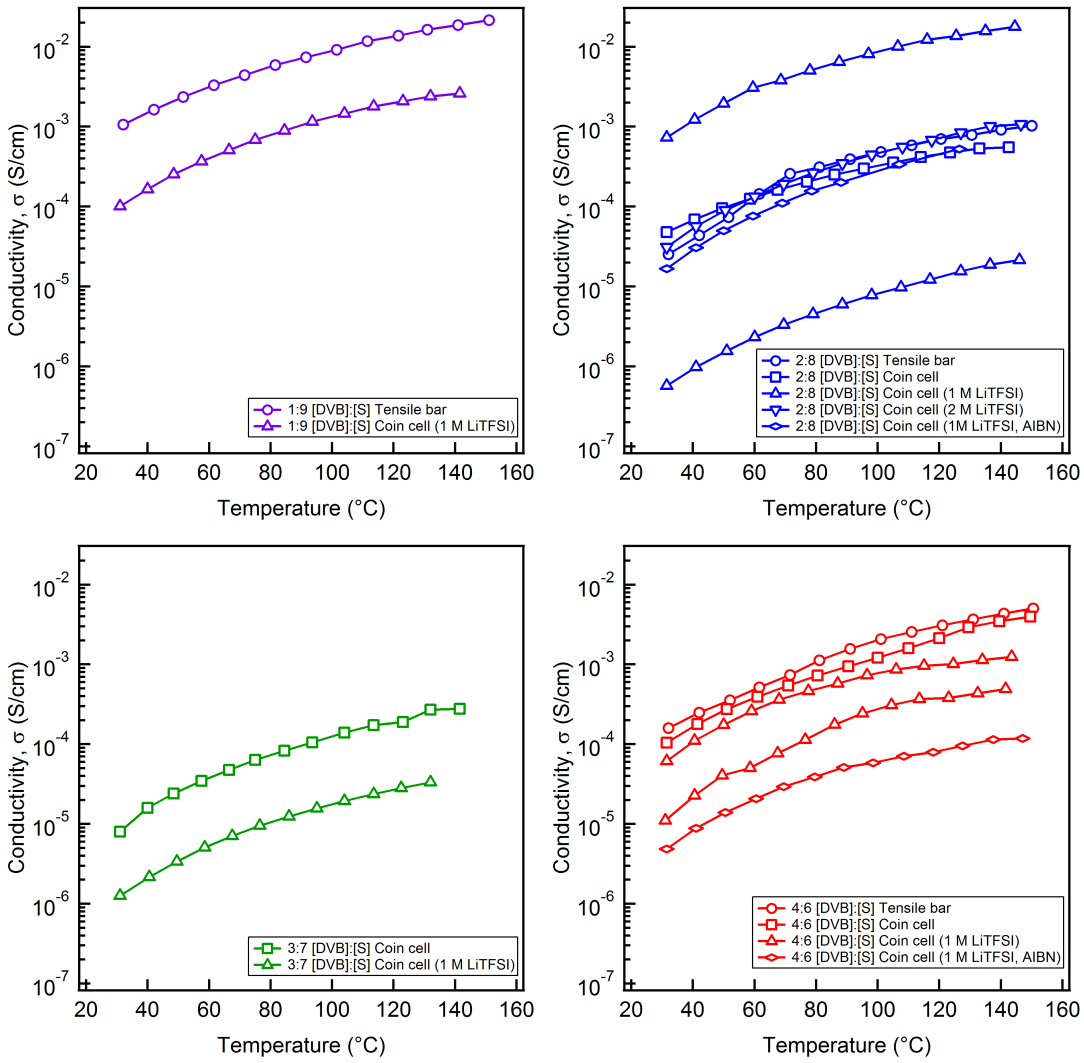

Figure 4.21: Representative ionic conductivity of samples prepared either in coin cells or as tensile bars, with various loadings of LiTFSI, and polymerized either with or without AIBN. Lines have been drawn to guide the eye and do not indicate fits to the data.

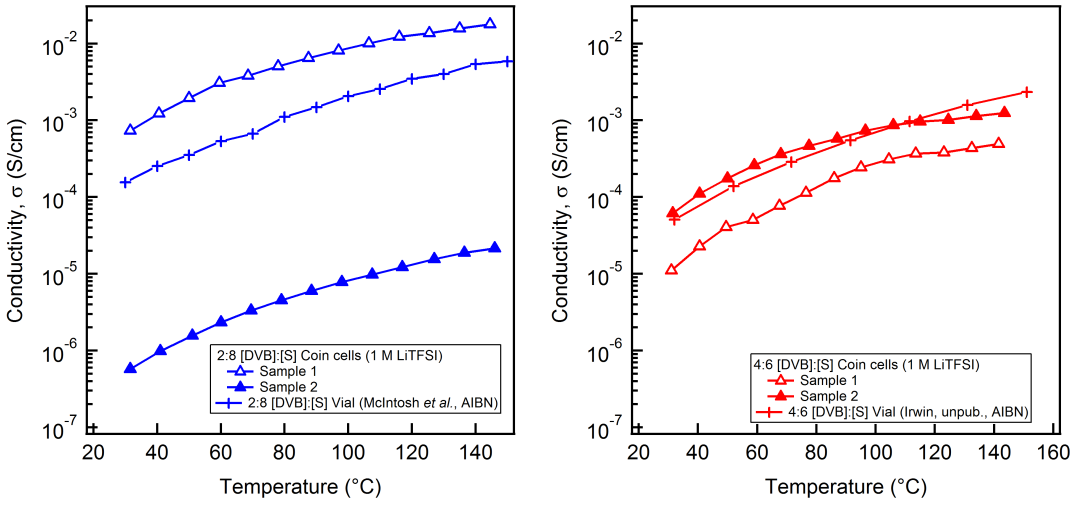

Figure 4.22: Examples of the lack of repeatability in the conductivity data for samples without AIBN containing [DVB]:[S] of (a) 2:8 and (b) 4:6. In both plots, representative data obtained from samples prepared in vials is also displayed. Lines have been drawn to guide the eye and do not indicate fits to the data.

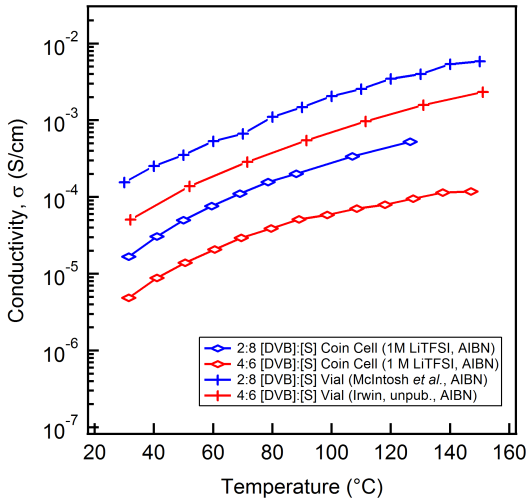

Figure 4.23: Examples of conductivity of electrolytes prepared with AIBN, 1 M of LiTFSI dissolved in the BMITFSI, and [DVB]:[S] of (a) 2:8 and (b) 4:6. The trend in the conductivity more closely matches that obtained in prior studies. In both plots, representative data obtained from samples prepared in vials is also displayed. Lines have been drawn to guide the eye and do not indicate fits to the data.

Cyclic voltammetry

When designing a polymer electrolyte for battery applications, it is important to understand the voltage range over which the electrolyte is electrochemically stable relative to the anode. By determining this voltage range, known as the electrochemical stability window, it is possible to understand what range of voltages can be safely accessed without degrading the electrolyte when it is used in a battery. Often, the biggest stability concern for battery applications is the compatibility between the electrolyte and the lithium metal anode, as the lithium is highly reactive and can thus become easily oxidized and undergo side reactions. If the lithium metal reacts extensively with the polymer electrolyte, a passivated surface on the lithium metal could form, inhibiting the transport of lithium ions and significantly reducing the capacity of the battery. In short, even if a polymer electrolyte has high conductivity and high modulus, it will not of practical use in battery applications unless it is stable relative to the lithium metal.

In order to determine the electrochemical stability window of the polymer electrolytes developed in this study, preliminary cyclic voltammetry experiments were carried out. For this experiment, an asymmetric coin cell was fabricated, with a lithium metal anode and a stainless steel (blocking) cathode, as described in the experimental section. The samples for this study were prepared using [DVB]:[S] of 3:7 and 4:6, and without AIBN. The results of these experiments are shown in Figure 4.24.

In both parts of the figure, there is a clear oxidation peak that occurs at approximately 0 V that corresponds to the Li/Li^+ reaction, likely due to lithium ions plating the lithium metal anode. In Figure 4.24a, there is an oxidation peak on increasing voltage at approximately 2.8 V that does not have a corresponding reduction peak upon decreasing the voltage. Although the origin of this peak is not clear, its irreversibility suggests there may be some degradation either in the electrolyte or on the lithium metal. Unfortunately, only the data presented here were collected, so it is difficult to tell if this undesirable feature is unique to the current sample, or would be a general feature of the polymer electrolytes developed in this work. In Figure 4.24b, the low resolution of the data makes it challenging to say whether or not there is also

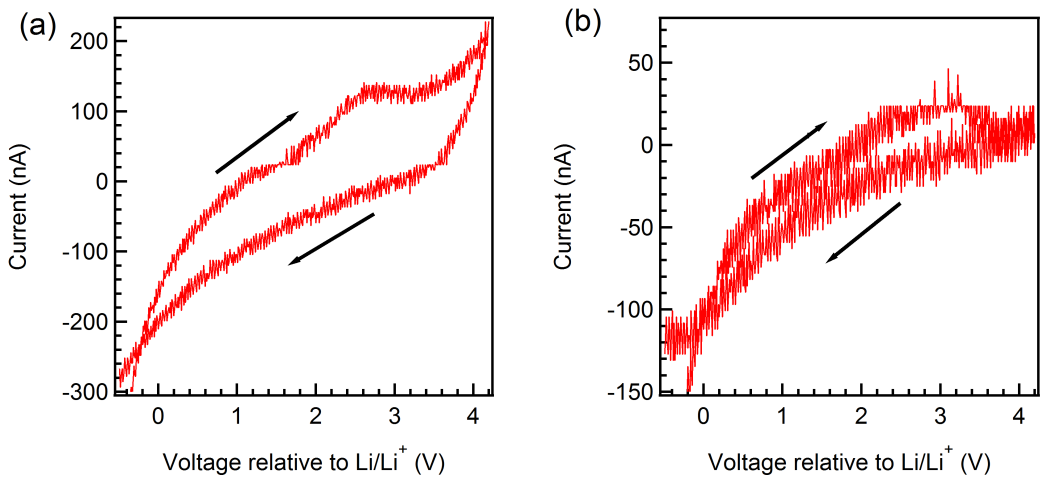

Figure 4.24: Cyclic voltammetry results for cells containing polymer electrolytes prepared with 1 M LiTFSI and [DVB]:[S] of (a) 3:7 and (b) 4:6. Voltage is relative to Li/Li^+. The limit of resolution of the instrument is $\pm$ 10 nA.

an oxidation peak in the same location. Except for the anomalous feature at 2.8 V , the samples appear to be stable between the voltage range of 2.5 V to 3.7 V. Therefore, this range will be considered the preliminary electrochemical stability window for the sake of battery cycling experiments.

Galvanostatic cycling

Galvanostatic cycling experiments were performed to assess how much charge can pass through the polymer electrolyte prior to failure, likely due to lithium dendrite growth. This test was performed in a symmetric, lithium-electrolyte-lithium cell. The result of this study for a sample prepared with 2 M LiTFSI in the BMITFSI, [DVB]:[S] of 2:8, and AIBN is shown in Figure 4.25.

The cell appeared to perform repeatably until day 7, when there was a sudden increase in the measured voltage, a sign of cell failure. The total amount of charge passed through the electrolyte prior to failure was 27.4 C/cm^2: 3.2 C/cm^2 during the break in cycles on days 1–4, and 24.2 C/cm^2 during the remaining cycles until cell failure on day 7. This lifetime is more than order of magnitude lower than that

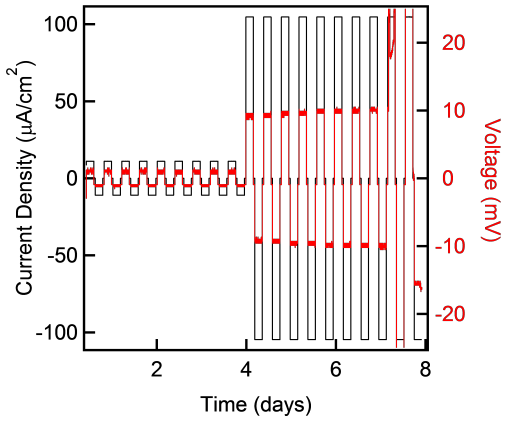

Figure 4.25: Galvanostatic cycling experiment performed in a symmetric coin cell (lithium electrodes) at charge densities of 11 (days 1–4) and 36 μA/cm^2. The sample was prepared with a solution of 2 M LiTFSI dissolved in BMITFSI, [DVB]:[S] of 2:8, and AIBN.

previously reported in previous a previous study on PS-PEO block copolymers doped with LiTFSI.[182] Ultimately, the failure of the cell could be due defects in the sample or the cell. Images of the electrolyte, and the PTFE washer in which it was prepared, before and after the cycling experiment are shown in Figure 4.26. In part (b) of the figure, there is extensive blackening where the lithium foil was in contact with the PTFE washer. Further, on the bottom and top left corners of the electrolyte, there are brown regions that are noticeably darker than other parts of the sample. It is possible that the measurement indicated sample failure when this region of the sample became degraded.

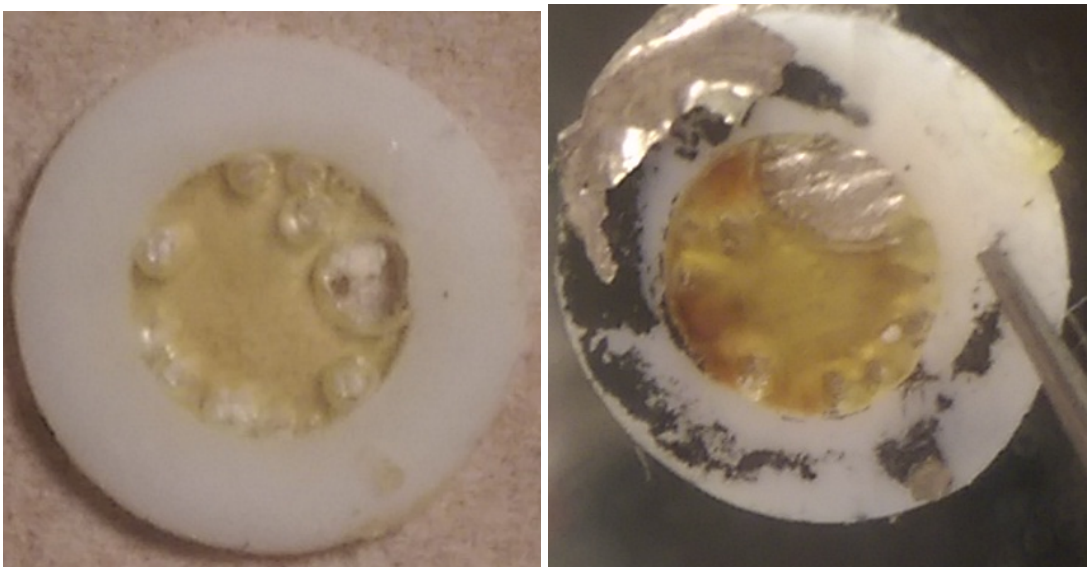

Figure 4.26: Images of sample (a) before and (b) after cycling. The silver foil is lithium metal, and the white washer is PTFE. The black marks on the PTFE suggest that the lithium metal reacted with the PTFE.

Battery testing

After using cyclic voltammetry to roughly estimate the electrochemical stability window of the cells (*ca.* 2.5 V to 3.7 V), a preliminary battery cycling experiment was performed. This was done to determine how many charge and discharge cycles could be completed before the batteries failed. The geometry of the cells used in this experiment was shown in Figure 4.5b.

One of the key challenges with developing a polymer electrolyte for lithium metal batteries is ensuring that the lithium metal remains stable over the lifetime of the battery. Thus, battery cycling experiments assess the ability of the polymer electrolyte both to suppress dendrites by extending battery lifetime while simultaneously delivering sufficient power. One method for quantifying the performance of a battery is to determine its specific cell capacity, S, during charging and discharging. This quantity is defined as:

$$S = \frac{\int I dt}{m_{\mathrm{LiFePO_4}}} \tag{4.4}$$

where I is the measured current and $m_{\mathrm{LiFePO_4}}$ is the mass of $LiFePO_4$, the active component of the cathode, in the cell. Another parameter of interest is the coulombic efficiency, η, which indicates the fraction of how much of the power used for charging was recovered in the discharge step, and is defined as:

$$\eta = S_{\mathrm{discharge}}/S_{\mathrm{charge}} \tag{4.5}$$

For the current study, the battery was assembled using [DVB]:[S] of 2:8, 1 M LiTFSI dissolved in the BMITFSI, and AIBN. The cell capacity upon charging and discharging with this polymer electrolyte is shown as a function of cycle number in Figure 4.27.

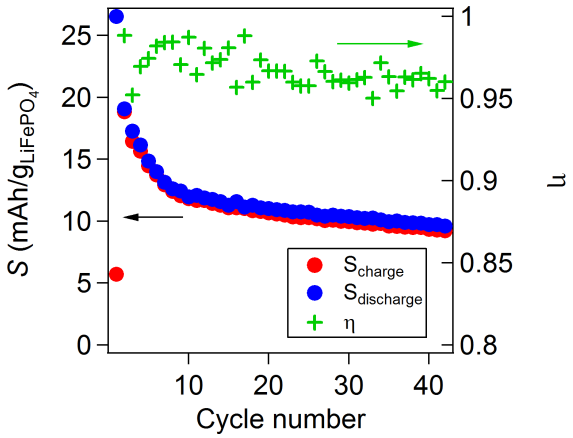

Figure 4.27: Results of battery cycling experiment for a cell containing a polymer electrolyte with (a) [DVB]:[S] of 2:8, 1 M LiTFSI relative to BMITFSI sample.

Ultimately, the battery cycling experiment was stopped after 43 cycles, which took place over the course of 250 hours. The cell had not yet failed as of that time. Presumably, the cell could have continued to be cycled beyond this point, but the experiment was stopped so that additional experiments could be attempted on other batteries. Unfortunately, all further tests after this initial round of testing were

unsuccessful, as no other batteries could be charged during the first cycle. Ultimately, however, these tests demonstrated the ability of the polymer electrolytes to suppress dendrite growth over the course of several days of cycling.

4.4 Discussion

From the outset, there were three primary goals for this work. The first goal was to determine the ratio of [DVB] to [S] in the initial reaction mixture that could enhance the mechanical properties of the resulting polymer electrolytes without sacrificing their ionic conductivity. Once this was accomplished, the second aim was to develop a method for preparing the polymer electrolytes *in situ* within coin cells. Once these efforts had been attempted, the final goal was to develop and perform preliminary battery testing routines to assess how well these polymer electrolytes could perform in rechargeable lithium batteries with lithium metal anodes.

Ultimately, all of these goals were plagued by the issue of macroscopic phase separation during the polymerization process, leading to samples that were heterogeneous and with properties that varied extensively depending on the sample preparation conditions. In retrospect, this phase separation likely occurred because the radical initiator AIBN was not used in the majority of the reaction mixtures prepared in this work. At high temperature, AIBN decomposes to form nitrogen gas and two radicals that can initiate free radical polymerization. In initial experiments, there was concern that the evolution of nitrogen gas would lead to entrapped bubbles within the final polymer electrolytes, so AIBN was not included. However, without AIBN, the most likely mechanism by which the polymerization proceeds is through the thermal initiation of a styrene or DVB monomer, which can then either react with other monomers or the chain transfer agent terminus of a PEO chain. Ultimately, based on the appearance of the samples in Figure 4.7, it appears that, in the absence of AIBN, significant homopolyerization of styrene and DVB occurs, which ultimately phase separates from the PEO-rich domain and crashes out as a white powder. The SAXS traces for these blends indicates that the yellow regions of these samples are still

highly structured, which indicates that the PEO-*b*-P(S-*co*-DVB) was formed to at least some extent. However, the lack of reproducibility in the mechanical and conductivity tests demonstrate that the macroscopic heterogeneities result in inconsistency in the final polymer electrolyte composition.

Despite the lack of repeatability in the data, the techniques developed in this chapter to prepare polymer electrolytes in coin cells and test them for use in battery application are anticipated to be of use for future work on this project. Specifically, Figure 4.8 demonstrates that when the reaction mixtures are prepared with AIBN and then reacted in coin cells, the polymer electrolytes are macroscopically homogeneous. Furthermore, the procedures detailed for galvanostatic cycling, cyclic voltammetry, and battery cycling could be readily used for other polymer electrolyte systems.

The next two sections will focus on what can be extracted from the information collected in this study. The first section will provide an analysis of the trend in the polymer electrolyte properties with DVB loading, while the second will provide a rough kinetic and thermodynamic argument for how the sample preparation results in the different morphological properties observed.

Relationship between cross-linker content and resulting properties

Although there was significant sample-to-sample variability in the resulting samples, it is worth considering the overall trend in the mechanical and structural properties that were determined in this work.

From the SAXS analysis of samples prepared in vials and as tensile bars and without AIBN, structural parameters were calculated and presented in Figure 4.11. Overall, blends prepared as tensile bars or within vials have significant microstructure. At all compositions, the amphiphilicity factor is consistently below about –0.90, indicating that the globally disordered morphology is highly structured.[101] For most formulations, the correlation length is relatively large compared to the domain spacing, and the SAXS traces exhibit higher order shoulders at $2q^*$ and, in some cases, $3q^*$, indicative of a highly correlated structure. A previous study of ternary polymer blends consisting of

polyethylene (PE), polycyclohexylethylene (PCHE), and PCHE-*b*-PE found that blends which form polymeric bicontinuous microemulsions with similarly low amphiphilicity factors consist of relatively pure PE and PCHE domains that are separated by a "dry brush" block copolymer interface that excludes homopolymer.[115] In the current work, this would, roughly, be analogous to the PEO-*b*-P(S-*co*-DVB) acting as a sharp interface between pure domains of (a) LiTFSI, BMITFSI, and residual PEO-CTA and (b) polystyrene and unreacted styrene and DVB monomers.

Beyond general conclusions about the overall structures of these blends, it is worth considering the trend in the structural data with increasing [DVB]:[S]. In Figure 4.11, the uncertainty in the parameters generally decreases as the DVB content is increased. This may suggest that the presence of relatively more DVB results in faster cross-linking of the sample, arresting the sample morphology prior to extensive macrophase separation. There also appears to be a decrease in the domain spacing with increasing DVB content, which suggests that the resulting average degree of polymerization of the cross-linked diblock copolymer is smaller when prepared with higher DVB loading.

Despite the significant issues with the repeatability of ionic conductivity and mechanical testing experiments, the overall performance of the polymer electrolytes can still be analyzed. Table 4.3 indicates that the elastic and Young's moduli of all blends, regardless of DVB loading, was close to the 0.1 GPa previously reported by Schulze *et al.* and McIntosh *et al.* for similar blends.[10,148] Similarly, even though the conductivity of samples prepared without AIBN exhibited orders-of-magnitude variations in conductivity, preliminary tests on samples prepared with AIBN qualitatively agreed with previous experiments that suggest that DVB loadings other than [DVB]:[S] of 2:8 detrimentally affect the ionic conductivity.[148]

The combination of galvanostatic cycling, cyclic voltammetry, and battery cycling experiments also brought new insights into the utility of these polymer electrolytes. Preliminary cyclic voltammetry experiments indicated that there was slight degradation of the polymer electrolyte in the presence of the lithium metal. Although galvanostatic cycling experiments suggested that there the polymer electrolytes can pass only a small amount of charge prior to failure, battery cycling experiments demonstrated that the

electrolytes were able to provide ion transport for more than 40 cycles. The discrepancy between these findings is yet another indicator that better control over the sample reaction, primarily through the inclusion of AIBN, is necessary.

Understanding the route to macroscopic phase separation by analogy with ternary polymer blends

Perhaps the primary lesson from this chapter is that the inclusion of AIBN into the reaction mixture is necessary to prevent macroscopic phase separation. However, this assertion alone does not explain (a) why samples without AIBN phase separate into structured and unstructured regions, or (b) the relationship between microstructure and relative loading of [DVB]:[S]. Therefore, this section seeks to provide a rough explanation for the route by which the structure forms and, in some cases, macrophase separation occurs in these polymer electrolytes.

The mechanism by which structure evolves in the polymer electrolytes during the course of the reaction was previously studied by McIntosh *et al.*[148] Through a combination of techniques including SAXS, DMS, impedance spectroscopy, and size exclusion chromatography, they found that the growth of structure in the electrolytes occurs in two parts: (a) growth of the PEO-*b*-P(S-*co*-DVB) diblock that leads to an increase in segregation strength and, thus, more significant composition fluctuations, followed by (b) gelation of the sample caused by the cross-linking of the insulating domain; this inhibits further chain reorganization and thus "locks in" the morphology at the segregation strength of the blend immediately prior to gelation. The evolution of the structure described in (a) was observed through *in situ* SAXS analysis, where, during the first two hours of the reaction, the magnitude of the primary scattering peak, $I(q^*)$, increased, and the position of that peak, q^*, decreased, which indicate that a morphology with greater structure and larger domain spacing was being formed. However, at a time corresponding to (b) the rheological gel point, SAXS analysis found that the primary peak intensity and position remained largely invariant with time, even though measurements of the conductivity indicated that the molecular-level structure

was still evolving as the system continued to cross-link and ultimately form a solid electrolyte. Looked at another way, the gelation of the sample kinetically trapped the microstructure of the electrolyte, preventing the blend from reaching the equilibrium morphology that it would otherwise achieve in the absence of cross-linking. As was asserted in the article, this kinetic trapping of the sample when it is disordered, yet microstructured due to large composition fluctuations, is advantageous, as it result in a co-continuous morphology free of grain boundaries that would reduce the ionic conductivity of the electrolyte.[54]

In the article by McIntosh *et al.*, the authors depict the growth of the microstructure through a simple example of how the segregation strength of a salt-doped diblock copolymer will increase during the polymerization of one of its blocks. This analysis made the simplifying assumption that the ionic liquid and unreacted styrene and DVB did not significantly affect the energetics of the system. Ultimately, this simple model was sufficient to describe the behavior of the polymer electrolytes in that study, which was identical to the blends prepared in this study with [DVB]:[S] of 2:8 and included AIBN. However, this "diblock growth" model cannot account for the phase separation seen in our system.

For this reason, we present an alternative explanation for the route by which both microstructure and macroscopic phase separation can occur during the course of the reaction. This explanation is based on the phase behavior of ternary polymer blends that consist of homopolymers A and B that are compatibilized by a diblock copolymer AB. In such systems, the most common part of the phase space explored is where the volume fraction of the A and B homopolymers is set equal to each other, *i.e.* $\phi_A = \phi_B = \phi_H/2$, where ϕ_H is the total homopolymer volume fraction. This allows the phase behavior of the blends to be studied as a function of temperature, T, and ϕ_H, where we note that $T \sim 1/\chi N$ and the fraction of block copolymer in the blend is given by $\phi_{AB} = 1-\phi_H$.

In the current study, there are numerous components within the mixture at any point during the reaction: PEO-CTA homopolymer, PS homopolymer, PEO-*b*-P(S-*co*-DVB) "block" copolymer, BMITFSI, LiTFSI and styrene and DVB monomers. For our model, we first assume that the reaction mixture can be simplified by three volume fractions:

1. $\phi_{PEO} \equiv \phi_{PEO-CTA} + \phi_{BMITFSI+LiTFSI}$: the PEO "homopolymer" fraction consists of unreacted PEO-CTA and the ionic liquid solution.
2. $\phi_{PS} \equiv \phi_{h-PS} + \phi_{S+DVB}$: the PS "homopolymer" consists of PS homopolymer fraction and unreacted styrene and DVB monomers.
3. $\phi_{PEO-P(S-co-DVB)}$: the "block copolymer" fraction consists of the total amount of the growing and cross-linking polymers.

We note that, in this model, the total "homopolymer" fraction is given by $\phi_H = \phi_{PEO} + \phi_{PS}$. With these simplifications in mind, we now make several more observations that guide the design of the model:

1. The reaction mixture is homogeneous and one-phase prior to the reaction.
2. When blends are reacted without AIBN, the reaction mixture macrophase separates, and the extent of macrophase separation appears to scale inversely with DVB loading (Figure 4.7).
3. When blends are prepared with AIBN, the reaction mixtures do not macrophase separate.
4. McIntosh *et al.* reported that, at the onset of gelation, the mass of solids was approximately 70 wt%. Taking into account the ionic liquid incorporated in the solids, this indicates that approximately 50 wt% of the reaction mixture was the growing PEO-*b*-P(S-*co*-DVB) "block" copolymer. Again, these blends incorporated [DVB]:[S] of 2:8.[148]

With all of these parameters in mind, we have drawn a schematic that maps the segregation strength of the blend as a function of reaction progress and block polymer content in Figure 4.28. We note that this is not a phase diagram, but rather a map that shows the approximate state of the reaction mixture prior to the onset of gelation. The blue circle in the top right corner represents the state of the initial reaction mixture, with or without AIBN. The arrows projecting from the blue circle indicate two routes by which the reaction may proceed depending on whether or not

AIBN has been incorporated. The green circle indicates the outcome of the reaction in the absence of any DVB cross-linker: a system containing approximately 79 vol% block copolymer and, in this case, 21 vol% ionic liquid. The red circle, on the other hand, makes an approximation that, in the absence of DVB and AIBN, significantly less block copolymer would be formed, and that the majority of the final polymer electrolyte would consist of the "homopolymer" components like PS homopolymer that are represented by ϕ_H. The arrows that connect the blue circle to the red and green circles track the change in the segregation strength and blend composition as the reaction proceeds; thus, points along the arrow correspond to the state of the reaction mixture at intermediate reaction times.

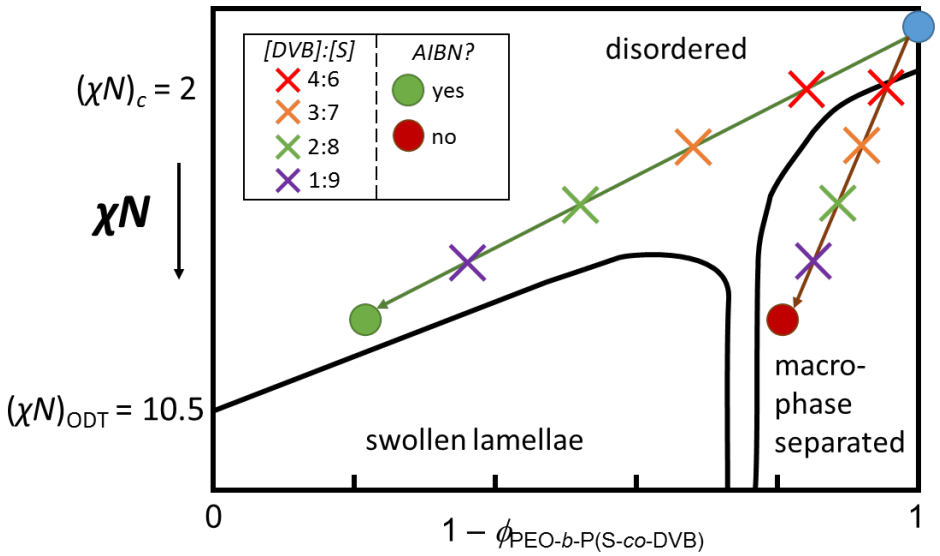

Figure 4.28: Schematic representation of two routes through which the polymerization reaction could proceed. The crosses note the approximate state of the reaction mixture immediately prior to the onset of cross-linking-induced gelation.

As detailed by McIntosh et al., the structure of polymer electrolytes grows until microphase separation is arrested by cross-linking-induced gelation of the insulating phase. To a first approximation, the point at which this gelation event occurs should be correlated with the amount of DVB cross-linker incorporated into the reaction mixture: samples that contain relatively more DVB should gel faster than samples with less. In

our schematic in Figure 4.28, we indicate various points along the reaction pathways, indicated by crosses, at which the gelation event is anticipated to occur and arrest phase separation. We note that the schematic suggests that samples containing AIBN and [DVB]:[S] of 2:8 should cross-link when there is approximately 50% block copolymer, which agrees well with the result from McIntosh *et al.*[148] This simple schematic also provides an explanation for several of the experimentally observed phenomenon in this chapter:

1. *Observation: Blends without AIBN are relatively more homogeneous when prepared with more DVB (Figure 4.7).*

   Explanation: The crosses along the red arrow in Figure 4.28 suggest that blends with less DVB traverse deeper into the macrophase separated region of the phase diagram prior to gelation. This increased depth increases the driving force for phase separation. The phase separation is complemented by the fact that samples with less DVB take longer to gel and, thus, are able to macrophase separate over longer time scales.

2. *Observation: there is only modest variability in the microstructure of polymer electrolytes prepared with different loadings of DVB, as suggested by the SAXS analysis in this work (for samples prepared without AIBN, see Figure 4.11) and in work by McIntosh et al. (for samples prepared with AIBN).*[148]

   Explanation: For samples with AIBN (green arrow), there difference between the segregation strength at gelation, $\chi N_{\text{gellation}}$, and χN_{ODT} is approximately constant regardless of DVB loading. In the case of samples without AIBN, the reduction in the error bars in the fitting parameters derived from the SAXS data as the DVB loading is increased (see Figure 4.11) suggests that reaching the gelation point faster leads to better sample reproducibility.

Although the schematic in Figure 4.28 provides a tool for understanding the mechanism through which the polymer electrolyte forms, it is important to emphasize that it should *not* be read as a phase diagram. Rather, the crosses simply mark the

approximate gelation points for the polymer electrolytes, which indicates where the microstructure of the polymer is "locked in". After this point, the remaining styrene and DVB monomers continue to react until most have incorporated into the insulating phase, as confirmed by mass yield experiments by McIntosh *et al.*[148]

We also briefly note that this diagram suggests that the final block copolymer would be disordered, while calculations by McIntosh *et al.* anticipated that such a system would consist of ordered lamellae. Our assignment is based on previous, unpublished SAXS data that strongly suggests that reaction mixtures with no DVB ultimately form a highly correlated, disordered structure.

4.5 Conclusions

In this chapter, we have detailed the preparation and performance of polymer electrolytes that could be used in rechargeable batteries that employ a lithium metal anode. These solid electrolytes were prepared by polymerizing DVB, which serves as a cross-linking agent, and styrene off a PEO-CTA in the presence of LiTFSI and BMITFSI, which leads to the development of microstructure in the electrolyte through polymerization-induced microphase separation (PIMS). By varying the ratio of the styrene to DVB in the initial reaction mixture, we intended to find the concentration of cross-linker that optimized both the modulus and ionic conductivity of the polymer electrolytes. Ultimately, however, formulations that did not include the radical initiator AIBN were plagued by macroscopic phase separation of the reaction mixture during the polymerization process. We proposed a rough model that suggests that the macroscopic phase separation was the result of too little of the styrene and DVB being incorporated into the PEO-CTA chains prior to cross-linking-induced gelation. Despite these setbacks, methods were developed to test the polymer electrolytes in battery applications, and preliminary results from galvanostatic cycling, cyclic voltammetry, and battery cycling experiments suggest that the polymer electrolytes developed in this study could be used for rechargeable lithium metal battery applications.

4.6 Acknowledgments

I would like to thank Prof. Nitash Balsara and Dr. Didier Devaux for providing instruction and insight into the assembly of the coin cells prepared in this work. Also, we thank Prof. Philippe Bühlmann and his research group for providing access to their Solartron electrochemical impedance spectroscopy equipment. We also thank Yuan Fang in the Stein group for his assistance with performing cyclic voltammetry experiments and determining the electrochemical stability window of the polymer electrolytes. Thanks also to Chang-Hyun Kim of the Frisbie group for developing the LawVIEW method that was used for battery cycling experiments. Finally, we would also like to thank Morgan Schulze and Sujay Chopade for their assistance with preparing the materials and initial samples for this study, respectively.

Chapter 5

Polymeric Bicontinuous Microemulsions as Versatile Templates for Structured, Functional Membranes

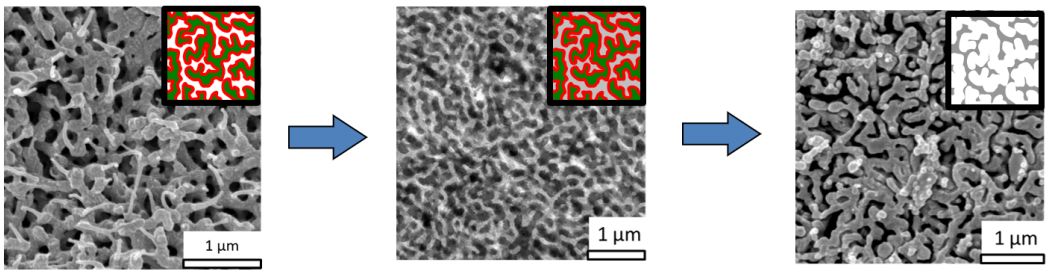

5.1 Abstract

This chapter details the development of a thin, sacrificial polyethylene (PE) membrane that was used as a template to make epoxy membranes with a well-controlled nanoscale morphology. These epoxy membranes were tested in the context of use in water filtration membranes, but the procedures described could be extrapolated to a wide

variety of applications where simultaneous control over morphology and material properties is required. The PE templates were generated *via* the selective removal of poly(ethylene-*alt*-propylene) (PEP) homopolymer from a polymeric bicontinuous microemulsion (BμE) consisting of PE and PEP homopolymers and a PEP-*b*-PE diblock copolymer. First, the phase behavior of PE/PEP/PEP-PE blends was established using a combination of dynamic mechanical spectroscopy (DMS) and transmission electron microscopy (TEM) to assess what temperatures and blend compositions give rise to a BμE morphology. Samples that appeared bicontinuous by TEM were rendered porous *via* dissolution of the PEP homopolymer and then further analyzed by small-angle X-ray scattering (SAXS), scanning electron microscopy (SEM), and nitrogen sorption. Surprisingly, this study only found a homogeneous BμE morphology at temperatures greater than the T_{ODT} of lamellae-forming blends; a region of phase space with a BμE channel in which the BμE morphology could be found independent of temperature was not found.

After establishing the phase behavior of the blends in the bulk, a hot pressing technique was developed to generate thin ($\leq$ 500 μm thick) films of the PE/PEP/PEP-PE ternary blends. These films were also rendered porous through selective PEP homopolymer removal to yield porous, majority PE membranes. Through a combination of SAXS, TEM, and SEM, it was found that the internal morphology of the membranes were bicontinuous, but the surfaces of the membranes exhibited a highly defective skin layer. However, because the internal pore structure was still accessible, the PE templates were able to be backfilled with epoxy precursors, which were then cured. The PE template was then dissolved using hot solvent, yielding a thin epoxy membrane that successfully retained the bicontinuous morphology of the original polymeric BμE.

The epoxy membranes were tested for use as water filtration membranes, but preliminary tests found that the membranes were unable to withstand the pressures required for filtration applications. Instead, the membranes failed at relatively low pressures, likely due to incomplete cross-linking of the epoxy precursors. As an alternative route to filtration membranes, the PE membranes, which had been used as

a template, were also tested for their ability to filter water, but the presence of the surface skin layer resulted in nearly zero flux. Despite these setbacks, the techniques developed through this work demonstrates that it is possible to retain a well-controlled morphology through several processing and templating steps using judicious materials selection.

5.2 Introduction

The development of methods to reliably and efficiently produce materials which simultaneously exhibit desirable electronic, mechanical, and/or chemical properties with well-controlled morphology at the nanometer length scale is critical for the improvement of technologies such as water filtration membranes,[52,89] bulk heterojunction solar cells,[11,90] and polymer electrolytes.[10,91,92] Often, templating is used as a means of imparting a preferred morphology onto a material of interest. However, templating techniques rarely provide absolute control of material properties, product thickness, and nanoscale structure. For example, track-etching, a top-down process in which cylindrical channels are produced in a solid polymer film, can produce membranes with a pore diameters ranging from 20 nm to several micrometers, but the technique results in low total porosities, and pore size control is limited by the irradiation source used to make the channels.[52,186] Membranes derived from block copolymers, on the other hand, are made by rendering a self-assembled block copolymer film porous by selectively etching one component.[187,188] Because self-assembly is driven by thermodynamics, the resulting pore size is well controlled. However, because the pore size is dictated by the size of one of the polymer blocks, pore diameters larger than about 15 nm are difficult to achieve, limiting their use in applications like rapid water filtration, where flux is proportional to the pore size squared.[103] Additionally, copolymer selection is limited to those which form either cylindrical or gyroid morphologies that allow for pore creation, and, furthermore, cylindrical morphologies must also be aligned prior to use.[89] Beyond this, aligned block polymers may still contain residual grain boundaries, which were shown in Chapter

3 to substantially inhibit transport properties. Thus, despite the complexity of these techniques, they typically fail to produce ideal membranes. Further, even when they do succeed, the developed methods are tailored to using only one set of starting materials, so the entire process must be reconfigured every time a different material is desired. These setbacks motivate the search for a more versatile technique that is amenable to a variety of chemistries while maintaining morphological control.

This chapter details work done to develop a general and versatile templating method to obtain materials with both desirable properties and a precisely controlled morphology. Specifically, this chapter describes the development of a thin, sacrificial polyethylene (PE) template, which was then used to fabricate a versatile epoxy membrane. This method expands upon the work of Jones *et al.* on thick, bulk PE templates.[124–127,189] Our process involved first developing a film of a polymeric BμE, then selectively removing one component of the blend to generate a thin, semi-crystalline PE template with a well-controlled, three-dimensional pore network. The pores of this template could then be filled with material precursors and subsequently cured. In this work, we selected epoxy monomers to ultimately generate a cross-linked, hydrophilic epoxy membrane. Next, the polyethylene template is removed to generate a porous material with the inverse structure of the template. This process is general and could be applied to the templating of a variety of materials, only requiring that the target materials are processable and curable at moderate temperature so the morphology of the PE template is not disrupted. Unlike membranes derived from block copolymers that achieve order *via* judicious choice of monomer identity and block lengths, the proposed templating method can give arbitrary materials with desirable physical, chemical, or electrical properties a very well-defined and controlled pore network.

Porous materials derived from polymeric BμEs

Polymeric bicontinuous microemulsions (BμEs) have been discussed in depth in Chapter 1. For the sake of brevity, the background on these systems will not be reproduced here. The reader is instead directed to the review in Chapter 1, Section

1.3.

Researchers in the Bates and Lodge labs have previously taken advantage of the co-continuous network structure of polymeric BμEs to develop porous materials.[112,124] Broadly speaking, these groups formed the porous samples by first forming the bicontinuous morphology in the melt, then trapping the morphology by vitrifying or crystallizing one of the domains, followed by selectively removing the other domain. Using this strategy, these researchers were able to generate porous materials with several desirable properties. (i) The bicontinuous, three-dimensional network structure removed the need for pore alignment, a major challenge in the development of materials from block copolymers with cylindrical morphologies.[23,112,190] (ii) Pore sizes up to 100 nm or greater could be readily obtained. This is in contrast to porous materials derived from the analogous gyroid phase in block copolymers, which is only observed over a narrow composition window and in which the domain size is often limited to roughly 5 – 30 nm.[103] Larger pore size is often desirable in filtration membranes because it permits rapid filtration, as flux through a pore scales with pore size squared.[112] (iii) The equilibrium nature of the bicontinuous morphology results in a material with a narrow distribution of pore sizes, while the globally disordered nature of the morphology avoids the grain boundaries that act as transport barriers in polycrystalline, ordered systems and thus improves pore network continuity. (iv) Unlike materials from pure block copolymers, the present materials are made from templates with as little as 11% block copolymer, typically the most expensive component of such a blend.[103,191] (v) The porosity of such materials is large and on the order of 50%, corresponding to the volume fraction of the domain which can be removed through dissolution.[112,126]

Zhou *et al.* first demonstrated the feasibility of generating a porous material from a polymeric BμE using a system of polyisoprene (PI)/polystyrene (PS)/PI-*block*-PS.[112] In this system, the BμE morphology was kinetically trapped by chemically cross-linking the PI domains. The PS homopolymer was subsequently removed by dissolution in hexane to yield a mesoporous, $\sim$1 mm thick cross-linked PI monolith with a pore size distribution tightly centered around 43 nm. However, the utility of this porous monolith was limited due to the material's brittle nature, and the chemical properties of

the system could not be readily tuned.

Following this work, Jones *et al.* sought to expand this strategy to use polymeric BμEs as a way to develop materials with tunable chemical or mechanical properties that retain the structure of the BμE. To this end, they developed a macroporous polyethylene template from a polymeric BμE of polyethylene (PE), poly(ethylene-*alt*-propylene) (PEP), and PE-*b*-PEP.[124] The porous PE template was obtained by forming the BμE morphology in the melt, then rapidly crystallizing the PE domain by quenching the blend below the crystallization temperature of PE. Then, at room temperature, the PEP homopolymer could be readily removed from the monolith by immersing the sample in tetrahydrofuran (THF) to yield a PE template with macropores averaging 78 nm in diameter. Semi-crystalline PE is intractable in any solvent at room temperature, but it can easily be dissolved in a solvent such as toluene at elevated temperature.[123] Jones *et al.* exploited these properties of PE by backfilling the pores of the PE templates with precursors to materials of interest, curing them, and removing the PE either by thermal degradation or selective dissolution to generate materials which maintained the BμE morphology and exhibited the inverse structure of the PE template. This general scheme is shown in Figure 5.1.

Using this technique, Jones *et al.* developed bulk, macroporous materials including a ceramic,[124] an epoxy,[125] a polyurethane,[125] and a conductive polymer (poly(3,4-ethylenedioxythiophene), or PEDOT).[126] Further, they were able to extend the above method to create hierarchically porous silica by backfilling the PE pores with a mixture of silica and ionic liquid, then subsequently removing the PE and ionic liquid phases.[127] Within the pores, the silica and ionic liquid mixture formed a disordered bicontinuous network, so after the silica was cured and both the PE and ionic liquid were dissolved, the resulting silica solid had a hierarchical pore networks with a bimodal pore size distribution centered around pore diameters of 7 nm and 100 nm.

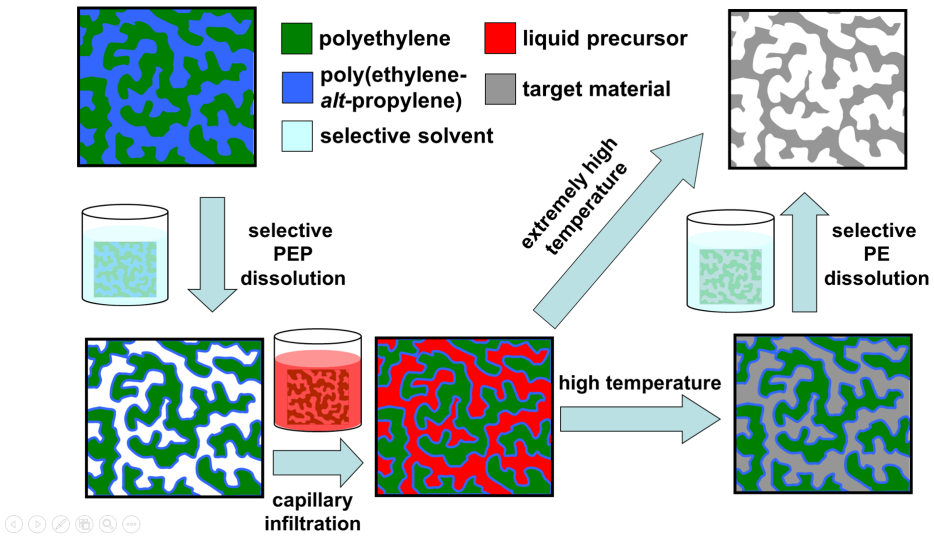

Figure 5.1: General scheme for the templating of porous materials from a polymeric bicontinuous microemulsion of PE/PEP/PE-PEP developed by Jones *et al.* A porous PE template is generated by selectively removing the PEP homopolymer. The pores of the template are then filled with material precursors. Then, either the material is cured at high temperature ($T < T_{m,PE}$) and the PE template is subsequently removed *via* dissolution, or the material is cured at extremely high temperature and the PE template is thermally degraded. Figure adapted with permission from Ref. 125. Copyright 2010 American Chemical Society.

Project overview

While extensive work has been done to demonstrate the versatility of using polymeric BμEs as templates for thick, bulk materials, little work has been done to adapt this general technique to develop materials that demonstrate both functionality and tunability. A combination of well-controlled, 10 to 100 nm feature sizes with a well-controlled three-dimensional network structure would be highly desirable in materials such as size-selective filtration membranes[89,190,192] and bulk heterojunction solar cells.[193,194] Unfortunately, the method developed by Jones *et al.* produces materials be too thick for such applications.

Therefore, the goal of the work described in this chapter was to expand upon the work performed by Jones *et al.* to develop a free-standing PE template less than 500 μm

thick from a polymeric BμE consisting of homopolymers PE and PEP and the diblock copolymer PEP-*b*-PE. A sufficiently thin template would permit the fabrication of thin, functional materials.

To achieve these goals, we first studied the phase behavior of PE/PEP/PEP-PE ternary blends in the bulk. The phase behavior was assessed *via* a combination of dynamic mechanical spectroscopy (DMS), transmission electron microscopy (TEM), small-angle X-ray scattering (SAXS), scanning electron microscopy (SEM), and nitrogen sorption. Once the phase behavior of blends was established in the bulk, a hot pressing technique was developed to maintain this bulk morphology in a thin ($\leq$ 500 μm) film which could then be used to template functional materials. Because flux through a membrane scales inversely with membrane thickness,[20] this membrane was designed so that it would allow sufficiently high throughput while still being thick enough to provide mechanical stability. The target material in this work was a thin epoxy membrane templated from the PE membrane.

Once the epoxy membrane was successfully synthesized with the desired morphology, it was tested in water filtration experiments. Initially, we intended to compare the experimentally measured flux of pure water through the membrane to theoretical predictions. This would have allowed determination of the extent of pore collapse or other defects. However, progress with these experiments was impeded by the poor mechanical properties of the epoxy membranes, as they would crack even under mild filtration conditions, likely due to incomplete cross-linking of the epoxy monomers. To overcome this obstacle, filtration experiments were instead attempted with the PE membrane which had previously been designed as a template, but a skin layer on each side of the PE membranes prevented flow through most of the membranes. Despite these setbacks, the work described in this chapter provides an in-depth look at the phase behavior of PE/PEP/PEP-PE systems, while the hot pressing technique developed through this work could be readily extended to other systems where control of thickness is important.

5.3 Experimental Section

Polymer synthesis

Polyethylene (PE), poly(ethylene-*alt*-propylene) (PEP), and PEP-*b*-PE were prepared following established procedures.[124] Briefly, polybutadiene (PB), polyisoprene (PI), and PI-*b*-PB were anionically synthesized in cyclohexane at 40 °C, then terminated with methanol. These precursors were then hydrogenated using a platinum/rhenium catalyst at 500 psi of H_2 and 170 °C in cyclohexane for 12 hours. The resulting solutions were then filtered, and the polymers were precipitated in a 3:1 volumetric mixture of methanol to isopropanol and dried under dynamic vacuum overnight. ^{1}H NMR spectroscopy indicated that the resulting polymers were fully saturated within experimental resolution, and SEC confirmed that the polymers did not degrade during hydrogenation. Differential scanning calorimetry (DSC) was performed at a ramp rate of 10 °C/min to determine the melting temperature (T_m) of the PE homopolymer and the PE block of PEP-PE.

Size exclusion chromatography (SEC)

The molecular weight of the unsaturated PI, PB, and PI-PB precursors was determined using a size exclusion chromatograph coupled with a multi-angle laser-light scattering detector. Absolute molecular weight was determined for the unsaturated precursors in THF using previously published values of the differential refractive index increment, dn/dc of 0.124 cm^3/g and 0.130 cm^3/g for PI and PB, respectively. For PI-PB, the average value of 0.127 cm^3/g was used. The molecular weights of the resulting, saturated PEP, PE and PEP-PE were calculated by taking into account the addition of two hydrogen atoms per monomer repeat unit.

Blend preparation

Blends were prepared *via* freeze-drying. Appropriate quantities of the three polymers were placed in a small volume of benzene, then heated to 70 °C and stirred until

the solution was homogeneously mixed. The solution was then quickly plunged into liquid nitrogen and, once frozen, quickly transferred to a room temperature vacuum oven. Blends were then dried under dynamic vacuum to the baseline pressure of the vacuum line ($<$ 100 mTorr) overnight to yield a fluffy, white polymer blend. For studies involving bulk monoliths, blends were then densified by transferring the fluffy blends to a glass ampule and heating the ampule to a desired temperature under vacuum, then quenching in either liquid nitrogen or a dry ice and isopropanol mixture.

Dynamic mechanical spectroscopy (DMS)

The linear-viscoelastic response of polymer blends was determined using a Rheometrics Scientific ARES strain-controlled rheometer. Blends were loaded onto a 25 mm diameter parallel plate geometry at room temperature, then brought to elevated temperature to allow the sample to flow and evenly fill the gap. Strain sweeps were first performed both above and below the order-disorder transition temperature (T_{ODT}) to determine the linear viscoelastic regime. Samples were then cooled below the anticipated T_{ODT}, and the storage (G') and loss (G'') moduli were measured as the sample was heated through the T_{ODT}. Upon heating, a sudden drop in G' was measured as the samples disordered. The width of this transition appeared to be a function of homopolymer loading, so the T_{ODT} was taken to be the average of this transition.

Transmission electron microscopy (TEM)

Samples for TEM analysis were prepared by heating blends above their T_{ODT} for at least 30 minutes to erase any thermal history, then cooling to the desired temperature and annealing overnight. Samples were then rapidly quenched in either liquid nitrogen or a mixture of dry ice and isopropanol. The rapid quench fixes the morphology through a combination of vitrification of both PEP and PE, then rapid crystallization of the PE upon warming. Samples were prepared for microtoming by trimming by hand to reveal a sample face with a superficial area of *ca*. 250 μm by 250 μm. These bulk samples were then stained with ruthenium tetroxide (RuO_4) vapors for 4 hours to enhance

contrast between microphases. RuO_4 selectively stains the liquid PEP domain, causing the PEP phase to appear darker than the semi-crystalline PE domain during TEM imaging. An additional benefit of bulk staining is that the RuO_4 vapors also harden the PEP domain, allowing the samples to be readily microtomed at room temperature. Thus, after staining, the samples were microtomed at room temperature with cut speeds of 2 to 4 mm/s using a Leica EM UC6 ultramicrotome and a MicroStar diamond knife. This unconventional procedure permitted the BμE-forming blends to be readily and rapidly microtomed to give sections approximately 70 nm thick. These sections were then collected on a tabbed copper grid (PELCO, 300 mesh, from Ted Pella, Inc.), and imaged using a FEI Tecnai G2 Spirit BioTWIN transmission electron microscope operating at a 120 kV accelerating voltage.

Scanning electron microscopy (SEM)

Samples which appeared bicontinuous *via* TEM were further analyzed *via* SEM. Samples were prepared by immersing blends annealed as described for TEM in THF to selectively remove the PEP homopolymer and yield a porous sample. Previous work by Jones has indicated that preparing samples for SEM analysis while preserving the morphology is nontrivial.[123] Thus, to preserve the internal morphology for proper imaging, bulk samples were trimmed to a small rectangular bar, then gripped using two sets of tweezers and subsequently fractured by snapping the sample outward like a twig while immersed in liquid nitrogen. The fresh face was then placed face-up on a metallic substrate and subsequently coated with platinum to minimize charging during imaging. Samples were imaged using a Hitachi S900 scanning electron microscope operating at an accelerating voltage set at either 3 or 5 kV.

Small angle X-ray scattering (SAXS)

Small angle X-ray scattering analysis was performed to further assess the morphology of samples. Due to the low inherent electron density contrast between PEP and PE, SAXS analysis could not be performed on bulk samples. Instead, SAXS analysis was

performed on samples that had been rendered porous by immersion in THF to remove the PEP homopolymer. These porous samples had greatly enhanced X-ray scattering contrast, allowing for well-resolved scattering data.

SAXS experiments were carried out at the Advanced Photon Source at Argonne National Laboratory at sector 12-ID-B. The porous samples were placed on Kapton tape and analyzed at room temperature. Isotropic scattering patterns were collected on a CCD area detector (Pilatus 2M). The 2D scattering patterns were azimuthally integrated to give the scattered intensity, $I(q)$, as a function of the scattering wave vector, $q = 4\pi\lambda^{-1}\sin(\theta/2)$.

Nitrogen sorption

Nitrogen sorption experiments were carried out using a Quantachrome Autosorb iQ (Boynton Beach, FL), which was used to assess the pore network and surface area of porous PE monoliths. This technique works based on the principle that a fluid confined within a pore will condense at a pressure, P, less than its bulk vapor pressure, P_0. Samples were placed in a glass stem and degassed for 24 hours prior to the start of the measurement. The vacuum chamber was then evacuated, the sample and a controlled amount of nitrogen was added to the stem. After the pressure equilibrated, the difference in the measured nitrogen pressure compared to the initial pressure was used to calculate the amount of nitrogen taken up by the porous sample. This process was repeated at a number of different nitrogen pressures, P, relative to its bulk vapor pressure, P_0, to track the volume of N_2 adsorbed as a function of relative nitrogen pressure, P/P_0. Throughout the experiment, the sample was maintained at a temperature of 77 K.

Preparation of epoxy membrane

An epoxy precursor solution was prepared using a previously described formulation.[195] Briefly, glycidyl end-capped poly(bisphenol A-*co*-epichloroydrin) (Sigma Aldrich, M_n = 348 g/mol) was combined with 4,4′-methylenedianiline in a 2:1 stoichiometric

ratio. Because these materials are, respectively, a viscous liquid and a solid at room temperature, these precursors were dissolved at ∼50 wt% in THF to yield a liquid precursor solution.

The epoxy membranes were prepared by backfilling the PE membranes with the epoxy precursors. PE membranes were placed on top of sheets of water-soluble plastic support film from Sulky (Kennesaw, GA). The epoxy monomer solution was then added drop-wise to each of the PE membranes. The pores of the membrane filled rapidly, as was evidenced by a change in the appearance of the membranes from opaque white to milky and transparent, consistent with a reduction in the refractive index contrast within the PE membranes as its pores were filled with solution. To remove the THF, the backfilled membranes were placed inside a desiccator and dried overnight under a steady flow of air. After drying, the surfaces of the membrane were gently wiped with a Kimwipe to remove any excess epoxy monomers. The epoxy was then cured by heating the membrane and support films to 90 °C overnight in air. The membranes were then placed into room temperature water to dissolve the support film and yield free-standing epoxy/PE membranes. Finally, the epoxy membranes were rendered porous by placing the membranes into toluene at 70 °C to remove the PE. Gravimetric analysis confirmed that both that the epoxy had successfully reacted and that the PE was completely removed within *ca*. 10% uncertainty.

5.4 Results: Phase behavior of bulk blends

While studying the phase behavior of blends to locate the bicontinuous microemulsion channel so that functional materials could be made, several interesting and unexpected findings occurred. This section of the chapter focuses on the work done that attempted to locate the channel, and concludes with the observation that, although the BμE morphology could be obtained, no BμE channel was found. In the subsequent discussion section, this finding will be presented in the context of previous work on PE/PEP/PE-PEP ternary blend systems.

For this study, two blend systems were synthesized and characterized. Although

both blend systems share a common PEP-PE diblock copolymer, the homopolymers used in each system are different. The first system consisted of PE and PEP homopolymers each with a M_n slightly more than 20% of the M_n of the block copolymer. This initial system was used both to establish the blend preparation procedure and also investigate the phase behavior of these systems. Unfortunately, after studying the phase behavior, there was not enough homopolymer remaining to begin the templating portion of the work. As a result, additional PE and PEP homopolymers were synthesized that each had a M_n slightly *less* than 20% of the block copolymer. Although the molecular weights of these sets of homopolymers are close, the resulting ternary blend phase behavior is slightly different, as will be seen. Thus, results from both systems will be considered in this chapter. Thus, this allows a comparative study between two systems that differ in homopolymer molecular weight, potentially allowing any findings to be applied more broadly.

Polymer characterization

A summary of the characteristics of the block copolymer and the two sets of homopolymers is shown in Table 5.1. Note that here, and in future sections, the sets of homopolymers were be differentiated and identified by their α, the ratio of the geometric average of the homopolymer degrees of polymerization to the degree of polymerization of the diblock, *i.e.* $\alpha = \sqrt{N_{PE}N_{PEP}}/N_{PEP-PE}$.

Table 5.1: Characteristics of the polymers used in this study.

Polymer	Name in notebook	M_n (kg/mol)[a]	N_n	$Đ$	1,4 addition[c]	T_m (°C)[d]	T_{ODT} (°C)	f^c_{PE}	α
PEP-PE	AM-PEP-PE-3	89	1879	1.02	95% (PEP) 92% (PE)	106	133	0.49	-
PEP	AM-PEP-3	21.5	457	1.03	94	-	-	0	0.24
PE	AM-PE-2	21.5	452	1.05	91	111	-	1	
PEP	MI-PEP-5	17.3	364	1.03	94	-	-	0	0.20
PE	MI-PE-1	18.6	394	1.02	91	111	-	1	

[a]determined *via* LS-SEC, [b]Using published densities (ref[140]) and $V_{ref} = 0.1\text{nm}^3$
[c]determined *via* ^{1}H NMR, [d]determined *via* DSC

All polymers were synthesized with low dispersities and amounts of 1,4 addition that are expected from anionic polymerization in cyclohexane. In addition, the value

of α varies only slightly between the system, with a value of 0.24 for the "high" molecular weight homopolymers and a value of 0.20 for the "low" molecular weight homopolymers. As was discussed in Chapter 1, most previous studies of ternary blends targeted a value of $\alpha = 0.2$. This target was chosen so that, at least in theory,[146] the order-disorder transition temperature (T_{ODT}) of the symmetric PEP-PE diblock copolymer would match the critical temperature (T_c) of the PE/PEP binary homopolymer blend, thus increasing the likelihood that any ternary blend would have thermally accessible transition temperatures regardless of the relative loading of the homopolymers and the block copolymer. Because $(\chi N)_{ODT,PEP-PE} = 10.5$ and $(\chi N)_{c,PE/PEP} = 2$, an α of $2/10.5 \approx 0.2$ would result in $T_{ODT} = T_c$, assuming that $\chi_{PEP-PE} = \chi_{PE/PEP}$.[146]

As has been done previously, blends were prepared by fixing the volumetric ratio of the homopolymers to be equal, *i.e.* $\phi_{PE} = \phi_{PEP}$. As has been done in many previous studies, the phase behavior was studied as a function of temperature and total homopolymer volume fraction, $\phi_H = \phi_{PE} + \phi_{PEP}$.

PEP and PE have low refractive index and electron density contrast, so determining the T_{ODT} or the T_c of blends at various ϕ_H *via* traditional optical or SAXS methods is not possible.[123] Thus, due to these experimental challenges, the phase behavior was established using a combination of DMS, TEM, and SEM. SAXS was performed only on samples rendered porous, which appeared to exhibit a BμE morphology. The following two sections will present the results of these studies.

Phase behavior of bulk blends with α = 0.24

To establish the phase behavior of the ternary blends and locate compositions that exhibited a BμE morphology, a combination of DMS and TEM analysis was performed. In Figure 5.2, the elastic (G') and storage (G'') moduli of various blends were measured at a frequently of 0.5 rad/s upon while temperature was changed at a rate of 0.5 °C/min. All data was collected on heating except for the blend containing ϕ_H = 0.84, which was collected on cooling.

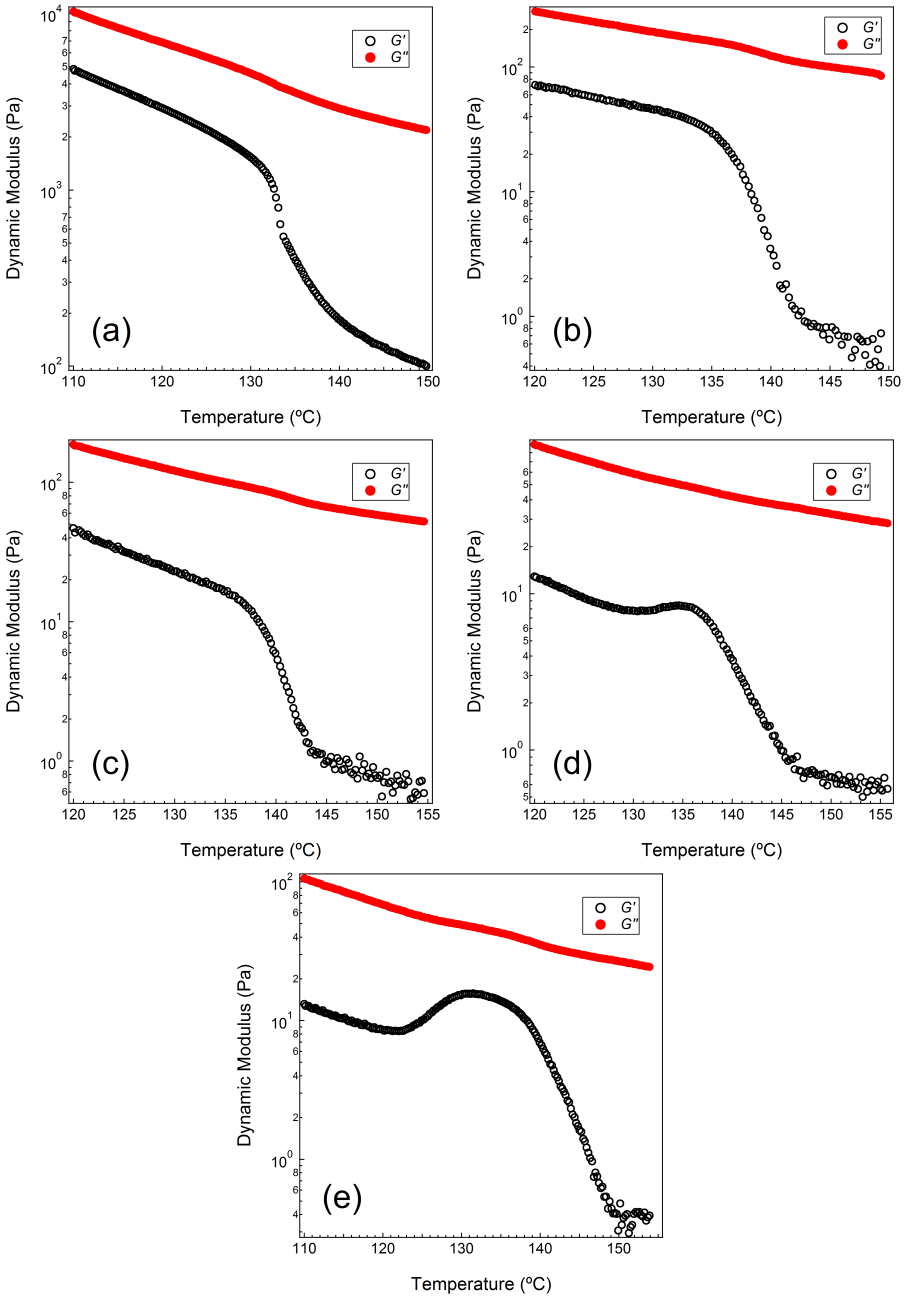

Figure 5.2: Temperature sweeps of blends (α = 0.24) containing (a) ϕ_H = 0, (b) ϕ_H = 0.84, (c) ϕ_H = 0.86, (d) ϕ_H = 0.9, and (e) ϕ_H = 0.92.

In all cases, the blends exhibit a sharp decrease in G' upon heating. This drop in modulus is expected to occur when a microstructured polymer with long-range order disorders, but such a drop in modulus may also be the result of phase separated blends with significant interfacial area going through a T_c. Additionally, blends with $\phi_H = 0.9$ and $\phi_H = 0.92$ show an increase in modulus prior to the sharp decrease, perhaps an indication of a morphological transition. Because this intermediate region exhibits a relatively high elastic modulus, it is possible that this transition region consists of a morphology with greater structure. The implications of this behavior will be further explored in the Discussion section.

After using rheology to probe the T_{ODT}s of the blends, TEM was performed to directly image both the diblock copolymer and various blend compositions that were prepared at several temperatures. As discussed in the Experimental section, the samples were stained with RuO_4 vapor, making the PEP domain appear dark. An assessment of the phase behavior, in addition to a phase diagram, will follow in the discussion section.

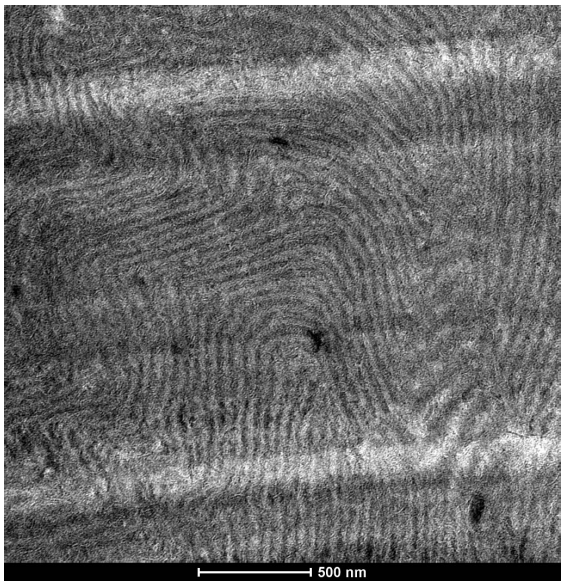

Figure 5.3: TEM of the disordered PEP-PE diblock after annealing at 135 °C.

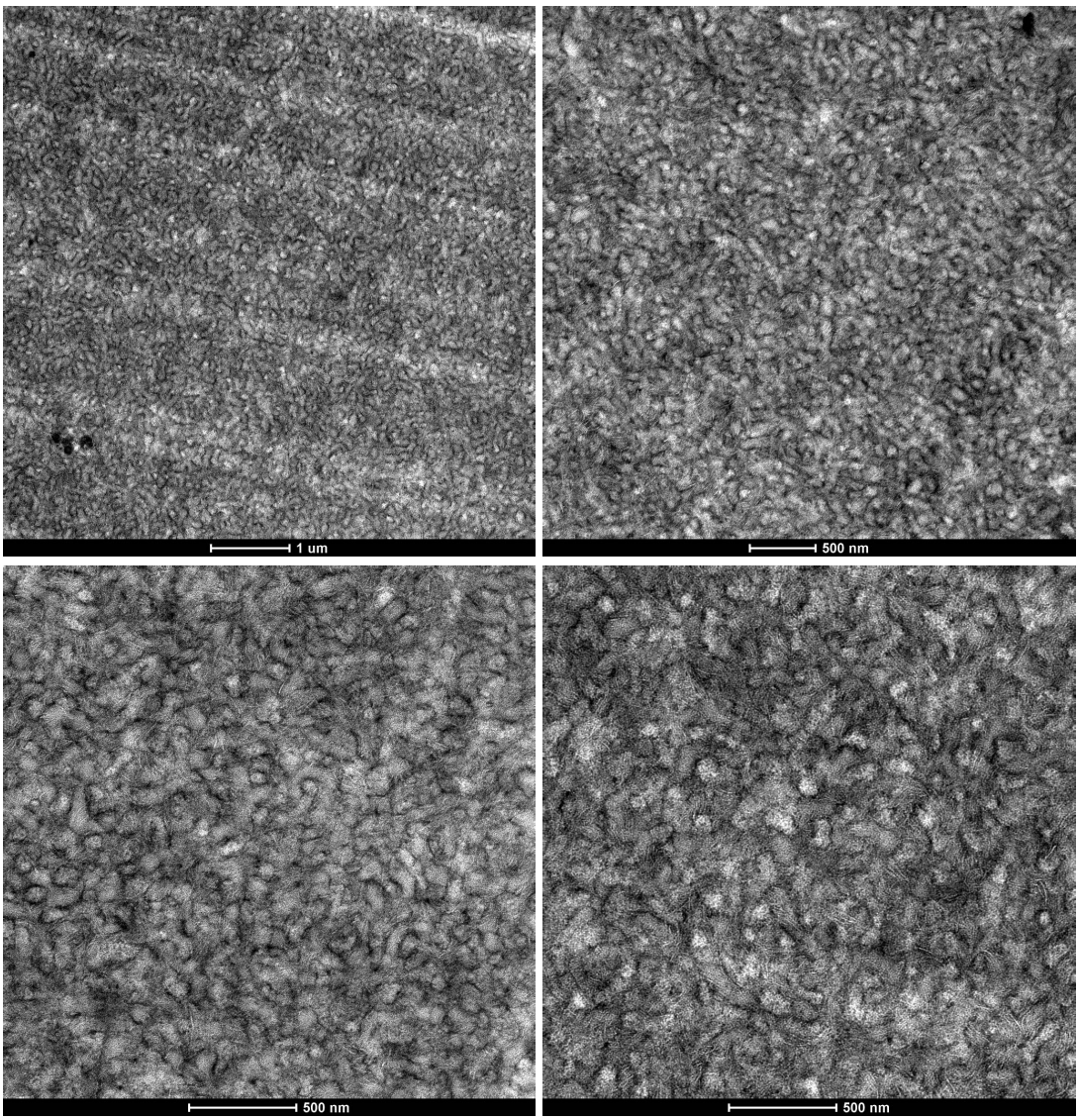

Figure 5.4: TEM of a blend (α = 0.24) containing ϕ_H = 0.80 annealed at 135 °C.

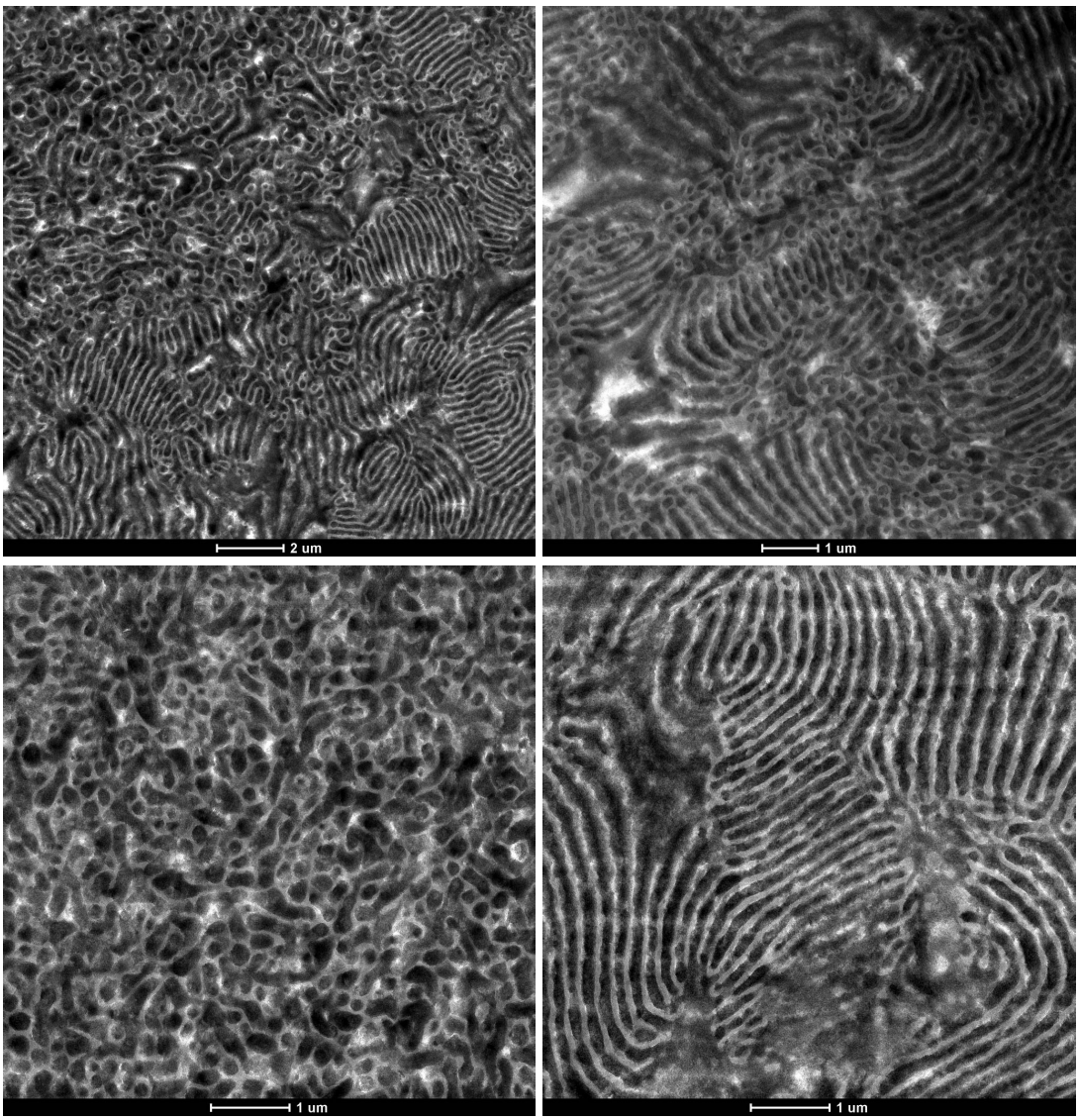

Figure 5.5: TEM of a blend (α = 0.24) containing ϕ_H = 0.84 annealed at 130 °C.

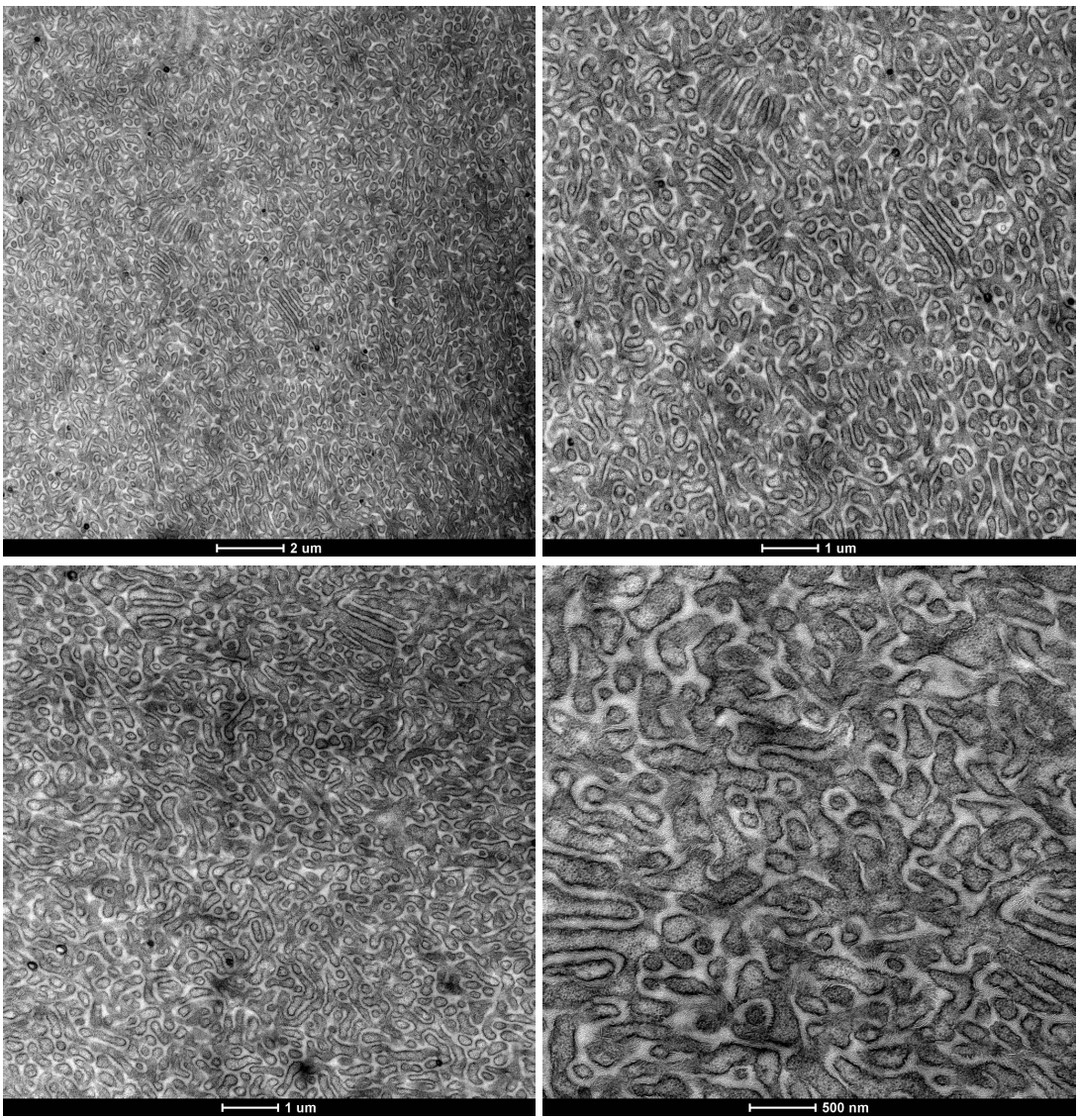

Figure 5.6: TEM of a blend (α = 0.24) containing ϕ_H = 0.85 annealed at 115 °C.

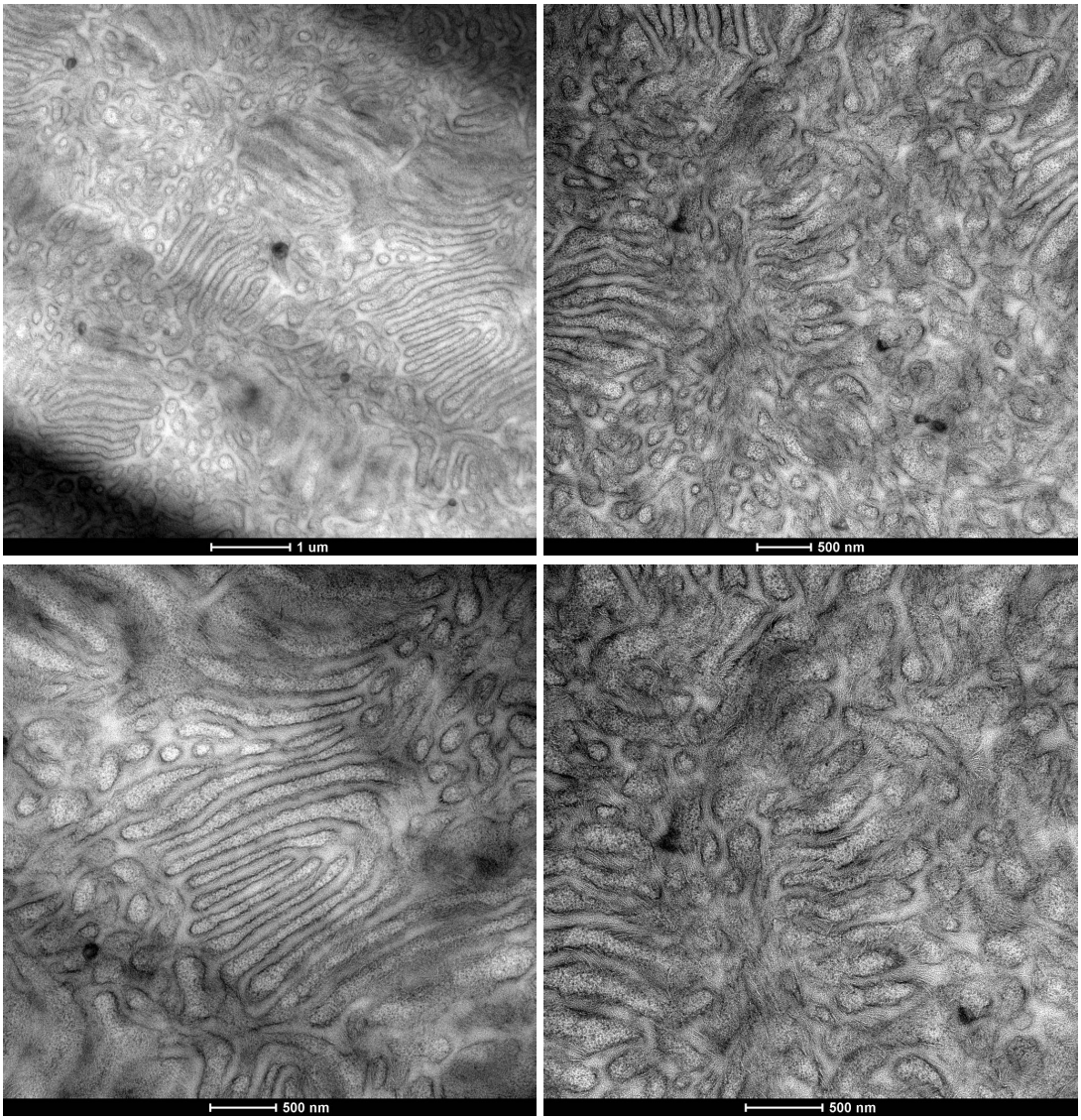

Figure 5.7: TEM of a blend (α = 0.24) containing ϕ_H = 0.85 annealed at 125 °C.

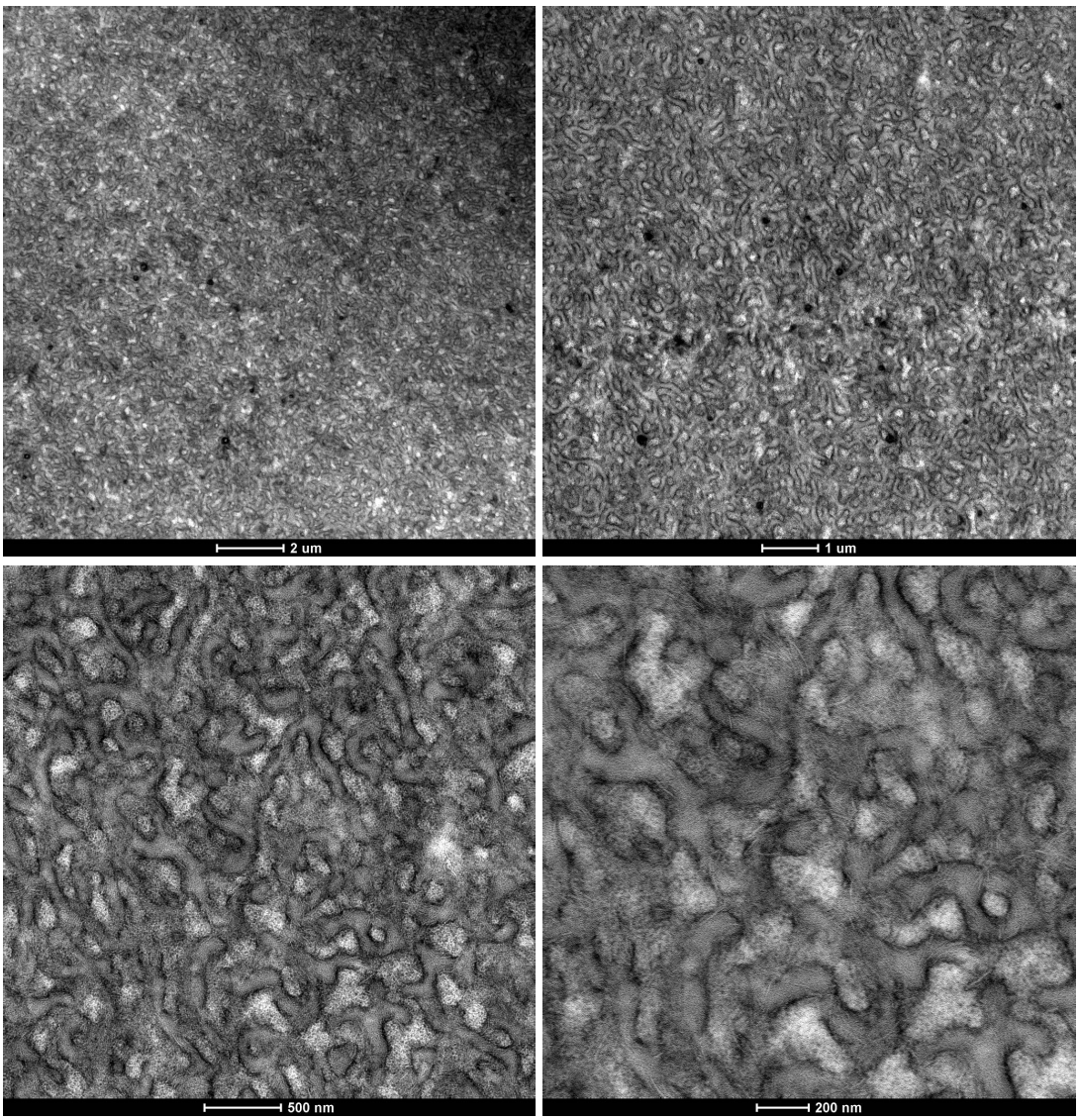

Figure 5.8: TEM of a blend (α = 0.24) containing ϕ_H = 0.85 annealed at 135 °C.

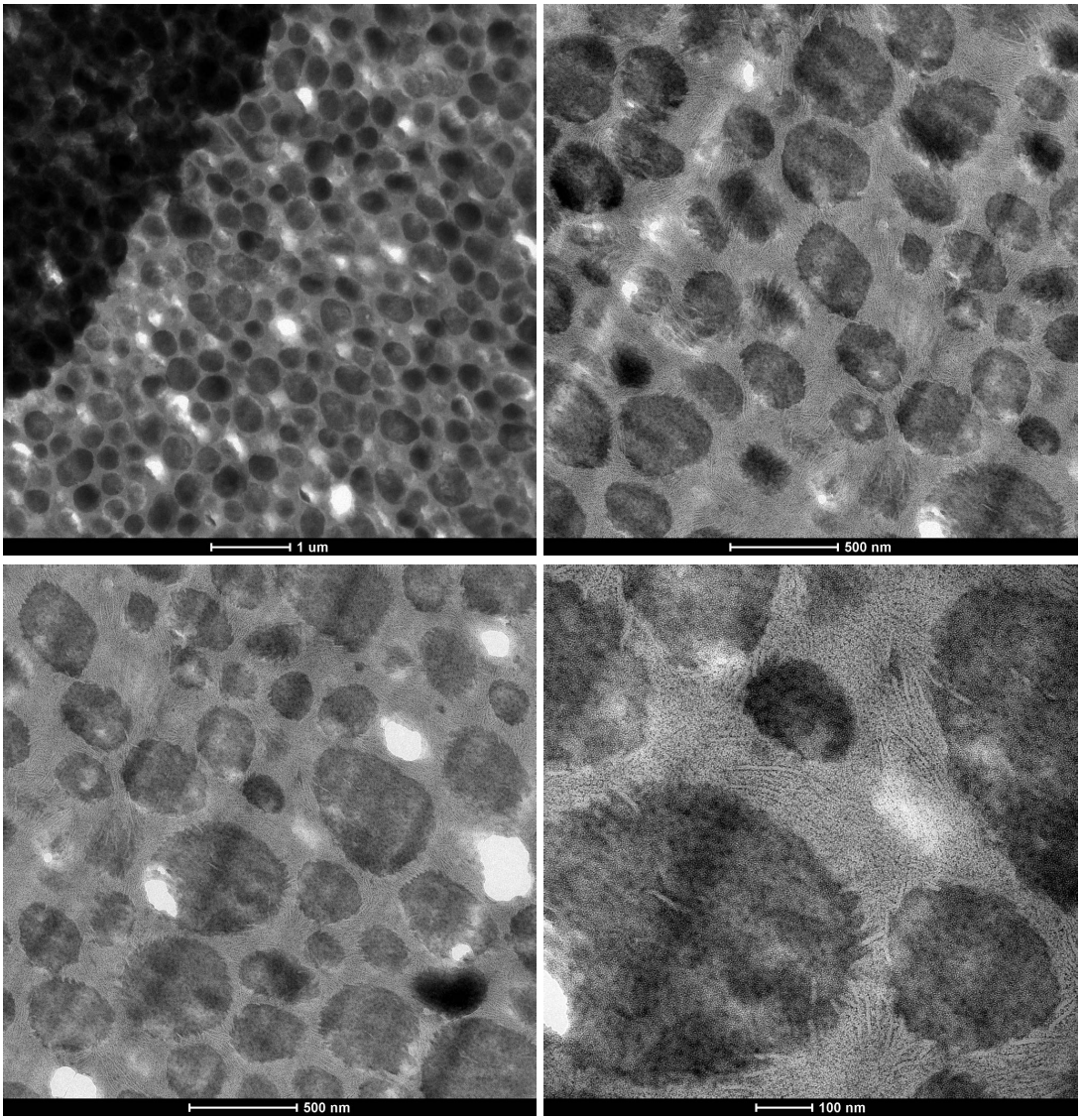

Figure 5.9: TEM of a blend (α = 0.24) containing ϕ_H = 0.86 annealed at 115 °C.

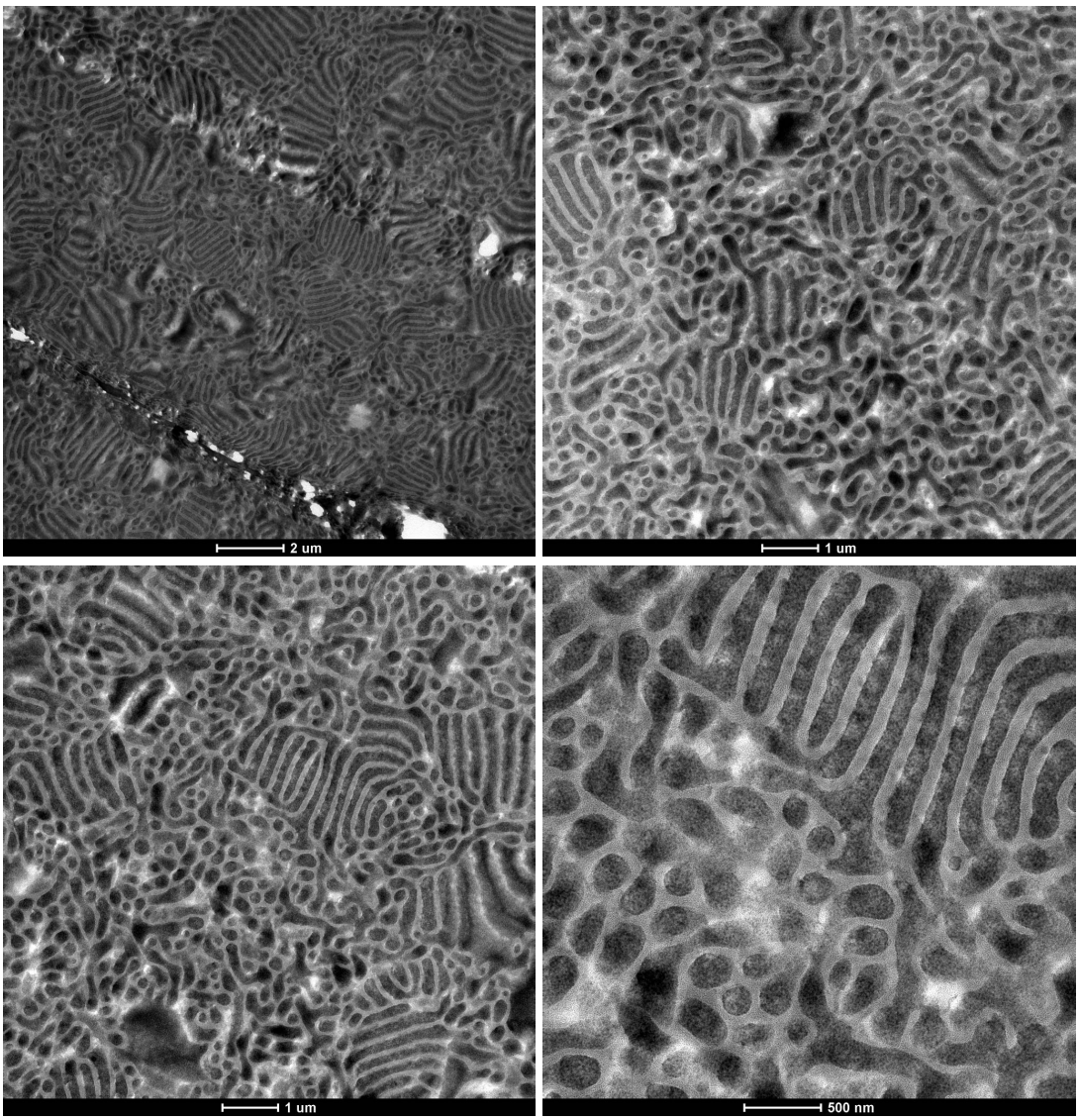

Figure 5.10: TEM of a blend (α = 0.24) containing ϕ_H = 0.86 annealed at 125 °C.

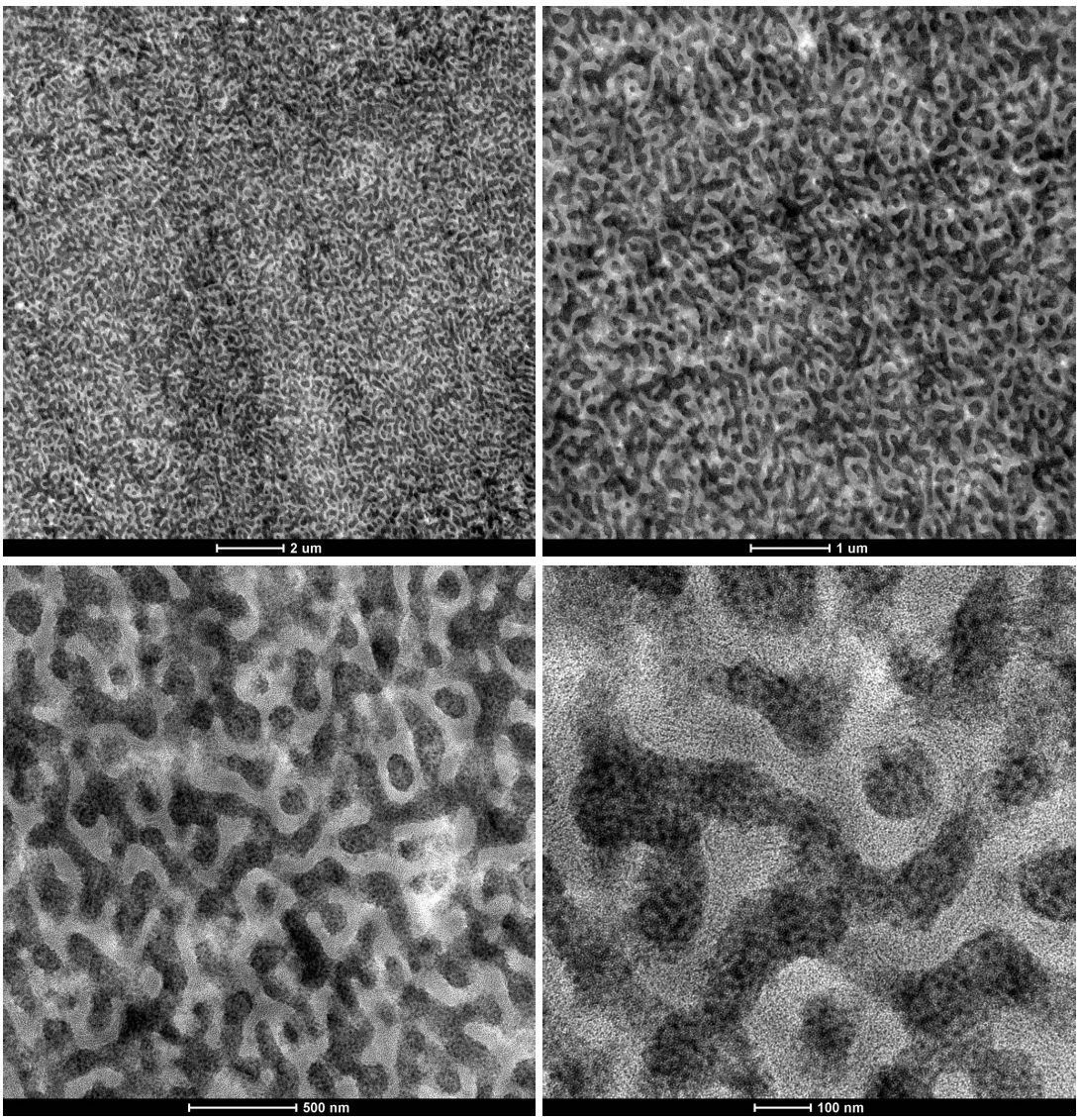

Figure 5.11: TEM of a blend (α = 0.24) containing ϕ_H = 0.86 annealed at 135 °C.

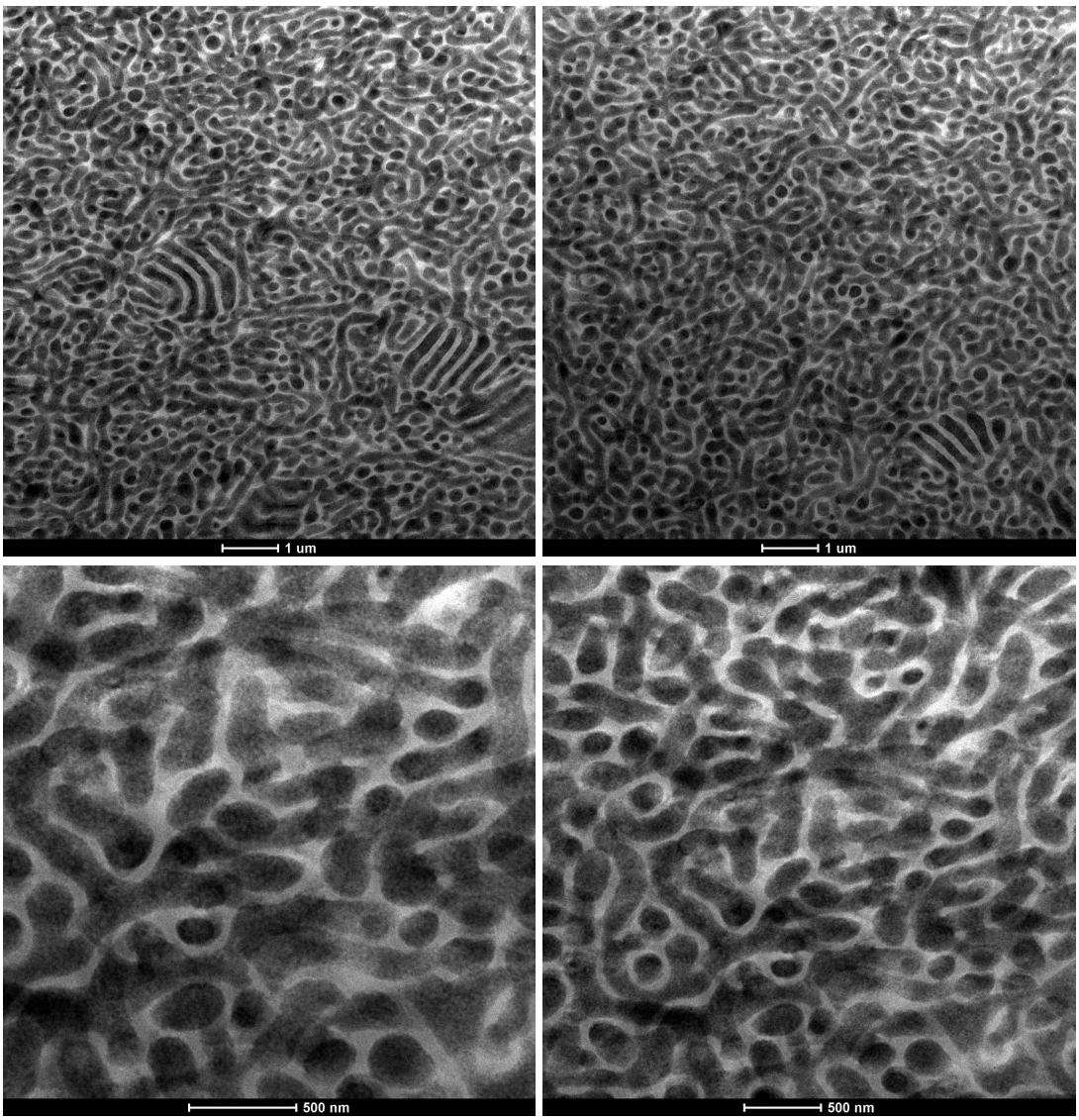

Figure 5.12: TEM of a blend (α = 0.24) containing ϕ_H = 0.87 annealed at 125 °C.

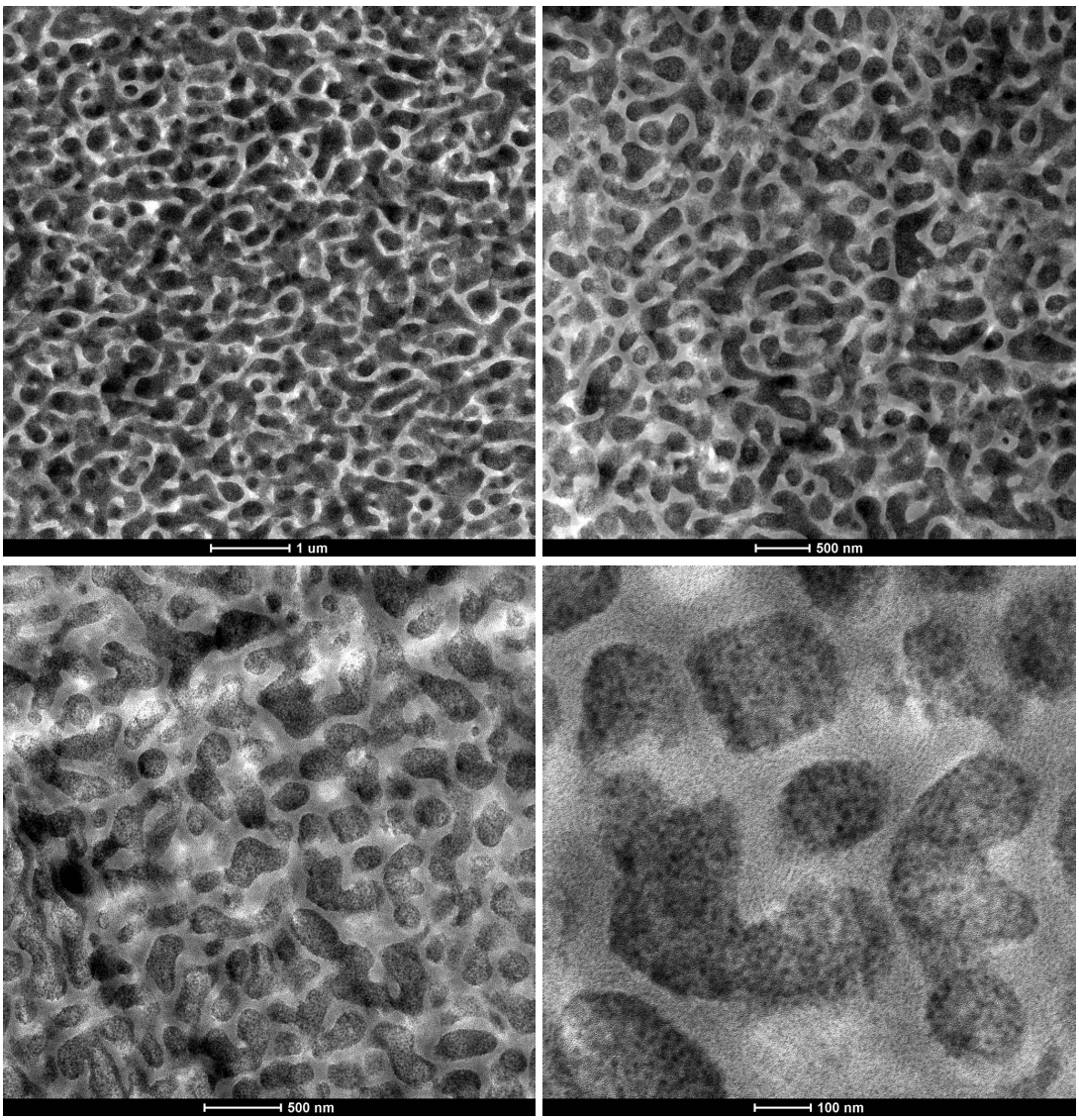

Figure 5.13: TEM of a blend (α = 0.24) containing ϕ_H = 0.87 annealed at 135 °C.

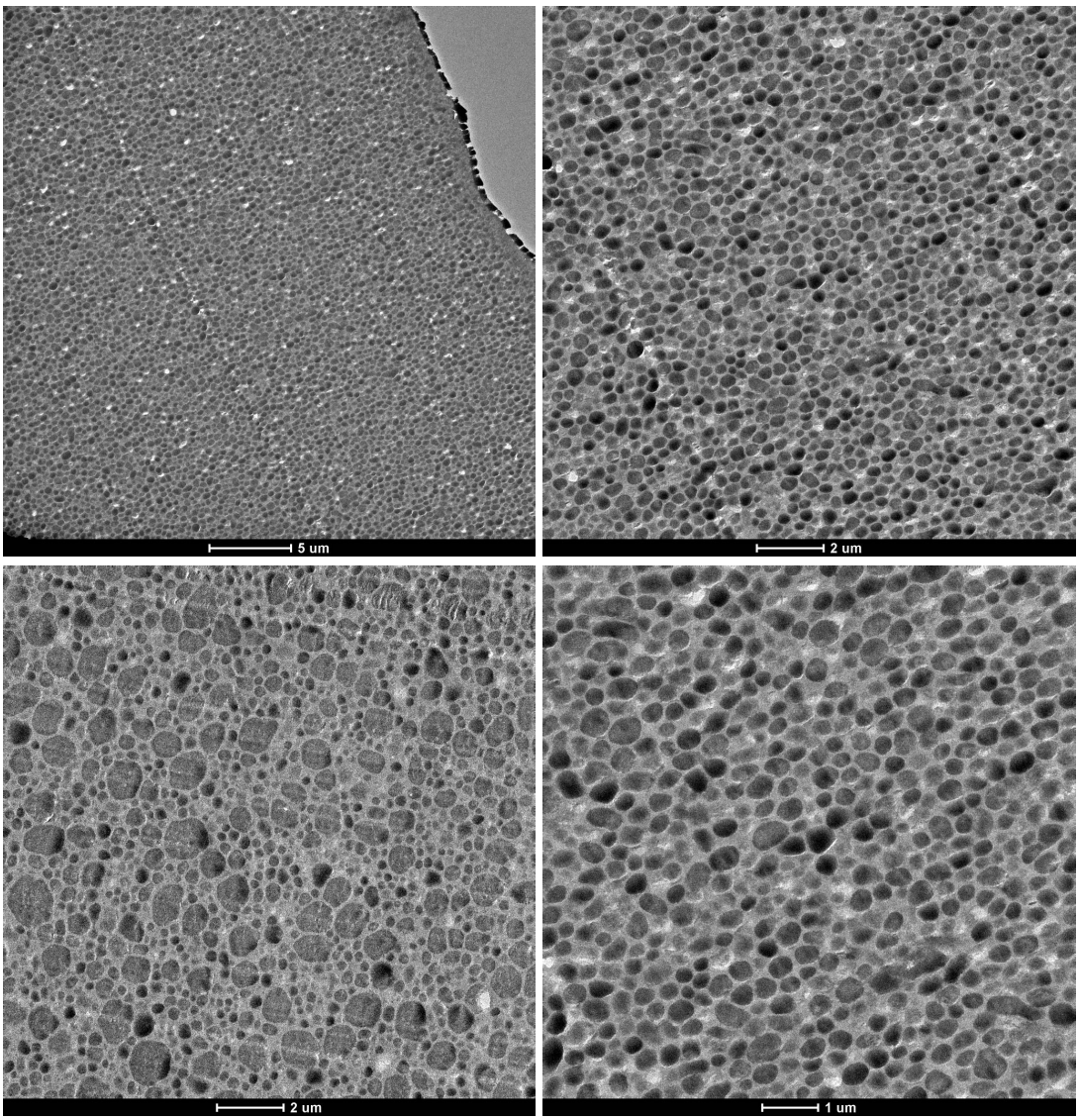

Figure 5.14: TEM of a blend (α = 0.24) containing ϕ_H = 0.88 annealed at 125 °C.

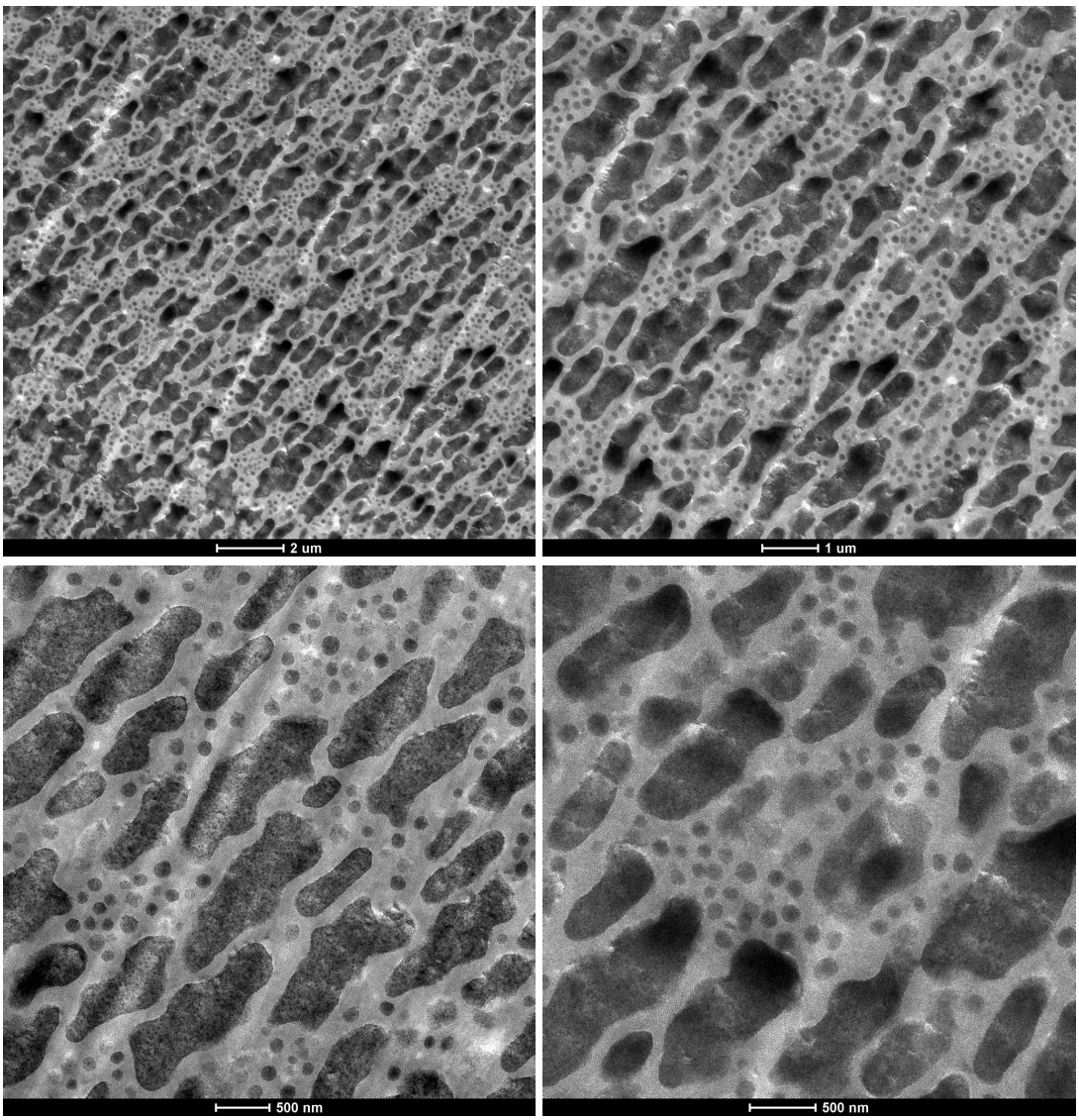

Figure 5.15: TEM of a blend (α = 0.24) containing ϕ_H = 0.91 annealed at 130 °C.

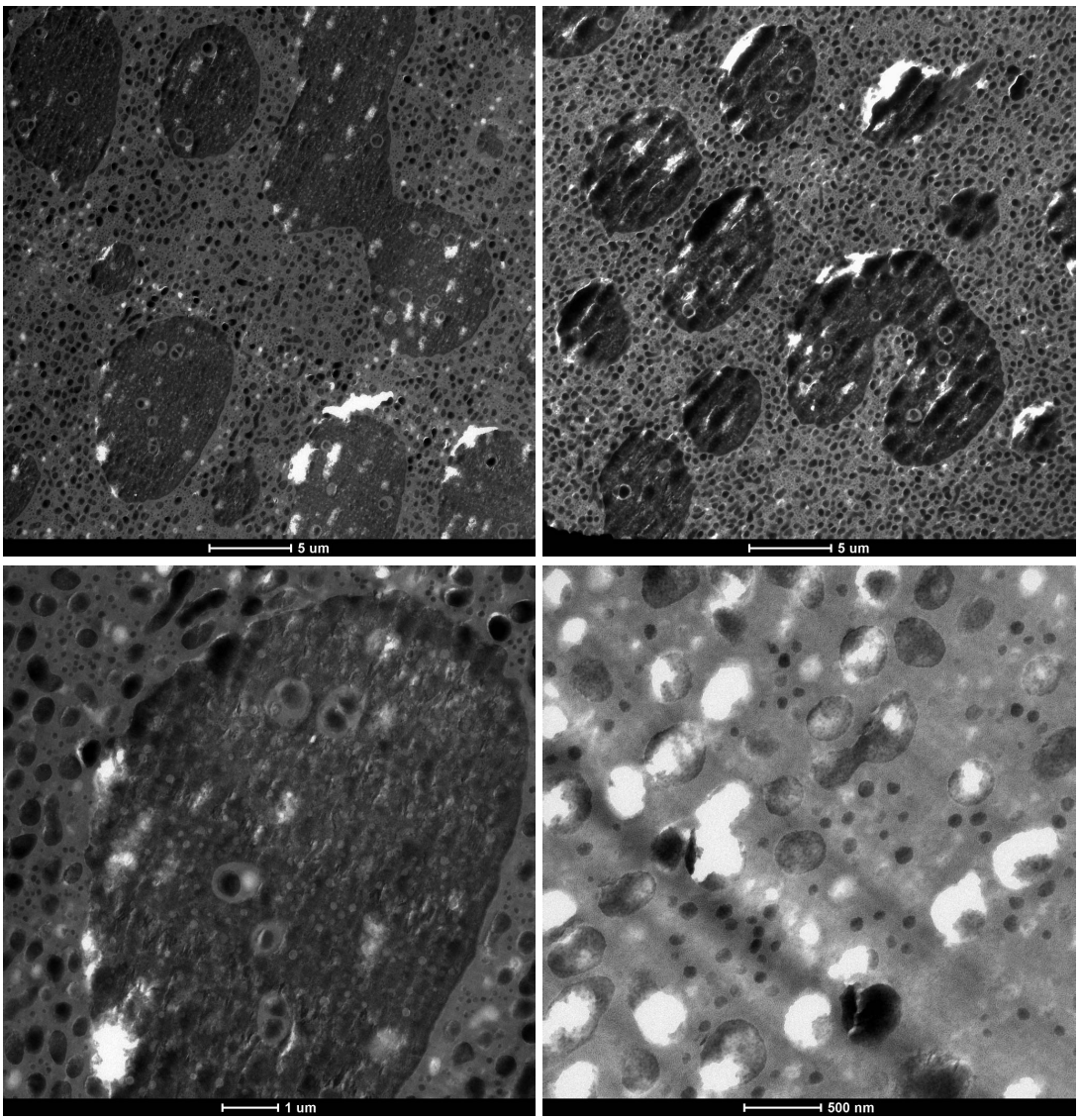

Figure 5.16: TEM of a blend (α = 0.24) containing ϕ_H = 0.92 annealed at 125 °C.

Phase behavior of bulk blends with α = 0.20

For the second set of homopolymers with α = 0.20, rheological analysis was not performed. Instead, TEM was again used to probe the morphology blend compositions close to the predicted Lifshitz composition where the BμE channel was expected to be found. Representative TEM images for several blend compositions and temperatures are shown in the following pages.

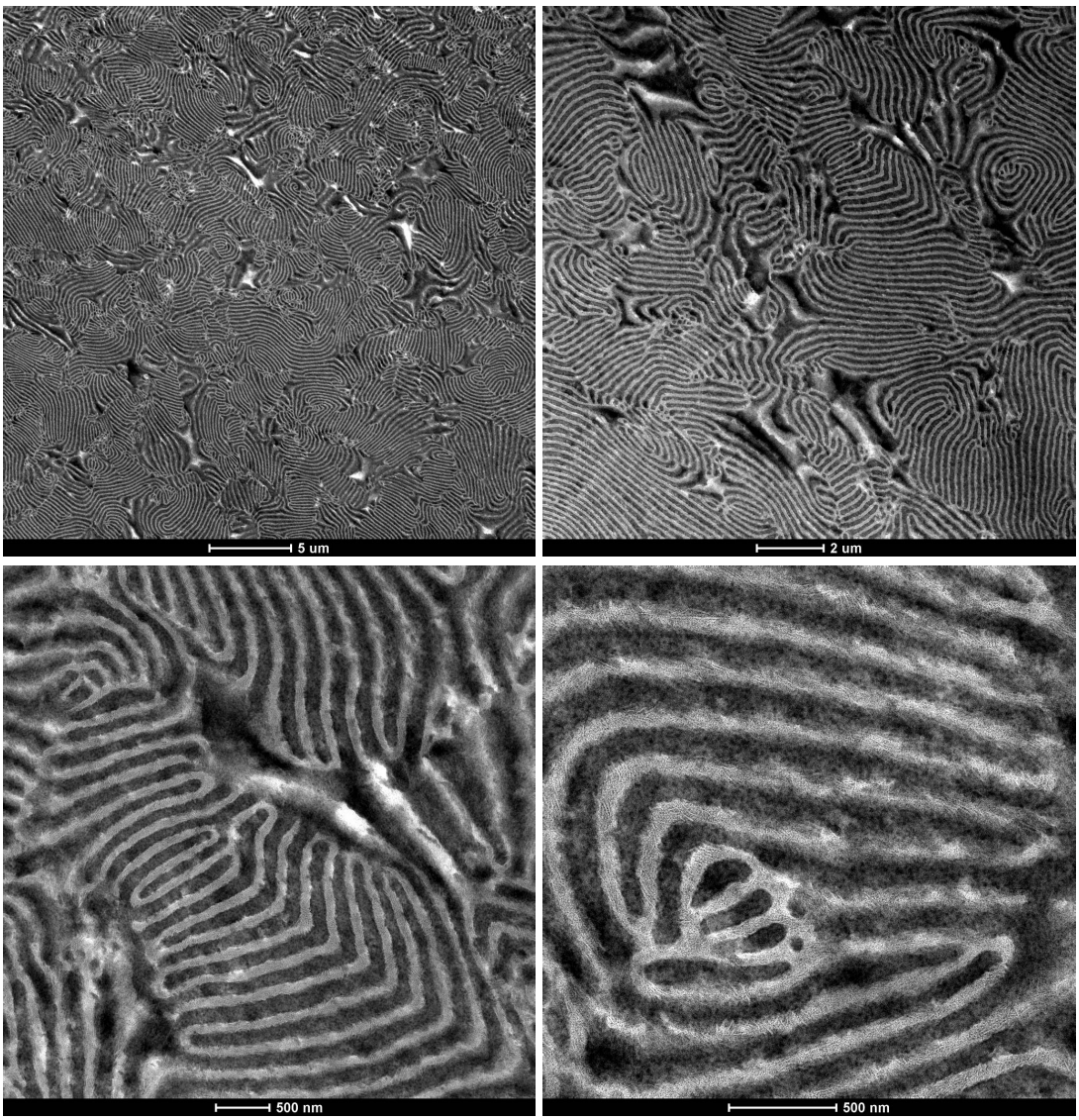

Figure 5.17: TEM of a blend (α = 0.20) containing ϕ_H = 0.86 annealed at 115 °C.

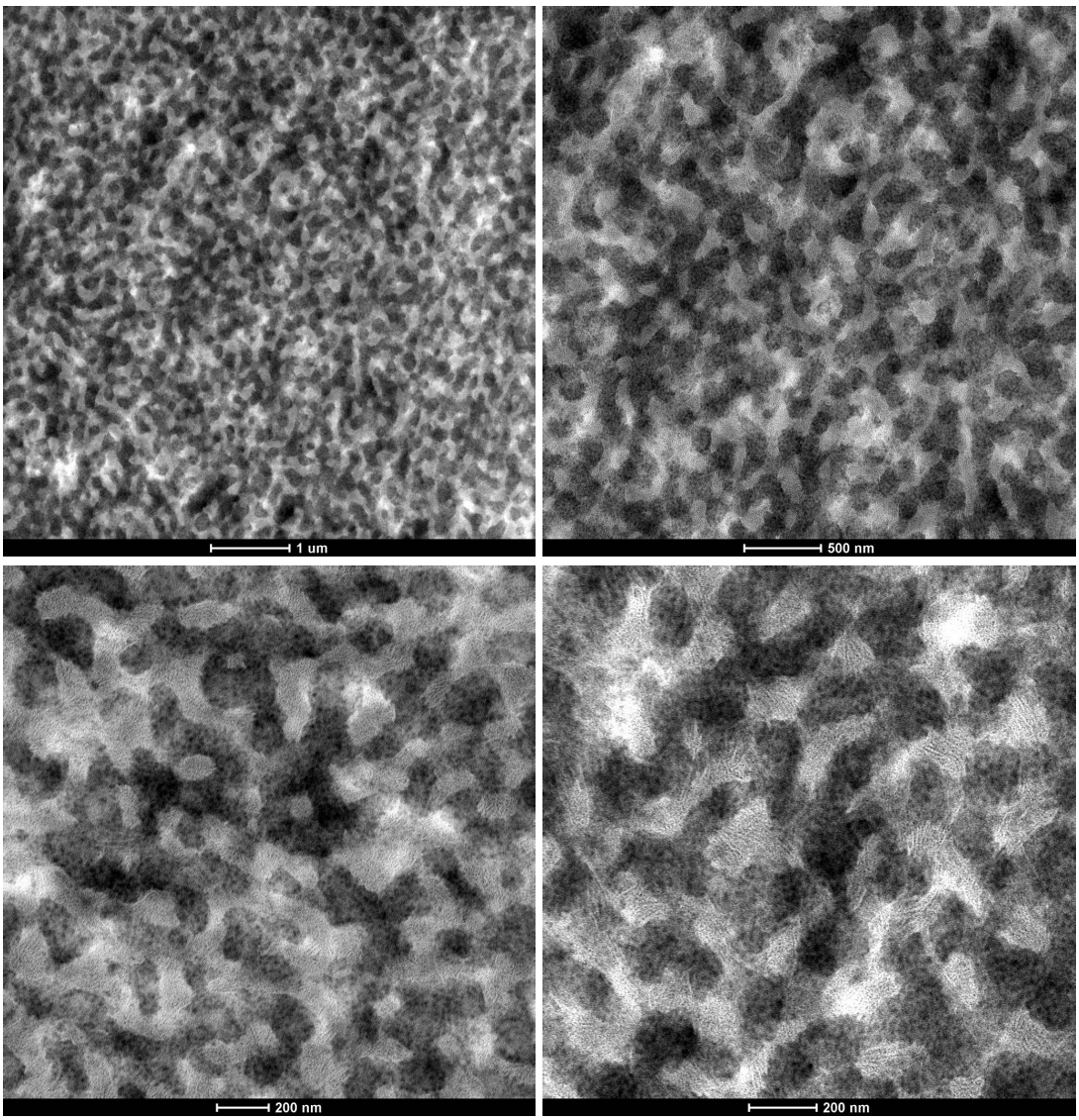

Figure 5.18: TEM of a blend (α = 0.20) containing ϕ_H = 0.87 annealed at 125 °C.

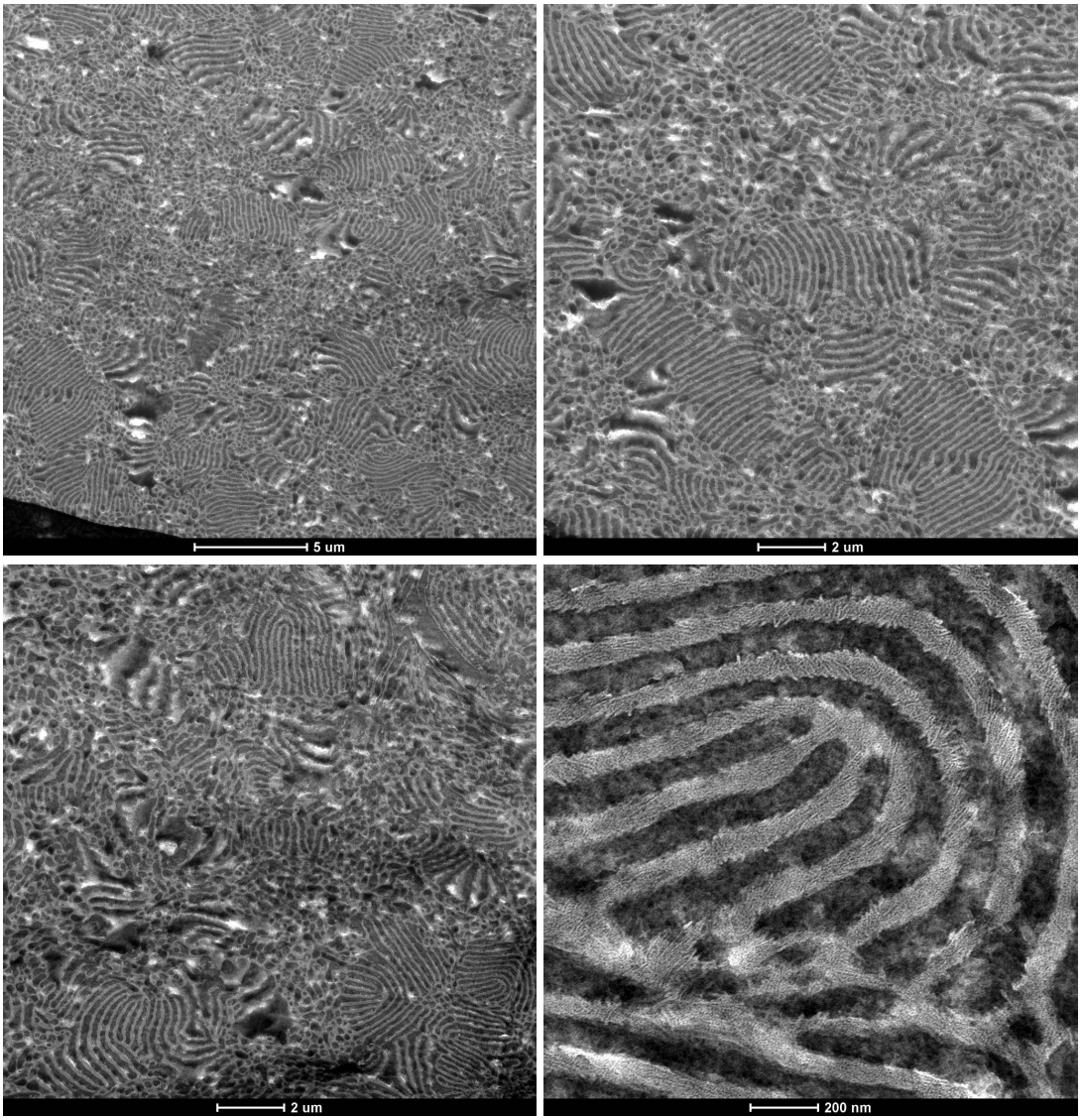

Figure 5.19: TEM of a blend (α = 0.20) containing ϕ_H = 0.88 annealed at 115 °C.

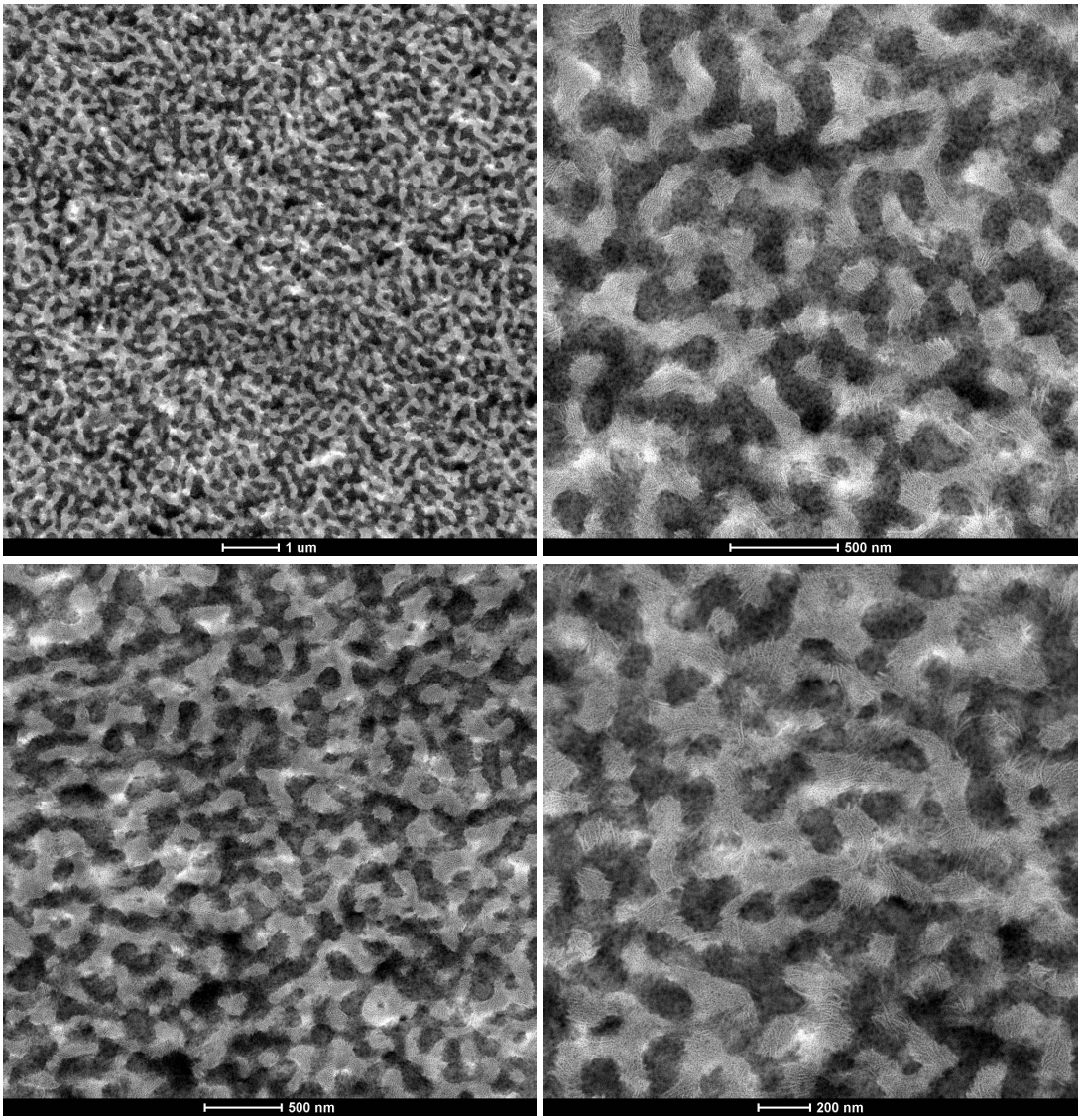

Figure 5.20: TEM of a blend (α = 0.20) containing ϕ_H = 0.88 annealed at 125 °C.

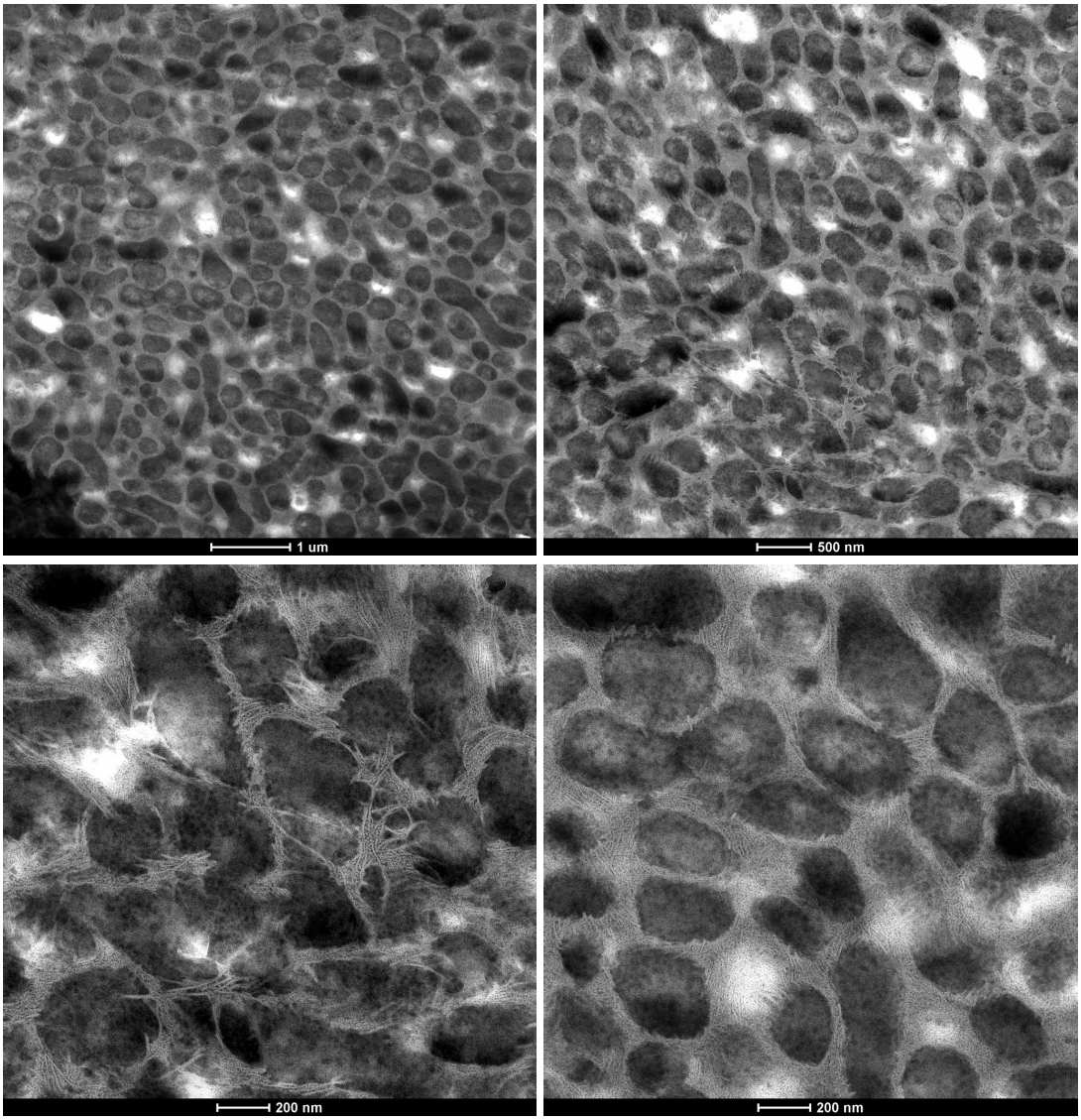

Figure 5.21: TEM of a blend (α = 0.20) containing ϕ_H = 0.89 annealed at 115 °C.

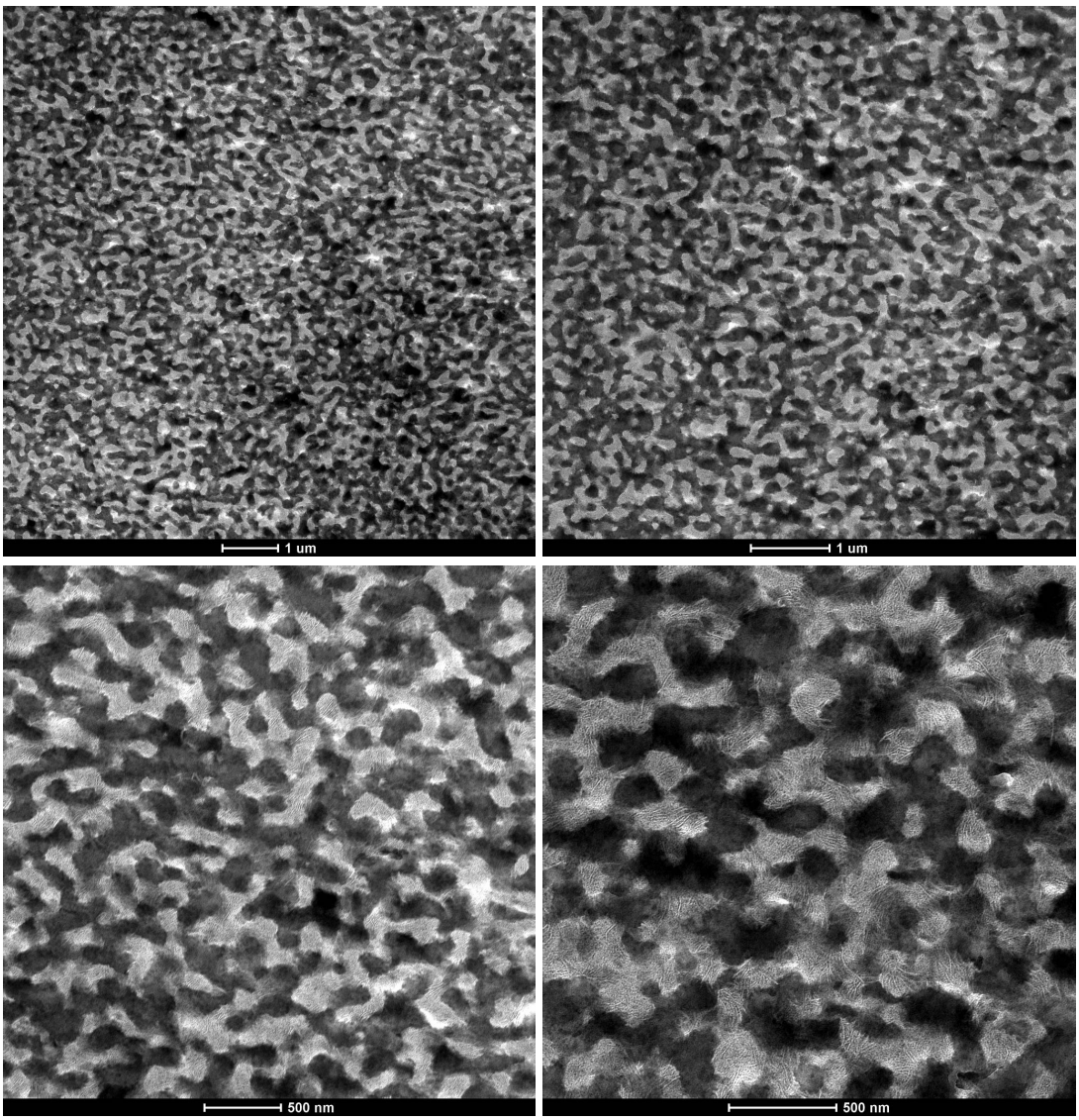

Figure 5.22: TEM of a blend (α = 0.20) containing ϕ_H = 0.89 annealed at 125 °C.

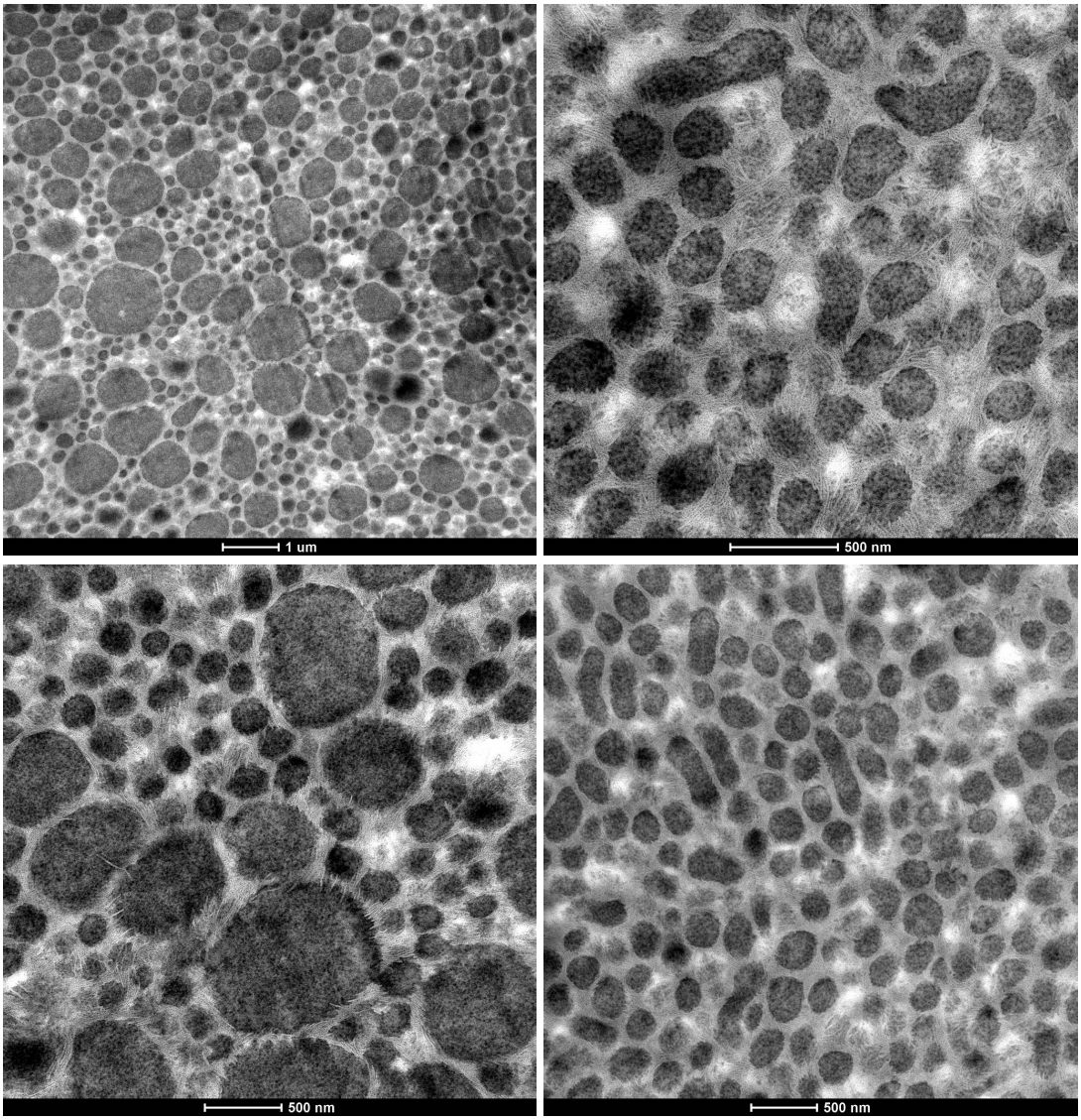

Figure 5.23: TEM of a blend (α = 0.20) containing ϕ_H = 0.90 annealed at 115 °C.

5.5 Discussion: Phase behavior of bulk blends

Figure 5.3 suggests that the pure diblock copolymer exhibits a disordered, but structured, morphology at 135 °C, as expected based on the rheological analysis. Unfortunately, no images of the diblock copolymer were obtained after annealing at $T < T_{ODT}$.

For the ternary blend system in which $\alpha = 0.24$, the TEM images provide direct visualization of both lamellar and multiphase systems at compositions close to what should be the BμE channel. A summary of possible morphological assignments based on the TEM analysis are plotted in Figure 5.24. Rheological transitions, with error bars representing the width of the transition, are also plotted in the phase diagram. Although such analysis is highly speculative due to the lack of scattering data, it allows some insight into the unexpected behavior of this system. Perhaps the most striking result from this study was the lack of a BμE channel. Instead, the typical location of the channel was replaced by a region of coexistence between LAM and BμE. The only samples which exhibited a homogeneous BμE morphology are those that are close to, but still below, the T_{ODT} measured using rheology.

The rheological transitions plotted in Figure 5.24 allow some additional insight. The T_{ODT} of the pure diblock copolymer is 133 $\pm$ 1 °C (Figure 5.2a). For the blends, the T_{ODT}s ($\phi_H \leq 0.86$) and T_cs ($\phi_H \geq 0.9$) increase with increasing ϕ_H, as expected because $\alpha = 0.24 > 0.2$, leading to $T_{ODT,PEP-PE} < T_{c,PEP/PE}$. However, one intriguing result from Figure 5.24 is the increasing breadth of the transitions, shown by error bars, with increasing ϕ_H. In addition, multiphase samples with ϕ_H = 0.9 and 0.92 appear to go through a morphological transition upon heating that results in an increase in G'. The temperature window over which this "hump" persists appears to increase with increasing homopolymer content. The identity of this intermediate structure is not apparent, and unfortunately, all TEM imaging was performed at temperatures at or just below the onset of this transition. However, even if TEM analysis had been performed, it would not be conclusive, as the characteristic length scale for each of the phases in the multiphase region (microns to millimeters) is much greater than the maximum length

scale that can be probed by TEM analysis (hundreds of nanometers).

A provisional phase diagram for the blend system in which $\alpha = 0.20$ is shown in Figure 5.25. Analysis of the TEM for this system indicates that there is no also BμE channel for this system. Instead, at 115 °C, the blends transition directly from a LAM+BμE morphology at ϕ_H = 0.88 to multiphase at ϕ_H = 0.89. At slight higher temperatures, there appears to be a BμE morphology for blends annealed at 125 °C with ϕ_H = 0.87 to 0.89.

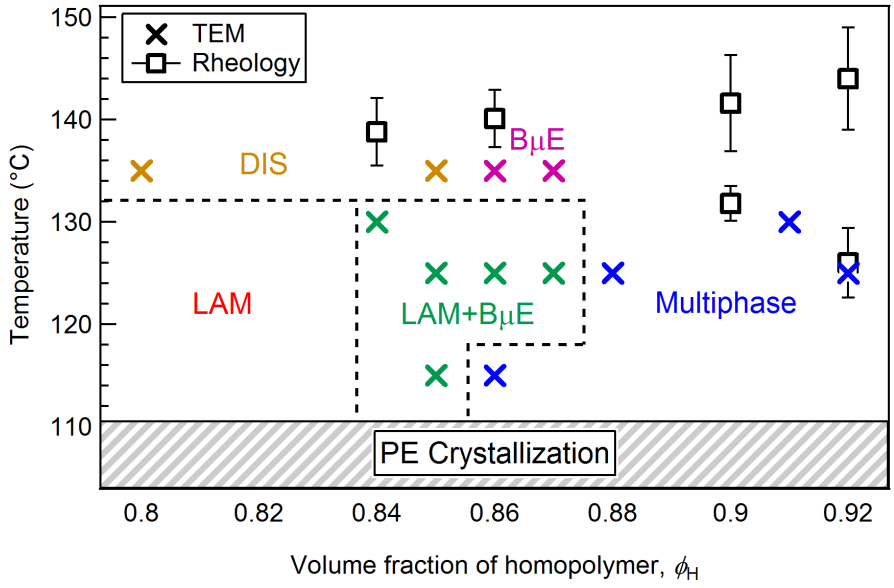

Figure 5.24: Phase digram for PE/PEP/PEP-PE blends with $\alpha = 0.24$. The dashed lines have been drawn to guide the eye.

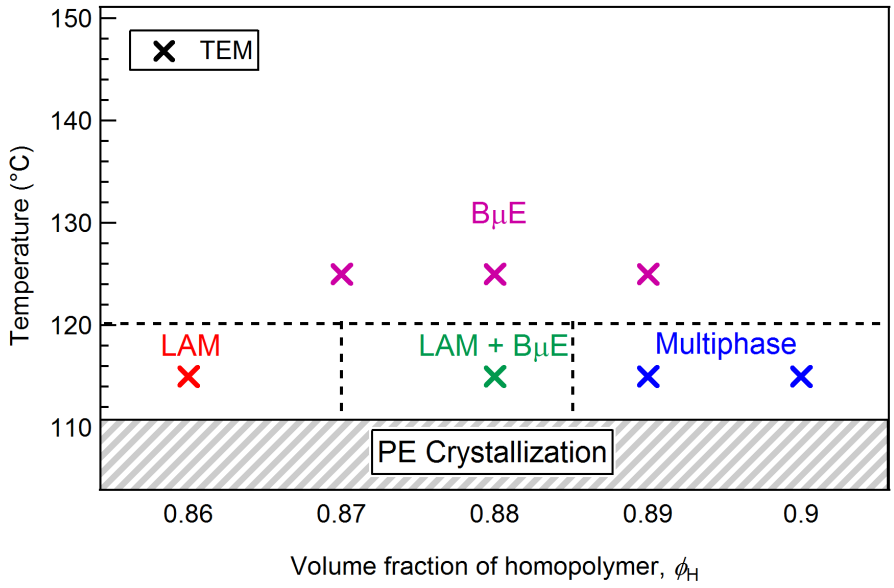

Figure 5.25: Phase digram for PE/PEP/PEP-PE blends with $\alpha = 0.20$. The dashed lines have been drawn to guide the eye.

Taken together, the limited analysis of both blend systems suggest several rather unexpected possibilities. (i) The PE/PEP/PE-PEP system does not exhibit a traditional BμE channel in which the BμE morphology can be found at a variety of temperatures at certain ϕ_H. (ii) Some morphologies that have previously been called a "bicontinuous microemulsion" are simply a highly structured and fluctuating disordered state that form just above the T_{ODT} of a LAM phase. (iii) The ability for a blend system to form a BμE channel depends on the block copolymer molecular weight. Each of these possible explanations will be explored in more detail below.

With regards to (i), it is possible that the limited TEM analysis simply failed to probe the correct homopolymer loadings, ϕ_H, where the BμE channel exists. Recent work by Hickey *et al.* has shown that the BμE channel can be as narrow as 0.5 vol% when blends are prepared along a congruent isopleth that takes into consideration the critical composition of the homopolymer mixture.[79] Thus, it is possible that a BμE channel could exist in the present system, but that it is confined to less than a 1 vol% window.

A BμE window that is this narrow would be surprising given prior studies on this blend system. The PE/PEP/PE-PEP system was first presented in 1997 by Bates *et al.*[94] In their work, a combination of small-angle neutron scattering (SANS) and TEM was used to show that the BμE morphology existed within a 2 vol% wide channel at temperatures below the extrapolated line of T_{ODT}s. Later, Jones *et al.* used a PE/PEP/PEP-PEP system for templating applications as described in the Background section of this chapter. In his thesis, Jones presented SANS data from blends over a 30 °C window and claimed that all samples exhibited a BμE morphology, but the data were abruptly cut off at low q at the onset of a scattering peak. The SANS data were fit with the Teubner-Strey model, but the lack of a complete peak and any low q scattering data limits the amount of information that should be extracted from the analysis.[123] TEM analysis could have confirmed the SANS analysis, but unfortunately, imaging was only performed at a single composition and temperature at the top of what was termed the BμE channel. This temperature was just slightly higher than where the anticipated T_{ODT} of the blend would have been, although no evidence of a LAM phase was found in the lower temperature SANS data.

Previous work by Hickey *et al.* has shown that disordered ternary blends with high homopolymer content have a highly structured disordered state that closely resembles the BμE morphology.[115] Thus, possibly in Jones' work and certainly in the current study, what has been called the BμE morphology may just be a disordered, but microstructured, LAM morphology, as described in point (ii) above. Even if this is the case, the formation of this "BμE"-like morphology in the disordered state does not preclude the existence of a BμE channel in the same system.

Considering the previous work with this and other similar systems, it is surprising that the current system does not exhibit an obvious BμE channel, especially given that both Bates *et al.* and Jones *et al.* reported a 2 vol% homopolymer wide channel.[94,123] One additional reason for the discrepancy could be tied to the overall molecular weight of the diblock copolymer (point (iii) above). In the Bates, Jones, and current studies, the molecular weights of the diblock copolymer, $M_{n,PEP-PE}$, were 119 kg/mol, 101 kg/mol, and 89 kg/mol, respectively.[94,123,168] Previous work by Cates *et al.* on

oil/water/surfactant systems has shown that the stability window of a microemulsion phase can be increased by lowering the bending modulus, κ, of the interface, which is dictated by the length of the surfactant.[196] Analogously, in ternary polymer blends, κ is primarily dictated by the block copolymer. As the molecular weight of the block polymer increases, then, the interfacial area per chain should decrease, which may result in a reduction in κ and an increase in the width of the BμE channel.

The challenge with confirming this conjecture, or drawing meaningful interpretations of any of the phase behavior described in this section, is that only a very limited number of experiments can be performed on the current system. Without the contrast necessary to perform X-ray or light scattering experiments, it is challenging to reach satisfying, definitive conclusions about the phase behavior of the systems presented in this chapter without using techniques such as small-angle neutron scattering.

5.6 Bulk PE templates generated from polymeric BμEs

After studying the phase behavior of blends in the bulk, compositions that were found to result in a BμE morphology were chosen for further analysis as potential candidates for porous templates. For all of the following templating studies, only the system with $\alpha = 0.20$ will be considered, as there was insufficient homopolymer from the $\alpha = 0.24$ system to perform a full templating study. As a reminder, the phase diagram for the $\alpha = 0.20$ system is shown in Figure 5.25.

To render the bulk PE/PEP/PEP-PE BμEs porous, the samples were immersed in THF for at least 12 hours, then dried. The weight loss in the sample through this process corresponded, within *ca.* 10% error, to the removal of all PEP homopolymer in the sample. It is important to note that only the PEP homopolymer is expected to be dissolved through this process; the PEP of the PEP-PE diblock remains due to the semi-crystallinity of the PE block.

In order to assess and confirm the blend morphology after washing out the PEP homopolymer, SEM was performed on the blends. Internal cross-sections of samples

generated from blends with ϕ_H = 0.88 and 0.89 are shown in Figures 5.26 and 5.27, respectively.

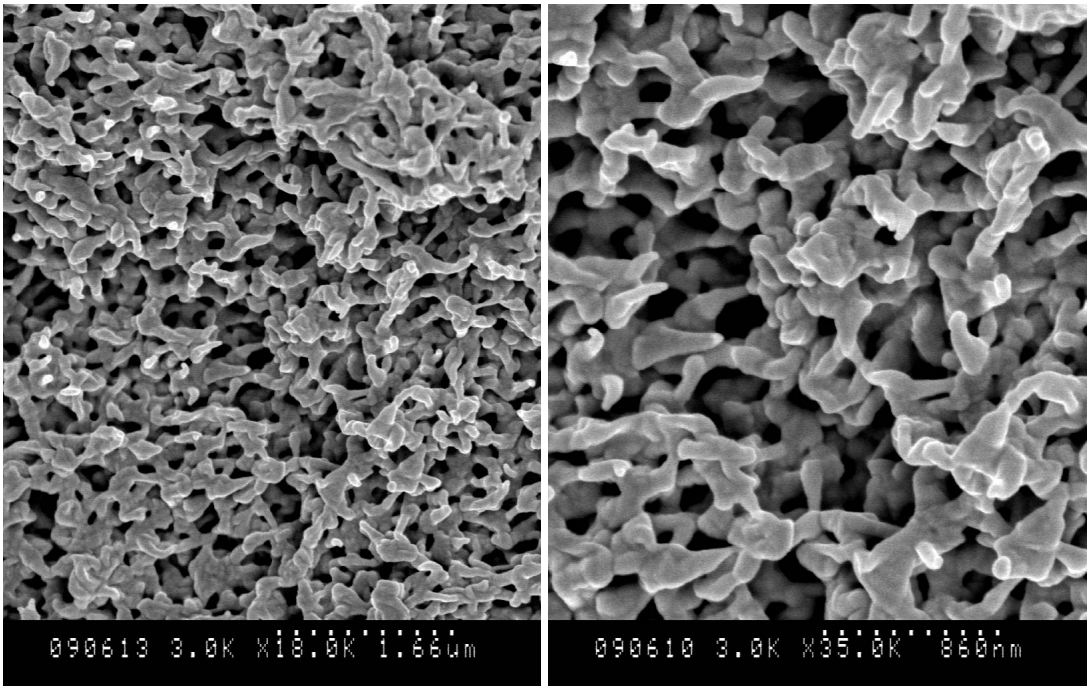

Figure 5.26: Cross-sectional SEM of a PE template generated from a blend containing ϕ_H = 0.88 annealed at 125 °C.

The appearance of the structures suggests that the bicontinuous morphology of the bulk blend was preserved during the washing-out process. To confirm this observation, small-angle X-ray scattering (SAXS) was performed on the porous monoliths. SAXS was also attempted on the blends prior to removal of the PEP homopolymer, but as discussed previously, the low electron density contrast between PEP and PE resulted in no detectable scattering. Shown in Figure 5.28 are the SAXS traces for porous templates made from blends containing ϕ_H = 0.88 and 0.89 that had been annealed at 125 °C.

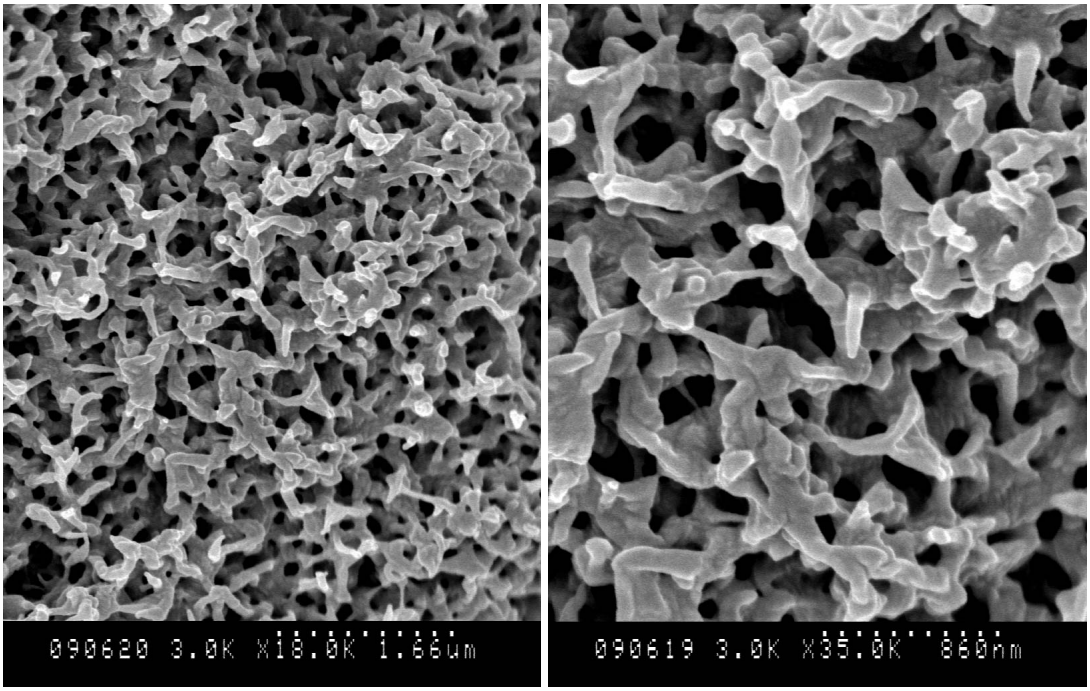

Figure 5.27: Cross-sectional SEM of a PE template generated from a blend containing $\phi_{\mathrm{H}} = 0.89$ annealed at 125 °C.

Also shown in Figure 5.28 are the fits of the data to the Teubner-Strey model, which is given by

$$I(q) = \frac{1}{a_2 + c_1 q^2 + c_2 q^4} \tag{5.1}$$

where $I(q)$ is the background-subtracted scattered intensity and a_2, c_1, and c_2 are fitting parameters.[100] From this model, several structural characteristics can be calculated. The domain spacing, d, correlation length, ξ, and amphiphilicity factor, f_{a}, are given by

$$d = 2\pi \left[\frac{1}{2} \left(\frac{a_2}{c_2} \right)^{1/2} - \frac{1}{4} \frac{c_1}{c_2} \right]^{-1/2} \tag{5.2}$$

$$\xi = \left[\frac{1}{2} \left(\frac{a_2}{c_2} \right)^{1/2} + \frac{1}{4} \frac{c_1}{c_2} \right]^{-1/2} \tag{5.3}$$

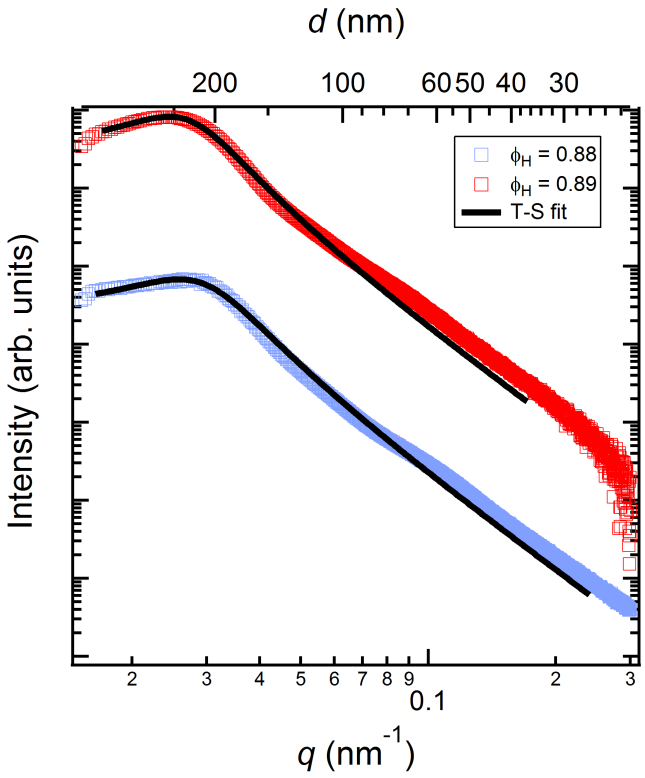

Figure 5.28: SAXS analysis of bulk porous PE from blends containing ϕ_{H} = 0.88 and 0.89 annealed at 125 °C.

$$f_{\mathrm{a}} = \frac{c_1}{(4a_2c_2)^{1/2}} \tag{5.4}$$

The amphiphilicity factor is a quantitative measure of structure in a microemulsion. A value of $f_{\mathrm{a}} = -1$ indicates that the system has a lamellar microstructure, while a value of $f_{\mathrm{a}} = 0$ corresponds to the crossover at which the spontaneous formation of interface is no longer energetically favorable.[100–102] Values for d, ξ, and f_{a} were calculated from the fits to the scattering data in Figure 5.28 and are presented in Table 5.2

To ensure that all of the porous network was accessible and of a constant size, nitrogen sorption experiments were performed. The data from these experiments are presented in Figure 5.29. The desorption branch of the nitrogen sorption data were modeled with the Barrett-Joyner-Halenda (BJH) model to obtain a pore size

Table 5.2: Structural parameters extracted from Teubner-Strey fits to the SAXS traces shown in Figure 5.28 from porous templates.

ϕ_H	d (nm)	ξ (nm)	f_a
0.88	227	102	−0.78
0.89	243	119	−0.81

distribution.[197] The pore size distribution obtained from this modeling is shown in Figure 5.30. The linear region of the nitrogen sorption data at low relative pressure were also used to calculate the total surface area of the porous PE templates using the Brunauer-Emmett-Teller (BET) equation.[198] These data, and the average pore size found from the BJH analysis, are shown in Table 5.3.

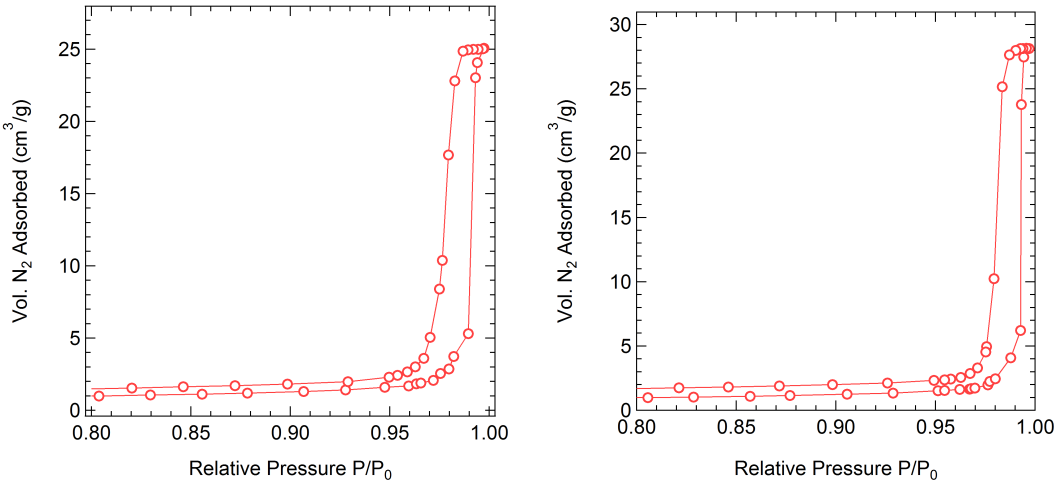

Figure 5.29: Nitrogen sorption isotherms collected from porous templates generated from blends containing (a) ϕ_H = 0.88 and (b) ϕ_H = 0.89.

Table 5.3: Properties of porous templates assessed *via* nitrogen sorption experiments.

ϕ_H	Average pore radius (nm)	Surface area (m^2/g)	Pore volume (cm^3/g)
0.88	45	20	0.52
0.89	53	24	0.69

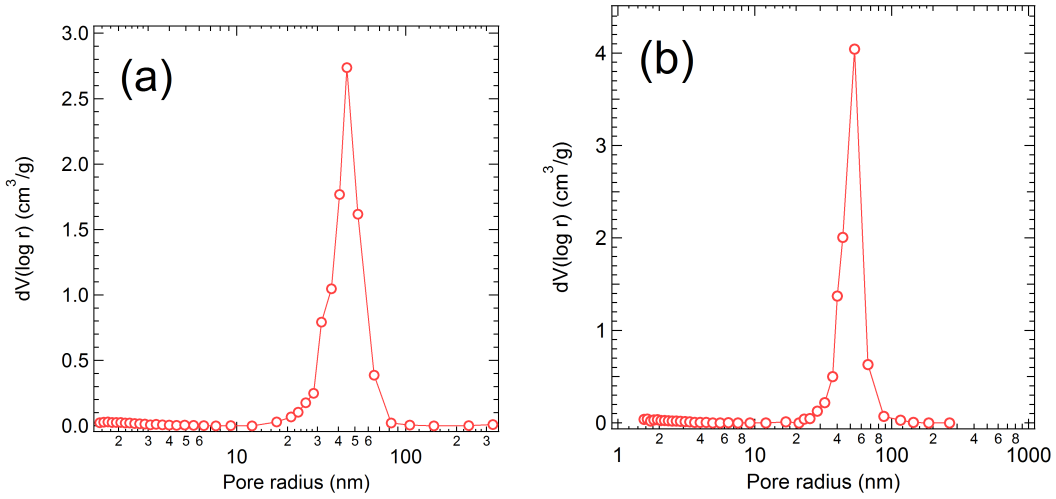

Figure 5.30: Pore size distribution of templates from BJH analysis of nitrogen desorption isotherms generated from blends containing (a) ϕ_H = 0.88 and (b) ϕ_H = 0.89.

5.7 Preparation and testing of epoxy membranes

Preparation of thin, polymeric BμE templates

After establishing that the BμE morphology is retained after the PEP homopolymer is washed out, a method was developed to retain this BμE morphology in thin membranes. Again, for this work, only the system with $\alpha = 0.20$ was used, the phase behavior of which is shown in Figure 5.25. Specifically, for filtration applications, the target was to obtain membranes of thickness no greater than 500 μm, a thickness that would to permit reasonable fluxes through the membrane while providing sufficient mechanical integrity.

Two methods were initially considered for the fabrication of thin, polymeric BμEs: solvent casting and hot pressing. In solvent casting, all three components would be mixed in appropriate ratios and then cast onto a substrate (*i.e.* stainless steel or PTFE), then dried and annealed. Though this method may work well for casting block polymer films, this general strategy was deemed inappropriate for ternary polymer blends, as previous work by Jones *et al.* demonstrated that such a technique results in preferential

wetting of both the substrate and air interfaces, leading to destruction of the BμE morphology.[199]

Thus, in order to minimize the effects of preferential wetting, a hot pressing technique was instead developed. In this scheme, freeze-dried bends were loaded into a nominally 90 μm thick stainless steel mold, then sandwiched between two PTFE-coated sheets. The samples were then placed on a hot press heated to a temperature $T > T_{m,PE}$ and allowed to equilibrate for 5 minutes at atmospheric pressure. After equilibration, samples were pressed at 2000 psi for 5 minutes. The blends were then quickly quenched by immersing the hot pressing mold into a bath of dry ice and isopropanol. Based on the bulk phase behavior, blends containing ϕ_H = 0.88 and 0.89 were used, and all samples were prepared at 125 °C in order to yield a BμE morphology. This hot pressing procedure is shown schematically in Figure 5.31.

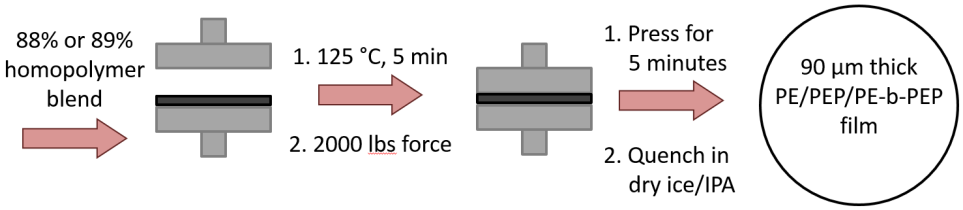

Figure 5.31: Schematic of hot pressing procedure. This process yields freestanding samples that have a diameter of 2 cm and are 90 μm thick.

To ascertain whether this hot pressing procedure successfully produced the BμE morphology observed in the bulk, TEM analysis of the films was performed. As was done for the bulk samples, the films were trimmed by hand with a razor blade, then stained with RuO_4 vapors for 4 hours. This allowed the films to be microtomed at room temperature directly without the need for embedding in epoxy. Images of a film containing $\phi_H = 0.88$ are shown in Figure 5.32.

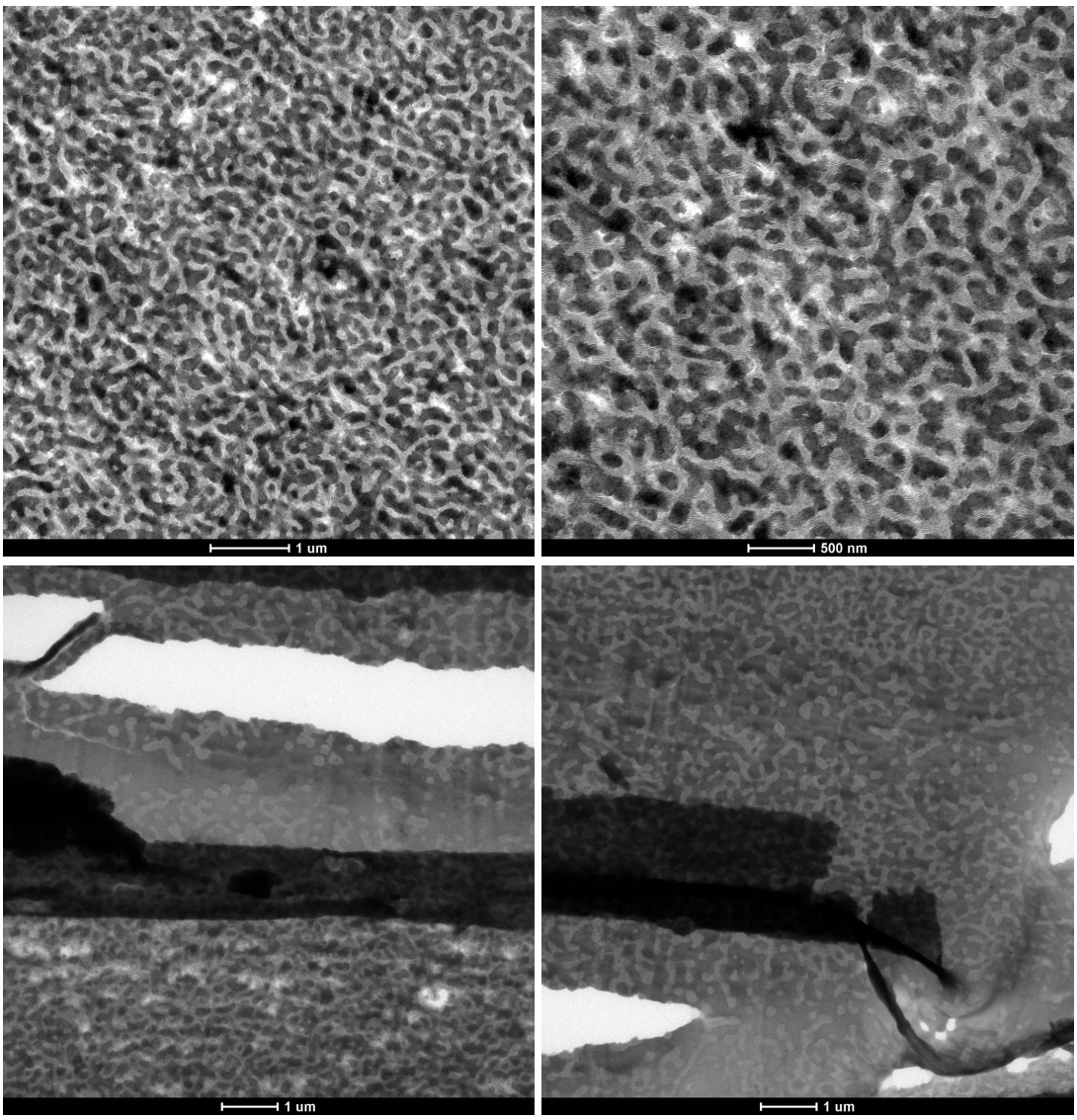

Figure 5.32: TEM of a hot pressed blend containing $\phi_H = 0.88$ prepared at 125 °C. The top two images are representative of the center of the film, while the bottom two images shows local enrichment of PEP close to the surface of the film. Blends were hot pressed between PTFE sheets.

The TEM images in Figure 5.32 show that the BμE morphology was largely retained during the hot pressing procedure, but that there was a region near the surface of the film that was locally enriched in PEP. This preferential wetting may be the result of small differences in surface tension between PEP and PE. To be more quantitative about this conjecture, surface tensions for PEP, PE, and PTFE are presented in Table 5.4.

Table 5.4: Surface tensions for PEP, PE, and PTFE at 130 °C from Ref. 199.

Polymer	Surface energy (mJ/m^2)
PEP	24
PE	28
PTFE	12

From the table, we can see that the surface energy of PEP is slightly closer to the surface energy of PTFE than that of PE. Thus, this slight imbalance in surface energies between PEP and PE could be the reason that the surface of the membrane is PEP-rich.

After hot pressing, the films were placed in THF to remove the PEP homopolymer and generate porous PE membranes. SEM analysis of the membrane was then performed to visualize the membrane surface. Representative SEM images of membranes containing $\phi_{\mathrm{H}} = 0.88$ and 0.89 are shown in Figures 5.33 and 5.34, respectively.

In the SEM images, it can be seen that large portions of the surface of the PE membranes appear minimally porous to nonporous due to a skin layer of PE. This result is surprising, as the TEM images in Figure 5.32 suggest that it was PEP, not PE, that preferentially wet the surface. One possible explanation for the presence of the PE skin layer could be that, after the PEP homopolymer was removed, the remaining PE collapsed, leading to a nonporous surface structure. In any case, because the internal pore structure was still accessible through some openings on the PE membrane surface, the presence of the skin layer was not expected to inhibit the use of these structures for templating applications. Therefore, the PE membranes were used as-fabricated as templates.

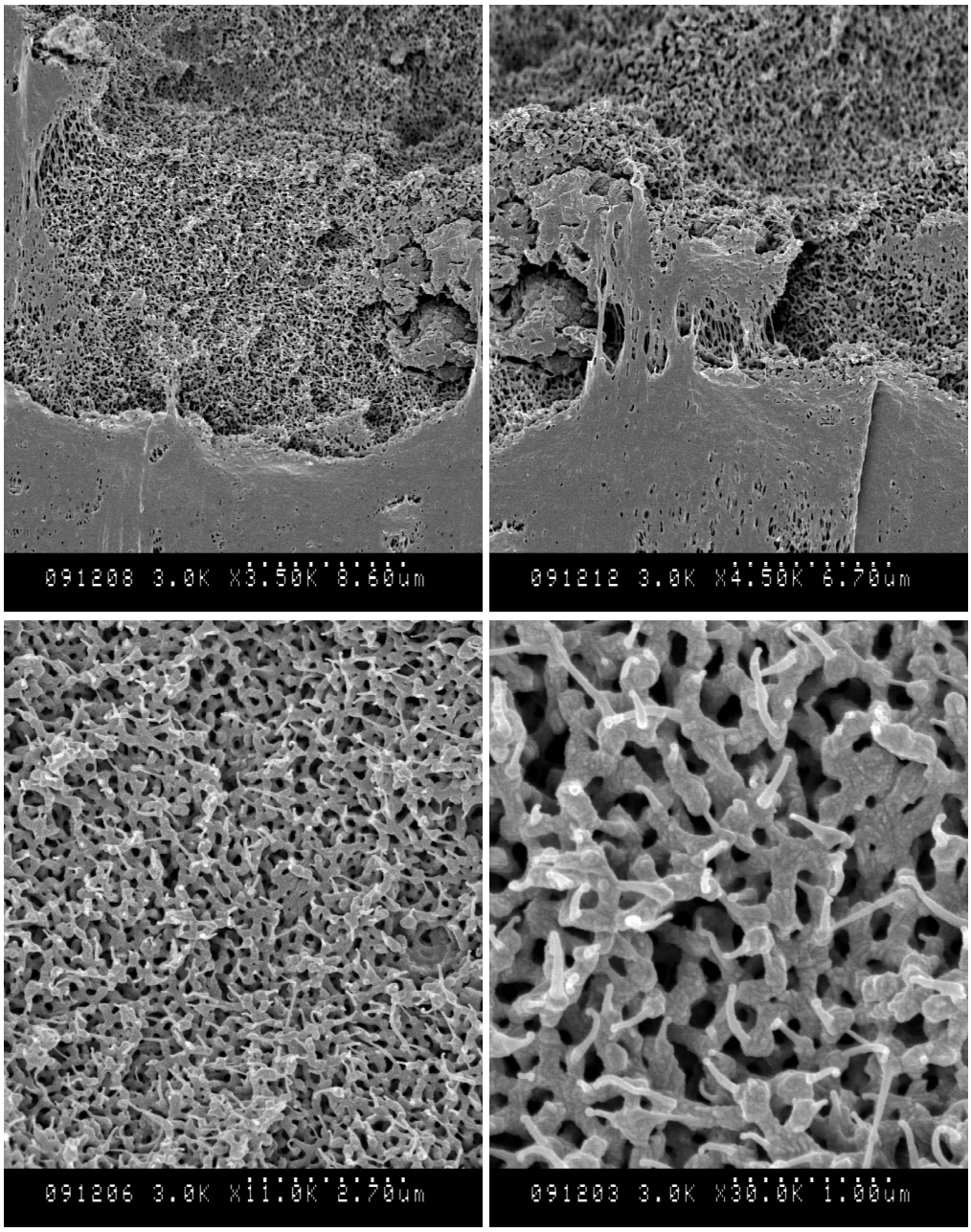

Figure 5.33: SEM images of a PE membrane from a blend containing ϕ_H = 0.88 hot pressed at 125 °C. The top two images show that the membrane surface is effectively nonporous, while some recessions in the membrane surface reveal the presence of a bicontinuous structure below the surface, as seen in the bottom two images. Samples have been coated with *ca*. 5 nm of platinum to reduce charging effects.

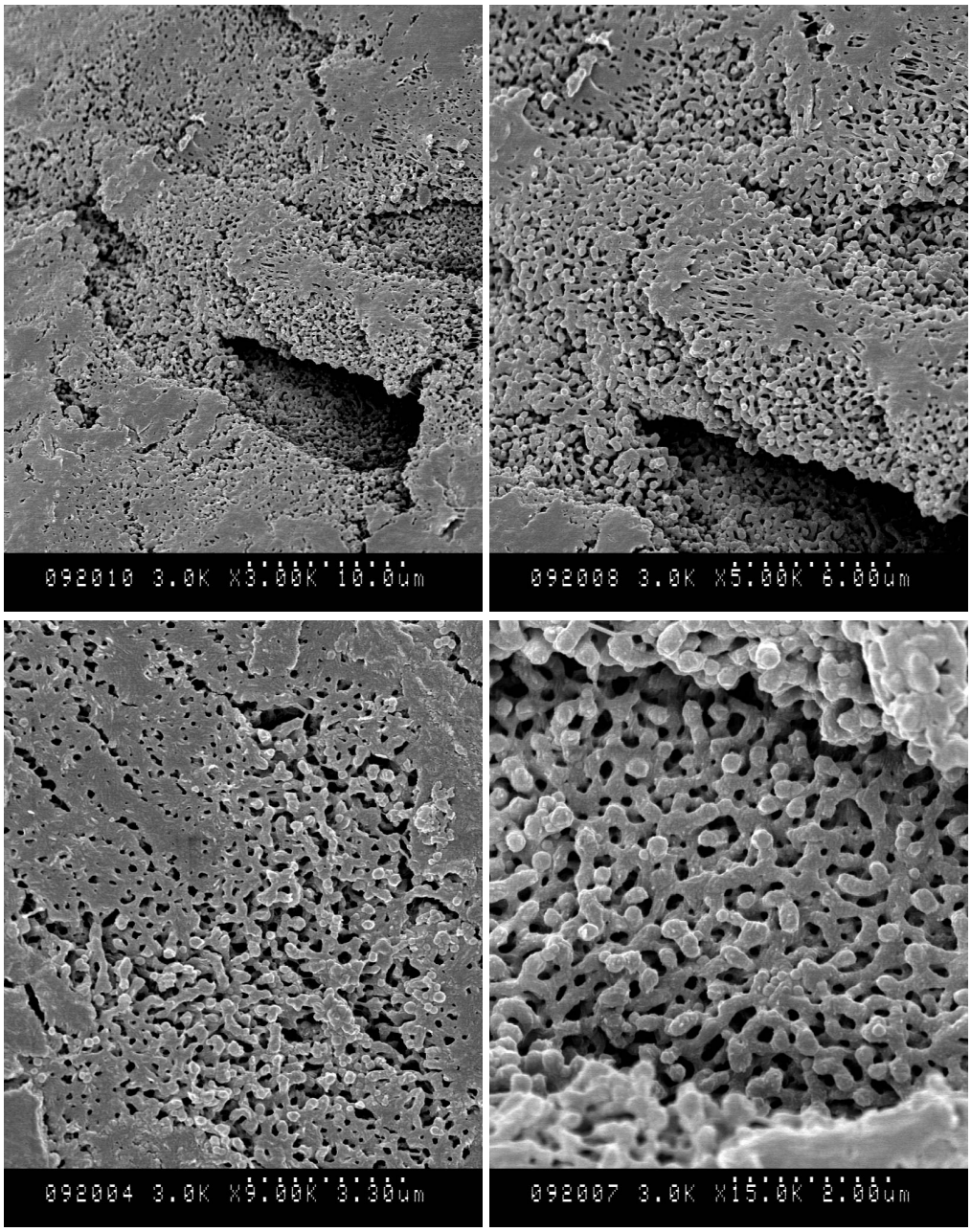

Figure 5.34: SEM images of a PE membrane from a blend containing ϕ_H = 0.89 hot pressed at 125 °C. The top two images show that the membrane surface is effectively nonporous, while some recessions in the membrane surface reveal the presence of a bicontinuous structure below the surface, as seen in the bottom two images. Samples have been coated with *ca*. 5 nm of platinum to reduce charging effects.

Generating epoxy membranes from thin PE templates

Once PE membranes were successfully prepared that retained the BμE morphology, they were used to template an epoxy membrane that could be used in water filtration. There are several reasons an epoxy membrane derived from a polymeric BμE would be desirable for filtration. Structurally, such membranes would have a well-controlled pore diameter centered at about 100 nm, high mechanical strength due to its cross-linked network structure, a three-dimensional pore network which does not need to be aligned prior to use, and high porosity of about 55% corresponding to volume of the PE template. The pore size would enable relatively rapid removal of harmful species such as bacteria and fungi from water.[200] Additionally, the epoxy hydrophilicity would reduce membrane fouling that could lead to blocked pore that would shorten membrane lifetimes.[201] These features are not found in other types of membranes. As discussed in the introduction, for instance, track-etched membranes have cylindrical pores that are produced by exposing a solid polymer film to ionizing radiation followed by a caustic solution. Although these membranes can be made to have pore diameters ranging from 20 nm to micrometers, they are limited to about 15% porosity.[52] Alternatively, membranes derived only from block copolymers, made by rendering porous a microphase separated block copolymer film by selectively etching one domain, have well controlled pore size. However, the upper limit of accessible pore sizes is limited by the scaling of the block polymer radius of gyration with block molecular weight, *i.e.* $R_g \sim M^x$, where x can range from 1/2 in the melt to 2/3 if stretched. Further, such membranes can only be made from a rather limited set of polymers which can form gyroid or perpendicularly-oriented cylindrical morphologies.[89]

Other groups have also worked to develop epoxy-based membranes. In several examples, porous epoxies were prepared for use as separation media in ion exchange columns *via* a polymerization-induced phase separation mechanism.[201–203] Although this route led to a material with a co-continuous network structure, any change to the formulation or desired pore size would require a time-intensive, trial-and-error based approach of repeated experimental design. Further, the large pore size inherent to this preparation route limits the number of applications such materials can be used in. Thus,

the templating approach discussed in this chapter provides a more systematic approach to well-controlled yet still tunable epoxy membranes.

The epoxy membrane was prepared following the method described by Jones *et al.*[125] for bulk samples of porous epoxy and as detailed in the Experimental section. Briefly, the epoxy precursors poly(bisphenol A-*co*-epichlorohydrin) and 4,4′-methylenedianylene were dissolved in THF at 50 wt%, and the solution was then applied drop-wise to the PE membrane until the membrane was filled. The solvent was then evaporated under a steady flow of air overnight. The surface of the membrane was then wiped off, then the membrane was heated to polymerize and cross-link the epoxy. The polyethylene template was then removed by submersing the membrane in toluene at 70 °C. This process is shown schematically in Figure 5.35.[125]

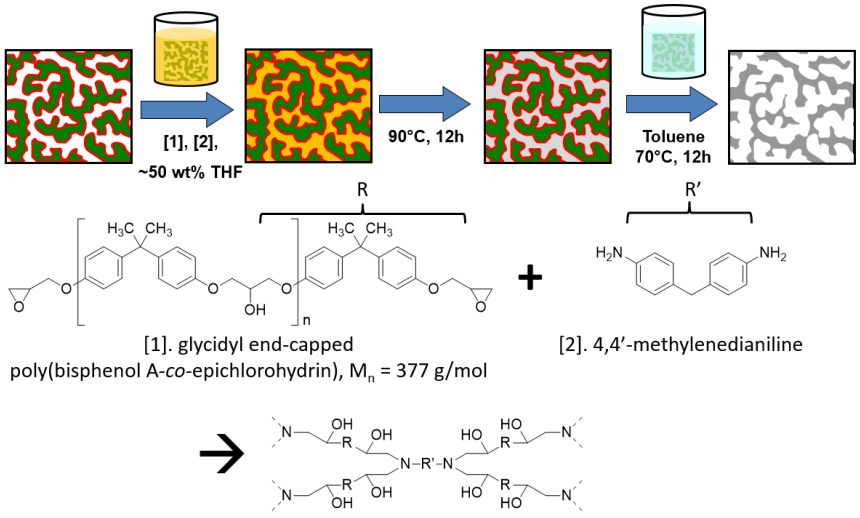

Figure 5.35: Reaction scheme for the epoxy. [1] poly(bisphenol A-*co*-epichlorohydrin) was reacted with [2] 4,4'-methylenedianylene to generate a hydrophilic, tightly cross-linked epoxy. Figure adapted from Ref. 123

In order to determine if the BμE morphology was retained through the templating process, a combination of SEM and SAXS analysis was performed on the resulting epoxy membranes. SEM images of epoxy membranes from films containing ϕ_H = 0.88 and 0.89 are shown in Figures 5.36 and 5.37, respectively.

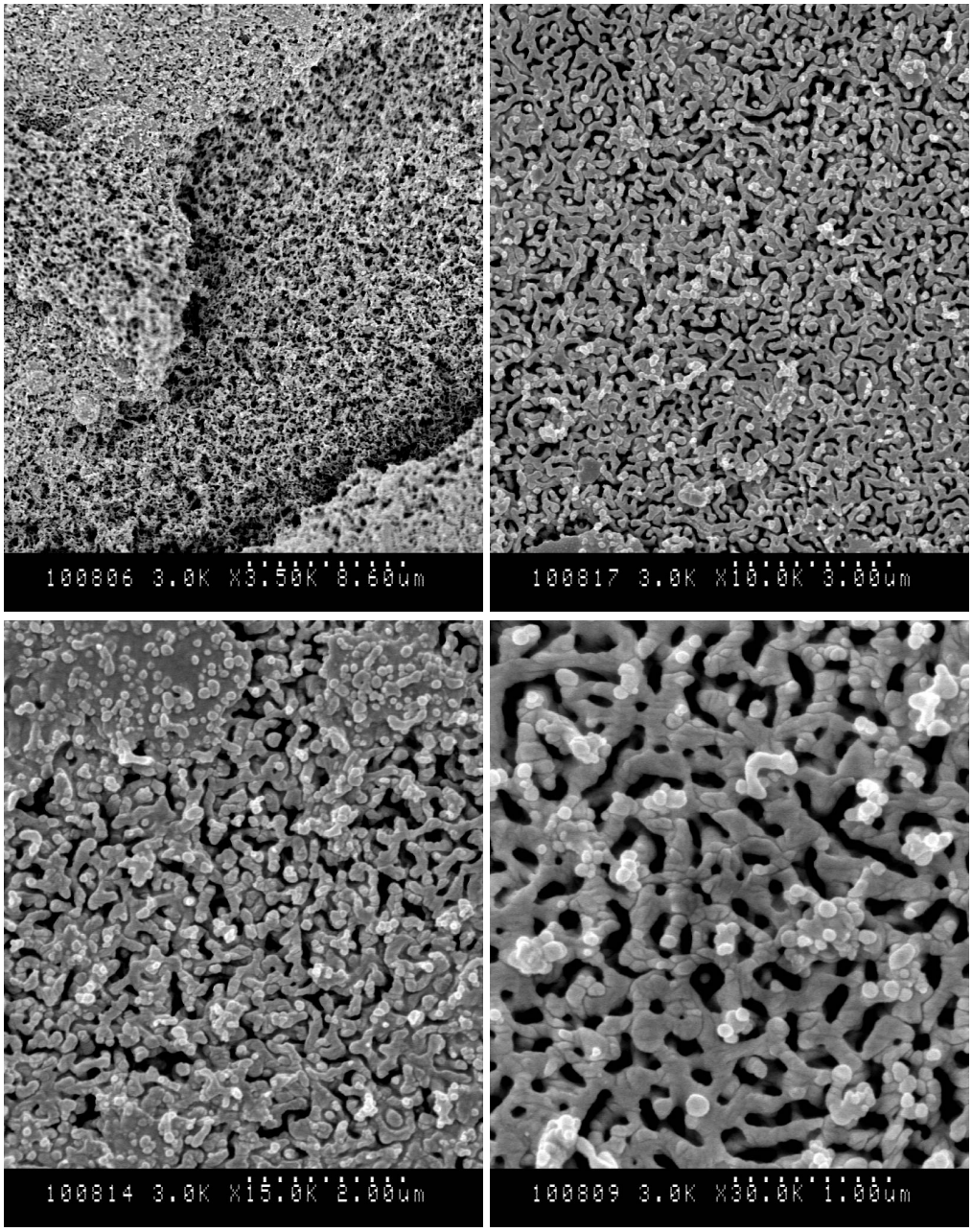

Figure 5.36: SEM of an epoxy membrane from a PE template that was made from a blend containing $\phi_H = 0.88$ hot pressed at 125 °C.

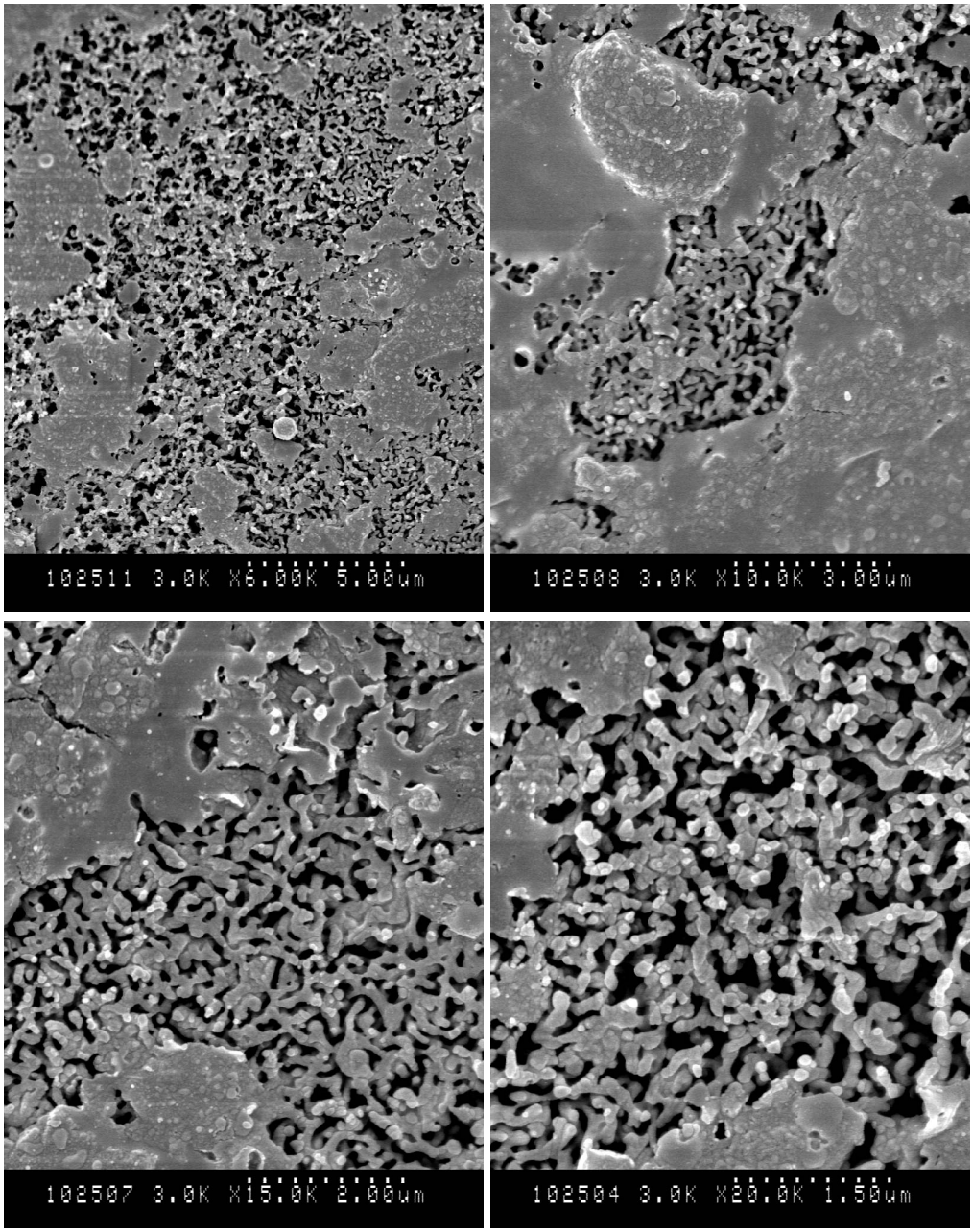

Figure 5.37: SEM of an epoxy membrane from a PE template that was made from a blend containing ϕ_H = 0.89 hot pressed at 125 °C.

SAXS experiments were also performed on the epoxy membranes. The results from this SAXS analysis are shown in Figure 5.38. For the sake of comparison, the scattering previously shown for the porous PE monoliths in Figure 5.28 and scattering from the porous PE membrane are also included in the figure.

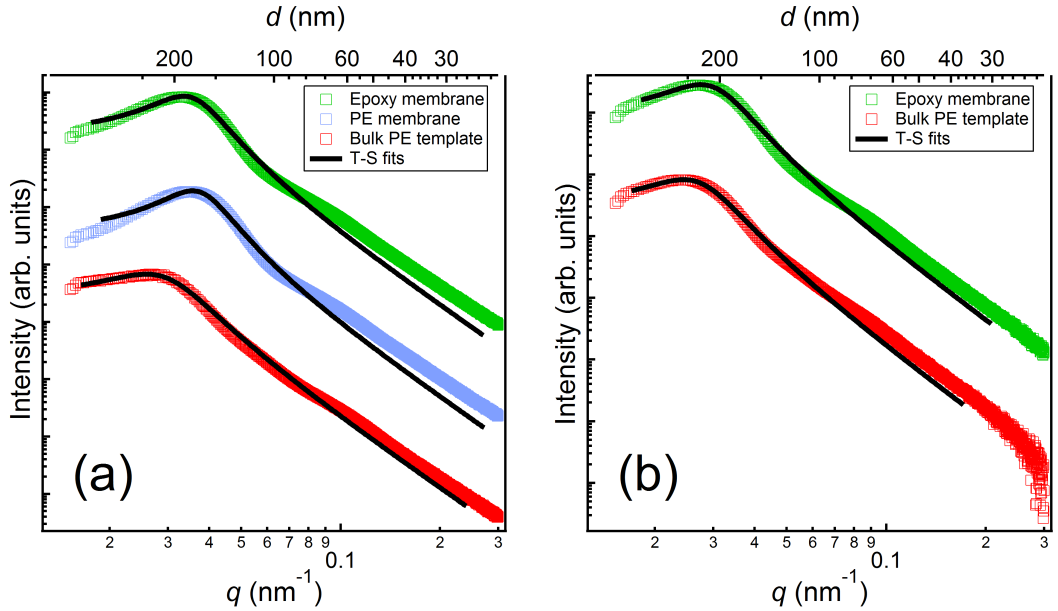

Figure 5.38: SAXS from the bulk, porous PE template, the thin PE membrane, and the templated epoxy membrane for blends containing ϕ_H of (a) 0.88 and (b) 0.89. The black lines are fits of the Teubner-Strey model to the data.

As was done for the bulk blends, the Teubner-Strey model, given by Equation 5.1, was fit to the data. From the fits, several structural characteristics were determined. The results of the fitting are summarized in Table 5.5.

From the SEM and SAXS data, it is evident that the bicontinuous structure of the original PE templates was preserved throughout all templating steps. This structure is preserved despite the difference in the domain spacing of $10-20\%$ between bulk and thin samples. For all blends, the large magnitude of the amphiphilicity factor and the correlation length indicate that the resulting structure is well ordered. Unfortunately, the SEM images in Figures 5.36 and 5.37 suggest that the surface of the membrane contains regions that are nonporous. The implications of this undesirable effect will be

Table 5.5: Structural parameters extracted from Teubner-Strey fits to SAXS traces from porous templates.

ϕ_H	Sample type	d (nm)	ξ (nm)	f_a
0.88	Bulk porous PE	227	102	−0.78
	PE membrane	172	117	−0.90
	Epoxy membrane	182	117	−0.88
0.89	Bulk porous PE	243	119	−0.81
	Epoxy membrane	218	118	−0.84

discussed in the next section.

Water filtration experiments with epoxy and PE membranes

After successfully demonstrating that the bicontinuous morphology was well maintained through all processing steps, water filtration experiments were performed using the epoxy membranes. The first goal of these experiments was to assess the performance of the epoxy membranes. This was to be done by measuring the flux of water through the membrane as a function of applied pressure, then comparing that measured flux to the theoretical maximum, as predicted by a modified Hagen-Poiseuille equation (Equation 5.5). This equation predicts the (lamellar) flow rate of a fluid through a tortuous, semi-cylindrical channel, and is given by

$$Q = \frac{\phi_{\text{void}}}{\tau}\left(\frac{\pi r^4 \Delta P}{8\mu L}\right) \tag{5.5}$$

In this model, the parameters are the volumetric flow rate through the membrane (Q), the void fraction (ϕ_{void}), the tortuosity of the pore network (τ), the average pore radius (r), the pressure difference across the membrane (ΔP), the solution viscosity (μ), and the membrane thickness (L). Although the tortuosity of the proposed system was not directly measured, values between 1.5 and 3 are typical for bicontinuous media.[10,20,112,147]

Unfortunately, water filtration experiments with the epoxy membranes were largely unsuccessful. In all, out of the 25+ samples tested, only 3 exhibited a measurable flux.

Of those, 2 exhibited fluxes that were higher than theoretically possible according to Equation 5.5, which suggested that a macroscopic defect like a hole or crack in the membrane resulted in most of the observed flux. The 3rd membrane, on the other hand, exhibited a flux that was only 1% of its theoretical maximum, suggesting that most of the pore network in the epoxy membrane was not accessible. The remainder of the approximately 22 epoxy membranes failed due to having no measurable flux through the membrane, cracking during filtration experiments, or both. To better understand why the epoxy membranes would crack despite having a cross-linked structure, it is worthwhile to consider how the epoxy membranes were loaded into the filtration cell, and what forces acted on the membrane during filtration. A schematic of the filtration cell is shown in Figure 5.39.

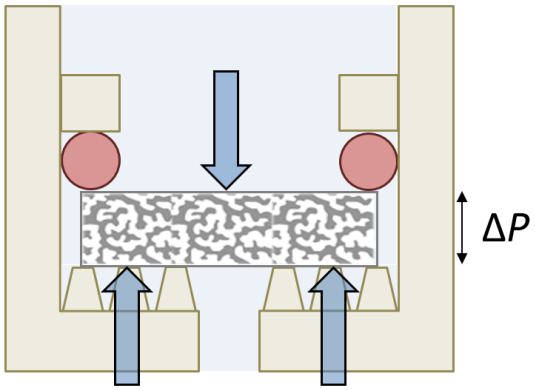

Figure 5.39: A cross-section of the apparatus that was used for water filtration experiments. The membrane is held in place by an o-ring (cross-section shown in red) and is supported below by the apparatus. The top and bottom arrows indicates the applied forces that result both from the applied water pressure and the support.

The applied water pressure (top blue arrow), combined with the pressure of the o-ring (a cross section of which is shown in red) and the support on the bottom of the filtration cell (circular posts whose cross sections are a trapezoid), produce uniaxial compression on the membrane. Though an epoxy membrane should have a sufficiently high modulus to remain intact during the experiment, it is anticipated that, in many samples, the epoxy may not have been fully interconnected or cross-linked, perhaps

due to incomplete backfilling of the original PE template. Thus, during the experiment, some sections of the membrane might fail mechanically, resulting in cracks or holes in the membrane. For membranes that produced no measurable flux, it is likely that there was residual epoxy precursor left on the PE membrane surface. This residual epoxy, once cured, would ultimately lead to epoxy membranes that were effectively nonporous on at least one side, inhibiting flow through the membrane. Although care was taken to remove excess of the epoxy precursors from the surface prior to curing, only a small amount of epoxy would have been needed to block the porous structure.

In light of the difficulties encountered with these epoxy membranes, several other strategies were also attempted. First, the thickness of the epoxy membranes was increased from 100 μm to 200 μm. Unfortunately, this increase in thickness did not prevent the membranes from cracking. In additional attempts to improve mechanical properties, the PE template was used to make a polyurethane membrane. This was done by backfilling the PE template with toluene diisocyanate (Aldrich) and glycerol propoxylate (Aldrich, $M_n \sim 266$ g/mol), as previously described by Jones *et al.*[125] One advantage of this technique is that it did not require dissolving the precursor materials in a solvent, thus potentially allowing for better pore backfilling. Unfortunately, the resulting polyurethane membranes still either failed by cracking or having a nonporous skin layer. These results indicated that the backfilling procedure and the curing process that were developed, rather than the choice of epoxy precursors, were likely the reason for the poor performance of the filtration membranes.

As a final attempt to use the techniques developed throughout this work to make filtration membranes, water filtration experiments were attempted with the PE membranes that had, until that point, simply been used as templates. Because polyolefins are hydrophobic, the membranes were soaked in methanol for at least 24 hours prior to the start of the experiment. By wetting the pores of the membrane ahead of time, it was then possible to use the otherwise hydrophobic membrane as a water filtration membrane. Unfortunately, the effectively nonporous surface structure of these PE membranes greatly reduced the permeability of these membranes. This result was not surprising, given the SEM images shown in Figures 5.33 and 5.34. After attempting

this experiment with a large number of PE membranes, only two samples produced any reasonable results. The flux as a function of pressure for these two membranes is shown in Figure 5.40. The measured flow rates are plotted alongside the theoretical flow rate calculated using the modified Hagen-Poiseuille equation (Eqn. 5.5), with $\phi_{\text{void}} = 0.44$, $\mu = 1$ mPa-s, and $L = 200$ μm. Based on the analysis of the pore size distribution obtained from nitrogen sorption experiments, $r = 45$ nm was used, and a range of tortuosities from $\tau = 1.5 - 3$ was used to account for a range of possible and reasonable tortuosities of co-continuous media.[10,20,112,147] In order to compare the theoretical flux through a single pore, given by Equation 5.5, to the macroscopic, measured flow rate, it was necessary to account for the superficial surface area of the membrane. Thus, Equation 5.5 was rearranged to calculate the superficial velocity, v, of fluid through the membrane, *i.e.*

$$v = \frac{Q}{\pi r^2} = \frac{\phi_{\text{void}}}{\tau}\left(\frac{r^2 \Delta P}{8\mu L}\right) \tag{5.6}$$

This superficial velocity was then multiplied by the superficial surface area of the membrane to give a theoretical flow rate, *i.e.*

$$Q = v \times \pi r_{\text{membrane}}^2 \tag{5.7}$$

For all samples, r_{membrane} was 1.25 cm, as set by the cell geometry, shown in Figure 5.39. A comparison of the measured flow rate through two different 200 μm thick PE membranes to the theoretical flow rates is shown in Figure 5.40.

We note that the units on the graph denote flow rates, rather than fluxes. Although this is conceptually easier to understand, it is not immediately apparent how the fluxes through these membranes compare to other systems. A standard set of units for filtration is L/(m^2·h·bar). Based on the radius of the membrane, the surface area of the membrane is given by $a = \pi r^2 = 0.04$ m^2. By then dividing by the pressure shown in the figure and performing some additional unit conversion, we find that the theoretical fluxes through the membrane for a tortuosity of 1.5 and 3 are 131 and 65 L/(m^2·h·bar), respectively. The data in Figure 5.40a indicate that the flux through that particular membrane is

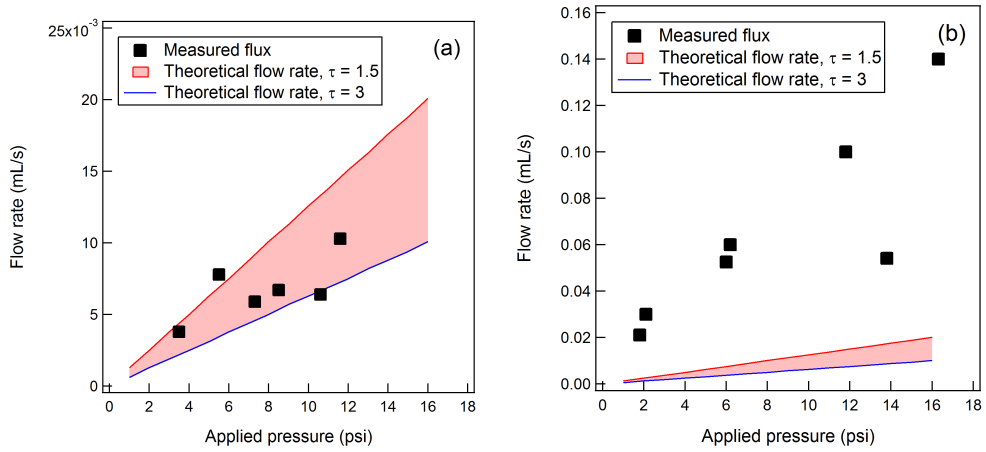

Figure 5.40: Representative flow rates of water through two different 200 μm thick PE membranes. Sample (a) exhibited reasonable flow rates, but failed after a few runs. The flux through samples (b) generally scaled quite linearly with applied pressure, but was about an order of magnitude higher than theoretically possible according to Equation 5.5.

pressure dependent, but typically between those two limits, while the flux through the membrane shown in Figure 5.40b is approximately 7 times larger. These values are in the ballpark for what one might expect for a membrane that is 200 nm thick; previous work by Phillip *et al.* found that 100 nm thick co-continuous membranes with a 14 nm average pore size and 40 vol% void fraction exhibited a flux of 6 L/(m^2·h·bar).[20]

Figure 5.40 represent the only meaningful data obtained from all of the work done to develop water filtration membranes. Note that these data were collected from PE membranes; no substantial data were collected from any of the epoxy membranes tested. Unfortunately, even these "best case" examples show a lack of repeatability and reproducibility. Although the measured flow rates in Figure 5.40a are within the range predicted by Equation 5.5, the lack of linearity in the data suggests that the membrane may be deforming irreversibly during the experiment. In fact, this sample ruptured after the six data points shown were collected, inhibiting additional data collection. On the other hand, Figure 5.40b shows a largely linear scaling of flow rate with applied pressure, but the measured flux is significantly higher than the maximum theoretical flux, suggesting that there are macroscopic defects or pores in the membrane that lead

to the majority of the measured flux.

Ultimately, the challenge with progress in this project was due to both the difficulty of the backfilling procedure during templating and the large number of processing steps required to ultimately make a membrane. In the future, a simpler route to functional materials with fewer processing steps would likely increase the chance of success for the project.

5.8 Conclusions

In this work, a unique route to templating thin materials that combines a well-controlled morphology with, in theory, good mechanical and chemical properties was developed. TEM analysis demonstrated that PE/PEP/PEP-PE ternary polymer blends exhibit unusual phase behavior in the bulk and no apparent BμE channel for two different sets of homopolymers. The reason for the lack of a BμE channel is not immediately obvious and is not consistent with previous work on this system. Unfortunately, further analysis of this phenomenon by techniques such as SAXS or light scattering are not possible due to the low electron density and refractive index contrast in the system, respectively. For future investigations into phase behavior of ternary blends, a system should be chosen that has higher inherent electron density and refractive index contrast so that SAXS and optical transmission measurements can be performed. Furthermore, studies should also pick a system where one of the domains is either semi-crystalline or vitrified at room temperature so that it can be readily microtomed and analyzed *via* TEM.

After PEP homopolymer was washed out of the polymer blends, SAXS, SEM, and nitrogen sorption analysis indicated that the BμE morphology was retained in the porous PE. Thus, after establishing the phase behavior of the blends in the bulk, a hot pressing technique was developed to yield nominally 100 μm thick ternary blend films. Again, TEM analysis indicated that these films exhibited a BμE morphology, with some evidence of PEP enrichment at the interface. After removing the PEP homopolymer, SEM and SAXS analysis confirmed that the bulk of the resulting PE membrane retained

a BμE morphology, though SEM also indicated the presence of a PE skin layer at the surfaces of the membrane.

Once successfully fabricated, the PE membranes were used to template epoxy membranes. After curing the epoxy and removing the PE template, SEM and SAXS analysis showed that the BμE structure was retained through the templating process. Initial water filtration experiments were carried out to measure the flux of deionized water as a function of applied pressure, but no membranes demonstrated sufficient robustness for further study. Ultimately, although this project was able to successfully generate epoxy membranes that were nominally 100 μm thick, it failed to produce membranes that were suitable for filtration applications.

Chapter 6

Summary and Future Work

6.1 Introduction

The work detailed in this thesis combined a variety of techniques to study the phase behavior and performance of block polymers and ternary polymer blends, both with and without lithium salts. Chapter 2 detailed a study wherein a variety of microstructured morphologies could be obtained through the addition of a prescribed amount of a lithium salt in asymmetric block polymers.[129] Chapter 3 furthered this design principle and demonstrated that lithium salt can also be used to induce structure in ternary polymer blends, then showed, though conductivity experiments, that disordered, yet structured morphologies provide better transport properties than ordered morphologies.[85,130] Chapter 4 detailed a route to high modulus, high conductivity polymer electrolytes through a polymerization-induced microphase separation scheme. Finally, Chapter 5 discussed a salt-free ternary polymer blend that was used ultimately to make epoxy-based water filtration membranes. Throughout all of this work, a primary goal was to develop quantitative and fundamental structure-property relationships through the use of accessible experimental techniques. In particular, the complex and sometimes unanticipated phase behavior of the salt-doped polymer blends described in this thesis indicates that there is still much to be learned about this relatively new field. Ultimately, one of the key findings from this thesis is that lithium

salts enable a route to inducing ordering in polymers that would otherwise exhibit low χN, either due to a small segment-segment interaction parameter (χ) or low molecular weight (N). Despite the progress described in this thesis, there is still significant work to must be done in order to fully understand these complex systems. In the following sections, I both summarize several of the key findings from each of the chapters and consider possible future work for each project.

6.2 Summary and future work

Salt-doped, asymmetric diblock copolymers

The work detailed in Chapter 2 revealed a route to readily tuning the phase behavior and segregation strength of asymmetric diblock copolymers *via* lithium salt addition. Despite the work done to assign and understand assign the morphology for the polymers at a variety of salt concentrations, for all systems, the equilibrium morphology of any given blend was not immediately apparent. This uncertainty was particularly evident for the the PS-PEO + salt blends. For example, at a salt concentration of $r = [Li^+]/[EO] = 0.06$, the PS-PEO block polymers exhibit scattering patterns that resemble a poorly-ordered Frank-Kasper σ phase. However, the peaks were relatively broad, perhaps due to the relatively short annealing times. Further, it was also observed that, at higher salt loading (*i.e.* $r > 0.06$), phases such as BCC and HEX could be observed. As discussed in Chapter 2, due to the high salt loading, it was hypothesized that these phases were kinetically trapped and likely not equilibrium phases. Finally, the scattering pattern for nearly all salt concentrations contained a broad scattering peak at low q, the origin of which was not immediately apparent. However, the peak position suggested that the lengthscale of this feature was significantly larger than the radius of gyration of the block polymer. Based on the lack of full understanding of the phase behavior of these systems, future annealing experiments should consider using longer annealing times and, potentially, higher annealing temperatures. Such experiments would allow the polymer to more time to equilibrate. By then comparing the observed morphology

as a function of annealing time and temperature, it may be possible to better understand the trajectory that the sample morphology follows on its way to approaching an equilibrium state. Ideally, these future annealing studies should consist not only of small angle X-ray scattering (SAXS) experiments, but also transmission electron microscopy (TEM) imaging. TEM imaging would allow for direct observation and confirmation of the morphology of the sample. However, performing TEM imaging on the samples described in Chapter 2 is non-trivial, as the presence of lithium salt in the sample makes sample preparation under atmospheric conditions challenging. In particular, the room-temperature bulk staining and microtoming techniques described in Chapter 5 do not work for lithium salt-doped samples; the lack of interconnectivity of the PEO domains means that they cannot be accessed and preferentially stained by a bulk-staining method, while the presence of salt causes the sample and the microtomed sections to rapidly take up water. As a result, future TEM experiments must be performed with great care in order to mitigate the uptake of water during sample preparation. An example of careful sample preparation can be found in work performed in the Balsara group by Gomez *et al.* in 2009, which detailed that microtoming was performed within a Teflon bag under a nitrogen environment (see Supporting Information of Ref. 86). However, more recent work from the Balsara group by Chintapalli *et al.* in 2016 indicated that samples are now often cryo-microtomed under atmospheric conditions, perhaps indicating that the careful procedure used by Gomez *et al.* is not necessary for routine imaging of samples.[78] Regardless of the method that is ultimately used, once TEM images can be obtained, a more definitive relationship between salt loading and morphology can be determined.

Beyond looking at longer annealing times for blends, there are additional analyses that could be performed on data that have already been collected. In the Discussion for Chapter 2, there are several pages dedicated to attempting to ascertain what morphologies different samples may exhibit based on indexing a variety of theoretical peak positions to the scattering traces. Morphologies considered included hexagonally-packed spheres, the Frank-Kasper σ phase, the A14 phase, and a dodecagonal quasicrystal. However, none of these assignments perfectly described all of the peak

positions, thus suggesting that the actual morphology of the sample could be a combination of phases or something else altogether. Thus, additional analysis should be performed that considers phases beyond those described in Chapter 2. Beyond this, many of the assignments made for these samples assumed coexistence between a particular morphology and face-centered cubic (FCC) spheres. However, the exact way in which the two morphologies coexisted with each other was not immediately apparent. It is worth noting that many of the morphological assignments in Chapter 2 suggest that, for samples with coexisting morphologies, both of the morphologies share a common primary peak position and, thus, characteristic lengthscale. As discussed above, future studies into this system should consider performing TEM experiments to obtain images of the blends and directly observe in real-space how multiple morphologies coexist. Ultimately, such TEM experiments would greatly assist with more definitively understanding the complex phase behavior of the samples in Chapter 2.

Salt-doped ternary polymer blends

The study described in Chapter 3 detailed an initial study of the phase behavior and relationship between structure and conductivity in salt-doped ternary polymer blends. Despite the conclusions reached, there is still significant work that could be done. One interesting finding in Chapter 3 was that χ_{eff} between the PS and dihydroxyl-terminated PEO homopolymers was approximately five times greater than that for the PS-PEO diblock copolymer. The reason for this unexpected behavior was not immediately apparent. As discussed in the chapter, some of the increase may be due to hydrogen bonding among the PEO homopolymer chains, but this alone is probably insufficient to describe the full magnitude of the increase in χ_{eff}. To better understand the reason for this unexpected behavior, future studies should determine χ_{eff} for PS/PEO homopolymer blends where both homopolymers are of the same molecular weight as that used in the study in Chapter 3, but the PEO is dimethoxy-terminated. This relatively simple study would determine to what extent hydrogen bonding of the

end groups affects the χ_{eff} reported in Chapter 3. Once this study has been completed, further studies could be done to determine the effects of molecular weight on χ_{eff}, as previous work by Teran *et al.* has shown that, for salt-doped PS-PEO block polymers, $\chi_{eff} = f(N)$ at low molecular weight.[82] Finally, once these relationships have been developed, salt could be added to PS/PEO blends to obtain χ_{eff} for blends as a function of salt loading. Ultimately, the goal of this work would be to determine a general form for χ_{eff} of PS and PEO homopolymers that disentangles the effects of end groups, molecular weight, and salt loading.

Beyond studies of homopolymer blends, additional work could be done to better understand the relationship between structure and conductivity in the ternary polymer blends. In the blends described in Chapter 3, there was generally a decrease in conductivity as the amount of homopolymer in the blends was increased. This trend was unanticipated, as naïvely one might expect the conductivity to increase as the amount of the low molecular weight components increases. Ultimately, this trend in conductivity with increasing homopolymer loading was largely attributed to a simultaneous increase in curvature toward the salt-doped PEO domains, which resulted in an increase in grain boundaries or dead ends that cut off conducting channels. Thus, perhaps the most straightforward and obvious study to conduct next would be to investigate the trend in conductivity along an isopleth wherein the only ordered morphology observed is lamellar. As detailed in Chapter 3, this could be done by adding more of the salt-doped PEO homopolymer relative to the PS homopolymer. By tailoring the loading of the two homopolymers so that the blends exhibit near-zero mean curvature regardless of homopolymer content, it would be possible to better understand and quantify the trends in ionic conductivity. For example, in the ordered state, it would be possible to compare the conductivity of well-structured lamellae at low homopolymer loading with that of swollen lamellae at high homopolymer loading directly, without the concern that asymmetries in curvature are leading to a large number of dead ends in conducting channels. In addition, by comparing the conductivity of disordered states, it would be possible to more directly compare the conductivity of a fluctuating disordered state (with low homopolymer content) to a

bicontinuous microemulsion (with high homopolymer content). Ultimately, studying the relationship between structure and conductivity along an isopleth that balances curvature symmetry would further strengthen the conclusions reached in Chapter 3 about which morphologies are best able to maximize ionic conductivity.

High conductivity, high modulus polymer electrolyte membranes

As detailed in Chapter 4, one of the largest challenges with the polymer electrolyte membrane work was the macrophase separation of the reaction mixture during the course of the polymerization. Despite this setback, the results in Chapter 4 are encouraging and suggest that the PIPS PEMS blends could be effective electrolyte membranes for lithium metal batteries. In order to carry this work forward, future studies should always include the radical initiator AIBN in all formulations. The inclusion of AIBN appears to be necessary to prevent macroscopic phase separation. Once this is done, the experiments detailed in Chapter 4 could be repeated as a function of relative crosslinker content to optimize the formulation in terms of modulus and conductivity. Ultimately, by performing additional battery testing experiments like the ones detailed near the end of the chapter, it would be possible to demonstrate that the PIPS PEMS systems is potentially useful for real-world applications.

Templating water filtration membranes using polymeric bicontinuous microemulsions

Despite the work done in Chapter 5 to develop water filtration membranes, the project ultimately failed to produce any meaningful results due to the challenge of reliably producing a porous structure in the epoxy water filtration membranes. The obstacles encountered in this work suggest that any future studies with templating should instead consider developing bulk porous materials, as opposed to membranes, where the ratio of surface area to volume can be minimized. In any case, treating the porous materials to a reactive ion etch may be necessary to remove any surface skin layers and reveal the underlying porous structure. Additionally, one major challenge faced in the work

detailed in Chapter 5 was that many processing steps were required to produce the epoxy water filtration membranes over the course of weeks, yet the filtration test would cause the membrane to fail in a matter of minutes or less. Future templating work should attempt to design altogether different strategies that minimize the number of potential processing steps while also targeting materials that could be characterized by non-destructive techniques. By developing a system that combines these two attributes, it would be possible to obtain meaningful data more quickly and reliably than was possible for the water filtration project.

References

[1] Bryner, M.; Clarke, G. M.; Jansen, A. N.; Patel, A.; Spotnitz, R. Lithium-ion Batteries. *Chemical Engineering Progress* **2013**, *October*.

[2] Zu, C.-X.; Li, H. Thermodynamic analysis on energy densities of batteries. *Energy & Environmental Science* **2011**, *4*, 2614.

[3] Monroe, C.; Newman, J. Dendrite Growth in Lithium/Polymer Systems. *Journal of the Electrochemical Society* **2003**, *150*, A1377.

[4] Harry, K. J.; Hallinan, D. T.; Parkinson, D. Y.; MacDowell, A. A.; Balsara, N. P. Detection of subsurface structures underneath dendrites formed on cycled lithium metal electrodes. *Nature Materials* **2014**, *13*, 69–73.

[5] Steiger, J.; Kramer, D.; Mönig, R. Mechanisms of dendritic growth investigated by in situ light microscopy during electrodeposition and dissolution of lithium. *Journal of Power Sources* **2014**, *261*, 112–119.

[6] Devaux, D.; Harry, K. J.; Parkinson, D. Y.; Yuan, R.; Hallinan, D. T.; MacDowell, A. A.; Balsara, N. P. Failure Mode of Lithium Metal Batteries with a Block Copolymer Electrolyte Analyzed by X-Ray Microtomography. *Journal of the Electrochemical Society* **2015**, *162*, A1301–A1309.

[7] Schauser, N. S.; Harry, K. J.; Parkinson, D. Y.; Watanabe, H.; Balsara, N. P. Lithium Dendrite Growth in Glassy and Rubbery Nanostructured Block Copolymer Electrolytes. *Journal of The Electrochemical Society* **2015**, *162*, 398–405.

[8] Harry, K. J.; Parkinson, D. Y.; Balsara, N. P. Failure Analysis of Batteries Using Synchrotron-based Hard X-ray Microtomography. *Journal of Visualized Experiments* **2015**,

[9] Monroe, C.; Newman, J. The Impact of Elastic Deformation on Deposition Kinetics at Lithium/Polymer Interfaces. *Journal of The Electrochemical Society* **2005**, *152*, A396.

[10] Schulze, M. W.; McIntosh, L. D.; Hillmyer, M. A.; Lodge, T. P. High-modulus, high-conductivity nanostructured polymer electrolyte membranes via polymerization-induced phase separation. *Nano Letters* **2014**, *14*, 122–126.

[11] Vanlaeke, P.; Swinnen, A.; Haeldermans, I.; Vanhoyland, G.; Aernouts, T.; Cheyns, D.; Deibel, C.; D'Haen, J.; Heremans, P.; Poortmans, J.; Manca, J. P3HT/PCBM bulk heterojunction solar cells: Relation between morphology and electro-optical characteristics. *Solar Energy Materials and Solar Cells* **2006**, *90*, 2150–2158.

[12] Thompson, B. C.; Fréchet, J. M. J. Polymer-fullerene composite solar cells. *Angewandte Chemie* **2008**, *47*, 58–77.

[13] Botiz, I.; Darling, S. B. Self-Assembly of Poly(3-hexylthiophene)-block-polylactide Block Copolymer and Subsequent Incorporation of Electron Acceptor Material. *Macromolecules* **2009**, *42*, 8211–8217.

[14] Brady, M. a.; Su, G. M.; Chabinyc, M. L. Recent progress in the morphology of bulk heterojunction photovoltaics. *Soft Matter* **2011**, *7*, 11065.

[15] Liu, B.; Png, R.-Q.; Zhao, L.-H.; Chua, L.-L.; Friend, R. H.; Ho, P. K. H. High internal quantum efficiency in fullerene solar cells based on crosslinked polymer donor networks. *Nature Communications* **2012**, *3*, 1321.

[16] Clark, M. D.; Jespersen, M. L.; Patel, R. J.; Leever, B. J. Predicting Vertical Phase Segregation in Polymer-Fullerene Bulk Heterojunction Solar Cells by Free Energy Analysis. *ACS Applied Materials & Interfaces* **2013**, *5*, 4799–4807.

[17] Vandewal, K.; Himmelberger, S.; Salleo, A. Structural Factors That Affect the Performance of Organic Bulk Heterojunction Solar Cells. *Macromolecules* **2013**, 130729154511008.

[18] Kipp, D.; Mok, J.; Strzalka, J.; Darling, S. B.; Ganesan, V.; Verduzco, R. Rational Design of Thermally Stable, Bicontinuous Donor/Acceptor Morphologies with Conjugated Block Copolymer Additives. *ACS Macro Letters* **2015**, *4*, 867–871.

[19] Chen, L.; Phillip, W. A.; Cussler, E. L.; Hillmyer, M. A. Robust nanoporous membranes templated by a doubly reactive block copolymer. *Journal of the American Chemical Society* **2007**, *129*, 13786–7.

[20] Phillip, W. A.; Amendt, M. A.; O'Neill, B.; Chen, L.; Hillmyer, M. A.; Cussler, E. L. Diffusion and flow across nanoporous polydicyclopentadiene-based membranes. *ACS Applied Materials & Interfaces* **2009**, *1*, 472–480.

[21] Phillip, W. a.; O'Neill, B.; Rodwogin, M.; Hillmyer, M. a.; Cussler, E. L. Self-assembled block copolymer thin films as water filtration membranes. *ACS Applied Materials & Interfaces* **2010**, *2*, 847–53.

[22] Bakhshayeshi, M.; Kanani, D. M.; Mehta, A.; van Reis, R.; Kuriyel, R.; Jackson, N.; Zydney, A. L. Dextran sieving test for characterization of virus filtration membranes. *Journal of Membrane Science* **2011**, *379*, 239–248.

[23] Jackson, E. A.; Lee, Y.; Hillmyer, M. A. ABAC Tetrablock Terpolymers for Tough Nanoporous Filtration Membranes. *Macromolecules* **2013**, *46*, 1484–1491.

[24] Saba, S. A.; Mousavi, M. P. S.; Bühlmann, P.; Hillmyer, M. A. Hierarchically Porous Polymer Monoliths by Combining Controlled Macro- and Microphase Separation. *Journal of the American Chemical Society* **2015**, *137*, 8896–8899.

[25] Bates, F. S.; Fredrickson, G. H. Block Copolymers - Designer Soft Materials. *Physics Today* **1999**, *52*, 32.

[26] Hiemenz, P. C.; Lodge, T. P. *Polymer Chemistry*, 2nd ed.; CRC Press: Boca Raton, FL, 2007.

[27] Niitani, T.; Shimada, M.; Kawamura, K.; Dokko, K.; Rho, Y.-H.; Kanamura, K. Synthesis of Li+ Ion Conductive PEO-PSt Block Copolymer Electrolyte with Microphase Separation Structure. *Electrochemical and Solid-State Letters* **2005**, *8*, A385–A388.

[28] Singh, M.; Odusanya, O.; Wilmes, G. M.; Eitouni, H. B.; Gomez, E. D.; Patel, A. J.; Chen, V. L.; Park, M. J.; Fragouli, P.; Iatrou, H.; Hadjichristidis, N.; Cookson, D.; Balsara, N. P. Effect of Molecular Weight on the Mechanical and Electrical Properties of Block Copolymer Electrolytes. *Macromolecules* **2007**, *40*, 4578–4585.

[29] Young, W. S.; Epps, T. H. Salt doping in PEO-containing block copolymers: Counterion and concentration effects. *Macromolecules* **2009**, *42*, 2672–2678.

[30] Matsen, M. W. The standard Gaussian model for block copolymer melts. *Journal of Physics: Condensed Matter* **2001**, *14*, R21–R47.

[31] Matsen, M. W.; Bates, F. S. Unifying Weak- and Strong-Segregation Block Copolymer Theories. *Macromolecules* **1996**, *29*, 1091–1098.

[32] Gillard, T. M. Phase Transitions and Fluctuations in Block Copolymer-Based Soft Materials. Ph.D. thesis, University of Minnesota, 2015.

[33] Leibler, L. Theory of microphase separation in block copolymers. *Macromolecules* **1980**, *13*, 1602–1617.

[34] Thompson, R. B.; Matsen, M. W. Improving polymeric microemulsions with block copolymer polydispersity. *Physical Review Letters* **2000**, *85*, 670–3.

[35] Hillmyer, M. A. Polydisperse block copolymers: Don't throw them away. *Journal of Polymer Science Part B: Polymer Physics* **2007**, *45*, 3249–3251.

[36] Lynd, N. A. The effects of polydispersity on block copolymer self-assembly. Ph.D. thesis, University of Minnesota, 2007.

[37] Lynd, N. A.; Meuler, A. J.; Hillmyer, M. A. Polydispersity and block copolymer self-assembly. *Progress in Polymer Science* **2008**, *33*, 875–893.

[38] Meuler, A. J. Network Morphologies in Monodisperse and Polydisperse Multiblock Terpolymers. Ph.D. thesis, University of Minnesota, 2009.

[39] Ellison, C. J.; Meuler, A. J.; Qin, J.; Evans, C. M.; Wolf, L. M.; Bates, F. S. Bicontinuous Polymeric Microemulsions from Polydisperse Diblock Copolymers. *The Journal of Physical Chemistry B* **2009**, *113*, 3726–3737.

[40] Widin, J. M.; Schmitt, A. K.; Schmitt, A. L.; Im, K.; Mahanthappa, M. K. Unexpected Consequences of Block Polydispersity on the Self-Assembly of ABA Triblock Copolymers. *Journal of the American Chemical Society* **2012**, *134*, 3834–3844.

[41] Matsen, M.; Schick, M. Stable and unstable phases of a diblock copolymer melt. *Physical Review Letters* **1994**, *72*, 2660–2663.

[42] Bates, F. S.; Fredrickson, G. H. Conformational Asymmetry and Polymer-Polymer Thermodynamics. *Macromolecules* **1994**, *27*, 1065–1067.

[43] Bates, F. S.; Schulz, M. F.; Khandpur, A. K.; Förster, S.; Rosedale, J. H.; Almdal, K.; Mortensen, K. Fluctuations, conformational asymmetry and block copolymer phase behaviour. *Faraday Discuss.* **1994**, *98*, 7–18.

[44] Almdal, K.; Hillmyer, M. A.; Bates, F. S. Influence of conformational asymmetry on polymer-polymer interactions: An entropic or enthalpic effect? *Macromolecules* **2002**, *35*, 7685–7691.

[45] Xie, N.; Li, W.; Qiu, F.; Shi, A.-C. σ Phase Formed in Conformationally Asymmetric AB-Type Block Copolymers. *ACS Macro Letters* **2014**, *3*, 906–910.

[46] Jo, G.; Ahn, H.; Park, M. J. Simple route for tuning the morphology and conductivity of polymer electrolytes: One end functional group is enough. *ACS Macro Letters* **2013**, *2*, 990–995.

[47] Gillard, T. M.; Medapuram, P.; Morse, D. C.; Bates, F. S. Fluctuations, Phase Transitions, and Latent Heat in Short Diblock Copolymers: Comparison of Experiment, Simulation, and Theory. *Macromolecules* **2015**, *48*, 2801–2811.

[48] Khandpur, A. K.; Foerster, S.; Bates, F. S.; Hamley, I. W.; Ryan, A. J.; Bras, W.; Almdal, K.; Mortensen, K. Polyisoprene-Polystyrene Diblock Copolymer Phase Diagram near the Order-Disorder Transition. *Macromolecules* **1995**, *28*, 8796–8806.

[49] Lee, S.; Bluemle, M. J.; Bates, F. S. Discovery of a Frank-Kasper Phase in Sphere-Forming Block Copolymer Melts. *Science* **2010**, *330*, 349–353.

[50] Lee, S.; Leighton, C.; Bates, F. S. Sphericity and symmetry breaking in the formation of Frank-Kasper phases from one component materials. *Proceedings of the National Academy of Sciences* **2014**, *111*, 17723–17731.

[51] Gillard, T. M.; Lee, S.; Bates, F. S. Dodecagonal quasicrystalline order in a diblock copolymer melt. *Proceedings of the National Academy of Sciences* **2016**, *113*, 5167–5172.

[52] Ulbricht, M. Advanced functional polymer membranes. *Polymer* **2006**, *47*, 2217–2262.

[53] Hoarfrost, M. L. Ion Transport in Nanostructured Block Copolymer/Ionic Liquid Membranes. Ph.D. thesis, University of California, Berkeley, 2012.

[54] Chintapalli, M.; Chen, X. C.; Thelen, J. L.; Teran, A. A.; Wang, X.; Garetz, B. A.; Balsara, N. P. Effect of Grain Size on the Ionic Conductivity of a Block Copolymer Electrolyte. *Macromolecules* **2014**, *47*, 5424–5431.

[55] McIntosh, L. D.; Kubo, T.; Lodge, T. P. Morphology, Modulus, and Conductivity of a Triblock Terpolymer/Ionic Liquid Electrolyte Membrane. *Macromolecules* **2014**, *47*, 1090–1098.

[56] Chopade, S. A.; So, S.; Hillmyer, M. A.; Lodge, T. P. Anhydrous Proton Conducting Polymer Electrolyte Membranes via Polymerization-Induced Microphase Separation. *ACS Applied Materials & Interfaces* **2016**, *8*, 6200–6210.

[57] Dean, J. M.; Grubbs, R. B.; Saad, W.; Cook, R. F.; Bates, F. S. Mechanical properties of block copolymer vesicle and micelle modified epoxies. *Journal of Polymer Science Part B: Polymer Physics* **2003**, *41*, 2444–2456.

[58] Declet-Perez, C.; Redline, E. M.; Francis, L. F.; Bates, F. S. Role of Localized Network Damage in Block Copolymer Toughened Epoxies. *ACS Macro Letters* **2012**, *1*, 338–342.

[59] Declet-Perez, C.; Francis, L. F.; Bates, F. S. Cavitation in Block Copolymer Modified Epoxy Revealed by In Situ Small-Angle X-Ray Scattering. *ACS Macro Letters* **2013**, *2*, 939–943.

[60] Redline, E. M.; Declet-Perez, C.; Bates, F. S.; Francis, L. F. Effect of block copolymer concentration and core composition on toughening epoxies. *Polymer* **2014**, *55*, 4172–4181.

[61] Xu, Y.; Thurber, C. M.; Lodge, T. P.; Hillmyer, M. A. Synthesis and Remarkable Efficacy of Model Polyethylene- graft -poly(methyl methacrylate) Copolymers as Compatibilizers in Polyethylene/Poly(methyl methacrylate) Blends. *Macromolecules* **2012**, *45*, 9604–9610.

[62] Xu, Y.; Thurber, C. M.; Macosko, C. W.; Lodge, T. P.; Hillmyer, M. A. Poly(methyl methacrylate)-block-polyethylene-block-poly(methyl methacrylate) Triblock Copolymers as Compatibilizers for

Polyethylene/Poly(methyl methacrylate) Blends. *Industrial & Engineering Chemistry Research* **2014**, *53*, 4718–4725.

[63] Thurber, C. M.; Xu, Y.; Myers, J. C.; Lodge, T. P.; Macosko, C. W. Accelerating Reactive Compatibilization of PE/PLA Blends by an Interfacially Localized Catalyst. *ACS Macro Letters* **2015**, *4*, 30–33.

[64] Kim, S. Y.; Kim, S.; Park, M. J. Enhanced proton transport in nanostructured polymer electrolyte/ionic liquid membranes under water-free conditions. *Nature Communications* **2010**, *1*, 88.

[65] Choi, I.; Ahn, H.; Park, M. J. Enhanced performance in lithium-polymer batteries using surface-functionalized Si nanoparticle anodes and self-assembled block copolymer electrolytes. *Macromolecules* **2011**, *44*, 7327–7334.

[66] Nakamura, I.; Balsara, N. P.; Wang, Z. G. First-order disordered-to-lamellar phase transition in lithium salt-doped block copolymers. *ACS Macro Letters* **2013**, *2*, 478–481.

[67] Bouchet, R.; Maria, S.; Meziane, R.; Aboulaich, A.; Lienafa, L.; Bonnet, J.-P.; Phan, T. N. T.; Bertin, D.; Gigmes, D.; Devaux, D.; Denoyel, R.; Armand, M. Single-ion BAB triblock copolymers as highly efficient electrolytes for lithium-metal batteries. *Nature Materials* **2013**, *12*, 452–457.

[68] Young, N. P.; Devaux, D.; Khurana, R.; Coates, G. W.; Balsara, N. P. Investigating polypropylene-poly(ethylene oxide)-polypropylene triblock copolymers as solid polymer electrolytes for lithium batteries. *Solid State Ionics* **2014**, *263*, 87–94.

[69] Inceoglu, S.; Rojas, A. A.; Devaux, D.; Chen, X. C.; Stone, G. M.; Balsara, N. P. Morphology-Conductivity Relationship of Single-Ion-Conducting Block Copolymer Electrolytes for Lithium Batteries. *ACS Macro Letters* **2014**, *3*, 510–514.

[70] Panday, A.; Mullin, S.; Gomez, E. D.; Wanakule, N.; Chen, V. L.; Hexemer, A.; Pople, J.; Balsara, N. P. Effect of Molecular Weight and Salt Concentration on Conductivity of Block Copolymer Electrolytes. *Macromolecules* **2009**, *42*, 4632–4637.

[71] Yuan, R.; Teran, A. A.; Gurevitch, I.; Mullin, S. A.; Wanakule, N. S.; Balsara, N. P. Ionic Conductivity of Low Molecular Weight Block Copolymer Electrolytes. *Macromolecules* **2013**, *46*, 914–921.

[72] Sax, J.; Ottino, J. M. Modeling of transport of small molecules in polymer blends: Application of effective medium theory. *Polymer Engineering and Science* **1983**, *23*, 165–176.

[73] Hallinan, D. T.; Balsara, N. P. Polymer Electrolytes. *Annual Review of Materials Research* **2013**, *43*, 503–525.

[74] Teran, A. A.; Mullin, S. A.; Hallinan, D. T.; Balsara, N. P. Discontinuous Changes in Ionic Conductivity of a Block Copolymer Electrolyte through an Order-Disorder Transition. *ACS Macro Letters* **2012**, *1*, 305–309.

[75] Wanakule, N. S.; Panday, A.; Mullin, S. A.; Gann, E.; Hexemer, A.; Balsara, N. P. Ionic conductivity of block copolymer electrolytes in the vicinity of order-disorder and order-order transitions. *Macromolecules* **2009**, *42*, 5642–5651.

[76] Wang, D. R.; Wujcik, K. H.; Teran, A. a.; Balsara, N. P. Conductivity of Block Copolymer Electrolytes Containing Lithium Polysulfides. *Macromolecules* **2015**, *48*, 4863–4873.

[77] Ganesan, V.; Pyramitsyn, V.; Bertoni, C.; Shah, M. Mechanisms underlying ion transport in lamellar block copolymer membranes. *ACS Macro Letters* **2012**, *1*, 513–518.

[78] Chintapalli, M.; Le, T. N. P.; Venkatesan, N. R.; Mackay, N. G.; Rojas, A. A.; Thelen, J. L.; Chen, X. C.; Devaux, D.; Balsara, N. P. Structure and Ionic

Conductivity of Polystyrene-block-poly(ethylene oxide) Electrolytes in the High Salt Concentration Limit. *Macromolecules* **2016**, *49*, 1770–1780.

[79] Hickey, R. J.; Gillard, T. M.; Irwin, M. T.; Morse, D. C.; Lodge, T. P.; Bates, F. S. Phase Behavior of Diblock Copolymer-Homopolymer Ternary Blends: Congruent First-order Lamellar-Disorder Transition. *Submitted to Macromolecules*

[80] Wanakule, N. S.; Virgili, J. M.; Teran, A. A.; Wang, Z.-G.; Balsara, N. P. Thermodynamic Properties of Block Copolymer Electrolytes Containing Imidazolium and Lithium Salts. *Macromolecules* **2010**, *43*, 8282–8289.

[81] Nakamura, I.; Balsara, N. P.; Wang, Z.-G. Thermodynamics of Ion-Containing Polymer Blends and Block Copolymers. *Physical Review Letters* **2011**, *107*, 198301.

[82] Teran, A. A.; Balsara, N. P. Thermodynamics of block copolymers with and without salt. *The Journal of Physical Chemistry B* **2014**, *118*, 4–17.

[83] Nakamura, I.; Wang, Z.-G. Thermodynamics of Salt-Doped Block Copolymers. *ACS Macro Letters* **2014**, *3*, 708–711.

[84] Ren, C.-L.; Nakamura, I.; Wang, Z.-G. Effects of Ion-Induced Cross-Linking on the Phase Behavior in Salt-Doped Polymer Blends. *Macromolecules* **2016**, *49*, 425–431.

[85] Irwin, M. T.; Hickey, R. J.; Xie, S.; Bates, F. S.; Lodge, T. P. Lithium Salt-Induced Microstructure and Ordering in Diblock Copolymer/Homopolymer Blends. *Macromolecules* **2016**, *49*, 4839–4849.

[86] Gomez, E. D.; Panday, A.; Feng, E. H.; Chen, V.; Stone, G. M.; Minor, A. M.; Kisielowski, C.; Downing, K. H.; Borodin, O.; Smith, G. D.; Balsara, N. P. Effect of ion distribution on conductivity of block copolymer electrolytes. *Nano Letters* **2009**, *9*, 1212–1216.

[87] Gilbert, J. B.; Luo, M.; Shelton, C. K.; Rubner, M. F.; Cohen, R. E.; Epps, T. H. Determination of Lithium-Ion Distributions in Nanostructured Block Polymer Electrolyte Thin Films by X-ray Photoelectron Spectroscopy Depth Profiling. *ACS Nano* **2015**, *9*, 512–520.

[88] Nakamura, I.; Wang, Z.-G. Salt-doped block copolymers: ion distribution, domain spacing and effective χ parameter. *Soft Matter* **2012**, *8*, 9356.

[89] Jackson, E. A.; Hillmyer, M. A. Nanoporous membranes derived from block copolymers: from drug delivery to water filtration. *ACS Nano* **2010**, *4*, 3548–3553.

[90] Helgesen, M.; Søndergaard, R.; Krebs, F. C. Advanced materials and processes for polymer solar cell devices. *Journal of Materials Chemistry* **2010**, *20*, 36–60.

[91] Jannasch, P. Recent developments in high-temperature proton conducting polymer electrolyte membranes. *Current Opinion in Colloid & Interface Science* **2003**, *8*, 96–102.

[92] Lodge, T. P. A unique platform for materials design. *Science* **2008**, *50*, 10–12.

[93] Bates, F. S.; Maurer, W. W.; Lodge, T. P.; Schulz, M.; Matsen, M.; Almdal, K.; Mortensen, K. Isotropic Lifshitz Behavior in Block Copolymer-Homopolymer Blends. *Physical Review Letters* **1995**, *75*, 4429–4432.

[94] Bates, F. S.; Maurer, W. W.; Lipic, P. M.; Hillmyer, M. A.; Almdal, K.; Mortensen, K.; Fredrickson, G. H.; Lodge, T. P. Polymeric Bicontinuous Microemulsions. *Physical Review Letters* **1997**, *79*, 849–852.

[95] Berk, N. Scattering properties of a model bicontinuous structure with a well defined length scale. *Physical Review Letters* **1987**, *58*, 2718–2721.

[96] Winsor, P. A. Hydrotropy, solubilisation and related emulsification processes. *Transactions of the Faraday Society* **1948**, *44*, 376.

[97] Scriven, L. E. Equilibrium bicontinuous structure. *Nature* **1976**, *263*, 123–125.

[98] Strey, R. Microemulsion microstructure and interfacial curvature. *Colloid & Polymer Science* **1994**, *272*, 1005–1019.

[99] Jahn, W.; Strey, R. Microstructure of microemulsions by freeze fracture electron microscopy. *The Journal of Physical Chemistry* **1988**, *92*, 2294–2301.

[100] Teubner, M.; Strey, R. Origin of the scattering peak in microemulsions. *The Journal of Chemical Physics* **1987**, *87*, 3195–3200.

[101] Washburn, N. R.; Lodge, T. P.; Bates, F. S. Ternary polymer blends as model surfactant systems. *The Journal of Physical Chemistry B* **2000**, *104*, 6987–6997.

[102] Morkved, T. L.; Chapman, B. R.; Bates, F. S.; Lodge, T. P.; Stepanek, P.; Almdal, K. Dynamics of ternary polymer blends: Disordered, ordered and bicontinuous microemulsion phases. *Faraday Discussions* **1999**, *112*, 335–350.

[103] Fredrickson, G. H.; Bates, F. S. Design of bicontinuous polymeric microemulsions. *Polymer Science Part B: Polymer* **1997**, *35*, 2775–2786.

[104] Hillmyer, M. A.; Maurer, W. W.; Lodge, T. P.; Bates, F. S. Model bicontinuous microemulsions in ternary homopolymer/block copolymer blends. *The Journal of Physical Chemistry B* **1999**, *103*, 4814–4824.

[105] Broseta, D.; Fredrickson, G. H. Phase equilibria in copolymer/homopolymer ternary blends: Molecular weight effects. *The Journal of Chemical Physics* **1990**, *93*, 2927–2938.

[106] Jeon, H.; Lee, J.; Balsara, N. An experimental study of the thermodynamic properties of multicomponent polyolefin blends with ordered and disordered phases. *Macromolecules* **1998**, *9297*, 3340–3352.

[107] Krishnan, K.; Almdal, K.; Burghardt, W. R.; Lodge, T. P.; Bates, F. S. Shear-Induced Nano-Macro Structural Transition in a Polymeric Bicontinuous Microemulsion. *Physical Review Letters* **2001**, *87*, 098301.

[108] Krishnan, K.; Burghardt, W. R.; Lodge, T. P.; Bates, F. S. Transient Rheology of a Polymeric Bicontinuous Microemulsion. *Langmuir* **2002**, *18*, 9676–9686.

[109] Caputo, F.; Burghardt, W. R.; Krishnan, K.; Bates, F.; Lodge, T. Time-resolved small-angle x-ray scattering measurements of a polymer bicontinuous microemulsion structure factor under shear. *Physical Review E* **2002**, *66*, 1–18.

[110] Burghardt, W. R.; Krishnan, K.; Bates, F. S.; Lodge, T. P. Linear Viscoelasticity of a Polymeric Bicontinuous Microemulsion. *Macromolecules* **2002**, *35*, 4210–4215.

[111] Corvazier, L.; Salou, C.; Young, R. Lamellar phases and microemulsions in model ternary blends containing amphiphilic block copolymers. *J. Mater. Chem.* **2001**, *11*, 2864–2874.

[112] Zhou, N.; Bates, F. S.; Lodge, T. P. Mesoporous membrane templated by a polymeric bicontinuous microemulsion. *Nano Letters* **2006**, *6*, 2354–2357.

[113] Zhou, N.; Lodge, T. P.; Bates, F. S. Influence of conformational asymmetry on the phase behavior of ternary homopolymer/block copolymer blends around the bicontinuous microemulsion channel. *The Journal of Physical Chemistry B* **2006**, *110*, 3979–89.

[114] Habersberger, B. M.; Gillard, T. M.; Hickey, R. J.; Lodge, T. P.; Bates, F. S. Fluctuation Effects in Symmetric Diblock Copolymer-Homopolymer Ternary Mixtures near the Lamellar-Disorder Transition. *ACS Macro Letters* **2014**, *3*, 1041–1045.

[115] Hickey, R. J.; Gillard, T. M.; Irwin, M. T.; Lodge, T. P.; Bates, F. S. Structure, viscoelasticity, and interfacial dynamics of a model polymeric bicontinuous microemulsion. *Soft Matter* **2016**, *12*, 53–66.

[116] Lee, J. H.; Balsara, N. P.; Krishnamoorti, R.; Jeon, H. S.; Hammouda, B. Designing Balanced Surfactants for Mixtures of Immiscible Polymers. *Macromolecules* **2001**, *34*, 6557–6560.

[117] Lee, J. H.; Ruegg, M. L.; Balsara, N. P.; Zhu, Y.; Gido, S. P.; Krishnamoorti, R.; Kim, M.-h. Phase Behavior of Highly Immiscible Polymer Blends Stabilized by a Balanced Block Copolymer Surfactant. *Macromolecules* **2003**, *36*, 6537–6548.

[118] Ruegg, M. L.; Reynolds, B. J.; Lin, M. Y.; Lohse, D. J.; Balsara, N. P. Microphase and Macrophase Separation in Multicomponent A/B/A-C Polymer Blends with Attractive and Repulsive Interactions. *Macromolecules* **2006**, *39*, 1125–1134.

[119] Ruegg, M. L.; Reynolds, B. J.; Lin, M. Y.; Lohse, D. J.; Krishnamoorti, R.; Balsara, N. P. Effect of Pressure on a Multicomponent A/B/A-C Polymer Blend with Attractive and Repulsive Interactions. *Macromolecules* **2007**, *40*, 355–365.

[120] Nedoma, A. J.; Lai, P.; Jackson, A.; Robertson, M. L.; Wanakule, N. S.; Balsara, N. P. Phase Behavior of Asymmetric Multicomponent A/B/A-C Blends with Unequal Homopolymer Molecular Weights. *Macromolecules* **2010**, *43*, 3549–3555.

[121] Fleury, G.; Bates, F. S. Hierarchically structured bicontinuous polymeric microemulsions. *Soft Matter* **2010**, *6*, 2751–2759.

[122] Habersberger, B. M.; Bates, F. S.; Lodge, T. P. Hierarchical microphase separation in bicontinuous ternary polymer blends. *Soft Matter* **2012**, *8*, 3429–3441.

[123] Jones, B. H. Polymeric Bicontinuous Microemulsions as Templates for Nanostructured Materials. Ph.D. thesis, University of Minnesota, 2011.

[124] Jones, B.; Lodge, T. High-temperature nanoporous ceramic monolith prepared from a polymeric bicontinuous microemulsion template. *Journal of the American Chemical Society* **2009**, *131*, 1676–1677.

[125] Jones, B. H.; Lodge, T. P. Nanoporous Materials Derived from Polymeric Bicontinuous Microemulsions. *Chemistry of Materials* **2010**, *22*, 1279–1281.

[126] Jones, B. H.; Cheng, K.-Y.; Holmes, R. J.; Lodge, T. P. Nanoporous Poly(3,4-ethylenedioxythiophene) Derived from Polymeric Bicontinuous Microemulsion Templates. *Macromolecules* **2012**, *45*, 599–601.

[127] Jones, B.; Lodge, T. Hierarchically Porous Silica Prepared from Ionic Liquid and Polymeric Bicontinuous Microemulsion Templates. *Chemistry of Materials* **2011**, 4824–4831.

[128] Hickey, R. J.; Gillard, T. M.; Lodge, T. P.; Bates, F. S. Influence of Composition Fluctuations on the Linear Viscoelastic Properties of Symmetric Diblock Copolymers near the Order-Disorder Transition. *ACS Macro Letters* **2015**, *4*, 260–265.

[129] Irwin, M. T.; Hickey, R. J.; Bates, F. S.; Lodge, T. P. Readily Tuning the Phase Behavior of Sphere-forming Block Polymers via Lithium Salt Addition. *Manuscript in Preparation.*

[130] Irwin, M. T.; Hickey, R. J.; Xie, S.; So, S.; Bates, F. S.; Lodge, T. P. Structure-Conductivity Relationships in Ordered and Disordered Salt-doped Diblock Copolymer/Homopolymer Blends. *Macromolecules* **2016**,

[131] Huang, Y. Y.; Hsu, J. Y.; Chen, H. L.; Hashimoto, T. Existence of fcc-packed spherical micelles in diblock copolymer melt. *Macromolecules* **2007**, *40*, 406–409.

[132] Cavicchi, K. A.; Lodge, T. P. Self-Diffusion and Tracer Diffusion in Sphere-Forming Block Copolymers. *Macromolecules* **2003**, *36*, 7158–7164.

[133] Cavicchi, K. A.; Lodge, T. P. Domain size equilibration in sphere-forming block copolymers. *Journal of Polymer Science Part B: Polymer Physics* **2003**, *41*, 715–724.

[134] Choi, S.-H.; Bates, F. S.; Lodge, T. P. Molecular Exchange in Ordered Diblock Copolymer Micelles. *Macromolecules* **2011**, *44*, 3594–3604.

[135] Zhang, J.; Sides, S.; Bates, F. S. Ordering of Sphere Forming SISO Tetrablock Terpolymers on a Simple Hexagonal Lattice. *Macromolecules* **2012**, *45*, 256–265.

[136] Zhang, J.; Bates, F. S. Dodecagonal Quasicrystalline Morphology in a Poly(styrene-b-isoprene-b-styrene-b-ethylene oxide) Tetrablock Terpolymer. *Journal of the American Chemical Society* **2012**, *134*, 7636–7639.

[137] Chanpuriya, S.; Kim, K.; Zhang, J.; Lee, S.; Arora, A.; Dorfman, K. D.; Delaney, K. T.; Fredrickson, G. H.; Bates, F. S. Cornucopia of Nanoscale Ordered Phases in Sphere-Forming Tetrablock Terpolymers. *ACS Nano* **2016**, *10*, 4961–4972.

[138] Arora, A.; Qin, J.; Morse, D. C.; Delaney, K. T.; Fredrickson, G. H.; Bates, F. S.; Dorfman, K. D. Broadly Accessible Self-Consistent Field Theory for Block Polymer Materials Discovery. *Macromolecules* **2016**, *49*, 4675–4690.

[139] So, S.; Lodge, T. P. Interfacial Tension-Hindered Phase Transfer of Polystyrene-b-poly(ethylene oxide) Polymersomes from a Hydrophobic Ionic Liquid to Water. *Langmuir* **2015**, *31*, 594–601.

[140] Fetters, L. J.; Lohse, D. J.; Richter, D.; Witten, T. A.; Zirkel, A. Connection between Polymer Molecular Weight, Density, Chain Dimensions, and Melt Viscoelastic Properties. *Macromolecules* **1994**, *27*, 4639–4647.

[141] Cochran, E. W.; Bates, F. S. Thermodynamic behavior of poly(cyclohexylethylene) in polyolefin diblock copolymers. *Macromolecules* **2002**, *35*, 7368–7374.

[142] Hiemenz, P. C.; Lodge, T. P. Light Scattering by Polymer Solutions 8.1. **2007**, 289–326.

[143] Zhang, J. Phase behaviors of ABAC tetrablock terpolymers. Ph.D. thesis, University of Minnesota, 2012.

[144] Iwami, S.; Ishimasa, T. Dodecagonal quasicrystal in Mn-based quaternary alloys containing Cr, Ni and Si. *Philosophical Magazine Letters* **2015**, *95*, 229–236.

[145] Hajiw, S.; Pansu, B.; Sadoc, J.-F. Evidence for a C14 Frank-Kasper Phase in One-Size Gold Nanoparticle Superlattices. *ACS Nano* **2015**, *9*, 8116–8121.

[146] Maurer, W. W.; Bates, F. S.; Lodge, T. P.; Almdal, K.; Mortensen, K.; Fredrickson, G. H. Can a single function for χ account for block copolymer and homopolymer blend phase behavior? *The Journal of Chemical Physics* **1998**, *108*, 2989–3000.

[147] Seo, M.; Hillmyer, M. A. Reticulated Nanoporous Polymers by Controlled Polymerization-Induced Microphase Separation. *Science* **2012**, *336*, 1422–1425.

[148] McIntosh, L. D.; Schulze, M. W.; Irwin, M. T.; Hillmyer, M. A.; Lodge, T. P. Evolution of Morphology, Modulus, and Conductivity in Polymer Electrolytes Prepared via Polymerization-Induced Phase Separation. *Macromolecules* **2015**, *48*, 1418–1428.

[149] Khurana, R.; Schaefer, J. L.; Archer, L. A.; Coates, G. W. Suppression of Lithium Dendrite Growth Using Cross-Linked Polyethylene/Poly(ethylene oxide) Electrolytes: A New Approach for Practical Lithium-Metal Polymer Batteries. *Journal of the American Chemical Society* **2014**, *136*, 7395–7402.

[150] Weber, R. L.; Ye, Y.; Schmitt, A. L.; Banik, S. M.; Elabd, Y. A.; Mahanthappa, M. K. Effect of nanoscale morphology on the conductivity of polymerized ionic liquid block copolymers. *Macromolecules* **2011**, *44*, 5727–5735.

[151] Kim, O.; Jo, G.; Park, Y. J.; Kim, S.; Park, M. J. Ion transport properties of self-assembled polymer electrolytes: The role of confinement and interface. *Journal of Physical Chemistry Letters* **2013**, *4*, 2111–2117.

[152] Cho, B.-K.; Jain, A.; Gruner, S.; Wiesner, U. Mesophase Structure-Mechanical and Ionic Transport Correlations in Extended Amphiphilic Dendrons. *Science* **2004**, *305*, 1598–1601.

[153] Bates, F. S.; Rosedale, J. H.; Fredrickson, G. H. Fluctuation effects in a symmetric diblock copolymer near the order-disorder transition. *The Journal of Chemical Physics* **1990**, *92*, 6255.

[154] Lee, S.; Gillard, T. M.; Bates, F. S. Fluctuations, Order, and Disorder in Short Diblock Copolymers. *AIChE Journal* **2013**, *59*, 3502–3513.

[155] Kahlweit, M.; Busse, G.; Winkler, J. Electric conductivity in microemulsions. *Journal of Chemical Physics* **1993**, *99*, 5605–5614.

[156] Kim, S. Y.; Yoon, E.; Joo, T.; Park, M. J. Morphology and conductivity in ionic liquid incorporated sulfonated block copolymers. *Macromolecules* **2011**, *44*, 5289–5298.

[157] Mark, J. E. *Physical Properties of Polymers Handbook*, 2nd ed.; Springer New York: New York, NY, 2007; p 1073.

[158] Lagues, M.; Sauterey, C. Percolation transition in water in oil microemulsions. Electrical conductivity measurements. *The Journal of Physical Chemistry* **1980**, *84*, 3503–3508.

[159] Chen, S. J.; Evans, D. F.; Ninham, B. W. Properties and structure of three-component ionic microemulsions. *The Journal of Physical Chemistry* **1984**, *88*, 1631–1634.

[160] Kahlweit, M.; Strey, R.; Haase, D.; Kunieda, H.; Schmeling, T.; Faulhaber, B.; Borkovec, M.; Eicke, H.-F.; Busse, G.; Eggers, F.; Funck, T.; Richmann, H.; Magid, L.; Söderman, O.; Stilbs, P.; Winkler, J.; Dittrich, A.; Jahn, W. How to study microemulsions. *Journal of Colloid and Interface Science* **1987**, *118*, 436–453.

[161] Fredrickson, G. H.; Helfand, E. Fluctuation effects in the theory of microphase separation in block copolymers. *The Journal of Chemical Physics* **1987**, *87*, 697.

[162] Thelen, J. L.; Teran, A. A.; Wang, X.; Garetz, B. A.; Nakamura, I.; Wang, Z.-G.; Balsara, N. P. Phase Behavior of a Block Copolymer/Salt Mixture through the Order-to-Disorder Transition. *Macromolecules* **2014**, *47*, 2666–2673.

[163] Epps, T. H.; Cochran, E. W.; Bailey, T. S.; Waletzko, R. S.; Hardy, C. M.; Bates, F. S. Ordered Network Phases in Linear Poly(isoprene-b-styrene-b-ethylene oxide) Triblock Copolymers. *Macromolecules* **2004**, *37*, 8325–8341.

[164] Brinker, K. L.; Mochrie, S. G. J.; Burghardt, W. R. Equilibrium Dynamics of a Polymer Bicontinuous Microemulsion. *Macromolecules* **2007**, *40*, 5150–5160.

[165] Qian, C. B.; Mumby, S. J.; Eichinger, B. E. Phase-Diagrams of Binary Polymer-Solutions and Blends. *Macromolecules* **1991**, *24*, 1655–1661.

[166] Orädd, G.; Edman, L.; Ferry, A. Diffusion: A comparison between liquid and solid polymer LiTFSI electrolytes. *Solid State Ionics* **2002**, *152-153*, 131–136.

[167] Mullin, S. A.; Stone, G. M.; Panday, A.; Balsara, N. P. Salt Diffusion Coefficients in Block Copolymer Electrolytes. *Journal of The Electrochemical Society* **2011**, *158*, A619.

[168] Rosedale, J. H.; Bates, F. S.; Almdal, K.; Mortensen, K.; Wignall, G. D. Order and Disorder in Symmetric Diblock Copolymer Melts. *Macromolecules* **1995**, *28*, 1429–1443.

[169] Devaux, D.; Bouchet, R.; Glé, D.; Denoyel, R. Mechanism of ion transport in PEO/LiTFSI complexes: Effect of temperature, molecular weight and end groups. *Solid State Ionics* **2012**, *227*, 119–127.

[170] Teran, A. A.; Tang, M. H.; Mullin, S. A.; Balsara, N. P. Effect of molecular weight on conductivity of polymer electrolytes. *Solid State Ionics* **2011**, *203*, 18–21.

[171] Zhu, K. J.; Chen, S. F.; Ho, T.; Pearce, E. M.; Kwei, T. K. Miscibility of copolymer blends. *Macromolecules* **1990**, *23*, 150–154.

[172] Sweat, D. P.; Kim, M.; Schmitt, A. K.; Perroni, D. V.; Fry, C. G.; Mahanthappa, M. K.; Gopalan, P. Phase Behavior of Poly(4-hydroxystyrene-block-styrene) Synthesized by Living Anionic Polymerization of an Acetal Protected Monomer. *Macromolecules* **2014**, *47*, 6302–6310.

[173] Janert, P. K.; Schick, M. Phase Behavior of Ternary Homopolymer/Diblock Blends: Influence of Relative Chain Lengths. *Macromolecules* **1997**, *30*, 137–144.

[174] Habersberger, B. M. Phase Behavior of Ternary Polymer Blends: Asymmetry, Segregation Strength, and Coexisting Phases. Ph.D. thesis, University of Minnesota, 2013.

[175] Park, M. J.; Balsara, N. P. Phase behavior of symmetric sulfonated block copolymers. *Macromolecules* **2008**, *41*, 3678–3687.

[176] Sing, C. E.; Zwanikken, J. W.; Olvera de la Cruz, M. Electrostatic control of block copolymer morphology. *Nature Materials* **2014**, *13*, 694–698.

[177] Helfand, E.; Wasserman, Z. R. Microdomain Structure and the Interface in Block Copolymer. *Developments in Block Copolymers* **1982**, *1*, 99–125.

[178] Schubert, K.-V.; Strey, R.; Kline, S. R.; Kaler, E. W. Small angle neutron scattering near Lifshitz lines: Transition from weakly structured mixtures to microemulsions. *The Journal of Chemical Physics* **1994**, *101*, 5343–5355.

[179] Schulze, M. W.; McIntosh, L. D.; Hillmyer, M. a.; Lodge, T. P. Supporting information for: High-modulus, high-conductivity nanostructured polymer electrolyte membranes via polymerization-induced phase separation. *Nano Letters* **2014**, *14*, 122–6.

[180] Webb, M. A.; Savoie, B. M.; Wang, Z.-G.; Miller III, T. F. Chemically Specific Dynamic Bond Percolation Model for Ion Transport in Polymer Electrolytes. *Macromolecules* **2015**, *48*, 7346–7358.

[181] Cussler, E. L. *Diffusion: Mass Transfer in Fluid Systems*, 3rd ed.; Cambridge University Press: Cambridge, UK, 2009.

[182] Hallinan, D. T.; Mullin, S. A.; Stone, G. M.; Balsara, N. P. Lithium Metal Stability in Batteries with Block Copolymer Electrolytes. *Journal of the Electrochemical Society* **2013**, *160*, A464–A470.

[183] Lai, J. T.; Filla, D.; Shea, R. Functional Polymers from Novel Carboxyl-Terminated Trithiocarbonates as Highly Efficient RAFT Agents. *Macromolecules* **2002**, *35*, 6754–6756.

[184] Tokuda, H.; Hayamizu, K.; Ishii, K.; Susan, M. A. B. H.; Watanabe, M. Physicochemical Properties and Structures of Room Temperature Ionic Liquids. 2. Variation of Alkyl Chain Length in Imidazolium Cation. *The Journal of Physical Chemistry B* **2005**, *109*, 6103–6110.

[185] McIntosh, L. D. Decoupling Mechanical and Ion Transport Properties in Polymer Electrolyte Membranes. Ph.D. thesis, University of Minnesota, 2014.

[186] Friebe, A.; Ulbricht, M. Controlled pore functionalization of poly(ethylene terephthalate) track-etched membranes via surface-initiated atom transfer radical polymerization. *Langmuir* **2007**, *23*, 10316–10322.

[187] Phillip, W. A. Block Polymer Membranes for Selective Separations. Ph.D. thesis, 2009.

[188] Hillmyer, M. A. In *Advances in Polymer Science*; Abetz, V., Ed.; Springer Berlin Heidelberg: Berlin, 2005; pp 137–181.

[189] Jones, B.; Lodge, T. Hierarchically Structured Materials from Block Polymer Confinement within Bicontinuous Microemulsion-Derived Nanoporous Polyethylene. *ACS nano* **2011**, 8914–8927.

[190] Amendt, M. A.; Roerdink, M.; Moench, S.; Phillip, W. A.; Cussler, E. L.; Hillmyer, M. A. Functionalized Nanoporous Membranes from Reactive Triblock Polymers. *Australian Journal of Chemistry* **2011**, *64*, 1074–1082.

[191] Matsen, M. W. Elastic properties of a diblock copolymer monolayer and their relevance to bicontinuous microemulsion. *The Journal of Chemical Physics* **1999**, *110*, 4658–4667.

[192] Uehara, H.; Kakiage, M.; Sekiya, M.; Sakuma, D.; Yamonobe, T.; Takano, N.; Barraud, A.; Meurville, E.; Ryser, P. Size-selective diffusion in nanoporous but flexible membranes for glucose sensors. *ACS Nano* **2009**, *3*, 924–932.

[193] Crossland, E. J. W.; Kamperman, M.; Nedelcu, M.; Ducati, C.; Wiesner, U.; Smilgies, D.-M.; Toombes, G. E. S.; Hillmyer, M. A.; Ludwigs, S.; Steiner, U.; Snaith, H. J. A Bicontinuous Double Gyroid Hybrid Solar Cell. *Nano Letters* **2009**, *9*, 2807–2812.

[194] Ma, W.; Yang, C.; Gong, X.; Lee, K.; Heeger, A. J. Thermally Stable, Efficient Polymer Solar Cells with Nanoscale Control of the Interpenetrating Network Morphology. *Advanced Functional Materials* **2005**, *15*, 1617–1622.

[195] Jones, B. H.; Lodge, T. P. Nanocasting nanoporous inorganic and organic materials from polymeric bicontinuous microemulsion templates. *Polymer Journal* **2012**, *44*, 131–146.

[196] Cates, M. E.; Andelmans, D.; Safran, S. A.; Roux, D. Theory of Microemulsions: Comparison with Experimental Behavior. *Langmuir* **1988**, *4*, 802–806.

[197] Barrett, E. P.; Joyner, L. G.; Halenda, P. P. The Determination of Pore Volume and Area Distributions in Porous Substances. I. Computations from Nitrogen Isotherms. *Journal of the American Chemical Society* **1951**, *73*, 373–380.

[198] Brunauer, S.; Emmett, P. H.; Teller, E. Adsorption of Gases in Multimolecular Layers. *Journal of the American Chemical Society* **1938**, *60*, 309–319.

[199] Jones, B. H.; Cheng, K.-Y.; Holmes, R. J.; Lodge, T. P. Nanoporous polyethylene thin films templated by polymeric bicontinuous microemulsions: evolution of morphology on non-neutral substrates. *ACS Applied Materials & Interfaces* **2011**, *3*, 4101–4111.

[200] Pendergast, M. M.; Hoek, E. M. A review of water treatment membrane nanotechnologies. *Energy & Environmental Science* **2011**, *4*, 1946–1791.

[201] Nguyen, A. M.; Dinh, N. P.; Cam, Q. M.; Sparrman, T.; Irgum, K. Preparation and characterization of sizable macroporous epoxy resin-based monolithic supports for flow-through systems. *Journal of Separation Science* **2009**, *32*, 2608–2618.

[202] Tsujioka, N.; Hira, N.; Aoki, S.; Tanaka, N.; Hosoya, K. A New Preparation Method for Well-Controlled 3D Skeletal Epoxy Resin-Based Polymer Monoliths. *Macromolecules* **2005**, *38*, 9901–9903.

[203] Dinh, N. P.; Cam, Q. M.; Nguyen, A. M.; Shchukarev, A.; Irgum, K. Functionalization of epoxy-based monoliths for ion exchange chromatography of proteins. *Journal of Separation Science* **2009**, *32*, 2556–2564.